



**HAL**  
open science

# Multitemporal SAR images denoising and change detection: applications to Sentinel-1 data

Weiying Zhao

► **To cite this version:**

Weiying Zhao. Multitemporal SAR images denoising and change detection: applications to Sentinel-1 data. Image Processing [eess.IV]. Université Paris Saclay (COMUE), 2019. English. NNT: 2019SACLT003. tel-02095817

**HAL Id: tel-02095817**

**<https://pastel.hal.science/tel-02095817>**

Submitted on 10 Apr 2019

**HAL** is a multi-disciplinary open access archive for the deposit and dissemination of scientific research documents, whether they are published or not. The documents may come from teaching and research institutions in France or abroad, or from public or private research centers.

L'archive ouverte pluridisciplinaire **HAL**, est destinée au dépôt et à la diffusion de documents scientifiques de niveau recherche, publiés ou non, émanant des établissements d'enseignement et de recherche français ou étrangers, des laboratoires publics ou privés.

# Multitemporal SAR images denoising and change detection—Applications to Sentinel-1 data

Thèse de doctorat de l'Université Paris-Saclay  
préparée à Télécom ParisTech

Ecole doctorale n°580 : sciences et technologies  
de l'information et de la communication (STIC)  
Spécialité de doctorat : traitement du signal et des images

Thèse présentée et soutenue à Paris, le 21 janvier 2019, par

**M. Weiyang Zhao**

## Composition du Jury :

Mme Bénédicte Fruneau MdC, HdR, UPEM, Université-Paris-Est-Marne-la-Vallée	Rapporteure
M. Jordi Inglada Ingénieur de recherche, HdR, CESBIO (CNES/CNRS/UPS/IRD), Toulouse	Rapporteur
M. René Garello Professeur, IMT Atlantique, Brest	Président
Mme Hong Sun Professeur, Université de Wuhan, Chine	Examinatrice
M. Frédéric Schmidt Professeur, Université Paris-Saclay	Examineur
Mme Florence Tupin Professeure, Télécom ParisTech	Directrice de thèse
M. Henri Maître Professeur émérite, Télécom ParisTech	Co-directeur de thèse



## Abstract

The inherent speckle which is attached to any coherent imaging system affects the analysis and interpretation of synthetic aperture radar (SAR) images. To take advantage of well-registered multi-temporal SAR images, we improve the adaptive nonlocal temporal filter with state-of-the-art adaptive denoising methods and propose a patch based adaptive temporal filter. To address the bias problem of the denoising results, we propose a fast and efficient multitemporal despeckling method. The key idea of the proposed approach is the use of the ratio image, provided by the ratio between an image and the temporal mean of the stack. This ratio image is easier to denoise than a single image thanks to its improved stationarity. Besides, temporally stable thin structures are well-preserved thanks to the multi-temporal mean. Without reference image, we propose to use a patch-based auto-covariance residual evaluation method to examine the residual image and look for possible remaining structural contents.

With speckle reduction images, we propose to use simplified generalized likelihood ratio method to detect the change area, change magnitude and change times in long series of well-registered images. Based on spectral clustering, we apply the simplified generalized likelihood ratio to detect the time series change types. Then, jet colormap and HSV colorization may be used to vividly visualize the detection results. These methods have been successfully applied to monitor farmland area, urban area, harbor region, and flooding area changes.

## Résumé

Le bruit de chatoiement (speckle) lié aux systèmes d'imagerie cohérente a des conséquences sur l'analyse et l'interprétation des images radar à synthèse d'ouverture (RSO). Pour profiter des séries temporelles d'images RSO bien recalées, nous améliorons le filtre adaptatif temporel non-local avec les méthodes de l'état de l'art en débruitage adaptatif et proposons un filtrage temporel adaptatif basé sur les patches. Pour lutter contre le problème de biais dans le résultat du débruitage, nous proposons une méthode rapide et efficace de débruitage multitemporel du speckle. L'idée principale de l'approche proposée est d'utiliser l'image de ratio, donnée par le ratio entre l'image et la moyenne temporelle de la pile. Cette image ratio est plus facile à débruiter qu'une image isolée grâce à une meilleure stationnarité. Par ailleurs, les structures fines stables dans le temps sont bien préservées grâce au moyennage multitemporel.

Avec les images débruitées, nous proposons d'utiliser la méthode du ratio de vraisemblance généralisé simplifiée pour détecter les zones de changement, l'amplitude des changements et les périodes de changements intéressantes dans de longues séries d'images correctement recalées. En utilisant le partitionnement spectral, on applique le ratio de vraisemblance généralisé simplifié pour caractériser les changements des séries temporelles. Nous visualisons les résultats de détection en utilisant l'échelle de couleur 'jet' et une colorisation HSV. Ces méthodes ont été appliquées avec succès pour étudier des zones cultivées, des zones urbaines, des régions portuaires et des changements dus à des inondations.



# Acknowledgment

Firstly, I would like to express my deep gratitude to my advisors for giving me the chance of conducting the Ph.D. research in Télécom ParisTech, for their kind supervision during the research. They opened the research door for me and gave me plenty of guidance during my research.

Besides my supervisors, I would like to thank the other Professors who collaborate to my thesis : Prof. Jean-Marie Nicolas, Dr. Loïc Denis, and Dr. Charles-Alban Deledalle, for their pleasant cooperation, which encourages me to widen my research from various perspectives; I also thank the members of the jury for their insightful comments and encouragement, which help me to improve my thesis again.

In addition, I am grateful to the China Scholarship Council (CSC) and Télécom ParisTech for providing financial support; to Université Paris Saclay for providing all the events and opportunities that helped me broaden my horizons.

I also would like to thanks the François-Mitterrand Library which provides a very quiet and comfortable place during the preparation of my thesis.

Last but not least, thanks to my parents and my relatives for supporting me spiritually throughout preparing for this thesis. Thanks to all the colleagues for their accompany and help during my daily life.

---



---

# Contents

<b>1</b>	<b>Introduction</b>	<b>1</b>
1.1	Interest of SAR time series . . . . .	2
1.1.1	Difficulties of SAR imagery and its application . . . . .	2
1.1.2	Interest of multitemporal series . . . . .	2
1.2	Considered issues and main contributions . . . . .	3
1.3	Organization of the document . . . . .	5
<b>I</b>	<b>Basics of SAR and used data</b>	<b>7</b>
<b>2</b>	<b>Basics of SAR statistics</b>	<b>9</b>
2.1	SAR data introduction . . . . .	9
2.2	SAR statistics . . . . .	11
2.2.1	Intensity and amplitude data distribution of SAR images . . . . .	12
2.2.2	Log-transformed data distribution . . . . .	14
2.2.3	Arithmetic mean . . . . .	14
2.2.4	Geometric mean . . . . .	15
2.3	ENL estimation . . . . .	17
2.4	Conclusion . . . . .	20
<b>3</b>	<b>Experimental dataset preparation</b>	<b>21</b>
3.1	Real SAR images . . . . .	21
3.1.1	Sentinel-1 and TerraSAR-X data bases . . . . .	21
3.1.2	Images registration . . . . .	25
3.1.3	Super-images . . . . .	30
3.2	Ground truth preparation . . . . .	30
3.2.1	Ground truth map in Saclay area . . . . .	31
3.2.2	Multitemporal ground truth map . . . . .	33
3.2.3	Other ground truth maps . . . . .	35
3.3	Simulated SAR images . . . . .	36
3.3.1	Unrealistic simulated images . . . . .	36
3.3.2	Realistic simulated SAR images . . . . .	37
3.4	Spatial correlation . . . . .	41
3.5	Conclusion . . . . .	43

---

---

<b>II</b>	<b>Multi-temporal denoising</b>	<b>45</b>
<b>4</b>	<b>Basics of despeckling</b>	<b>47</b>
4.1	Main despeckling approaches . . . . .	47
4.1.1	Spatial despeckling methods . . . . .	47
4.1.2	Multitemporal despeckling methods . . . . .	50
4.2	Similarity measures . . . . .	52
4.2.1	Probabilistic based similarity measure . . . . .	52
4.2.1.1	Likelihood ratio test for Gamma distributed data . . . . .	52
4.2.1.2	Likelihood ratio test for Rayleigh-Nakagami distributed data . . . . .	52
4.2.1.3	Likelihood ratio test for Fisher-Tippett distributed data . . . . .	53
4.2.2	Geometric approach . . . . .	53
4.2.3	Kernel method . . . . .	53
4.2.4	Correlation coefficient for interferometric data . . . . .	54
4.2.5	Feature based similarity . . . . .	55
4.3	Evaluation method for denoising results . . . . .	55
4.3.1	Visual analysis . . . . .	55
4.3.2	Quantitative evaluation . . . . .	57
4.4	Conclusion . . . . .	59
<b>5</b>	<b>Despeckling by weighted temporal averaging</b>	<b>61</b>
5.1	Unbiased temporal average (UTA) . . . . .	61
5.2	Nonlocal temporal filter (NLTF) . . . . .	62
5.3	Adaptive nonlocal temporal filter (ANLTF) . . . . .	64
5.3.1	Adaptive spatial averaging . . . . .	64
5.3.2	Multitemporal denoising . . . . .	64
5.4	Patch based adaptive temporal filter (PATF) . . . . .	64
5.5	Experimental results and discussion . . . . .	66
5.5.1	Estimation of different adaptive denoising approaches for ANLTF . . . . .	66
5.5.2	Despeckling results comparison using simulated data . . . . .	68
5.5.2.1	Simulated data without change . . . . .	69
5.5.2.2	Simulated Sentinel-1 data with changes . . . . .	69
5.5.3	Despeckling results comparison with SAR data . . . . .	71
5.5.3.1	With long time series . . . . .	71
5.5.3.2	Comparison with state-of-the-art methods . . . . .	73
5.6	Conclusion . . . . .	76
<b>6</b>	<b>Ratio based multi-temporal SAR images denoising</b>	<b>77</b>
6.1	Principle of the proposed method . . . . .	77
6.2	Super-image computation . . . . .	79
6.2.1	Arithmetic mean . . . . .	79
6.2.2	Binary weighted arithmetic mean . . . . .	79
6.2.3	Denoising the super-image . . . . .	80
6.3	Ratio image denoising . . . . .	81
6.3.1	Statistical analysis of the ratio . . . . .	81
6.3.2	MuLoG adaptation . . . . .	82
6.4	Online processing of long SAR time series . . . . .	83
6.4.1	Strategy to update the arithmetic mean . . . . .	84

---

---

6.4.2	Using binary weighted arithmetic mean . . . . .	85
6.5	Experimental results . . . . .	86
6.5.1	Which super-image gives the best denoising? . . . . .	87
6.5.1.1	Using simulated radar images . . . . .	87
6.5.1.2	Using Sentinel-1 images . . . . .	89
6.5.1.3	Computation time . . . . .	92
6.5.2	Denoising performances of RABASAR compared to existing methods . . . . .	92
6.5.2.1	Quantitative comparison . . . . .	94
6.5.2.2	Simulated SAR data with different ENL . . . . .	94
6.5.2.3	Sentinel-1 and TerraSAR-X image denoising . . . . .	94
6.5.3	Updating strategy with a new image . . . . .	100
6.6	Conclusion . . . . .	100
<b>III</b>	<b>Multi-temporal images change detection</b>	<b>101</b>
<b>7</b>	<b>Introduction to SAR and optical images change detection</b>	<b>103</b>
7.1	Optical remote sensing images change detection . . . . .	105
7.1.1	Comparison operators . . . . .	106
7.1.2	Deep learning based optical images change detection . . . . .	106
7.2	SAR images change detection . . . . .	108
7.2.1	Ratio and log-ratio based change detection . . . . .	108
7.2.1.1	Generalized likelihood ratio test (GLRT) . . . . .	109
7.2.1.2	Multitemporal GLRT . . . . .	110
7.2.1.3	GLRT combining noisy and denoised values . . . . .	111
7.2.2	Coherent change detection . . . . .	112
7.2.3	Image texture and structure based change operator . . . . .	112
7.2.4	Deep learning based SAR images change detection . . . . .	112
7.2.5	Decision threshold . . . . .	113
7.2.6	Change detection performance evaluation . . . . .	114
7.3	Multisensor images change detection . . . . .	114
7.4	Conclusion . . . . .	117
<b>8</b>	<b>Multitemporal SAR data change analysis based on simplified GLR</b>	<b>119</b>
8.1	Simplified GLR based change detection . . . . .	119
8.1.1	Similarity test with simplified GLR . . . . .	119
8.1.2	Changed area detection . . . . .	121
8.1.3	Change magnitude index for visualization . . . . .	122
8.1.4	Multitemporal SAR images change classification . . . . .	122
8.1.4.1	Change Criterion Matrix (CCM) . . . . .	122
8.1.4.2	Clustering by spectral clustering method . . . . .	123
8.1.4.3	Change type recognition . . . . .	124
8.2	Experimental results and discussion . . . . .	124
8.2.1	Image pair change detection . . . . .	125
8.2.2	Continuous change monitoring . . . . .	127
8.2.3	Change classification . . . . .	127
8.2.3.1	Test on simulated temporal images . . . . .	129
8.2.3.2	Change classification with Sentinel-1 data . . . . .	130

---

---

8.3	Conclusion	132
<b>9</b>	<b>Detection of change times of interest in multitemporal SAR data and visualization with extended REACTIV</b>	<b>133</b>
9.1	REACTIV visualization method	134
9.1.1	Hue (H)	134
9.1.2	Saturation (S)	134
9.1.3	Value (V)	135
9.2	Change time visualization method	135
9.2.1	Times of interest (Hue)	135
9.2.2	Changed area detection (Saturation)	137
9.2.3	Background value (Value)	137
9.2.4	Other visualization strategy	137
9.3	Experimental results and discussion	137
9.3.1	Change detection performance with different kinds of data	138
9.3.2	Change time detection	142
9.3.3	Applications with Sentinel-1 GRD data	143
9.4	Conclusion	146
<b>10</b>	<b>Conclusion and perspective</b>	<b>147</b>
10.1	Conclusion	147
10.2	Limitations and perspectives	149
	<b>Bibliography</b>	<b>168</b>

---

# Notations

## SAR Fundamentals :

$z = Ae^{j\theta}$	complex value of SAR image ;
$j$	imaginary number such that $j^2 = -1$ ;
$\phi$	phase of $z$ ;
$y = A^2$	intensity of SAR image ;
$A$ or $ z $	Amplitude of SAR image ;
$v$	multiplicative noise following a Gamma distribution ;
$x$	log-transformed data with $x = \log y$ ;
$g$	signal-independent additive noise ;
$\mathcal{G}[u, L]$	Gamma distribution with with mean $u$ and variance $u/L$ ;
$\mathcal{RN}[u_A, L]$	Rayleigh-Nakagami distribution with parameter $u_A = \sqrt{u}$ ;
$\mathcal{F}_A[u_A, L, M_f]$	Fisher distribution with three statistical parameters $u_A, L, M_f$ ;
$\mathcal{FT}[u_f, L]$	Fisher-Tippett distribution with with mean $u_f$ and variance $L$ ;
$\mathcal{MA}_{\mathcal{G}[u,L]}[N]$	the arithmetic mean distribution of $N$ samples according to a Gamma distribution of mean $u$ and number of looks $L$ ;
$k_1, k_2, k_3$	log-cumulants ;
$m_1, m_2$	first and second order moments ;
$\Sigma$	covariance matrix ;
$\sigma$	standard deviation ;
$m_1, m_2, m_3, m_4$	order moments ;
<b>Images :</b>	
• $y, y_1, y_2$	SAR intensity data ;
• $y_t, y_{t'}$	SAR intensity data acquired at different times $t$ and $t'$ ;
• $u, u_1, u_2, u_{12}$	noise free values of the intensity data ;
• $\hat{u}, \hat{u}_1, \hat{u}_2$	estimated values of the noise free values or pixel values of the denoised intensity data ;
• $\hat{u}_1^{\text{ML}}, \hat{u}_2^{\text{ML}}, \hat{u}_{12}^{\text{ML}}$	maximum likelihood estimated data ;
• $L, L_1, L_2$	original ENL of intensity data ;
• $L_t, L_{t'}$	original ENL of different intensity data $y_t, y_{t'}$ ;
• $\hat{L}_1, \hat{L}_2$	ENL of the denoised data, corresponding to $\hat{u}_1, \hat{u}_2$ respectively ;
$R$	Ratio between two pixels values ;

**Spatial and temporal index :**

- $N$  the number of pixels ;
- $M$  the number of temporal images ;
- $t, t'$  index of the number of temporal images, with  $1 \leq t \leq M$  and  $1 \leq t' \leq M$  ;
- $s, i$  pixel locations ;
- $k$  patch shift parameter to visit all the pixels centered around pixel  $s$  ;

**Patches :**

- $\mathbf{y}(s)$  patch of intensity values centered around location  $s$  ;
- $\mu$  estimated mean value of patches ;

**Operators :**

- $D(\cdot, \cdot)$  Difference between two pixels ;
- $\rho_c(z_1, z_2)$  the correlation coefficient of two complex vectors ;
- $\mathbb{E}[\cdot]$  Expectation operator ;
- $\text{Var}[\cdot]$  Variance operator ;
- $\text{Cov}[\cdot, \cdot]$  covariance operator ;
- $K(\cdot, \cdot)$  Kernel function ;
- $\text{GLR}(y_1, y_2)$  GLR test between  $y_1$  and  $y_2$  ;
- $S_{\text{GLR}}(y(s), y(i))$  Simplified generalized likelihood ratio similarity between patch  $y(s)$  and  $y(i)$  ;
- $S_{\text{KL}}(\hat{u}(s), \hat{u}(i))$  Kullback-Leibler divergence similarity between patch  $\hat{u}(s)$  and  $\hat{u}(i)$  ;
- $\omega(y_t(s), y_{t'}(s))$  weight between  $y_t(s)$  and  $y_{t'}(s)$  ;
- $\varphi[\cdot]$  binary transformation operator ;

# Chapter 1

## Introduction

Remote sensing is an acquisition technique which measures the objects or phenomena without direct physical contact with them. In general terms, it references to the technology of acquiring information through airborne or spaceborne sensors (e.g. multispectral scanner, thematic mapper, panchromatic camera, synthetic aperture radar, etc.). These sensors are powerful scientific tools which can help us better understanding the Earth and its environment. Among these different kinds of sensors, Synthetic Aperture Radar (SAR) is popularly used because of its all-time and all-weather measuring capability. The past few years have seen the launch of numerous SAR sensors, like TerraSAR-X, Cosmo-SkyMed, ALOS-2 and more recently Sentinel-1. New sensors will also be launched soon, such as TSX-NG, Cosmo-SkyMed second generation, Radarsat constellation and NISAR (Fig.1.1). A huge amount of SAR data has been acquired from different sensors with different wavelength, resolution, incidence and polarization. It has been widely used for many years, especially for Earth observation and surveillance. The combined exploitation of these images will allow reaching novel applications if the combination of images is well mastered.

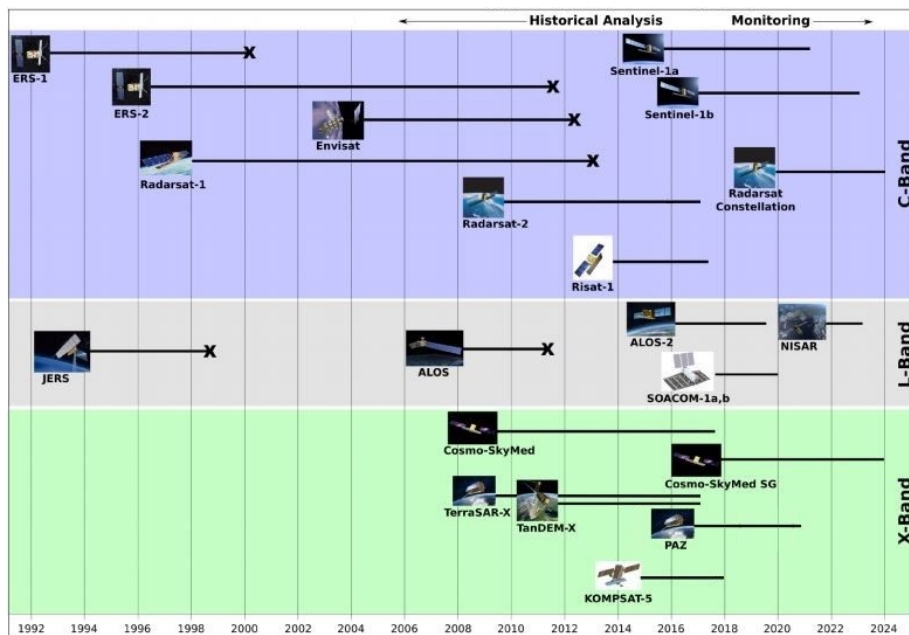


FIGURE 1.1: SAR satellite programs (presented by UANVCO with some modifications)

## 1.1 Interest of SAR time series

### 1.1.1 Difficulties of SAR imagery and its application

SAR imagery is still difficult to fully exploit because of the strong speckle noise of coherent imagery, and the sensitivity to the geometric configuration of the objects relative to the incidence angle. These issues directly cause difficulties for information extraction from SAR images and for joint use of images acquired by different sensors.

#### SAR speckle noise

In coherent imaging systems, speckle is a signal dependent noise which visually strongly degrades the appearance of images [Argenti et al., 2013]. Speckle is an inherent problem in SAR imaging. It is due to the coherent summation of backscattered signals from multiple distributed targets, which leads to image interpretation difficulties [Tupin et al., 2014]. The speckle has always been considered as an undesired information which corrupts SAR textures.

#### Combining SAR images

When acquiring SAR images with different platforms or different acquisition modes, their joint use is very difficult. A preliminary registration step is needed before exploiting SAR images. Difficulties arise on hills or mountainous terrains, and even more difficult are the cases of abrupt three dimensional (3D) changes like in urban regions. It is also very hard to combine images acquired through ascending and descending passes or covering areas with strong geometric deformations due to angular diversity.

#### Extracting pertinent information

Side-looking active system imagery causes distortion in SAR images. Dealing with images acquired by different systems is a hard problem because the Earth surface scattering mechanism depends on the radar frequency, incidence angle and polarization. The difference of data acquisition modes leads to radiometric noise and poor contours in SAR images. Thus, it raises difficulties for classification or pattern recognition tasks.

#### Combining information from various images

The way to combine heterogeneous pieces of information is still difficult. Heterogeneous data (such as multisensor, multiresolution and multimodal images) may locate in different geometric coordinate systems. The same object may have different characteristics in different kinds of images (SAR, optical images, multi-spectral images, LIDAR, etc.), which brings great difficulties for their accurate matching. The same area may have different geometric shapes in different sensor data. Joint use of multi-source information is still under exploration.

### 1.1.2 Interest of multitemporal series

SAR imagery has the main advantage of being an all-time and all-weather sensor, with a very good accuracy for the acquisition geometry and with few atmospheric effects for amplitude data. It is sensitive to dielectric properties of the surface, surface roughness, the

---

---

geometry of man-made objects and target structure. It also has the capability of subsurface penetration. We discuss here the interest of having multitemporal data.

### **Revisit time**

Thanks to SAR constellations, SAR data can be acquired in a shorter time interval, which helps monitoring dynamic changes or managing emergency events. It also provides highly correlated data for interferometric techniques, which are widely used for topography or displacement monitoring. Through collecting and comparing high temporal resolution data, the object evolution can be well monitored. This is especially useful for the monitoring of short-lived phenomena (such as a sudden disaster), vegetation seasonal changes, etc.

### **Large amount of time series information for the same object**

With a high temporal resolution of SAR images, the evolution (seasonal behavior, abrupt changes, long time displacement, etc.) of the objects can be surveyed and real features of the stable objects can be acquired through multitemporal denoising, with good resolution preservation. Based on the abundant time series information, the classification results can be undoubtedly improved.

### **Different geometry information for the objects**

With data acquired through multi-direction and different incidence angles, the influence of the geometry can be analyzed. It is especially interesting for the 3D urban area monitoring, 3D reconstruction of Earth surface or 3D change detection.

### **Different characteristics of the objects**

With multi-resolution SAR images, we can acquire the different characteristics of the same object. It can be used for multi-scale (pixel, patch, objects, global, etc.) analysis of the objects.

### **Current successful applications and possible applications**

Because of the advantages of SAR imaging, it has been widely used in land observation (crop yields, topography, mapping, soil, forestry), disaster management (flood, earthquake, volcano, landslide), atmospheric chemistry, climatology, ocean and ice (coastal geomorphology, ocean waves, ship traffic, ocean currents and topography), hydrology, surveillance and emergency management, etc. For all these applications, having long multitemporal series will be of high interest to follow the evolution.

## **1.2 Considered issues and main contributions**

The aim of this PhD is to define new approaches able to combine different satellite SAR images, in particular, acquired with similar viewing angles and along-track directions, ascending or descending, or different polarizations; and even with different platforms. These methods will be particularly evaluated with Sentinel-1 sensor which is delivered freely available images of the whole Earth. Based on the registered multitemporal SAR images, new despeckling and change analysis methods are expected.

---

## (1) Designing multitemporal denoising methods

A large number of despeckling methods have been proposed during the past decades. They recover the ground reflectivity through suppressing signal-dependent speckle variability [Tupin, 2011]. However, most of the previous methods belong to spatial despeckling methods, which only use one image during the restoration. They have to deal with a trade-off between spatial resolution preservation and noise reduction [Coltuc et al., 2002]. Non-local approach [Buades et al., 2005], which stands like a milestone in denoising field, has been successfully and widely used in SAR image denoising. We propose three kinds of frameworks which can help spatial denoising method to benefit from temporal information :

- (a) Based on the unbiased temporal denoising method proposed by [Lee, 1981b, Quegan and Yu, 2001], we utilize the state-of-the-art spatial denoising methods to estimate the initial noise free value.
- (b) In an effort to suppress the changed object effects on the multitemporal denoising results, a patch based adaptive temporal filter (PATF) is proposed. Spatial adaptive denoising methods can be utilized to improve the patch based weighted temporal average image. When the time series is large enough, spatial adaptive denoising step is optional.
- (c) The temporal average of multitemporal SAR images (called “super-image”) presents less noise, especially for stable targets. We propose a new method based on the use of “super-image”. The proposed approach can be divided into three steps : 1) estimation of a “super-image” by temporal averaging and possibly spatial denoising ; 2) denoising of the ratio between the noisy image of interest and the “super-image” ; 3) computation of the denoised image by re-multiplying the denoised ratio by the “super-image”. Because of the improved spatial stationarity of the ratio images, denoising these ratio images with a speckle-reduction method is more effective than denoising images from the original multi-temporal stack. The amount of jointly processed data is also reduced compared to other methods through the use of the “super-image” which sums up the temporal stack. In addition, we also propose some compression ways to reduce the “big data” problem, arising from manipulating long time series. This is one of the main contributions of our work [Zhao et al., 2018, 2019].

## (2) Detecting and analyzing multitemporal changes

Timely, accurately and continuously monitoring land cover and land use changes is important for land resource management. Because of all-weather property and short revisit time, change detection is a very important application of SAR imagery. Although many methods have already been proposed, we aim at comparing and improving these approaches. With the denoising data obtained with our proposed multitemporal denoising method, the change detection results can be effectively improved. Most of the traditional change detection methods only determine if the pixels changed or not. We propose methods to detect the change magnitude, change types and change times of the changed areas.

## (d) Change area detection and visualization

Current spatial adaptive denoising methods always provide denoised data with spatially variable equivalent number of looks (ENL), which is an important parameter of SAR statistics. We propose a simplified generalized likelihood ratio

( $S_{GLR}$ ) method assuming that corresponding temporal pixels have the same equivalent number of looks. The theoretical threshold can be calculated through the use of chi-square cumulative distribution function. This method has the ability to identify and measure building area and farmland area changes. To distinguish increase from decrease of backscattering values, we used a signum function  $sign()$  to convert  $S_{GLR}$  to positive values and negative values. With rainbow index color, we propose a more intuitive change magnitude visualization. The change magnitude is combined with the denoised image, which makes the detection results more intuitive.

(e) Change type detection

During the time series acquisition, changes may occur at multiple times and with different magnitudes. To detect the change types, we propose an improved change classification method inspired by NORCAMA method [Su et al., 2015] and spectral clustering method [Shi and Malik, 2000, Ng et al., 2002]. Thanks to data processed by RABASAR [Zhao et al., 2018], theoretical threshold definition method and improved spectral clustering method, we obtain much better change type detection. The output consists of different colors which represent different change types.

(f) Change time visualization

Understanding the state of changed areas requires that precise information be given about the changes. Thus, detecting different kinds of changes is important for land surface monitoring. Changes usually represent transitions that occur between states [Aminikhanghahi and Cook, 2017]. Using colorful image can vividly demonstrate the detection results. In change detection field, a number of studies have used different colors to show different changes. However, none of them associate the colors with different long time series change times. We adapt Rapid and EAsy Change detection in radar Time-series by Variation coefficient (REACTIV) method [Koeniguer et al., 2018a] to integrate our proposed denoising results. In addition, we apply a generalized likelihood ratio test in this framework to detect the change starting and ending times, the maximum change magnitude time and the maximum change significance time.

(3) Applications : joint use of multitemporal Sentinel data and study of Saclay area

Among the launched SAR satellites, Sentinel images are particularly interesting because of their free and open access, short revisit time, multiple-acquisition mode and abundant data acquired by Sentinel missions. We will pay attention to the joint use of different Sentinel images acquired using different sensors, specifically, applying the proposed new methods for the registration of images acquired by different sensors or modes (optical / SAR, ascending / descending or multi-aspect and multi-baseline SAR data), denoising, change detection. We intend to apply the developed methods in Saclay area, with the development of a ground truth map and providing a history of the construction area. Experiments are started with a time series SAR images acquired with the same orbit, same sensor and same mode. In addition, we will apply the proposed method to monitor flooding areas and the development of some cities.

### 1.3 Organization of the document

The arrangement of this document is as follows. Part I presents the basics of SAR and used data. Chapter 2 presents different SAR data (multilook complex SAR data, intensity,

amplitude, geometric mean and arithmetic mean) probability distribution functions and some parameter estimation approaches. We choose Saclay area as our main test place. The database and its preparation will be described in chapter 3. In this part, the spatial correlation in the SAR images and several reduction approaches are also discussed. Then, the speckle denoising approaches are reviewed in Part II. Along with the improvement of unbiased multitemporal denoising method, the proposed patch-based weighted temporal average and the proposed ratio based multitemporal denoising method (RABASAR [Zhao et al., 2018]). In Part III, we mainly pay attention to the change detection techniques. After reviewing the current popularly used change detection methods, we introduce the change area, change magnitude, change classes and change time detection methods. Finally, conclusion and perspectives are presented.

---

## Part I

# Basics of SAR and used data

---



## Chapter 2

# Basics of SAR statistics

Synthetic-aperture radar (SAR) is a technique for remotely sensing on object and creating two-dimensional or three-dimensional images. The sensor is typically installed on a moving platform, such as an aircraft or spacecraft, and looking at the ground in side. To create a SAR image, successive pulses of radio waves are transmitted to sense a target scene, and the backscattered waves are received and recorded. The pulses are transmitted and the backscattered waves are received using a single beam-forming antenna, with wavelengths of several millimeters up to a meter. During the movement of the aircraft or spacecraft mounted with SAR device, the antenna location with respect to the target scene changes with time. Signal processing of the successive recorded radar backscattered waves allows the combination of the records from the multiple antenna positions. The synthetic antenna aperture, which can create higher-resolution images than a given physical antenna, is formed through this process [Griffiths et al., 2014].

Thanks to its properties, SAR imaging technology has many applications. It can provide information on natural disaster areas (such as flooding, earthquake or firing areas) for emergency issues, soil moisture for the agricultural applications, ice hazard and sea state maps to navigators, etc. All this significant useful information is contained in the SAR data.

Extracting information from SAR images is usually based on some prior knowledge which is encapsulated in models for both the data and scene properties [Oliver and Quegan, 2004b]. In this chapter, we will introduce some popularly used SAR image statistical models which will be used in the following chapters.

### 2.1 SAR data introduction

A Synthetic Aperture Radar, or SAR, is a coherent side-looking radar system which uses the flight path (in the azimuth direction with speed  $V_{S/C}$ ) of the platform to simulate an extremely large antenna or aperture electronically, and to generate high-resolution remote sensing imagery [Baghdadi and Zribi, 2016]. The SAR-processor transmits pulses and receives signals in the slant range direction (Fig.2.1(a)), then stores all the returned signals, as complex values.

Because of the slant range sampling, slant range distortions (such as foreshortening, layover, shadowing effects) occur when the radar beam reaches an object with different height compared to the surrounding objects. These distortions (Fig.2.1(b)) result in a varying image scale related to the range distances.

---

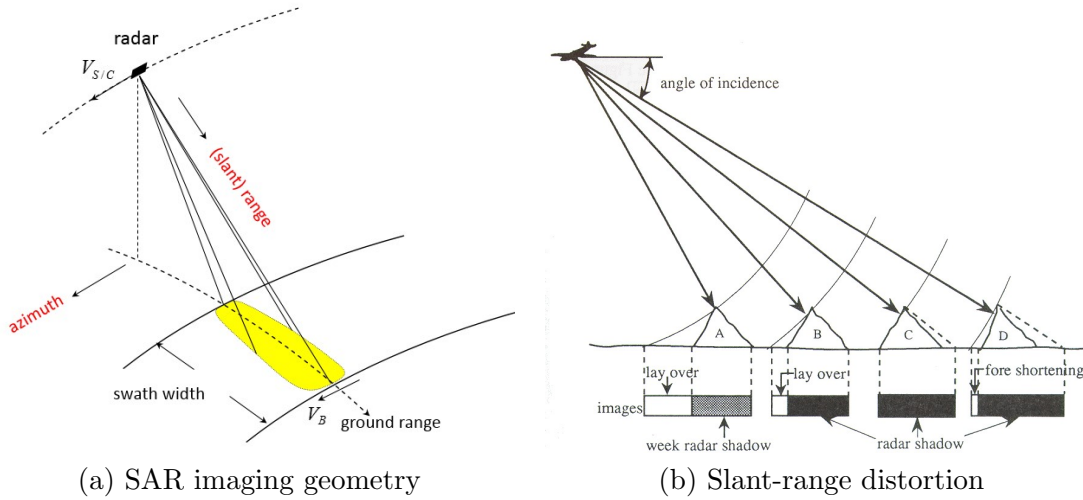


FIGURE 2.1: SAR imaging geometry and some distortions. Images are provided by : (a) SAREDU (<https://saredu.dlr.de/>), (b) ACRoRS (<http://wtlab.iis.u-tokyo.ac.jp/~wataru/lecture/rsgis/>).

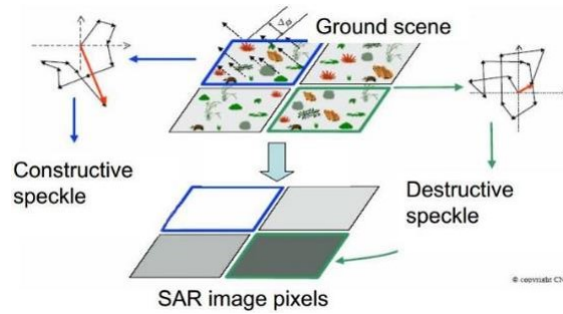


FIGURE 2.2: Physical characteristics of each pixel in the SAR image

As can be seen from figure 2.2, each pixel in the SAR image corresponds to a small region of the ground. Usually, the wavelength of the SAR signal is smaller than the resolution cell. The summation of the radar signals in a resolution cell can be expressed as a resulting complex value which contains an amplitude  $A$  and phase  $\phi$  information :

$$z = Ae^{j\phi} \quad (2.1)$$

$$y = A^2 \quad (2.2)$$

where  $j$  is the imaginary number,  $y$  is the intensity or reflectivity.

As shown in figure 2.3, the imaginary and real components of the complex data are very noisy. They only show limited structures. In addition, the phase angle appears like noise and shows no structure. However, the amplitude image, although noisy, is easier to interpret. The statistical behavior of these images is modeled as speckle [Oliver and Quegan, 2004b]. This phenomenon is caused by the large amount of independent random backscatters in each resolution cell.

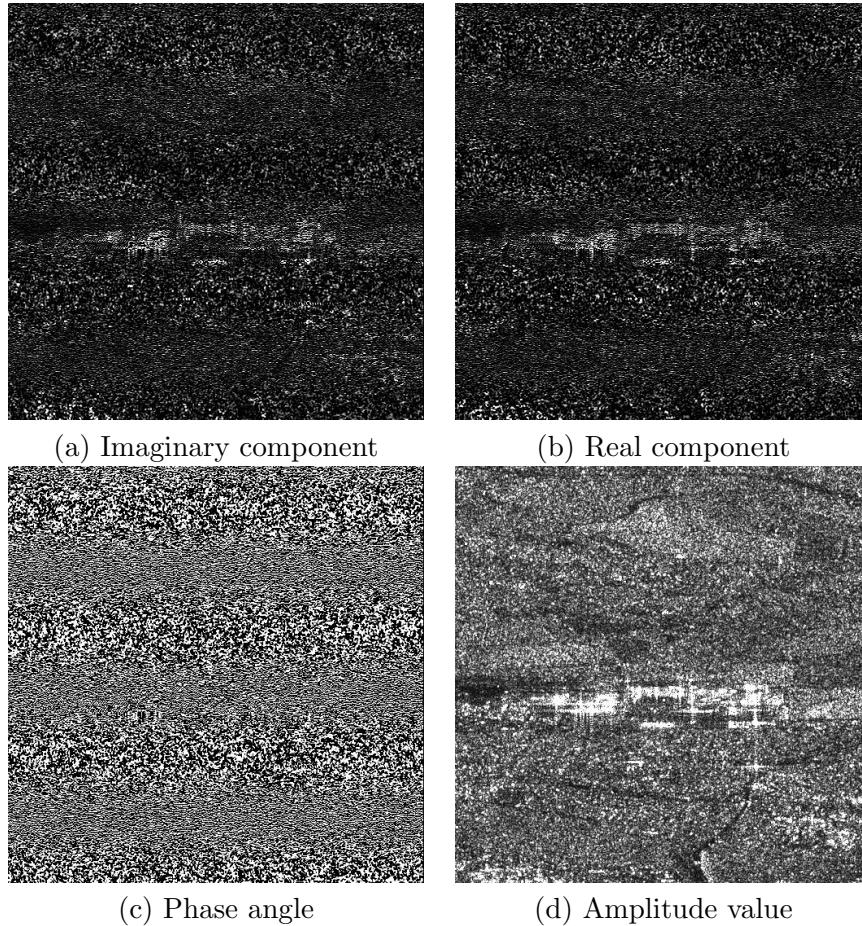


FIGURE 2.3: Different representations of the complex Sentinel-1 IW SLC image. The SAR image was acquired over Saclay area, South of Paris, France.

Giving two well registered complex images  $z_1$  and  $z_2$ , we can compute the correlation coefficient  $\rho_c(z_1, z_2)$  through :

$$\rho_c(z_1, z_2) = \frac{\mathbb{E}[z_1 z_2^\dagger]}{\sqrt{(\mathbb{E}[|z_1|^2] \mathbb{E}[|z_2|^2])}} \quad (2.3)$$

with

$$A_1^2 = \mathbb{E}[|z_1|^2], \quad A_2^2 = \mathbb{E}[|z_2|^2] \quad (2.4)$$

$$\phi = \arg(z_1 z_2^\dagger) \quad (2.5)$$

where  $\dagger$  represents the complex conjugate and  $\mathbb{E}[\cdot]$  is the expectation operator.

## 2.2 SAR statistics

The electromagnetic scattering mechanisms result in a Goodman's speckle noise [Goodman, 1976]. Fortunately, there is one well grounded statistical model of scattering, which can be expressed as multiplicative noise and is widely used when processing SAR images. Many models have been proposed, some relying on physical hypotheses of scattering mechanisms, others more empirical. These different models have been proposed because of

the great variety of physical situations and because of the different needs of the user [Tison et al., 2004].

### 2.2.1 Intensity and amplitude data distribution of SAR images

Resolution cells are made up of many scatterers with different phases, leading to interferences and a noise-like effect known as speckle. To limit the effect of speckle, usually  $L$  pixels are averaged ( $L$  is called the number of looks). The distributions of intensity (square of the modules of the backscattered signal) and amplitude (module of the backscattered signal) for homogeneous cases are Gamma (Eq.2.6) and Rayleigh-Nakagami distributions (Eq.2.10) [Tupin et al., 2014], respectively.

Under Goodman's hypothesis [Goodman, 2007], the fully developed intensity speckle follows a Gamma distribution  $\mathcal{G}[u, L]$  depending on the number of looks  $L$  and the mean reflectivity  $u$  of the scene :

$$\mathcal{G}[u, L](y) = \frac{L}{u\Gamma(L)} \left(\frac{Ly}{u}\right)^{L-1} e^{-\frac{Ly}{u}} \quad (2.6)$$

Gamma distribution with different parameters is shown as figure 2.4. Speckle in coherently processed SAR data acts like a multiplicative noise and the speckle model can be expressed as [Lee, 1981b] :

$$y = uv \quad (2.7)$$

$$\mathbb{E}[y] = u \quad (2.8)$$

$$\text{Var}[y] = u^2/L \quad (2.9)$$

where  $v$  follows a Gamma distribution  $\mathcal{G}[1, L]$ ,  $\text{Var}[\cdot]$  represents the variance operator. With the increase of the number of looks  $L$ , the variance  $u^2/L$  decreases. A multiplicative signal model can be used to describe both intensity and amplitude data.

For amplitude data, we obtain a Rayleigh-Nakagami probability density function (pdf) :

$$\mathcal{RN}[u_A, L](A) = \left(\frac{L}{u_A^2}\right)^L \frac{2A^{2L-1}}{\Gamma(L)} \exp\left[-\frac{LA^2}{u_A^2}\right] \quad (2.10)$$

with  $u_A = \sqrt{u}$ .

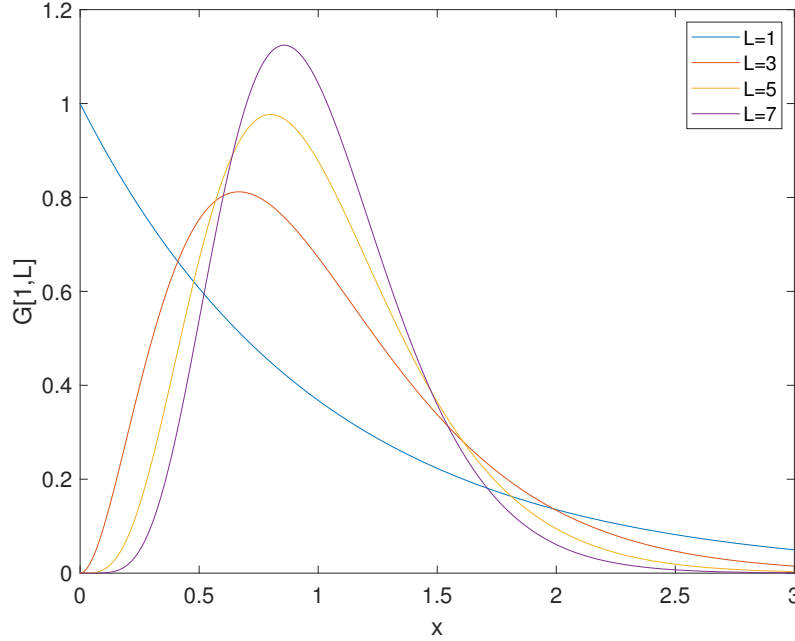


FIGURE 2.4: Gamma distributions with  $L$  equal to 1, 3, 5 and 7, with mean equal to 1. The distribution tends to narrow as  $L$  increases.

If a texture of the scene is taken into account, more complex distributions have to be used. For most cases, Fisher distribution fits very well with the amplitude SAR data histogram when measuring SAR backscattering statistics [Tison et al., 2004].

If we consider the speckle is modeled by Rayleigh-Nakagami distribution  $\mathcal{RN}[u_A, L]$  and the texture is modeled by an inverse Rayleigh-Nakagami distribution  $\mathcal{RN}\mathcal{I}(u_A, M)$ , the resulting Fisher distribution [Quin et al., 2014] can be computed using the Mellin convolution  $\hat{\star}$  [Nicolas, 2017] :

$$\mathcal{F}_A[u_A, L, M_f] = \mathcal{RN}[u_A, L] \hat{\star} \mathcal{RN}\mathcal{I}(u_A, M_f) \quad (2.11)$$

with

$$\mathcal{RN}\mathcal{I}(u_A, M_f)(A) = \frac{2 \left( \frac{\sqrt{M_f} u}{A} \right)^{2M_f} \exp \left[ - \left( \frac{\sqrt{M_f} u}{A} \right)^2 \right]}{A \Gamma(M_f)} \quad (2.12)$$

Then, the Fisher distribution can be expressed as :

$$\mathcal{F}_A[u_A, L, M_f](A) = \frac{2\Gamma(L + M_f)}{\Gamma(L)\Gamma(M_f)} \frac{\sqrt{\frac{L}{M_f}} \left( \frac{\sqrt{\frac{L}{M_f}} A}{u_A} \right)^{2L-1}}{\left( 1 + \left( \frac{\sqrt{\frac{L}{M_f}} A}{u_A} \right)^2 \right)^{L+M_f}} \quad (2.13)$$

where  $M_f$  is one of the statistical parameters of Fisher distribution.

The three parameters of Fisher distribution can be obtained with the mathematical expression of log-cumulants as follows [Nicolas, 2006] :

$$\tilde{k}_1 = \log(u) + \frac{1}{2}(\Psi(L) - \log(L)) - (\Psi(M_f) - \log(M_f)) \quad (2.14)$$

$$\tilde{k}_2 = \frac{1}{4}(\Psi(1, L) + \Psi(1, M_f)) \quad (2.15)$$

$$\tilde{k}_3 = \frac{1}{8}(\Psi(2, L) + \Psi(2, M_f)) \quad (2.16)$$

where  $\Psi(\cdot)$  is the digamma function,  $\Psi(n, \cdot)$  is the  $n$ -th polygamma function.

Empirical expressions for the three first orders, which can be used for the computation of the first three log-cumulant estimators, are as follows [Tison et al., 2004, Nicolas, 2006].

$$\hat{k}_1 = \frac{1}{N} \sum_{i=1}^N [\log(\sqrt{y_i})] \quad (2.17)$$

$$\hat{k}_2 = \frac{1}{N} \sum_{i=1}^N [\log(\sqrt{y_i}) - \hat{k}_1]^2 \quad (2.18)$$

$$\hat{k}_3 = \frac{1}{N} \sum_{i=1}^N [\log(\sqrt{y_i}) - \hat{k}_1]^3 \quad (2.19)$$

where  $y_i$  are the observed intensity values,  $N$  is the number of used samples.

### 2.2.2 Log-transformed data distribution

After applying a homomorphic transformation to the intensity data, the multiplicative noise is changed to an additive one, and the log-transformed data follows Fisher-Tippett distribution [Xie et al., 2002b] ( $\mathcal{FT}$ ) :

$$\mathcal{FT}[u_f, L](x) = \frac{L^L}{\Gamma(L)} e^{L(x-u_f)} \exp(-Le^{x-u_f}) \quad (2.20)$$

where  $x = \log y$ ,  $u_f = \log u$ .

$$x = u_f + g \quad (2.21)$$

$$\mathbb{E}[x] = u_f - \log L + \Psi(L) \quad (2.22)$$

$$\text{Var}[x] = \Psi(1, L) \quad (2.23)$$

$g$  is a signal-independent additive noise with Fisher-Tippett pdf and  $\Psi(1, L)$  is the first-order Polygamma function. Equation (2.22) implies that averaging log-transformed values should be followed by a debiasing step to recover the mean value.

### 2.2.3 Arithmetic mean

As said before, a simple way to reduce speckle fluctuations is multi-looking which makes the average of  $L$  values ( $L$  being the number of looks or the equivalent number of looks for correlated data). This averaging can be extended to  $N$  spatial or temporal samples.

## (1) Arithmetic mean with intensity data

With a long time series  $\{y_1, y_2, \dots, y_N\}$ , the arithmetic mean is calculated as :

$$y^{AM} = \frac{1}{N} \sum_{i=1}^N y_i \quad (2.24)$$

It is possible to express the distribution  $\mathcal{MA}_{\mathcal{G}[u,L]}[N](y)$  of the arithmetic mean distribution of  $N$  samples according to a Gamma distribution [Nicolas, 2006]. It is also a Gamma distribution, because Gamma distribution verifies the addition theorem :

$$\mathcal{MA}_{\mathcal{G}[u,L]}[N](y) = \mathcal{G}[u, NL](y) \quad (2.25)$$

Then, the order moments can be calculated with :

$$m_{1,\mathcal{MA}} = u \quad (2.26)$$

$$m_{2,\mathcal{MA}} = u^2 \left( \frac{NL + 1}{NL} \right) \quad (2.27)$$

Based on the two moments, we can calculate the associated standard deviation :

$$\sigma_{\mathcal{MA}} = \sqrt{m_2 - m_1^2} = \frac{u}{\sqrt{NL}} \quad (2.28)$$

In practice, the arithmetic mean is computed with intensity values following the Gamma pdf. It can be used to reduce speckle when dealing with multitemporal data.

## (2) Arithmetic mean with amplitude data

Unlike Gamma distributed random variables, the sum of Rayleigh-Nakagami distributed random variables is not known in closed-form. Usually, people do not use the arithmetic mean of amplitude data because the pdf would be much more complicated. The mean value computed based on  $\mathcal{RN}[u_A, L](A)$  belongs to quadratic mean, which is the square root of intensity geometric mean.

In the following, we will use the term ‘‘arithmetic mean’’ for short. It should be understood as the arithmetic mean of intensity images, displayed in amplitude format for the figures.

### 2.2.4 Geometric mean

One can also use the geometric mean instead of the arithmetic mean [Quin et al., 2014]. A full study of this mean can be found in the PhD thesis of G.Quin [Quin, 2011]. Taking the logarithm of the data converts the multiplicative noise in an additive noise. Arithmetic mean of the logarithmic is equal to the logarithm of the geometric mean.

## (1) Geometric mean of intensity data

With a long time series  $\{y_1, y_2, \dots, y_N\}$ , the geometric mean is calculated as :

$$y^{GM} = \left( \prod_{i=1}^N y_i \right)^{\frac{1}{N}} \quad (2.29)$$

The geometric mean of intensity data follows a Meijer G-function [Nicolas, 2006, Quin et al., 2014]

$$\mathcal{MG}[u, L, N](y) = N \left( \frac{L}{u\Gamma(L)} \right)^N y^{N-1} \bar{G}_{0,N}^{N,0} \left( \left( \frac{L}{u} \right)^N y^N \mid \begin{array}{c} L_1 - 1, \dots, L_N - 1 \\ \vdots \end{array} \right) \quad (2.30)$$

The order 1 moment of the geometric mean is expressed as :

$$m_{1,\mathcal{MG}} = \frac{u}{L} \left( \frac{\Gamma(\frac{NL+1}{N})}{\Gamma(L)} \right)^N \leq u \quad (2.31)$$

As shown in equation (2.31), the first order moment of SAR intensity geometric mean is biased. When the number  $N$  tends to infinite, we have :

$$\lim_{N \rightarrow \infty} m_{1,\mathcal{MG}} = \lim_{N \rightarrow \infty} \frac{u}{L} \left( \frac{\Gamma(\frac{NL+1}{N})}{\Gamma(L)} \right)^N = u \frac{e^{\Psi(L)}}{L} \quad (2.32)$$

So, it is possible to apply a correction factor  $\frac{L}{e^{\Psi(L)}}$  to convert  $m_{1,\mathcal{MG}}$  to  $u$ .

## (2) Geometric mean with amplitude data

The geometric mean of amplitude data also follows a Meijer G-function [Quin, 2011]. Using a similar way for the bias calculation of intensity geometric mean, we have :

$$\lim_{N \rightarrow \infty} m_{1,\mathcal{MG},A} = \lim_{N \rightarrow \infty} u \frac{\Gamma(\frac{1}{2} \frac{2NL+1}{N})^N}{\sqrt{L} \Gamma(L)^N} = u \frac{e^{\frac{\Psi(L)}{2}}}{\sqrt{L}} \quad (2.33)$$

To get a better understanding of the geometric mean distribution and their bias, some simulation experiments are done using the SARLAB platform<sup>1</sup> developed by Jean-Marie Nicolas. Based on the statistical models of SAR images, the geometric mean distribution are tested, and results are shown on figure 2.5. The parameters of simulated data are computed based on Gamma distribution noise, and the parameters of real intensity data are set according to [Quin et al., 2014]. We can see that the mean value of geometric mean image is smaller than the mean value of images used for the geometric mean image calculation.

---

1. SARLAB platform : <http://perso.telecom-paristech.fr/nicolas/SARLABBETA/>

---

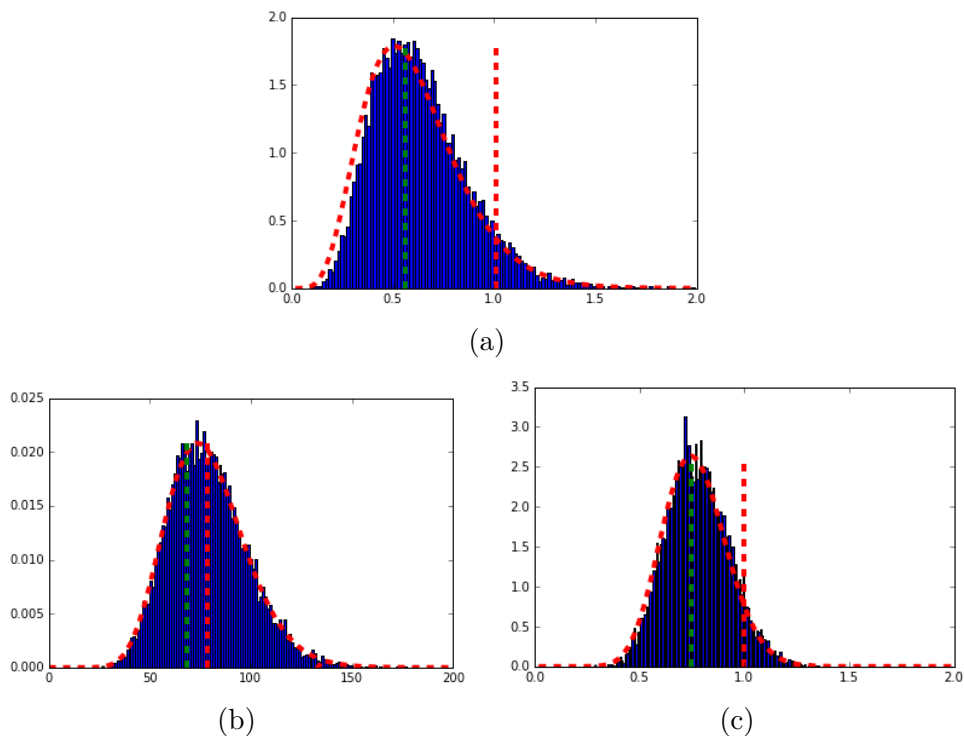


FIGURE 2.5: Different geometric mean images histogram fitting results obtained with SAR-LAB platform. The horizontal axis represents the used values, while the vertical axis represents the unnormalized probability density. (a) Fitting results of simulated intensity data ( $L = 0.9846$ ,  $u = 1.0083$  and  $N = 10$ ). (b) Fitting results of realistic intensity data ( $L = 2$ ,  $u = 100$  and  $N = 10$ ). (c) Fitting results of simulated amplitude data ( $L = 1.0023$ ,  $u = 0.9998$  and  $N = 10$ ). Red vertical line corresponds to the mean value of each simulated image, green vertical line is the mean value of their geometric mean image (in temporal domain).

## 2.3 ENL estimation

The equivalent number of looks (ENL) is a significant parameter of the multilooked SAR images, which can reflect the speckle reduction level of the filtered images [Anfinson et al., 2009]. Adaptive denoising methods generate spatially varying ENL. To well estimate the speckle reduction level, ENL can be estimated locally after despeckling. Four different kinds of ENL estimation methods can be used : maximum likelihood estimation method [Tison et al., 2004], moment methods for intensity and amplitude data, and log-cumulant method [Nicolas, 2017].

(1) Moment method for intensity data

$$\hat{L} = \frac{\mathbb{E}(y)^2}{\text{Var}(y)} \quad (2.34)$$

(2) Moment method for amplitude data

$$m_1 = \frac{1}{N} \sum_{i=1}^N \sqrt{y_i} \quad (2.35)$$

$$m_2 = \frac{1}{N} \sum_{i=1}^N y_i \quad (2.36)$$

With the empirical moment estimation results, the ENL can be calculated through :

$$\hat{L} = \frac{1}{8(\sqrt{m_2}/m_1 - 1)} \quad (2.37)$$

(3) Maximum likelihood estimation

$$u = \sqrt{m_2} \quad (2.38)$$

According to Tison et al. [2004], the empirical ENL estimation is :

$$\hat{L} = 0.1346 + \frac{0.504}{\log u^2 - m_2} \quad (2.39)$$

(4) Log-cumulant method

As introduced by [Nicolas, 2017], the theoretical expression of  $\hat{k}_2$  can be expressed as :

$$\hat{k}_2 = \frac{1}{4} \psi(1, L) \quad (2.40)$$

Joint using the empirical expressions (Eq.(2.17-2.18)), an empirical ENL estimation function can be given by rational polynomials [Nicolas, 2017] :

$$\hat{L} = \frac{1. + 3.5232\hat{k}_2 + 1.57472\hat{k}_2^2 + 4.8288 \cdot 10^{-2}\hat{k}_2^3}{-1.705 \cdot 10^{-5} + 4.004\hat{k}_2 + 5.9856\hat{k}_2^2 + 8.6208 \cdot 10^{-1}\hat{k}_2^3}$$

Based on the aforementioned ENL estimation methods, we studied the effects of variable variance, estimation window size and the number of temporal averaged images on the ENL estimation results.

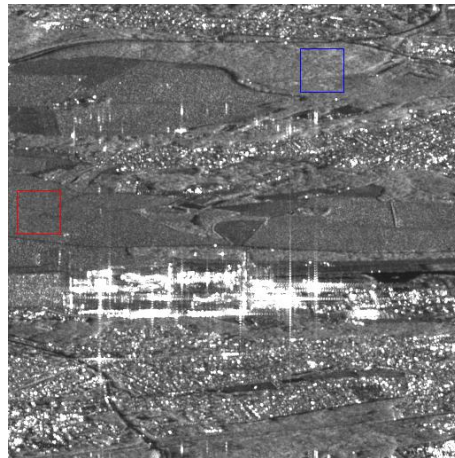


FIGURE 2.6: Spatial ENL estimation areas with size  $50 \times 50$ . Red : farmland area, blue : forest area. The image is the temporal arithmetic mean of 69 well-registered single look Sentinel-1 images.

Theoretically, the homogeneous areas have bigger ENL than heterogeneous areas because of the smaller spatial variance. We evaluate the ENL characteristics using farmland and forest areas (Fig.2.6 red and blue rectangle areas). Moment method for intensity data is taken as an example for the spatial ENL estimation. Some experimental results are shown in figure 2.7.

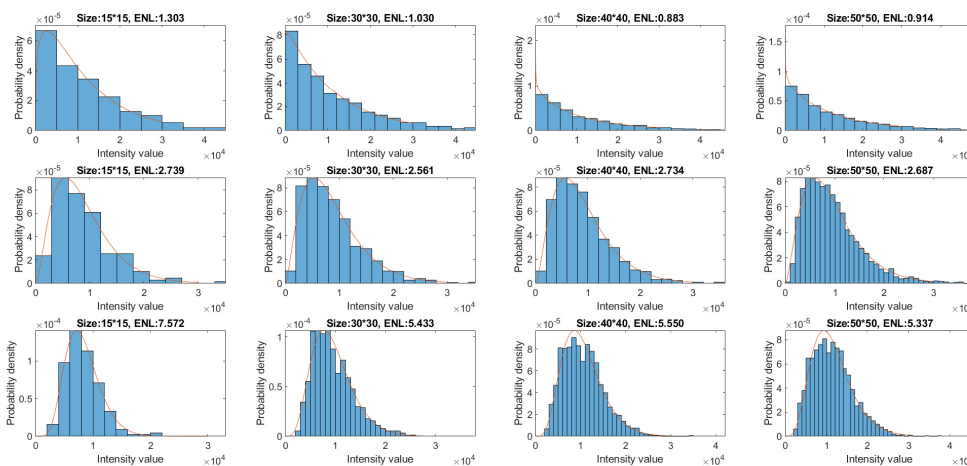


FIGURE 2.7: Spatial ENL estimation and Gamma distribution fitting results over farmland area. The farmland area shown in figure 2.6 are used. The used images are averaged using different numbers of temporal images, top : 1, middle : 5, bottom : 15.

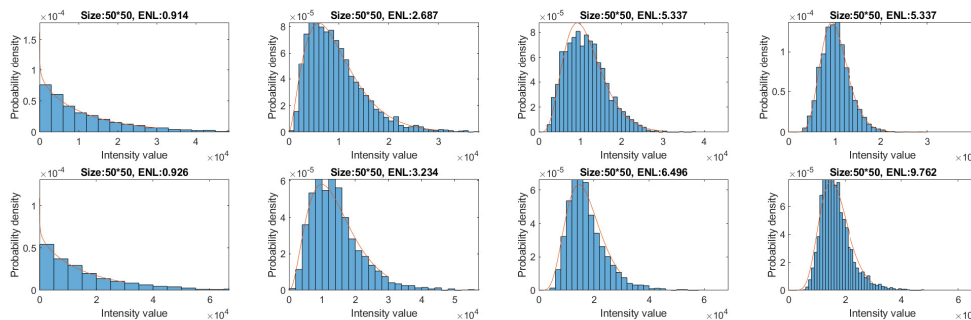


FIGURE 2.8: Spatial ENL estimation and Gamma distribution fitting results over farmland and forest areas. First row : farmland area, second row : forest area. The used images are averaged using different numbers of temporal images (from left to right) : 1, 5, 15 and 30.

The relationship of ENL with different estimation window sizes is studied based on the farmland area (Fig.2.8). For the estimation results with one single look image and different estimation window sizes, the estimation results are around 1. The float may be caused by the spatial correlation and spatial variance. For the results estimated with temporally multilooked data, the estimated results are always smaller than the number of used images. This may be caused by the temporal correlation and time series changes.

The relationship of ENL with different numbers of temporal averaged images and different objects are studied over farmland and forest areas with estimation window size  $50 \times 50$ . For the intensity value, the temporal change magnitude in farmland area is larger than forest area. The obtained ENL in forest area is always larger than that in farmland

area, especially when more images are used for temporally multilooking. However, all the ENL estimated using multilooked images are smaller than the number of images.

To better simulate the local statistics of SAR images, the ENL needs to be estimated. Since farmland and forest areas tend to have large ENL, we could take these estimated values as the index of homogeneous areas and use it to evaluate the denoising results. In the following chapters, the used spatial ENL estimation window sizes are dictated by specific applications.

## 2.4 Conclusion

We briefly introduced the principles of SAR imagery in this chapter. The probability distribution function of single SAR image (intensity, amplitude and log-transformed data) and multitemporal SAR images (different temporal averaged data) are studied. To acquire the ENL which is a vital parameter in SAR statistics, we presented several ENL estimation methods. Based on the SAR image statistics, we will propose new denoising and change detection algorithms in the following chapters.

---

---

## Chapter 3

# Experimental dataset preparation

In this chapter, we mainly pay attention to the pre-processing Sentinel-1 and TerraSAR-X images. The parameters and the acquisition mode of Sentinel-1 images and TerraSAR-X images will be described. Several SAR image registration methods which are used in the following experiments will be presented. To allow for quantitative evaluations, different kinds of simulated SAR images will be built. In addition, the spatial correlation of the data will be discussed.

### 3.1 Real SAR images

#### 3.1.1 Sentinel-1 and TerraSAR-X data bases

##### (1) Sentinel-1 images

ESA has developed the Copernicus programme which is composed of 6 Sentinel missions. Each of the Sentinels is based on a constellation of two satellites to fulfill revisit and coverage requirements, providing robust datasets for Copernicus Services. Different Sentinel missions focus on different aspects of Earth observation, Atmospheric, Oceanic, and Land monitoring, and the data will be of use in many applications.

The Sentinel-1 mission comprises a constellation of two polar-orbiting satellites, performing all-weather and day-and-night C-band synthetic aperture radar imaging. The main purpose of Sentinel-1 mission is to provide C-Band SAR data following the end of mission ERS-2 and Envisat. Both Sentinel-1A and Sentinel-1B share the same orbit plane. Sentinel-1 has four kinds of observation modes (Tab.3.1), with different applications for each of them. Their repeat frequency (important for interferometric coherence) is 6 days, and the revisit frequency (asc/desc & overlap) is around 2 days near Paris. The pixel spacing of Sentinel-1 Interferometric Wide swath (IW) single look complex (SLC) data is variable depending on the latitude. The images we will use have a spacing resolution of  $3.37 \times 13.87$  m (rg  $\times$  az).

We mainly use the Sentinel-1 IW Level-1 data to do the urban area change detection. Level-1 focused data are the generally available products intended for most data users. All the data can be downloaded from Copernicus Open Access Hub<sup>1</sup>. We mainly pay attention to the Sentinel-1 IW data acquired over Saclay area, South of Paris in the following chapters (Fig.3.1).

---

1. Copernicus Open Access Hub : <https://sentinels.copernicus.eu/web/sentinel/sentinel-data-access/access-to-sentinel-data>

---

TABLE 3.1: Sentinel-1 Observation Scenario

Modes	Polarization	Pixel spacing $rg \times az$	Application
Stripmap (SM)	Dual or single	1.5×3.6 m to 3.1×4.1 m	emergency observation
Interferometric Wide swath (IW)	Dual or single	about 2.3×14.1 m	land, predefined area
Extra Wide swath (EW)	Dual or single	5.9×34.7 m	seas and polar areas
Wave (WV)	HH or VV	1.7×4.1 m and 2.7×4.1 m	oceans

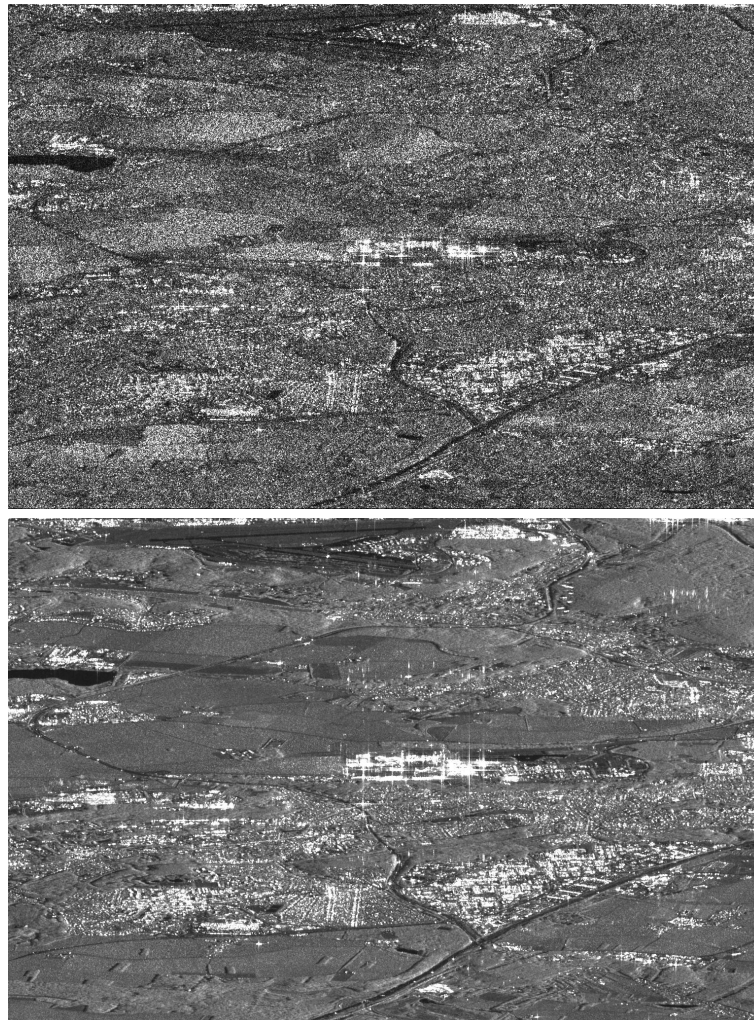


FIGURE 3.1: Sentinel-1 noisy image (up) and temporal arithmetic mean image (bottom) displayed in amplitude. 69 well-registered Sentinel-1A IW SLC images, which are acquired through the same orbit, same sensor, with descending track, are used.

(a) Sentinel-1 IW SLC image

Sentinel-1 single look complex products ( $z$ ) consist of focused SAR data, geo-referenced data (orbit and attitude data) from the satellite, and provided in slant-range geometry. It comprises both the amplitude information ( $A$ ) and phase information ( $\phi$ ).

## (b) Sentinel-1 IW GRD image

Sentinel-1 Ground Range Detected (GRD) images are obtained after multilooking, de-bursting and projecting to ground range (using WGS84) of Sentinel-1 SLC data. Only the amplitude information ( $A$ ) is kept, with multilook processing in the range direction. After processing, the GRD data has approximately square resolution pixels and square pixel spacing with reduced speckle at the cost of reduced geometric resolution (Fig.3.2).

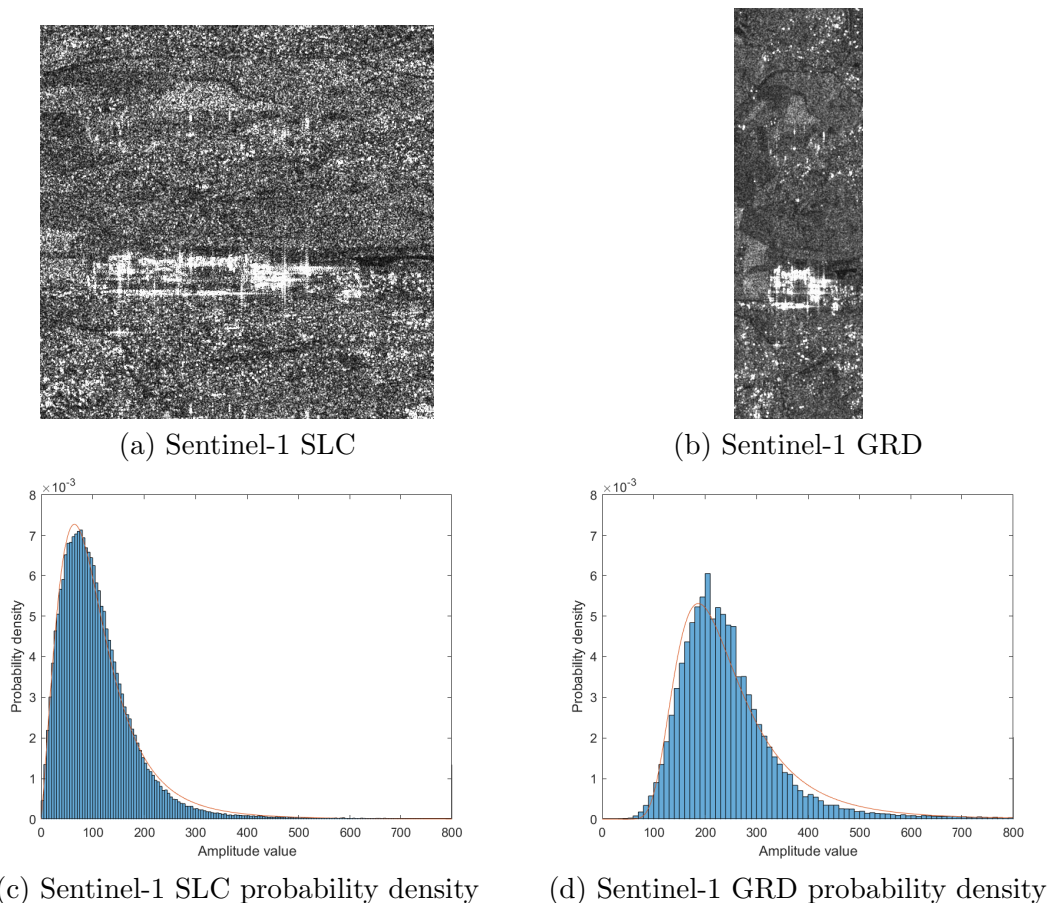


FIGURE 3.2: Comparison of Sentinel-1 SLC and GRD images. The images are acquired in 05/02/2016 over Saclay area, South of Paris. Fisher distribution is used to fit the histogram of the whole image. Sentinel-1 SLC image is in slant range coordinates, while Sentinel-1 GRD image is in ground range coordinates.

## (2) TerraSAR-X images

TerraSAR-X SAR images have lots of advantages, such as high geometric and radiometric resolution, multi-polarization mode capability, multi-temporal imaging, repeat-pass interferometry, etc. Furthermore, it is different from Sentinel-1 images (different bands and different resolutions, etc). TerraSAR-X images will also be used in the following chapters, so as to make a round test and evaluation for the proposed methods.

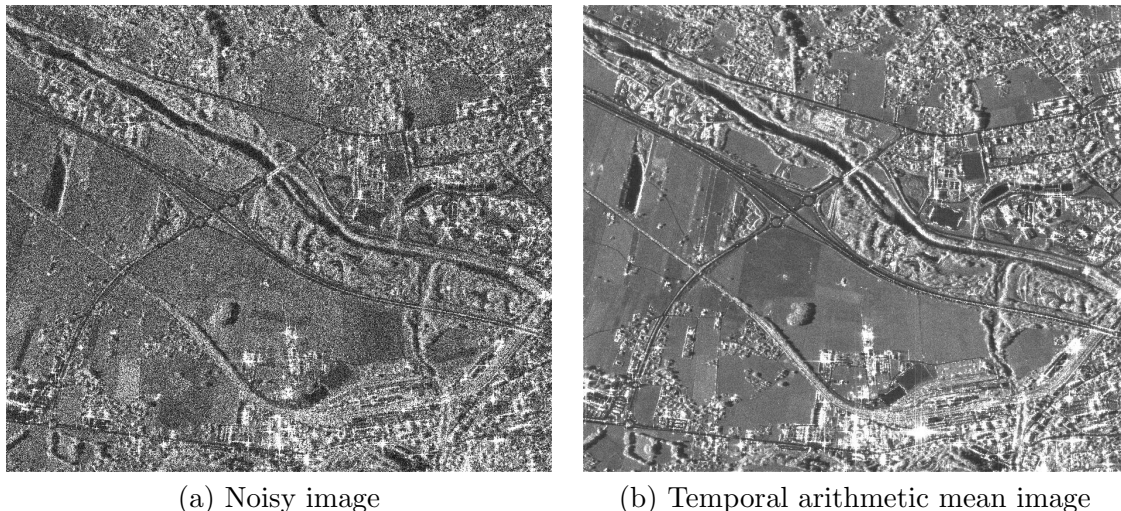


FIGURE 3.3: TerraSAR-X noisy image and temporal arithmetic mean image. 26 well registered images are used, which are acquired over Saint-Gervais-les-Bains, South-East of Geneva.

26 single-look TerraSAR-X images (13 images are sensed in 2009 and the other 13 images in 2011) acquired over Saint-Gervais-les-Bains, South-East of Geneva, (project DLR-MTH0232) are used (Fig.3.3). The acquisition modes of these data are shown in table 3.2 and their acquisition time is shown in table 3.3. These images are taken over a highly mountainous countryside, with a narrow inhabited valley concentrating many human artifacts (roads, bridges, dams). Since the original images are large, specific parts will be used according to the experimental evaluation purpose.

TABLE 3.2: TerraSAR-X data acquisition mode

Satellite height	Beam ID	Polarization	Mean incidence angle
515 km	SSC_SMLS	HH	44.52
Sampling frequency	Slant/ground range spacing	Azimuth spacing	Baselines (mean/max)
109.9 MHz	1.36/1.94 m	1.98 m	-568/526m

TABLE 3.3: Acquisition time of TerraSAR-X images

No.	Time	No.	Time	No.	Time	No.	Time
1	31/05/2009	8	16/08/2009	14	05/05/2011	21	21/07/2011
2	11/06/2009	9	27/08/2009	15	16/05/2011	22	01/08/2011
3	22/06/2009	10	18/09/2009	16	27/05/2011	23	12/08/2011
4	03/07/2009	11	29/09/2009	17	07/06/2011	24	23/08/2011
5	14/07/2009	12	10/10/2009	18	18/06/2011	25	03/09/2011
6	25/07/2009	13	21/10/2009	19	29/06/2011	26	25/09/2011
7	05/08/2009			20	10/07/2011		

In addition, we also prepared 9 TerraSAR-X images acquired over *Sendai*. These images mainly have large magnitude changes and they will be used in the change detection section.

### 3.1.2 Images registration

The registration step is necessary for many multitemporal SAR image processing, as it ensures that each ground target contributes to the same (range, azimuth) pixel in different images. SAR time series image registration, in the general sense, deals with the accurate matching of images acquired through multitemporal, multisensor, different incidence angle or multibaseline modes.

SAR image registration is mainly done using feature-based approaches (SAR-SIFT [Dellinger et al., 2015], GeFolki [Plyer et al., 2015, Brigot et al., 2016]), frequency-domain approaches and geometric based methods [Small and Schubert, 2008, Nicolas et al., 2012], etc.

#### (1) SAR image registration with cross-correlation method

Cross-correlation is widely used in image processing, pattern recognition, and other fields to register similar signals. It can efficiently determine the most similar SAR pixels by using patches [Zitova and Flusser, 2003]. For small Sentinel-1 SAR images (512×512) on almost flat terrain which are acquired through the same orbit with similar incidence angle, they have similar shift values for each pixel before registration.

##### (a) Coarse registration

Find one or two common points in both images and extract the offsets (range and azimuth) from the coordinate differences ( $\Delta x_{rg}$  and  $\Delta x_{az}$ ).

##### (b) Fine registration

Cut central regions (128×128) from images acquired by coarse registration. Estimate the sub-pixel accuracy offsets using cross-correlation method in frequency domain. The shift values are determined by the peak of correlation. Then, use the rounded shift values to cut the data matrices.

Although this method is popularly used for SAR images registration, it may create registration errors when the pixel offsets are not similar.

#### (2) Geometric registration of complex SAR images

Most traditional subpixel registration approaches use similarity measurements which are dependent on the image content (textured or homogeneous areas), and very sensitive to surface changes (snow fall, seasonal variations ...) and variations of the incidence angles. For SAR images acquired in urban areas, these problems are quite serious.

Because of the high precision on the geometric sensor parameters, it is possible to rely on geometric equations to do images registration. Here we used the method of subpixel images registration [Nicolas et al., 2012]. It<sup>2</sup> only uses pure geometric information associated to the radar principle and the SAR systems to re-sample the slave image over the master one. A digital elevation model (DEM) can be used if necessary.

In this thesis, a database of Sentinel-1 images has been created with 69 images (Tab. 3.4). This database will be used to evaluate the methods developed in this PhD. All the SLC images have been finely registered. A ground truth on this area will be done (see Section 3.2).

In the change detection chapter, Sentinel-1 images will be used for detecting building and farmland area changes. 2 registered Sentinel-1 SAR images (pixel spacing : 3.37×13.87 m) are illustrated in figure 3.4.

---

2. XIMA : <https://perso.telecom-paristech.fr/nicolas/XIMA/index.html>

TABLE 3.4: Acquisition time of Sentinel-1A IW SLC images

No.	Time	No.	Time	No.	Time	No.	Time
1	24/12/2014	19	21/08/2015	37	17/04/2016	55	19/11/2016
2	05/01/2015	20	02/09/2015	38	29/04/2016	56	01/12/2016
3	17/01/2015	21	14/09/2015	39	11/05/2016	57	13/12/2016
4	29/01/2015	22	26/09/2015	40	23/05/2016	58	25/12/2016
5	10/02/2015	23	08/10/2015	41	04/06/2016	59	06/01/2017
6	06/03/2015	24	01/11/2015	42	16/06/2016	60	18/01/2017
7	18/03/2015	25	13/11/2015	43	28/06/2016	61	30/01/2017
8	30/03/2015	26	25/11/2015	44	10/07/2016	62	11/02/2017
9	11/04/2015	27	07/12/2015	45	22/07/2016	63	23/02/2017
10	23/04/2015	28	19/12/2015	46	03/08/2016	64	07/03/2017
11	05/05/2015	29	31/12/2015	47	15/08/2016	65	19/03/2017
12	17/05/2015	30	12/01/2016	48	27/08/2016	66	31/03/2017
13	29/05/2015	31	24/01/2016	49	08/09/2016	67	12/04/2017
14	10/06/2015	32	05/02/2016	50	20/09/2016	68	24/04/2017
15	04/07/2015	33	17/02/2016	51	02/10/2016	69	06/05/2017
16	16/07/2015	34	29/02/2016	52	14/10/2016		
17	28/07/2015	35	24/03/2016	53	26/10/2016		
18	09/08/2015	36	05/04/2016	54	07/11/2016		

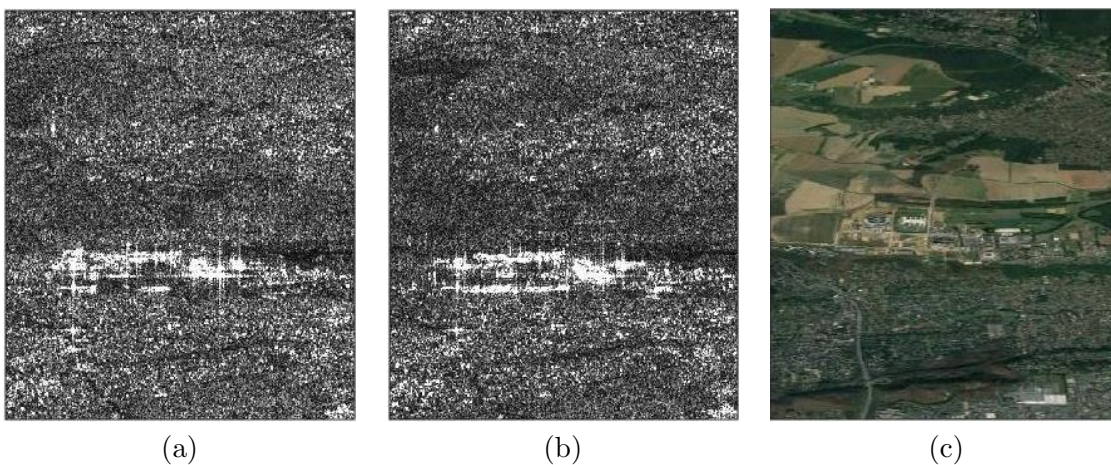


FIGURE 3.4: Registered Sentinel-1 SAR images over Paris Saclay area which were obtained on 05/01/2015 (left) and 18/01/2017 (middle), with the same orbit and observation mode. These images will be used for change detection evaluation. Compared with the optical image (right), SAR images seem stretched and transformed.

### (3) Geometric registration of heterogeneous images

Cross-correlation method is mainly useful for the registration of SAR images acquired through the same orbit and similar incidence angle.

Although the geometric registration method proposed by Nicolas et al. [2012] can obtain good registration results, the Terrain Observation with Progressive Scans SAR (TOPSAR) mode (with sub-swaths and a series of bursts) limits its popularly use. For different sensor data, the resolution and the reflectivity may be different, thus making cross-correlation methods fail. In addition, optical remote sensing images often have multi-bands.

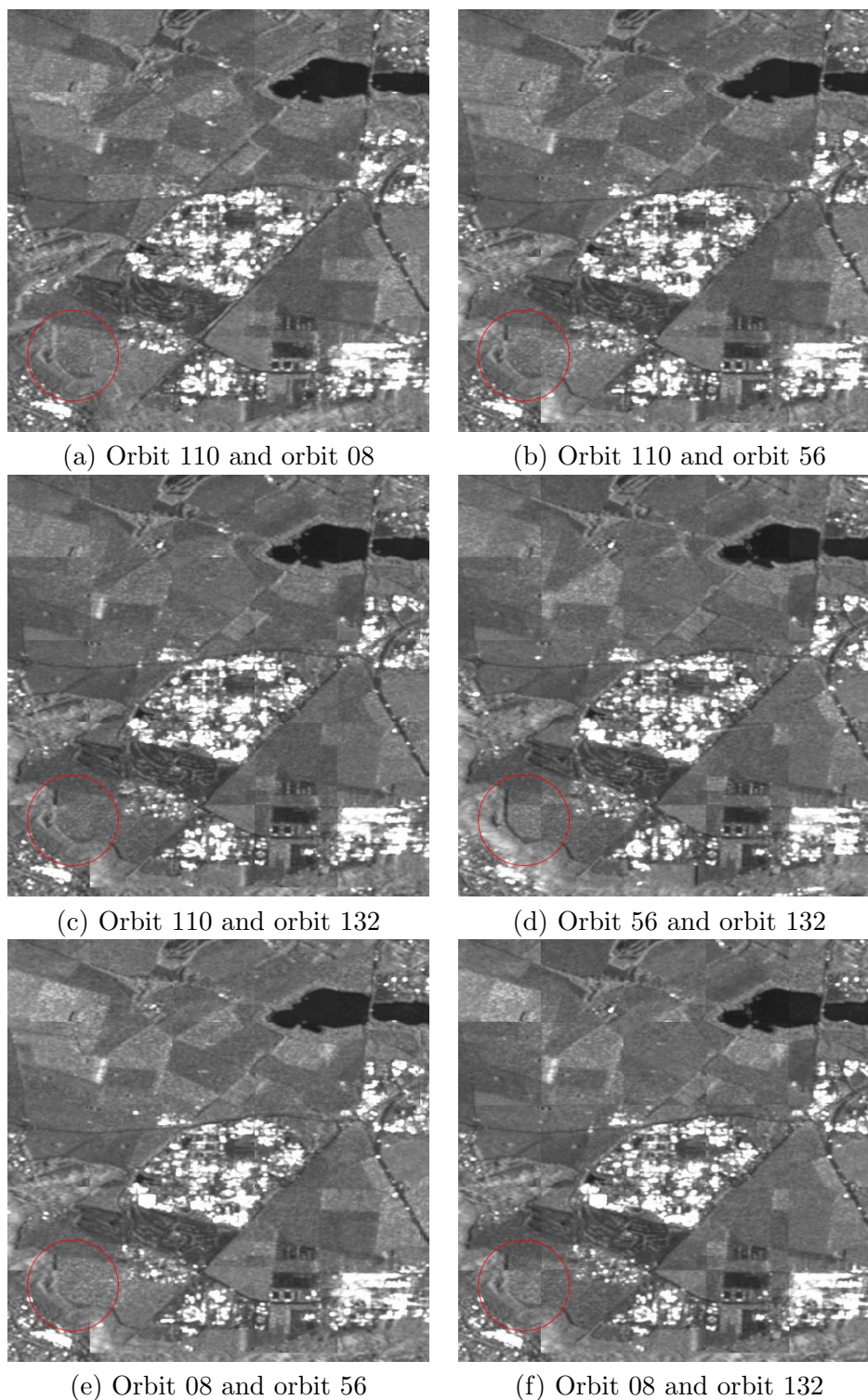


FIGURE 3.5: Chessboard overlay for coregistered Sentinel-1 GRD images which are acquired through different orbits, over Saclay area, South of Paris. The images acquired through orbits 08 and 110 are in descending mode, while the others are acquired through ascending mode. The arithmetic mean images (computed using about 30 images) are used for the comparison, so as to obtain better visual results. The registered images are in WGS-84 coordinate system.

A popular heterogeneous image registration method is based on mutual information [Chen et al., 2003, Inglada and Giros, 2004]. However, the heavy time consumption limits its popularly use, especially for a large amount of data. Current satellite always provide accurate geolocation information together with the images. Thus, the multitemporal or multisensor images over the same area can be well registered by using their geolocation information. This information is obtained using a digital elevation model. The precision of the digital elevation model will influence the registration results. It allows multiple image products to be quickly combined, e.g., SAR interferometry (InSAR) coregistration or layered with other data sources, such as different application maps (vegetation area, building area, etc.), digital elevation models [Schubert et al., 2015]. SNAP software<sup>3</sup> will be used to register the heterogeneous images in this section. After geocoding by SNAP, Sentinel-1 SAR image values will be converted to decibel scale (dB value) with radiometric calibration. This ensures that images acquired from different times, through different sensors (Sentinel-1A/B) or locate in different parts of the images are comparable.

The Sentinel-1 platform provides highly accurate pointing knowledge (better than  $0.004^\circ$ ) on each axis, high pointing accuracy (about  $0.01^\circ$  on each axis), and real time orbit determination together with a dedicated propulsion system for precise orbit control [Torres et al., 2012]. The absolute location accuracy of Sentinel-1 IW SLC/GRD data is about 7 meters [Aulard-Macler, 2012]. Data products from synthetic aperture radar sensors that have been accurately geometrically calibrated permit a straightforward combination of multiple data taken with one another [Schubert et al., 2012], not only simplifying their inter-comparison, but also speeding up applications such as near-real-time disaster mapping.

To verify the geolocation accuracy of Sentinel-1 and Sentinel-2 images in the areas of interest, we implemented some experiments (Fig.3.5-3.6). The parameters of selected data are introduced in table 3.5. Open access SRTM-3 digital elevation model is used for this experiment.

TABLE 3.5: Sentinel-1 and Sentinel-2 parameters comparison

	Coordinate system	Resolution rg $\times$ az	Pixel Spacing	Mode	Absolute geolocation uncertainty
Sentinel-1 IW GRD	WGS-84	20.3 $\times$ 21.6- 20.5 $\times$ 21.7m	10 $\times$ 10 m	IW mode	7 m (Near-Real-Time)
Sentinel-2 Band 2	UTM	10 $\times$ 10m	10 $\times$ 10m	Band 2	20 m $2\sigma$ without GCPs

With high resolution, the object backscattering values in SAR images are sensitive to the change of incidence angles, which leads to difficult combination. Thus, we mainly pay attention to line feature locations to make the comparison (Fig.3.5-3.6).

Visually, there is no obvious offset for Sentinel-1 GRD images acquired through different orbits. The line features in the homogeneous areas are well registered. However, we could find several pixels offset in some areas (Fig.3.5), especially in the boundaries between the objects which have different height (such as the forest and farmland area boundaries in the red circle). This phenomenon is caused by the different looking incidence angle. When comparing with Sentinel-2 images, the differences in these areas

3. SNAP software : <http://step.esa.int/main/download/>

are more obvious (Fig.3.6) for the images acquired through descending orbits (orbit 08 and orbit 110). For Sentinel-1 images acquired through orbits 08 and 110, there are small offset in the whole image. For the images acquired through ascending mode, the images are well registered.

Since only SRTM-3 DEM is used for the terrain correction, the slant-range distortion areas (Fig.2.1(b)) will provide unreliable results after geocoding. Thus, coregistration residual evaluation method and fine registration are needed.

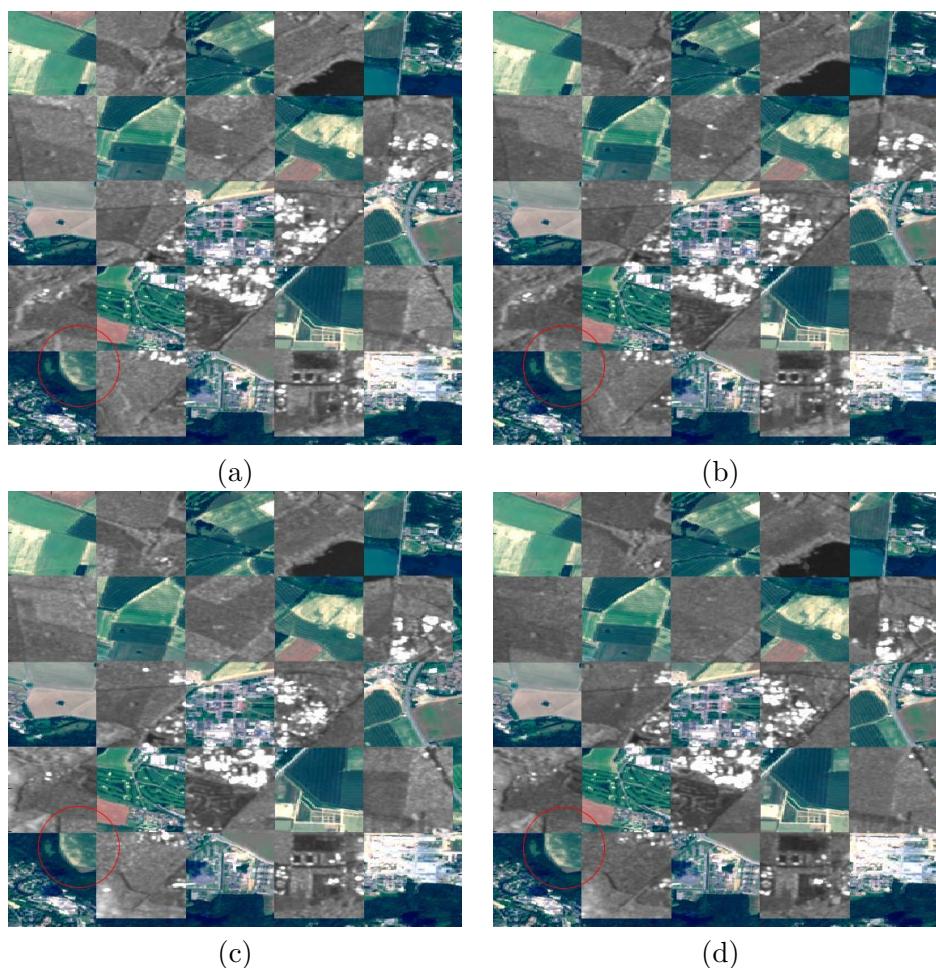


FIGURE 3.6: Chessboard overlay for coregistered Sentinel-2 (color image) and Sentinel-1 GRD images. The Sentinel-1 GRD images are acquired through : (a) orbit 08, (b) orbit 110, (c) orbit 59, (d) orbit 132.

According to the previous comparison, it is better to only use ascending or descending SAR images for multitemporal SAR image change detection. For the combining use of ascending and descending SAR images, special attention should be paid to boundary areas. To keep the original backscattering values of mountain area, it is better to use the Sentinel-1 SAR images without calibration. For the combined use of Sentinel-1 and Sentinel-2 images, we can use the geometric coregistration method to convert them to the same coordinate system.

### 3.1.3 Super-images

With a long time series, different temporal averages (such as arithmetic mean, geometric mean, harmonic mean, etc.) can be computed. We call the images derived from different temporal averages as “super-images” [Quin et al., 2014]. 69 registered Sentinel-1 images (Tab. 3.4) are used for the calculation of the super-images. Unlike Sentinel-1 GRD images which are computed with a spatial multilooking process, the average images are obtained by temporal multilooking which could effectively preserve the spatial resolution. With a long time series  $\{y_1, y_2, \dots, y_M\}$ , the temporal arithmetic mean and geometric mean are calculated based on Eq. (2.24) and Eq. (2.29).

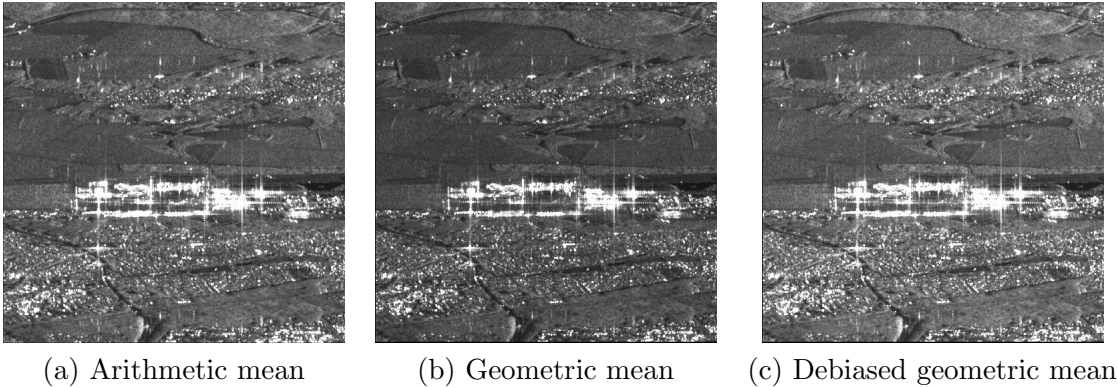


FIGURE 3.7: Temporal multilooked amplitude SAR image comparison. Compared to the geometric mean, the debiased geometric mean is more similar to arithmetic mean.

As shown in figure 3.7 and the discussion in chapter 2, geometric mean has an obvious bias. It is debiased using equation (2.33). Based on 69 well registered Sentinel-1 images, the speckle noise is highly reduced in the temporal averaged images. According to the experimental results (Fig.3.7), temporal geometric mean is less sensitive to the short term changing points than arithmetic mean.

## 3.2 Ground truth preparation

Saclay area has been chosen since it has been chosen to receive the future scientific area of the Paris-Saclay University. It is an almost flat plateau limited on one side by a deep valley where most of the former universities are located. Former ground occupation of the plateau was with grass fields, corn and wheat fields, small woods and sparse farms. Starting in 2010, constructions and public works were decided to convert agricultural terrains into research and education buildings, mostly 2 to 5 storey compact and geometrical structures made of concrete, steel and glass. Many plots have been bared from vegetation, the excavated heavy plant machineries and trucks have been parked in some places. Cranes and lifting equipments were displaced from site to site. Then parking lots for cars were distributed around emerging buildings, large roads were traced to link the various plants of the work site.

All these elements greatly influence the SAR reflectivity.

### 3.2.1 Ground truth map in Saclay area

Ground truth data is done by direct observation of maps, optical and SAR data and regular visits to Saclay area. It will be used in the validation and analysis of change detection algorithms. The prepared ground truth shown in figure 3.8 corresponds to the SAR image acquired on February 29th, 2016. Different classes, associated values and some corresponding examples of this area are shown in table 3.6.

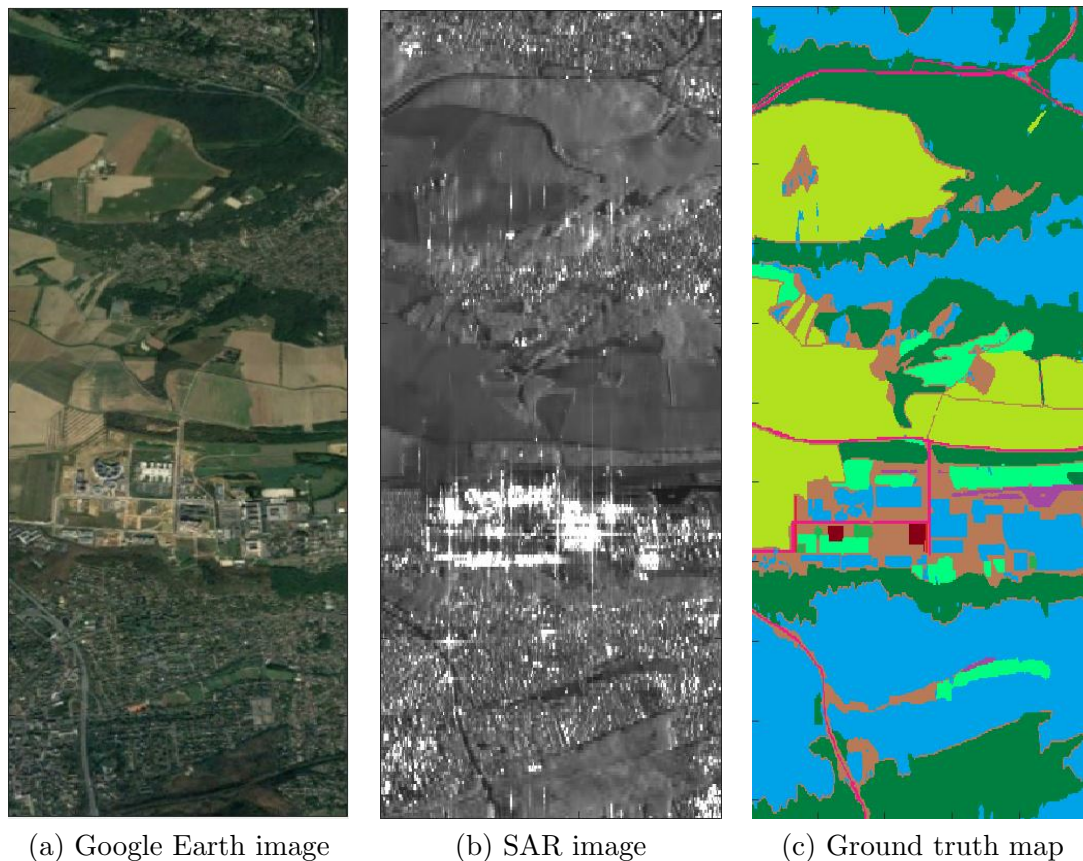


FIGURE 3.8: Comparison of SAR ground truth map with optical and SAR images. According to the objects distribution in this area, 10 classes were used for the representation. Each class was indexed using specific corresponding color and value (see Tab.3.6). Both the Google Earth image and SAR image were acquired on February 29th, 2016.

The difficulties to build the ground truth for our applications are the following :

- Ground occupations and ground changes are mostly visible on optical images (either from satellite or from aerial survey).
- Because of the complex surface of Orsay site (with a deep valley close to the area of interest), the geometry of optical images is different from the geometry of SAR images, and registration is possible only with a fine digital elevation model.
- As it is not the purpose of our study to precisely register SAR images with optical images, we decided to detect changes on optical images using prior information, but transform the results of manual delineation in the geometry of SAR images. For this purpose, we made use of the SAR average mean as a geometric background.

TABLE 3.6: Different classes, associated values and some corresponding examples. The color around each category name is the same as in figure 3.8 (c). Google Earth is used for preparing the images.

Category Representation values	<b>Building area</b> 3 	<b>Metal fence</b> 4 	<b>Parking area</b> 5 
Category Representation values	<b>Water</b> 6 	<b>Farmland</b> 7 	<b>Forest</b> 8 
Category Representation values	<b>Grass land</b> 9 	<b>Planning area</b> 10 	<b>Roads</b> 11 
Category Representation value	<b>Unclassified area</b> 12 	<b>Unclassified area</b> 12 	<b>Unclassified area</b> 12 

### 3.2.2 Multitemporal ground truth map

Due to the construction of University of Paris-Saclay, plenty of new buildings in this area are under construction. For the study of SAR image change detection, we mainly pay attention to this area. It has several changed types, such as appearing buildings, disappearing buildings, parking areas, metal fences and appearing bare soil.

According to the start changing time of the multitemporal images, 10 SAR images (red colored in Tab.3.4) were chosen for creating the ground truth map (Fig.3.9-3.10).

Although farmland area, forest area and grass land area have seasonal changes, their coverage area did not change. So, these kinds of areas and no change building areas were created according to the SAR average map. Google map and Sentinel-2A visible range images were used for the reference.

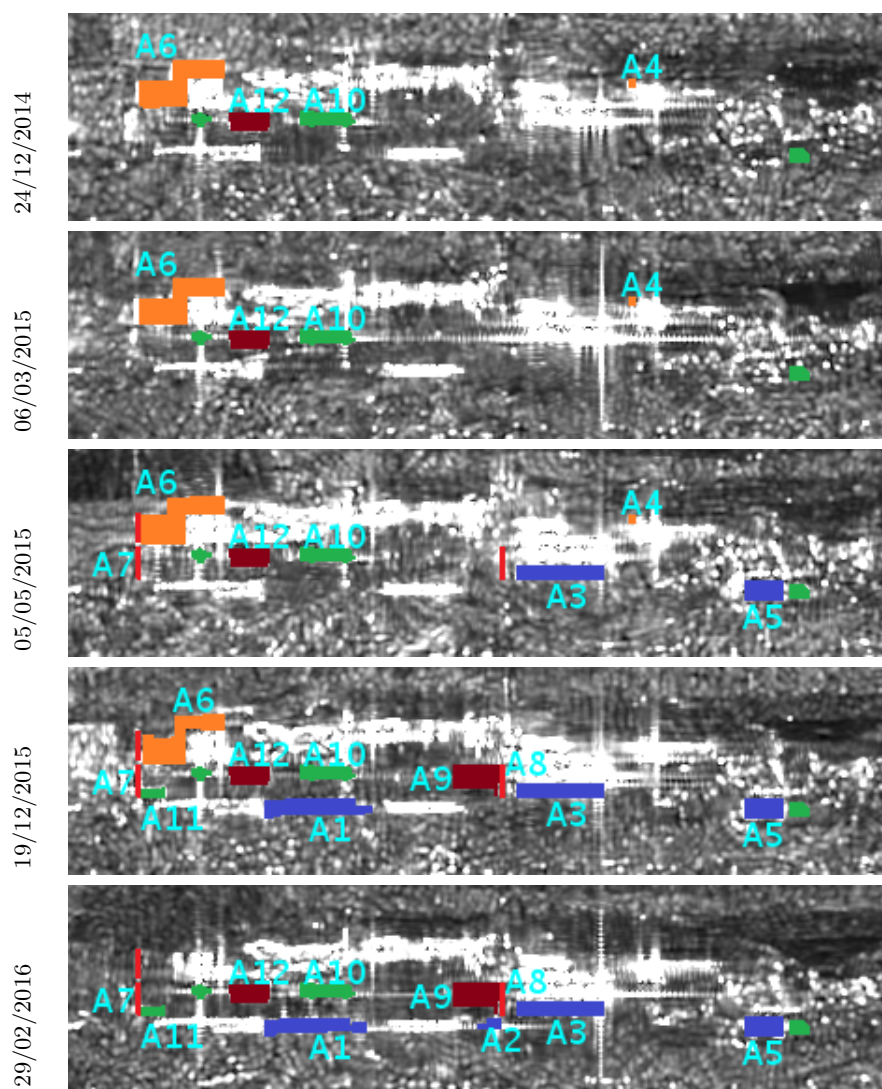


FIGURE 3.9: Reference map of different change types (A) (from 24/12/2014 to 18/01/2017). The start and stop change of each change area is shown in Tab.3.7. Images are acquired over Saclay area, South of Paris.

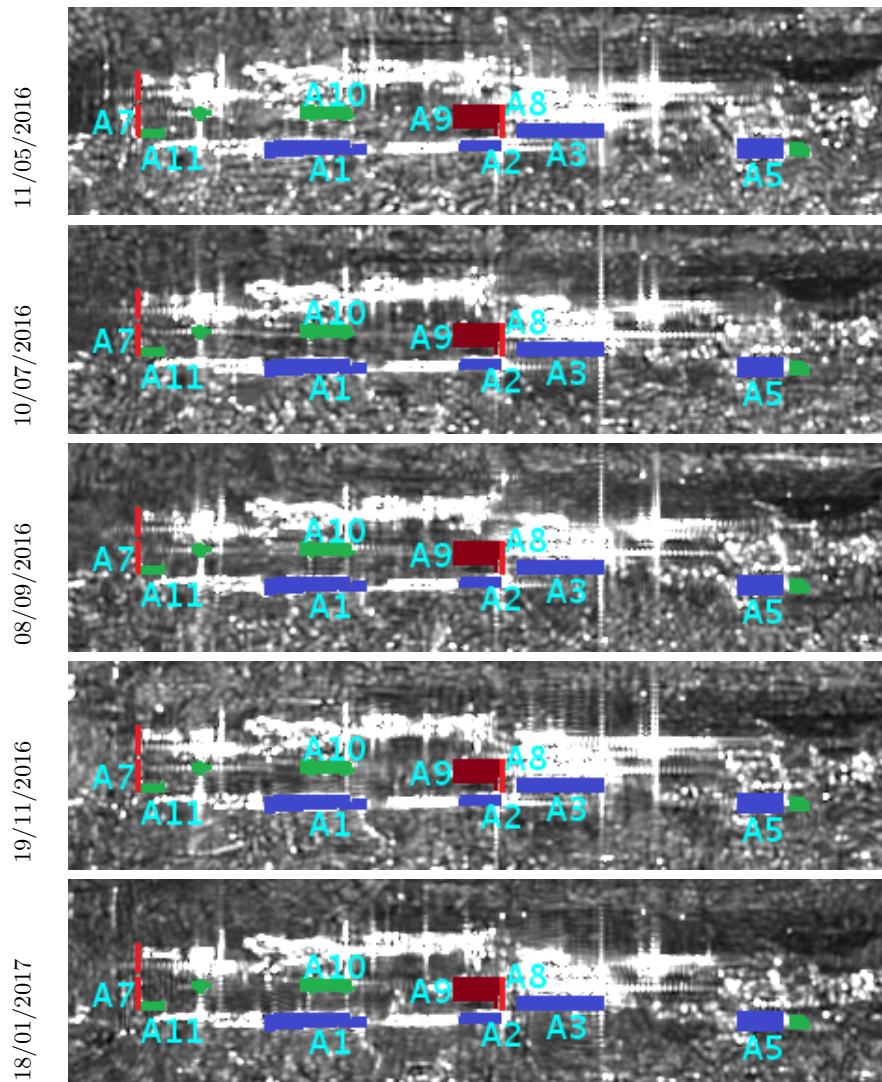


FIGURE 3.10: Reference map of different change types (B) (from 24/12/2014 to 18/01/2017). Blue : appearing building, red : metal fence, green : parking area, magenta : bare soil (planning for the construction), orange : disappearing building. The start and stop change of each change area is shown in Tab.3.7.

(1) High backscattering points changed areas

Normally, the parking area keeps changing during the acquisition of SAR images, unless it was constructed during that time. When preparing the multitemporal ground truth maps, the start time and stop time of changes will be taken into account.

(2) Study of the multi-temporal changes

Based on the study of changed area and changed time, the multitemporal ground truth maps could be created. Because of the visibility of the bright points in SAR images, the changed areas which have big backscattering values will be taken into account. Before the construction finished, the building area will suffer continuous changes.

TABLE 3.7: Start and stop times of changes for each area. The start and stop changing index numbers corresponding to the 10 red index time in Tab.3.4. Different colors represent different change types.

Areas	Classes	Start changing	Stop	Areas	Classes	Start changing	Stop
A1	Building 1	4	10	A7/A8	Metal fence	3	7
A2	Building 2	5	10	A9	Bare soil	4	10
A3	Building 3	3	10	A10	Parking	1	10
A4	Building 4	Before 1	3	A11	Parking	4	10
A5	Building 5	3	10	A12	Bare soil	1	6
A6	Building 6	Before 1	5				

### 3.2.3 Other ground truth maps

In order to evaluate the change detection method performance, the ground truth map of different urban areas has been prepared (Tab.3.11).

The steps to build the ground truth map using Sentinel-1 SLC data are :

- Preparation of the multitemporal images (table 3.8) ;
- SAR images registration using subpixel level registration method (XIMA<sup>4</sup> or SAR-SIFT [Dellinger et al., 2015]) ;
- Selecting the image pairs according to the available optical images (Spot-5 images or Google Earth images) ;
- Denoising SAR images using RABASAR method (see chapter 6) ;
- Detecting the changed areas using  $S_{GLR}$  (see chapter 8) based change detection method ;
- Labelling the changed pixels with the reference of optical images, denoised SAR images and change detection results.

TABLE 3.8: Ground truth preparation of changed building areas

Location	Amount	Image size	Registered
École Polytechnique area	69	1024×1024	XIMA
CentraleSupélec area	69	1024×1024	XIMA
Jinan West railway station area	10	1024×1024	SAR-SIFT
TianJin South railway station area	10	1024×1024	SAR-SIFT

In addition, we also prepared the corresponding SAR image pairs according to the Sentinel-2 database<sup>5</sup> released by Daudt et al. [2018].

4. <https://perso.telecom-paristech.fr/nicolas/XIMA/index.html>

5. <http://dase.ticinumaerospace.com/>

### 3.3 Simulated SAR images

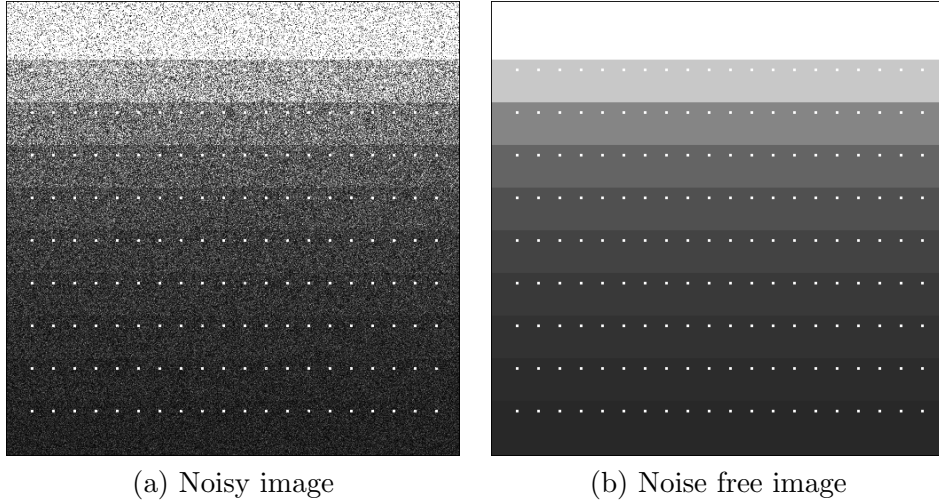


FIGURE 3.11: A simulated data and corresponding noise free image.

In order to have a control on the performances of our algorithms, we simulate realistic images with controlled modifications. To do so, we used a noise free SAR image multiplied by a Gamma distributed speckle noise ( $v$ ). By modifying the noise-free image before introducing the noise, we are able to have images with controlled changes in them. Depending on the noise free SAR image, we distinguish unrealistic images from realistic images as explained in the following sections.

#### 3.3.1 Unrealistic simulated images

##### (1) Simulated data with changes

The noise free components of 40 simulated images have different targets with  $u_{target}$  and 5 different background values  $u_{back}$  with  $u_{target}/u_{back}$  varying from 2 to 10. For each area, bright points appear at time 1~20 and 21~40 images.  $u_{target}$  value is chosen as 1600 according to the real value of building areas in a Sentinel-1 SAR image. Then, the noise-free intensity images  $u_t$  are multiplied by a Gamma distribution noise  $v_t$ .

$$y_t = u_t v_t \quad (3.1)$$

where  $t$  is the number of temporal image. One simulated image and the corresponding noise free image are shown in figure 3.11.

##### (2) Simulated images without change

To make other comparisons, one optical image (Fig.3.12) which is often used in other papers is chosen for SAR image simulation. Since the value range of the optical image is  $[0 \ 255]$ , the simulated intensity SAR image is created through :

$$y_t = A^2 v_t \quad (3.2)$$

where  $A$  represent the optical image.

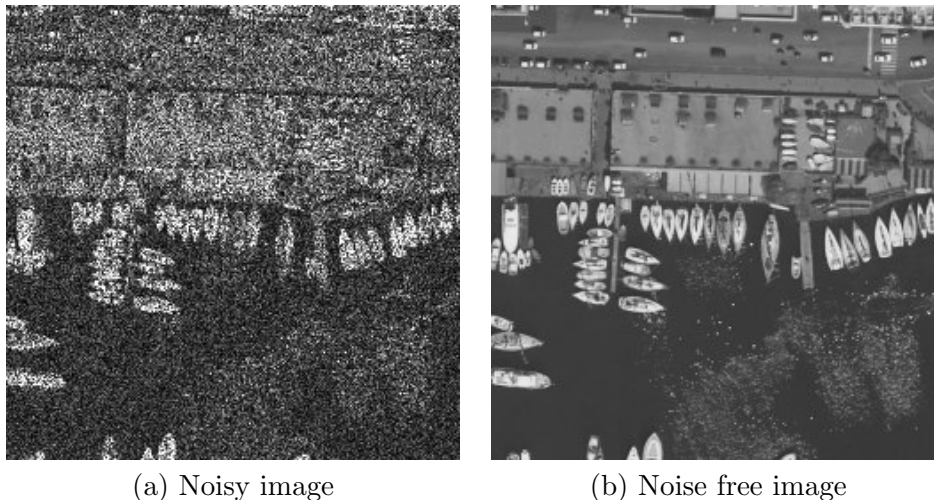


FIGURE 3.12: The simulated data and corresponding noise free image.

### 3.3.2 Realistic simulated SAR images

Many simulations are based on reflectivity maps obtained from optical images. However, real SAR images exhibit strong and persistent scatterers, especially in urban areas which can hardly be simulated using optical images. Therefore, we propose to use the arithmetic mean image of long time-series of SAR images, considered as a noise free image (a reflectivity map  $u$ ) to create realistic simulations of SAR images. For specific applications, dedicated sequences will be created over various areas (Fig.3.15(a, c, d) and Fig.3.16(b, c)) : forests, farmlands, building areas etc. Different temporal changes may also be simulated as shown in (Fig. 3.13, Fig.3.15(b) and Fig.3.16(a)). Changed values are extracted from the corresponding real SAR time series. All the pixels in the same rectangular at time  $t$  have the same noise free value.

#### (1) Simulated SAR data without changes

Based on the acquired arithmetic mean image  $y^{AM}$ , we can simulate different temporal images through multiplying  $y^{AM}$  with different simulated Gamma distribution noise  $v_t$ .

$$y_t = y^{AM} v_t \quad (3.3)$$

The synthetic time series data which correspond to the same ground truth (Fig.3.15 (a,c,d) and Fig.3.16(b,c)) are simulated by this way.

#### (2) Simulated SAR data with changes

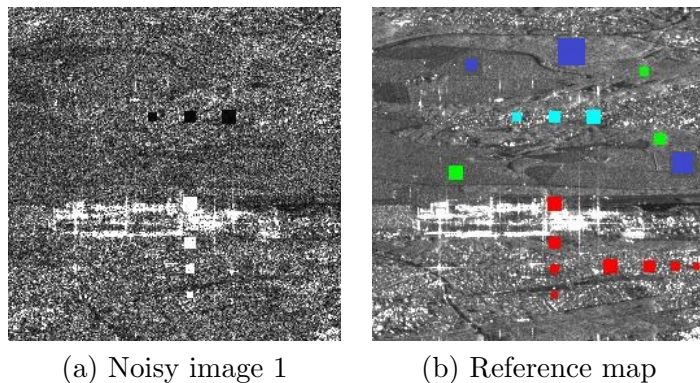


FIGURE 3.13: Realistic simulated SAR image 1 and reference image. The background image is obtained from an average of 69 Sentinel-1 images. The change types (the corresponding time series are shown in Fig.3.14) are : **red : step change**, **green : impulse change**, **blue : cycle change** and **cyan : complex change**. This simulated time series will be used for the change classification.

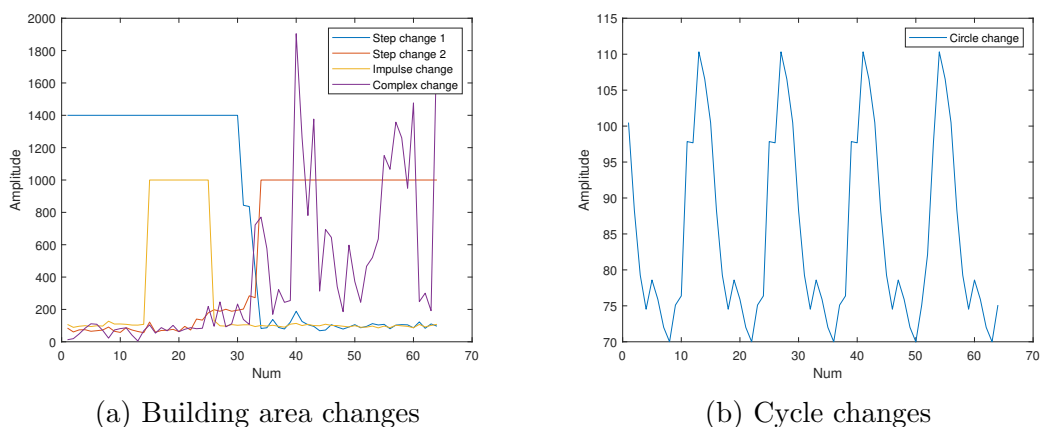


FIGURE 3.14: Different time series changes introduced in figure 3.13.

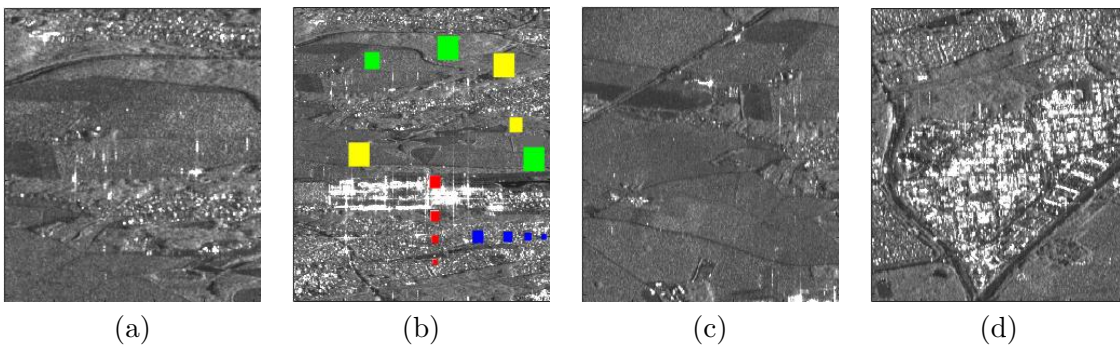


FIGURE 3.15: Different Sentinel-1 arithmetic mean images over different land covers. Different colors represent different changes (the corresponding time series are shown in Fig.3.17) : **green=farmland**, **yellow=forest**, **red=appearing**, **blue=appearing then disappearing**.

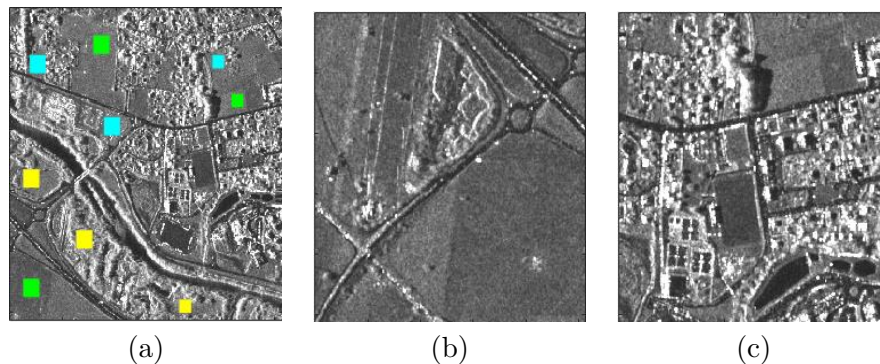


FIGURE 3.16: Arithmetic mean of TerraSAR-X images over different areas. Different colors represent different changes (the corresponding time series are shown in Fig.3.17) : green=farmland, yellow=forest, cyan=disappearing.

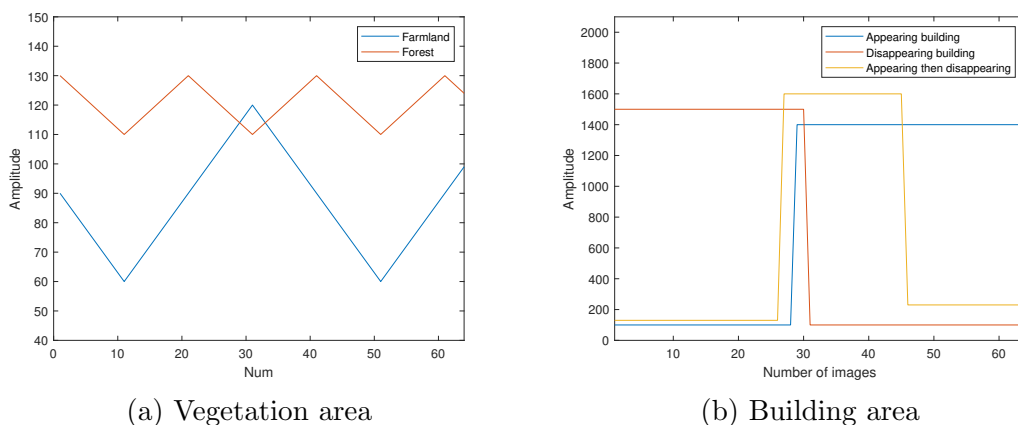


FIGURE 3.17: Simulated time series changes. Vegetation area changes have been introduced to the simulated Sentinel-1 images and simulated TerraSAR-X images. Disappearing building changes are introduced to TerraSAR-X images, while the other building area changes are introduced to Sentinel-1 images.

Man-made structures such as buildings, fences or transmission towers produce very strong back-scattering. They usually have large intensities for some geometric configurations [Lobry et al., 2016a]. To control the real changed areas in the SAR images, several changed patches were introduced in the images, corresponding to isolated buildings with rectangular shapes (Fig.3.13).

Since different objects have different change magnitude, we also introduced different changing objects into the simulated temporal SAR images. Three typical objects are used : farmland, forest and changed building areas (Fig.3.13(b), Fig.3.15(b) and Fig.3.16(a)). The values before and after changes are extracted from the real temporal SAR data and introduced in the noise free temporal SAR images  $y_t^{AM}$ . Then, the temporal data are simulated using :

$$y_t = y_t^{AM} v_t \quad (3.4)$$

(3) Simulated SAR data with different ENL

The speckle effects are different with different ENL. To simulate time series SAR data with different ENL, we used :

$$y_t = y_t^{AM} \left( \frac{1}{L} \sum_{i=1}^L v_i \right) \quad (3.5)$$

where  $L$  equals the ENL of the simulated data,  $i$  is the time at which Gamma distribution noise is generated. The ENL is global for the images in this simulation.

When there are no change in the time series, the time series can be simulated using :

$$y_t = y^{AM} \left( \frac{1}{L} \sum_{i=1}^L v_i \right) \quad (3.6)$$

#### (4) Simulated SAR data with spatially varying ENL

Since spatial adaptive denoising methods can introduce a spatially variable ENL, we can simulate multilooked data with different ENL. These data can reflect the situation of a denoised image with a spatially variable ENL. The noisy images are simulated using Sentinel-1 arithmetic mean image ( $y^{AM}$ ) and multiple Gamma distribution noise  $v$  with :

$$y_t(s) = y_t^{AM}(s) \left( \frac{1}{L(s)} \sum_{i=1}^{L(s)} v_i \right) \quad (3.7)$$

where  $s$  corresponds to the pixel locations.

Some of the simulated data are shown in figure 3.18. There are some changes between the simulated images. The denoised images are simulated using 210 different ENL shown as in figure 3.18(c). If the ENL equals 1, the denoised values are the same as the original values. These simulated images can be used to evaluate the use of adaptive thresholds or adaptive ENL. Apart from these different noise free images, we could also use remotely sensed optical images to simulate SAR data [Aiazzi et al., 1998].

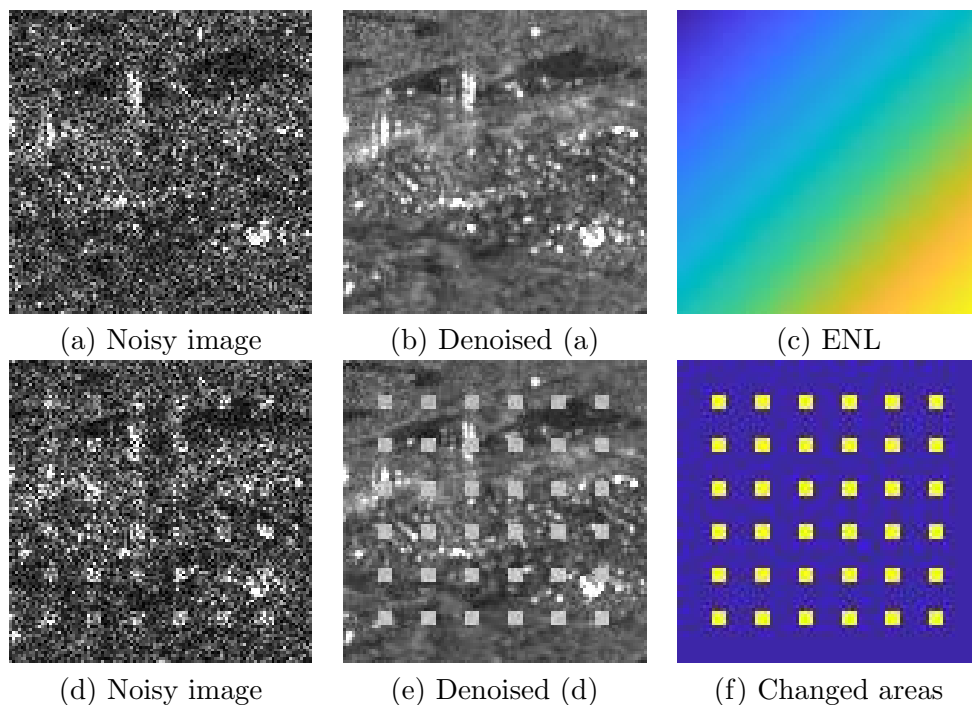


FIGURE 3.18: Original data and denoised simulated Sentinel-1 data with associated ENL. The blue color in the ENL figure (c) represents smaller ENL. The two denoised data have the same ENL, which is the sum of the row and the column number of each pixel.

TABLE 3.9: Simulated time series SAR data

	Noise free image	Figures	Changes	ENL	Amount	Equation
1	Simulated image	Fig.3.11	Yes	1	40	Eq.(3.1)
2	Optical image	Fig.3.12	No	1	64	Eq.(3.2)
3	Sentinel-1 AM	Fig.3.13(b)	Yes	1	64	Eq.(3.5)
4	Sentinel-1 AM	Fig.3.15(a)	No	1	100	Eq.(3.3)
5	Sentinel-1 AM	Fig.3.15(b)	Yes	1, 2, 4, 8	100	Eq.(3.5)
6	Sentinel-1 AM farmland	Fig.3.15(c)	No	1, 2, 4, 8	64	Eq.(3.6)
7	Sentinel-1 AM building	Fig.3.15(d)	No	1, 2, 4, 8	64	Eq.(3.6)
8	TerraSAR-X AM	Fig.3.16(a)	Yes	1, 2, 4, 8	64	Eq.(3.5)
9	TerraSAR-X AM farmland	Fig.3.16(b)	No	1, 2, 4, 8	64	Eq.(3.6)
10	TerraSAR-X AM building	Fig.3.16(c)	No	1, 2, 4, 8	64	Eq.(3.6)

### 3.4 Spatial correlation

Since the transmitted beam is wider than the radar cross section (RCS) area of the target [Goodman, 2007], spatial correlation is usual in SAR images. Spatial variance is influenced by the spatial correlation of pixels, so the spatial correlation should be taken into account during the parameter estimation. However, nearly all the denoising methods hypothesized that speckle is independent and identically distributed. The spatial correlations lead to negative effect on the denoising results. Hence, a spatial decorrelation step could be useful before despeckling using these methods.

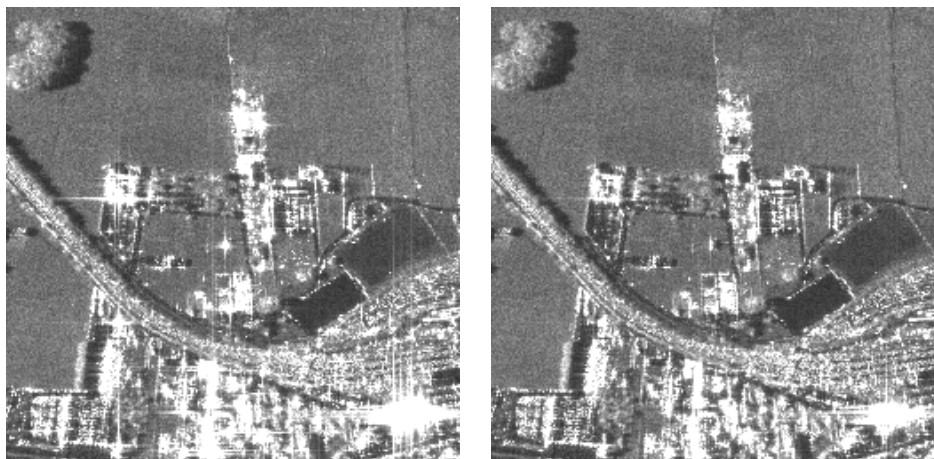
Since the correlation is usually limited to the nearest neighbors, under-sampling is the simplest way to reduce the spatial correlation effects, but it will result in losing detail information and in reducing spatial resolution. This method will be used for some experiments by labeling one pixel over 2 or 3 in range and azimuth directions. SAR-BM3D<sup>6</sup> is utilized to process the original and resampled Sentinel-1 images (Fig.3.19).



(a) SAR-BM3D with original Sentinel-1 (b) SAR-BM3D with resampled Sentinel-1

FIGURE 3.19: SAR-BM3D denoising result comparison based on original Sentinel-1 data and resampled Sentinel-1 data. The under-sampling step is 2 along azimuth and range directions.

A method [Abergel et al., 2018] to select only the useful part of the complex spectrum followed by apodization and irregular resampling has been proposed. It reduces the sidelobes induced by the strong targets and preserves spatial resolution.



(a)

(b)

FIGURE 3.20: Comparison between original and revisited CLEAN algorithm [Abergel et al., 2018] generated data. (a) arithmetic mean of 26 TerraSAR-X images, (b) arithmetic mean of the 26 TerraSAR-X images processed by revisited CLEAN algorithm.

6. SAR-BM3D : <http://www.grip.unina.it/research/80-sar-despeckling/80-sar-bm3d.html>

Another way of suppressing the sidelobes due to strong targets relies on a revisited CLEAN algorithm<sup>7</sup> [Abergel et al., 2018]. It decomposes the SAR data into a speckle component  $v_s$  and a target component  $u_p$ . This method can keep the initial resolution of the data, suppress sidelobes and preserve speckle statistics in fully developed speckle areas (Fig.3.20). Through despeckling the speckle component  $v_s$  and combined component  $v_s + u_p$ , three kinds of results which are denoised speckle component, denoised speckle component with the target component and denoised combined component can be obtained.

### 3.5 Conclusion

This chapter has presented the database that will be used in the following chapters. 69 Sentinel-1 IW SLC data and 26 TerraSAR-X images have been registered with subpixel accuracy. Then, their super-images which play a vital role in the preparation of ground truth map and synthetic SAR images have been analyzed. Several kinds of ground truth maps have been prepared, which will be used to evaluate the proposed change detection and change classification methods. In addition, different simulated SAR data have been prepared, so as to control the changes in the time series. Since most denoising algorithms hypothesized that SAR images affected by i.i.d. speckle, we briefly discussed the correlation issue.

---

7. Revisited CLEAN algorithm : <http://www.math-info.univ-paris5.fr/~rabergel/index.html>

---



## Part II

# Multi-temporal denoising

---



## Chapter 4

# Basics of despeckling

Synthetic aperture radar (SAR) imaging is a widely used remote measuring method. However, the inherent speckle which is attached to any coherent imaging system affects the analysis and interpretation of SAR images. Therefore, a preliminary speckle reduction step is often proposed for a successful exploitation of SAR images. Plenty of SAR image denoising methods (such as PPB [Deledalle et al., 2009], NL-SAR [Deledalle et al., 2015], SAR-BM3D [Parrilli et al., 2012], etc.) have been proposed in the past decades (see [Argenti et al., 2013] for a review) working on a single image. With large time series data, jointly processing multichannel has been proposed to provide better denoising results. This chapter gives an overview of denoising approaches both for single look SAR images and multitemporal series. Some similarity test which could be applied to calculate patch similarities will be described. In the end, we will introduce some popularly used denoising evaluation methods, along with the proposal of two new evaluation methods.

### 4.1 Main despeckling approaches

Speckle is an inherent problem of SAR images and it unavoidably limits SAR image interpretation. Therefore, image filtering plays a significant role in the successful exploitation of SAR images. The main problems of SAR image denoising are spatial resolution preservation, edge preservation, texture areas denoising, bias canceling and strongly reflecting target preservation.

#### 4.1.1 Spatial despeckling methods

Spatial denoising methods only pay attention to one image using the spatial information, for instance, by using weighted pixels to estimate the noise free pixel values. As we discussed before, noise is randomly distributed in SAR images. Most speckle reduction methods are based on the statistical characteristics of the noise, such as multiplicative Gamma noise, Rayleigh-Nakagami noise, additive Gaussian noise, Poisson noise, etc. In table 4.1, we reference some of the popular methods which have been divided into 4 families : Bayesian methods in the spatial domain, Bayesian methods in the transform domain, selection-based filtering and other non-Bayesian approaches.

---

### Bayesian methods in spatial domain

Speckle can be regarded as an unwanted information in SAR images. It acts like multiplicative noise and can be modeled with specific probability density functions.

The first model based despeckling method is probably be Lee filter [Lee, 1980]. To overcome the smoothness of edges, Lee [1981a] proposed to take the local gradient information into account during spatial sample selection. Based on local statistics, [Frost et al., 1982] derived an autocorrelation function of the reflectivity. It is used to better estimate the reflectivities. Lately, more denoising methods are derived based on SAR statistical properties, such as Kuan filter [Kuan et al., 1985], MAP filters [Lopes et al., 1993], denoising using TV regularization [Rudin et al., 2003], etc. Using Bayesian inference approach can effectively reduce the noise and extract desired information.

### Spatial filtering in transform domain

The principle of most transformation based denoising methods can be expressed as looking for a good  $\hat{u}$ , so that

$$\hat{u} = \mathcal{T}^{-1}(\varphi[\mathcal{T}(y)]) \quad (4.1)$$

where  $\mathcal{T}$  and  $\mathcal{T}^{-1}$  are the transformation function and inverse transformation function, and  $\varphi$  is the shrinking function.

The most popular used transformation approach is wavelet transformation. It is a linear transformation and it can keep the original statistic distribution of the data. Guo et al. [1994] applied the wavelet shrinkage to decompose the log-transformed SAR image into multiresolution channels. After applying a hard thresholding method, the denoised image can be obtained through an inverse transformation. Meanwhile, Gagnon and Jouan [1997] tested the soft thresholding method. Lately, [Foucher et al., 2001] extended Gamma-MAP filter to wavelet transformation domain. Beside the improvement with Bayesian approach, new statistical models [Xie et al., 2002a], undecimated wavelet transformation [Argenti and Alparone, 2002] and nonlocal method [Parrilli et al., 2012] are also utilized.

Apart from wavelet transformation, [Meer et al., 1994] proposed to transform the multiplicative noise  $v$  to signal-dependent additive noise  $g'$  :

$$\begin{aligned} y &= uv \\ &= u + (v - 1)u \\ &= u + g' \end{aligned} \quad (4.2)$$

Then, a spatial adaptive average is performed based on this transformation model. Unlike [Meer et al., 1994], Guo et al. [1994] proposed using homomorphic approach to transfer the multiplicative noise to additive noise :

$$\log y = \log u + \log v$$

Then, the Wavelet Shrinkage method, which can preserve the spatial resolution, is applied to reduce the noise. Since the log-transformed intensity SAR data are not totally following a Gaussian distribution, Xie et al. [2002b] applied Fisher-Tippet distribution function to describe its statistics. Based on this statistical improvement, Deledalle et al. [2017] proposed a framework which can extend Gaussian denoisers to pursue multi-channel speckle reduction.

In addition, [Aiazzi et al., 1998] used a ratio Laplacian pyramid (RLP) to transform the speckle corrupted image into multiresolution images. Then it estimates the reflectivities through an adaptive statistics filtering.

## Selection-based filtering

A most popular used statistical model ( $y = uv$ ) of intensity SAR image supposes the textures corrupted by Gamma distribution noise with unit mean ( $\mathbb{E}[v] = 1$ ). If enough samples which have the same reflectivities are selected, the simple way to estimate SAR reflectivity  $u$  is computing the arithmetic mean, which also belongs to the maximum likelihood estimation.

The similar candidates can be selected in different ways. Lee [1983] proposed selecting the neighboring pixels within two noise standard deviations ( $y - 2\sigma, y + 2\sigma$ ) in the searching window, with  $\sigma$  represents the standard deviation of the speckle. In addition, an adaptive window is also used to select the similar candidates, such as different orientation windows [Lee, 1981a], adaptive in size window [Park et al., 1999] and adaptive in shape window [Vasile et al., 2006], etc.

Currently, non-local methods are popularly used to select similar samples, which may be not connected with each other. This method relies on the self-similarity of images. To collect similar patches, numerical ways can be used to compute patch similarities  $S$ , as introduced in [Deledalle et al., 2012]. Then, their weight  $w(i, j)$  can be calculated with similar to weight transformation function  $\varphi$ .

$$w(i, j) = \varphi(S[\mathbf{y}(i), \mathbf{y}(j)])$$

After selecting  $N$  similar patches, the reflectivity can be estimated through weighted average. Non-local means technique has been widely used in SAR images denoising [Deledalle et al., 2009, Parrilli et al., 2012, Deledalle et al., 2015].

TABLE 4.1: A brief review of spatial despeckling methods

	Categories	Despeckling methods
1	Bayesian methods in spatial domain	Lee filter [Lee, 1980], Refined Lee filter [Lee, 1981a], Frost filter [Frost et al., 1982], Kuan filters [Kuan et al., 1985], MAP filters [Lopes et al., 1993], despeckling using TV regularization [Rudin et al., 2003], etc.
2	Bayesian methods in transform domain	Meer’s filter [Meer et al., 1994], RLP filter [Aiazzi et al., 1998], Homomorphic filtering in wavelet domain [Gagnon and Jouan, 1997], Non-homomorphic filtering in wavelet domain [Foucher et al., 2001], etc.
3	Selection-based filtering	Sigma filter [Lee, 1983], Probabilistic patch-based filter [Deledalle et al., 2009], Bilateral filtering [Zhang et al., 2011], NL-SAR [Deledalle et al., 2015], SAR block matching 3-D filter [Parrilli et al., 2012], etc.
4	Other non-Bayesian approaches	Order statistics and morphological filters [Alparone et al., 1996], Anisotropic diffusion [Yu and Acton, 2002], Despeckling based on compressed sensing [Foucher, 2008], etc.

## Other non-Bayesian approaches

Recently, convolutional neural networks have shown a high capability of denoising data affected by additive white Gaussian noise (AWGN) [Zhang et al., 2017]. Application to

SAR images has also been proposed, either through homomorphic approach [Chierchia et al., 2017a] or directly applying Gamma distribution based method [Wang et al., 2017a]. Unlike traditional SAR image denoising methods, these methods predict the noise free value through well estimating its multiplicative speckle. These proposed techniques provide comparable despeckling results w.r.t. state-of-the-art approaches, both in signal noise ratio (simulated data) and feature preservation. With the development of new neural network toolboxes such as Deep Neural Network library<sup>1</sup> and MatConvNet<sup>2</sup>, this kind of methods seems designated to a bright future.

Spatial denoising methods only pay attention to one image using the spatial information, for instance, by using weighted pixels to estimate the noise free pixel values. This can induce biased denoised values when participating pixel candidates are not well selected. In addition, even using powerful spatial denoising approaches (such as SAR-BM3D [Parrilli et al., 2012] and NL-SAR [Deledalle et al., 2015]), the tiny structures can be damaged.

Since most SAR remote sensing scientists are familiar to the traditional spatial denoising techniques, we will try to propose a new framework which can apply these spatial denoising approaches to temporal domain.

#### 4.1.2 Multitemporal despeckling methods

With well registered multi-temporal images, both spatial and temporal information can be exploited in the denoising process, which gives the potential of providing better denoising results than using only a single image. Most of the multitemporal despeckling methods are extended from the single image denoising techniques. This section classifies multitemporal denoising methods in 4 categories.

##### Weighted temporal average

To overcome the resolution broadening of spatial denoising approach, Lee et al. [1991] take the multi-channel and multi-frequency information into account during the filtering. Adaptive moving rectangle window is utilized to estimate the correlation coefficient. [Quegan and Yu, 2001] proposed different ways of dealing with correlated and uncorrelated multitemporal images, along with recursive implementations. This method has been successfully applied to forest mapping [Quegan et al., 2000a].

The significant advantage of these kinds of filter is that temporal SAR images acquired using different sensors can be jointly filtered. However, using a box window may destroy fine features, bring spatial blurring and introduce wrong results near the bright points.

##### Binary weighted temporal average

To suppress the negative effects of changed points, [Lê et al., 2014, Lê et al., 2015, Su et al., 2014] proposed to use only the unchanged candidates to complete the filtering. This approach can effectively suppress the changed bright points effect. However, the denoising results are highly influenced by the change detection threshold. An improper threshold may lead to bias denoising results, especially in the seasonal changed areas whose change are hard to be detected.

---

1. <https://developer.nvidia.com/cudnn>

2. <http://www.vlfeat.org/matconvnet/>

---

### 3D neighborhood based methods

In [Ciuc et al., 2001], only the adjacent similar pixels, which have the same distribution as the target pixel, are used to estimate the noise free value. It extends the spatially based denoising method to the spatial-temporal domain. This method has the capability to preserve fine textures.

### Non-local based methods

SAR images usually exist with self-similarities. This makes it possible to use non-local filtering. Non-local means has been applied to multitemporal SAR image denoising, such as 2SPPB [Su et al., 2014], Nonlocal temporal filter (NLTF) [Chierchia et al., 2017b], Multitemporal SAR-BM3D [Chierchia et al., 2017b]. All these methods used the generalized likelihood ratio (GLR) [Deledalle et al., 2009] to calculate the patch similarities. These approaches can provide much better denoising results and can be recognized as state-of-the-art despeckling methods.

In addition, the temporal denoising can also be processed in a transformed domain. After performing logarithm and Discrete Cosine Transformation, Coltuc et al. [2000] proposed applying refined Lee filtering to denoise the image in the spatial domain. Furthermore, MSAR-BM3D [Chierchia et al., 2017b] pursued the denoising in wavelet transformation domain.

These methods exploit different search approaches to select similar points, such as fixed rectangle window size, adaptive 3D window size, 3D selected patches, etc. However, large time series will increase computational complexity and lead to higher computing storage requirement. A summary of the references is given in table 4.2.

Multitemporal denoising methods could take advantage of more and more available SAR images to solve the spatial denoising problems, for the benefit of resolution preservation. We aim at improving filtering results by exploiting temporal information. In addition, when enough images are available, the temporal average image carries significant information. We will propose new methods based on the use of the so-called “super-image” in the next chapter.

TABLE 4.2: Multitemporal SAR images denoising methods

	Categories	Despeckling methods
1	Weighted temporal average	Multitemporal Lee Sigma [Lee et al., 1991], Texture compensation multichannel filter (TCMF) [Bruniquel et al., 1997], Optimal unbiased linear despeckling [Yu and Quegan, 2000, Quegan et al., 2000b,a]
2	Binary weighted temporal average	Adaptive multitemporal SAR image filtering [Lê et al., 2014], Two-Step multitemporal nonlocal means for SAR images [Su et al., 2014]
3	3D neighborhood based methods	Multitemporal filtering using three-dimensional (3D) adaptive neighborhoods [Ciuc et al., 2001]
4	Non-local based methods	2SPPB [Su et al., 2014], Nonlocal temporal filter (NLTF) [Chierchia et al., 2017b], Multitemporal SAR-BM3D [Chierchia et al., 2017b]

## 4.2 Similarity measures

Intensity SAR images are corrupted by multiplicative Gamma noise with mean equal to 1. To select enough candidates, non-local means [Buades et al., 2005] is a popular approach. It can transfer different points or patch similarities  $S$  to corresponding weights  $w(i, j) = f(S[\mathbf{y}(i), \mathbf{y}(j)])$ . A similarity metric specifically represents the likelihood that two intensity observations correspond to the same unknown noise free scene. Similarity measures are very important in image processing, they have been widely used in image denoising, segmentation, classification, change detection and object detection. It can be obtained by calculating the distance or quantifying the pairwise interrelationships such as dissimilarity and correlation. Hereafter, we introduce several similarity methods which are popularly used in SAR image processing.

### 4.2.1 Probabilistic based similarity measure

Under a statistical signal processing perspective, SAR image similarity can be calculated using mutual information, variational information, mixed information, Kullback-Leibler divergence techniques, etc [Cui et al., 2016]. In addition, based on specific probability distributions, other similarity measurements could be applied to SAR image processing.

#### 4.2.1.1 Likelihood ratio test for Gamma distributed data

For the similarity of intensity SAR images, [Lombardo and Oliver, 2001, Conradsen et al., 2003] proposed an estimation method using a likelihood-ratio test. Given two intensity values  $y_1$  and  $y_2$  following Gamma distributions with different numbers of look  $L_1$  and  $L_2$ , it can be shown that this test is :

$$GLRT(y_1, y_2) = (L_1 + L_2)^{L_1+L_2} \frac{(y_1)^{L_1} (y_2)^{L_2}}{(L_1 y_1 + L_2 y_2)^{L_1+L_2}} \quad (4.3)$$

During a patch comparison with two dates, if the pixels in the patch are i.i.d.,  $L_1$  and  $L_2$  are the ENL of the two dates. Then, the patch similarity can be expressed as [Su et al., 2014] :

$$S_{GLR}(\mathbf{y}_1(s), \mathbf{y}_2(s)) = \frac{(\sum_{k_1} y_1(s+k_1))^{L_1} (\sum_{k_2} y_2(s+k_2))^{L_2}}{(\sum_{k_1} y_1(s+k_1) + \sum_{k_2} y_2(s+k_2))^{L_1+L_2}} \frac{(L_1 + L_2)^{L_1+L_2}}{L_1^{L_1} L_2^{L_2}} \quad (4.4)$$

The detailed derivative will be introduced later.

#### 4.2.1.2 Likelihood ratio test for Rayleigh-Nakagami distributed data

With noisy amplitude data, the test is expressed as Deledalle et al. [2009] :

$$S_{GLR}(A_1, A_2) = (2L - 1) \log \left( \frac{A_1}{A_2} + \frac{A_2}{A_1} \right) \quad (4.5)$$

where  $A_1$  and  $A_2$  correspond to different amplitude values of the SAR images with same ENL ( $L_1 = L_2 = L$ ). Similarly, we can compute the patch similarities through :

$$S_{GLR}(\mathbf{A}_1(s), \mathbf{A}_2(s)) = (2L - 1) \sum_k \log \left( \frac{A_1(s+k)}{A_2(s+k)} + \frac{A_2(s+k)}{A_1(s+k)} \right) \quad (4.6)$$

where  $s$  is the pixel location and  $k$  is used to locate all the pixels near it.

### 4.2.1.3 Likelihood ratio test for Fisher-Tippett distributed data

As introduced in the previous section, the log-transformed intensity SAR data follow Fisher-Tippett distribution [Deledalle et al., 2017]. Using the likelihood ratio test we obtain the similarity estimation function :

$$S_{GLR}(x_1, x_2) = \frac{(L_1 + L_2)^{L_1+L_2}}{L_1^{L_1} L_2^{L_2}} \frac{1}{(x_1 - x_2)^{L_1} (x_2 - x_1)^{L_2}} \quad (4.7)$$

where  $x_1$  and  $x_2$  are the log-transformed intensity data, with ENL equal to  $L_1$  and  $L_2$ , respectively.

### 4.2.2 Geometric approach

This distance is one kind of log-Euclidean distance introduced in [Arsigny et al., 2006] :

$$D(S_1, S_2) = \|\log(S_1^{-\frac{1}{2}} \cdot S_2 \cdot S_1^{-\frac{1}{2}})\| \quad (4.8)$$

where  $S_1$  and  $S_2$  are two symmetric matrices. D'Hondt et al. [2013] applied it to polarization SAR similarity estimation with :

$$D(\Sigma_1, \Sigma_2) = \|\log(\Sigma_1^{-\frac{1}{2}} \cdot \Sigma_2 \cdot \Sigma_1^{-\frac{1}{2}})\|_F \quad (4.9)$$

where  $\Sigma$  is the empirical polarimetric covariance matrix and  $\|\cdot\|_F$  is the Frobenius norm. When processing single polarization SAR images, it becomes to be the square distance between homomorphic transformed estimated intensity values, and the dissimilarity calculation boils down to [Deledalle et al., 2014] :

$$D_{geo}(\hat{u}_1, \hat{u}_2) = (\log(\hat{u}_2) - \log(\hat{u}_1))^2 \quad (4.10)$$

where  $\hat{u}_1$  and  $\hat{u}_2$  are the estimated noise free intensity values. This method is easily applied to patch-based version  $D_{geo}(\mathbf{y}_1(s), \mathbf{y}_2(s)) = \sum_k (\log(y_1(s+k)) - \log(y_2(s+k)))^2$ .

### 4.2.3 Kernel method

As introduced in [Vert et al., 2004], common kernel functions can be viewed as similarity functions. Directly SAR images similarity processing always in a nonlinear way [Oliver and Quegan, 2004b]. Using kernel function mapping data points into high dimensional Hilbert space or feature space, we can process SAR image linearly [Camps-Valls et al., 2008] for application tasks. One can flexibly define a kernel for a specific purpose, as long as it fulfills Mercer's theorem [Mercer, 1909].

Radial basis function (RBF) kernel is a popularly used kernel function which requires that the variables belong to Gaussian distributions. Based on the aforementioned analysis, we could apply this kernel method to the debiased log-transformed SAR data.

$$K(x, x') = \exp\left(-\frac{\|x - x'\|^2}{2\sigma^2}\right) \quad (4.11)$$

where  $x$  and  $x'$  are the log-transformed intensity data,  $\|x - x'\|^2$  is the Euclidean distance and  $\sigma$  is a free parameter to be tuned. It should be noted that the generalized likelihood ratio of Gaussian distribution also has this kind of similarity.

#### 4.2.4 Correlation coefficient for interferometric data

Correlation coefficient can be used to qualify the correlation and dependency between two or more complex values of interferometric images. It could also be used for binary change detection. With two complex vectors, the correlation coefficient  $\rho_c(z_1, z_2)$  is defined as equation (2.3). To suppress the effect of high variability speckle, spatial multilooking can be made which results in a loss of spatial resolution. With scattering vectors  $z_1, z_2, z_3, \dots, z_N$  from a spatial neighborhood centered at pixel  $s$  :

$$\rho_c(z_1, z_2) = \frac{|\sum_{i \in W} z_1(i) z_2(i)^\dagger|}{\sqrt{(\sum_{i \in W} z_1(i) z_1(i)^\dagger) (\sum_{i \in W} z_2(i) z_2(i)^\dagger)}} \quad (4.12)$$

where  $N$  represents for the number of pixels in window  $W$ .

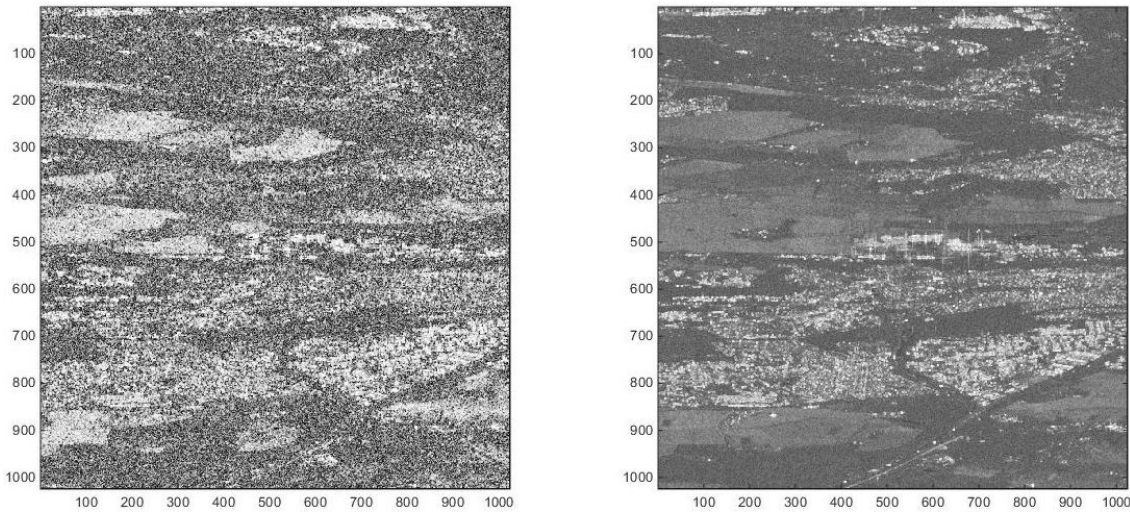


FIGURE 4.1: Spatial coherence on a  $3 \times 3$  window between 2 Sentinel-1 images (left) and the geometric mean of the temporal coherence images (right). Homogeneous farmland areas and building areas have high temporal coherence. 69 well registered complex images are used for the acquisition of geometric coherence map. The coherence images are calculated using single look complex (Sentinel-1 Interferometric Wide swath mode VV polarisation) SAR data with respect to the 68th image.

With  $M$  single look complex SAR images, the correlation coefficient  $\rho_c$  could be computed spatially and temporally (Fig.4.1). Spatial coherence can be used to define the adjacent pixels belonging to the same object or not, while temporal coherence reflects the temporal behaviors of the objects. To illustrate the temporal changes of coherence coefficient with respect to one specific time  $t$ , the geometric mean of coherence maps is calculated using :

$$\rho_t^{geo}(s) = \left( \prod_{t'=1}^M \rho(z_t(s), z_{t'}(s)) \right)^{\frac{1}{M}} \quad (4.13)$$

where  $M$  is the number of temporal images,  $z_t$  is the reference image and  $s$  is the pixel coordinate in one image. For bi-temporal coherence maps, the geometric mean is computed

using :

$$\rho^{geo}(s) = \left( \prod_{t=1}^{M-1} \rho(z_t(s), z_{t+1}(s)) \right)^{\frac{1}{M-1}} \quad (4.14)$$

Similarly, the arithmetic mean of temporal coherence maps and bi-temporal coherence maps are calculated using :

$$\rho_t^{AM}(s) = \frac{1}{M} \left( \sum_{t'=1}^M \rho(z_t(s), z_{t'}(s)) \right) \quad (4.15)$$

$$\rho^{AM}(s) = \frac{1}{M-1} \left( \sum_{t=1}^{M-1} \rho(z_t(s), z_{t+1}(s)) \right) \quad (4.16)$$

As shown in figure 4.1, different objects have different characteristics in the temporal average image. For example, farmland areas have uniform coherence values, building areas have much larger coherence values, forest and water areas have lower coherence values, etc. We can exploit this coherence information during the time series analysis.

#### 4.2.5 Feature based similarity

Feature information can be extracted through some image algebra operators, such as differencing, ratio, log-ratio and image transformation. Then, feature similarity can be analyzed with clustering, thresholding, extreme learning machine (ELM), etc. In addition, some local descriptors such as SIFT, shape context, orientation, persistent scatterers and distributed scatterers could also be used to measure the similarities.

### 4.3 Evaluation method for denoising results

Qualitative and quantitative measures of speckle reduction performances is a challenging task, especially when noise free data are unavailable. Visually checking the despeckling results is an immediate and subjective way for quality evaluation, but it is limited by human vision ability. To overcome this limitation, numerical measurements should be used, although they are usually blind to local artifacts. Some of the commonly used assessment methods are introduced in the following part.

#### 4.3.1 Visual analysis

After image restoration, speckle reduction in homogeneous areas, feature preservation, absence of artifacts can be checked visually [Oliver and Quegan, 2004b]. To make the examination more obvious and specific, we used the following methods.

##### (1) Ratio between noisy data and denoised result

The ideal despeckling should totally remove the random Gamma distribution noise, and the ratio of the noisy image with the denoised image should only contain pure noise (so-called “method noise” in the image domain). In the case of imprecise denoising, a geometric texture could be seen in the ratio image. Checking the residual structure in the ratio image ( $y/\hat{u}$ ) [Oliver and Quegan, 2004b], especially in the changed areas, is an easy way to evaluate the denoising performances.

## (2) Ratio between the noise free image and denoised data

The goal of denoising is to acquire the reflectivity of the speckle corrupted image. Since most of the denoising methods use the spatial information to estimate the noise free values, the bright targets and the line features may be destroyed. This phenomenon is especially serious in building areas. When the noise free image is available, visually checking the ratio between noise free image and denoised image can help us distinguish the ruined textures.

To clearly illustrate the bias in the restoration image, we can use the change magnitude detection method to acquire the vivid results as shown in figure 4.2. The change magnitude detection method will be introduced in chapter 8.

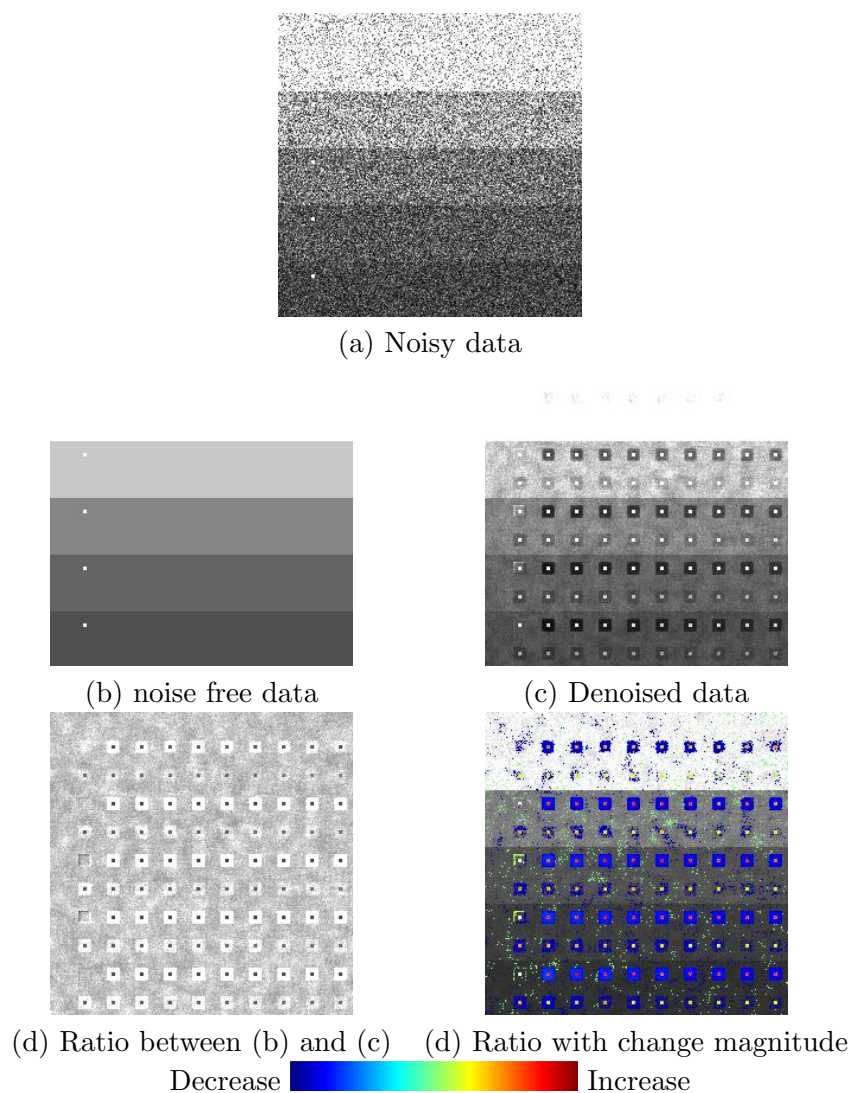


FIGURE 4.2: Denoising performance evaluation with ratio image. The ratio in (c) is calculated with noise free and denoised data. Only part of the ratio is selected with a predefined threshold in (d), which uses the denoised data as the background. Blue area : denoised values are smaller than original image, red area : denoised values are larger than original image.

In addition, this evaluation method can be transformed to quantitative evaluation method with the use of dissimilarity test  $\exp[-(\log(u/\hat{u}))^2]$ . Under the null hypothesis,  $u/\hat{u}$  distributes like Fisher distribution [Conradsen et al., 2003]. The dissimilarity areas can be chosen according to the threshold calculated based on cumulative Fisher distribution function. Then, some total scores can also be acquired.

(3) Changed area comparison for temporal denoising

Changes could not be avoided during the acquisition of temporal SAR images, both in vegetation and building areas. Since temporal information is exploited during the multitemporal denoising, changed points may bring wrong information to the denoising results. Visually checking the denoised changed areas can help us compare the denoising methods. The temporal evolution of the changed areas can also be visualized.

### 4.3.2 Quantitative evaluation

Measurement of speckle reduction performances is a challenging task, especially when noise free data are unavailable. Visually checking the despeckling results is an immediate and important way for quality evaluation, but it lacks objectivity. To overcome this limitation, peak signal-noise-ratio (PSNR) and structure similarity (SSIM) indexes may be used, but their limits have been abundantly discussed.

(1) PSNR : Peak signal-noise-ratio

PSNR is a commonly used approach to evaluate the quality of noise free reflectivity restoration results. The denoising results can be quantified by the PSNR with :

$$\text{PSNR} = 10 \cdot \log_{10} \frac{|u_A|_{max}^2}{\mathbb{E}[(u_A(s) - \hat{u}_A(s))^2]} \quad (4.17)$$

where  $|u_A|_{max}$  is the maximum amplitude value in the noise free data and  $\hat{u}_A$  is the denoised amplitude value.

(2) MSSIM : Mean structure similarity index

To evaluate the preservation of image features, structural similarity index measurement (SSIM) [Wang et al., 2004] is often preferred to PSNR. From the SSIM, we derive the mean structural similarity index measurement (MSSIM) values which provide a comprehensive measure of the whole image :

$$\text{MSSIM} = \frac{1}{N} \sum_{i=1}^N \left[ \frac{2 \cdot \widehat{\mathbb{E}}[u_A] \cdot \widehat{\mathbb{E}}[\hat{u}_A] + \alpha_1}{\widehat{\mathbb{E}}[u_A^2] + \widehat{\mathbb{E}}[\hat{u}_A^2] + \alpha_1} \frac{2 \cdot \widehat{\text{Cov}}[u_A, \hat{u}_A] + \alpha_2}{\widehat{\text{Var}}[u_A] + \widehat{\text{Var}}[\hat{u}_A] + \alpha_2} \right]$$

where  $u_A$  and  $\hat{u}_A$  are noise free and denoised patches,  $\text{Cov}[\cdot, \cdot]$  is the measure of covariance,  $\alpha_1$  and  $\alpha_2$  are suitable constants,  $N$  is the number of local windows in the image.

(3)  $\alpha\beta$  estimator for ratio images

When despeckling real SAR data, the noise free image are usually unavailable. In this case, we could use  $\alpha\beta$  index value [Gomez et al., 2016] to evaluate the denoising performances :

$$\alpha\beta = \{\alpha \cdot |\delta_{\text{ENL}}| + (1 - \alpha)|\delta_u|\} + \beta_{ratio} \quad (4.18)$$

where  $\alpha \in [0, 1]$  is defined experimentally, so as to adjust the weight of  $|\delta_{\text{ENL}}|$ .  $\delta_{\text{ENL}}$  represents the residual ENL (equal to  $\text{ENL}_{\text{noisy}} - \text{ENL}_{\text{ratio}}$ ),  $\delta_u$  is the residue mean value of the speckle ( $1 - u_{\text{ratio}}$ ). All these values should be estimated in homogeneous areas.  $\beta_{\text{ratio}}$  is estimated by the edge detector introduced in [Gomez et al., 2016].

(4) ENL comparison in homogeneous areas

With the same estimation window size, the best despeckling results in the homogeneous areas should be smoothed with bigger ENL, because generated artifacts or poor denoising results will increase the variance, which leads to decreasing ENL (Eq.2.9). This method is useful for real SAR image despeckling when there are no available reference indexes.

(5) M-estimator

Gomez et al. [2017] propose an evaluation method without using the ground truth. It can automatically select homogeneous areas and provide a score for the evaluation. After selecting  $N$  homogeneous areas, the first-order residual  $r_{\widehat{\text{ENL}}, \hat{u}}$  is calculated through :

$$r_{\widehat{\text{ENL}}, \hat{u}} = \frac{1}{2} \sum_{i=1}^N (r_{\widehat{\text{ENL}}}(i) - r_{\hat{u}}(i)) \quad (4.19)$$

$$r_{\widehat{\text{ENL}}}(i) = \frac{\widehat{\text{ENL}}_{\text{noisy}}(i) - \widehat{\text{ENL}}_{\text{ratio}}(i)}{\widehat{\text{ENL}}_{\text{noisy}}(i)} \quad (4.20)$$

$$r_{\hat{u}}(i) = |1 - \hat{u}_{\text{ratio}}(i)| \quad (4.21)$$

where  $\widehat{\text{ENL}}_{\text{noisy}}$  and  $\widehat{\text{ENL}}_{\text{ratio}}$  are the local ENL estimated from the noisy image and ratio image using a sliding window, and  $\hat{u}_{\text{ratio}}$  represents the local mean in the ratio image calculated with the same window size.

Then, Gomez et al. [2017] applied the co-occurrence matrix  $C(i, j)$  to measure the remaining geometrical content in the ratio image. The normalized co-occurrence matrix is computed through :

$$c(i, j) = C(i, j)/K \quad (4.22)$$

where  $K$  is a constant. A high  $c$  value represents a high textural variation.

$$h = \sum_i \sum_j \frac{1}{1 + (i - j)^2} \cdot c(i, j) \quad (4.23)$$

$$\delta h = 100|h_0 - \bar{h}_g|/h_0 \quad (4.24)$$

where  $h_0$  and  $h_g$  are the mean values of selected homogeneous areas from the ratio image and the randomly permuting ratio image, respectively.  $\bar{h}_g$  is the mean value of the randomly permuting ratio values where  $c \geq 1$ .

Then, we can compute the M-index score through :

$$M_{\text{score}} = r_{\widehat{\text{ENL}}, \hat{u}} + \delta h \quad (4.25)$$

We will use this evaluation method to evaluate the denoising performances in the following chapters.

## (6) Analysis of the residual with autocovariance

The evaluation method proposed here follows the idea presented in [Riot et al., 2017] which examines the residual image and looks for possible remaining structural elements in this residual image. Unlike maximum ENL estimation or  $\alpha\beta$  estimation [Gomez et al., 2016] method, this method is automatic and does not rely on a supervised selection of homogeneous regions. It also provides a global score for the whole image. The ratio between noisy data  $y$  and denoised data  $\hat{u}$  is computed through :

$$R = \frac{y}{\hat{u}} \quad (4.26)$$

After denoising, it is expected that the ratio  $R$  contains pure speckle, except in regions where some structures were lost during the denoising procedure. In [Riot et al., 2017], the remaining structures are evaluated with autocorrelation. In our case, the autocovariance is used for the residuals evaluation. The autocovariance estimator  $C_{P_{s+k}}$  on a noisy patch  $P$  of size  $W_s$ , centered at location  $s$ , for all surrounding patches  $P(s+k)$  is equal to :

$$C_{P_{s+k}} = P(s)P(s+k) \quad (4.27)$$

The mean value of the ratio is removed during the calculation. We propose to estimate a normalized residuals autocovariance  $C_{P_s}^{norm}$  on each patch  $P_s$  of the residual as :

$$C_{P_s}^{norm} = \frac{N_1^2}{N_1^2 - 1} \cdot \frac{\|C_{P_s}\|_2^2 - \|C_{P_s}(0,0)\|_2^2}{\sum_{s+k \in W_s} (R_{s+k}^2 - \mathbb{E}[R])} \quad (4.28)$$

with  $N_1^2$  the patch size and  $\mathbb{E}[R] = 1$ , because of the unit mean of Gamma distribution noise. Then, we can aggregate the  $C_{P_s}^{norm}$  covariances computed over each patch to obtain a quality map at each pixel  $s'$  :

$$W_{map}(s') = \frac{\sum w(s, s') C_{P_{s,s'}}^{norm}}{\sum w(s, s')} \quad (4.29)$$

where  $w(s, s') = 1$  if the pixel in position  $s'$  of the residual is used in the patch  $P_s$ ,  $C_{P_{s,s'}}^{norm}$  represents the autocovariance value of  $s'$  in the patch  $P_s$ . Then, a global score can be obtained with an average :

$$W_{score} = \frac{1}{N} \sum_{(s')} W_{map}(s') \quad (4.30)$$

where  $N$  is the number of pixels in the image.

In practice, we will limit the autocovariance to displacements of one pixel in both vertical and horizontal directions to speed up the process, following the recommendation of Dabov et al. [2007]. In the quality map  $W_{map}(s')$ , low values inform where an efficient denoising has been obtained. The residuals evaluation method does not need any ground truth. Therefore, it is suited for evaluating denoising of real SAR images.

## 4.4 Conclusion

In this chapter, spatial despeckling and multitemporal noise reduction approaches have been briefly summarized. Then, several groups of similarity tests were presented. We also

introduced the popularly used visual examination and numerical despeckling evaluation methods. Furthermore, we proposed using the jet colormap to index biased denoising results and using autocovariance to highlight the remaining textures in the residual image. In the following part, we will study more specifically some multitemporal SAR denoising methods.

---

## Chapter 5

# Despeckling by weighted temporal averaging

One of the oldest ways to exploit a multitemporal series is temporal multilooking. In this chapter, we review some of the weighted temporal averagings that have been proposed and present an improvement to these approaches.

### 5.1 Unbiased temporal average (UTA)

Coherent processing of SAR data makes the speckle acts like multiplicative noise (Eq.2.7). Then the speckle model can be expressed as [Lee, 1981b] :

$$y_t(s) = u_t(s)v_t(s) \quad t = 1, \dots, M \quad (5.1)$$

where  $y_t(s)$  is the intensity value,  $u_t(s)$  the noise-free value,  $v_t(s)$  the Gamma distribution noise,  $s$  is the position in one image and  $t$  is the serial number of  $M$  images. When averaging  $L$  independent samples, the strength of the speckle in featureless areas can be measured by [Lee, 1986] :

$$\sigma_v = \frac{\sqrt{\text{Var}(y)}}{\mathbb{E}(y)} = \frac{1}{\sqrt{L}} \quad (5.2)$$

where  $\sigma_v$  is the standard deviation of the speckle, and  $\mathbb{E}()$  is the mathematical expectation.

Thus, a simple way to reduce the speckle noise in the temporal domain is by averaging the multitemporal values  $y_1(s), y_2(s), \dots, y_M(s)$  to increase the ENL. However, the reflectance can vary because of the geometry of acquisition (different incidence angles) or temporal changes (variations of dielectric properties on the ground). Besides, the temporal samples are usually correlated (and thus not independent), especially when acquired in interferometric conditions. So, appropriate weights in the average should be used. For multitemporal SAR images, the linear estimation of  $\hat{u}_t$  could be [Lee et al., 1991] :

$$\hat{u}_t(s) = \mu_t \sum_{t'=1}^M \frac{w_{t'}}{\mu_{t'}} y_{t'}(s) \quad (5.3)$$

where  $\mu_t = \mathbb{E}(y_t)$  represents the expected value of  $y_t$ ,  $w = [w_1, \dots, w_M]^\top$  are the generalized weights to be optimized. For the unbiased linear estimation,  $\sum_{t'=1}^M w_{t'} = 1$  and we get :

$$w = D^{-1}C \quad (5.4)$$

where  $C = [c_1, c_2, \dots, c_M]$  is a vector with  $c_1 = 1$  and  $c_t = 0$  for  $t = 2, \dots, M$ , and  $D = [D_{tt'}]_{1 \leq t \leq M, 1 \leq t' \leq M}$  is defined as [Lee et al., 1991, Chierchia et al., 2017b] :

$$D_{tt'} = \begin{cases} 1, & \text{if } t = 1 \\ \rho_{1t'} - \rho_{tt'}, & \text{if } t = 2, \dots, M. \end{cases} \quad (5.5)$$

$\rho_{tt'}$  denotes the correlation coefficient between  $y_t$  and  $y_{t'}$ , which is given by :

$$\rho_{tt'} = \frac{\mathbb{E}[(y_t - \mu_t)(y_{t'} - \mu_{t'})]}{\sqrt{\mathbb{E}[(y_t - \mu_t)]^2 \mathbb{E}[(y_{t'} - \mu_{t'})]^2}} \quad (5.6)$$

with  $\rho_{tt'} = \rho_{t't}$  and  $\rho_{tt} = 1$ .

In [Quegan and Yu, 2001], experiments have been done with  $w_{t'} = \frac{1}{M}$  in equation 5.3, expressing that there is no correlation between different images and only a little loss was observed in the results. In this case, the denoised value is given by :

$$\hat{u}_t(s) = \frac{\mu_t}{M} \sum_{t'=1}^M \frac{y_{t'}(s)}{\mu_{t'}} \quad (5.7)$$

where  $\mu_t$  is a local spatial average estimating  $\mathbb{E}[y_t]$  :

$$\mu_t(s) = \frac{1}{N} \sum_{s+k \in W} y_t(s+k) \quad (5.8)$$

The unbiased temporal average method is optimal for uncorrelated data and suboptimal for correlated data [Lee et al., 1991]. It could also be applied to multi-sensor and multi-baseline SAR data [Quegan and Yu, 2001]. However, the spatial average approach may oversmooth boundaries and causes wrong estimation results around bright targets.

## 5.2 Nonlocal temporal filter (NLTF)

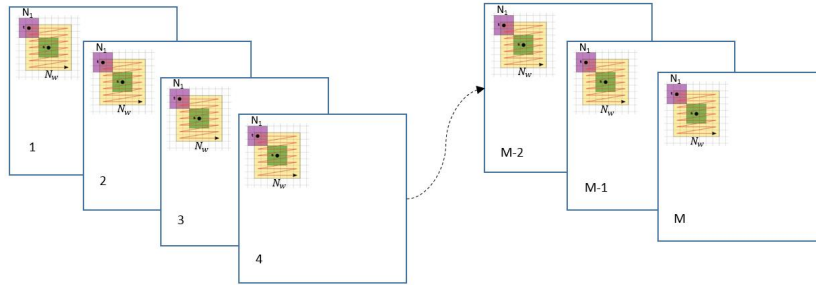


FIGURE 5.1: NLTF flowchart. For each point  $s$ , the similarity points are selected with patch  $N_1^2$  in a search window  $N_w^2$ .

To improve the reflectivity estimation part, Chierchia et al. [2017b] proposed a nonlocal temporal filtering method (Fig.5.1). The nonlocal method is used by calculation of patch similarities within the search window of size  $N_w^2$ , so as to acquire similar patches of size

$N_1^2$  in the image around pixel  $s$ . After acquiring  $N_2$  similar patches, the mean value  $\mu$  is obtained by averaging all the pixels in the similar patches :

$$\mu_t(s) = \frac{1}{N_2 N_1^2} \sum_{n=1}^{N_2} \sum_k y_t(s_n + k) \quad (5.9)$$

where  $s_n$  represents the center location of different patches,  $k$  is a 2-dimensional shift indicating the location within each patch of size  $N_1^2$ . The corresponding variance is estimated as follows :

$$\sigma_t^2(s) = \frac{1}{N_2 N_1^2} \sum_{n=1}^{N_2} \sum_k [y_t(s_n + k) - \mu_t(s)]^2 \quad (5.10)$$

Note that similar patches could have structured information (edge, texture, ...) which is not taken into account by the averaging step of equation (5.9). Block similarity estimated based on generalized likelihood ratio test [Deledalle et al., 2009, Parrilli et al., 2012] is equal to :

$$d_1[y_t(s), y_t(i)] = (2L - 1) \sum_k \log \left( \sqrt{\frac{y_t(s+k)}{y_t(i+k)}} + \sqrt{\frac{y_t(i+k)}{y_t(s+k)}} \right) \quad (5.11)$$

where  $s$  and  $i$  are the center locations of compared patches. To iteratively refine the estimated weights, the symmetric Kullback-Leibler (KL) divergence is used :

$$d_2[y_t(s), y_t(i)] = \sum_k \left[ (2L-1) \log \left( \sqrt{\frac{y_t(s+k)}{y_t(i+k)}} + \sqrt{\frac{y_t(i+k)}{y_t(s+k)}} \right) + \gamma L \frac{|\hat{y}_t(s+k) - \hat{y}_t(i+k)|^2}{\hat{y}_t(s+k)\hat{y}_t(i+k)} \right] \quad (5.12)$$

After acquiring the estimated value  $\mu$ , the correlation coefficients between different 3-D patches are estimated as :

$$\rho_{t,t'}(s) = \sum_{n=1}^{N_2} \sum_k \frac{[y_t(s_n + k) - \mu_t(s)][y_{t'}(s_n + k) - \mu_{t'}(s)]}{\sigma_t(s)\sigma_{t'}(s)N_2N_1^2} \quad (5.13)$$

After having estimated the statistics, the temporal weight vector is estimated as in equation (5.4), and the pixels in the patches are filtered as in equation (5.3). For every  $s_n \in N_2$  we have :

$$\hat{u}_t(s_n, k) = \mu_t(s) \sum_{t'=1}^M \frac{w_{t'}(s)y_{t'}(s_n + k)}{\mu_{t'}(s)} \quad (5.14)$$

Because of the unavailability of similar blocks, isolated bright targets can be the cause of wrong denoised results around them. To avoid this phenomenon, a target detection method is used so as to prohibit the denoising around it. With a predefined threshold  $\tau$ , targets are detected using :

$$\xi(s) = \max_{1 \leq t \leq M} \frac{\hat{\sigma}_t^2(s)}{\hat{u}_t^2(s)} \quad (5.15)$$

where  $\hat{\sigma}_t$  and  $\hat{u}_t$  are spatially estimated through a sliding window. When  $\tau \leq \xi(s)$ , the time series  $y_1, y_2, \dots, y_M$  are not filtered. Although this care allows to preserve some significant image features, it prevents filtering noise close from targets.

### 5.3 Adaptive nonlocal temporal filter (ANLTF)

We present here a simple improvement of Quegan's approach (Eq.(5.7)) by replacing the spatial average with a nonlocal estimation. This improvement is a minor contribution of this thesis.

#### 5.3.1 Adaptive spatial averaging

Because fine textures are present in SAR images, using the spatial average (Eq.5.8) is often not suitable. Fine edges, point targets and fine features are smeared by large search windows, and the spatial similarity points acquired by NLTF may belong to different objects. In order to get a better reflectance estimation, an adaptive spatial averaging method can be used. Many selection based methods could be used. SAR-BM3D [Parrilli et al., 2012], PPBNakagami [Deledalle et al., 2009], MuLoG-BM3D and homomorphic-BM3D [Deledalle et al., 2017] are used in the following experiments. A brief description of these methods is given in Section 4.1. These methods average similar points using adaptive weights deduced from patch comparison. Any other adaptive denoising method could be used in place of these methods.

For an adaptive nonlocal average, with a search window  $N_w^2$  and patch size  $N_1^2$ , the means and variances are estimated as [Deledalle et al., 2015] :

$$\mu_t^{\text{NL}}(s) = \frac{\sum_{i \in N_w^2} \omega(s, i) y_t(i)}{\sum_{i \in N_w^2} \omega(s, i)} \quad (5.16)$$

$$\sigma_t^{\text{NL}^2}(s) = \frac{\sum_{i \in N_w^2} \omega(s, i) y_t^2(i)}{\sum_{i \in N_w^2} \omega(s, i)} - \mu_t^{\text{NL}^2}(s) \quad (5.17)$$

where  $\omega(s, i)$  is the weight between two patches centered in  $s$  and  $i$ .

#### 5.3.2 Multitemporal denoising

We propose to use the improved  $\mu_t^{\text{NL}}(s)$  values in the temporal filtering. After computation of the mean and variance, spatial varying ENL ( $L_{t'}$ ) are estimated, and the multitemporal images are denoised using [Quegan and Yu, 2001] :

$$\hat{u}_t(s) = \frac{\mu_t^{\text{NL}}(s)}{M} \sum_{t'=1}^M \frac{y_{t'}(s)}{\mu_{t'}^{\text{NL}}(s)} \quad (5.18)$$

Using the target detection method, adjacent pixels may also be detected as bright targets and the targets which have changed could also be selected. Unlike NLTF, we take into account all the points during the speckle reduction process.

### 5.4 Patch based adaptive temporal filter (PATF)

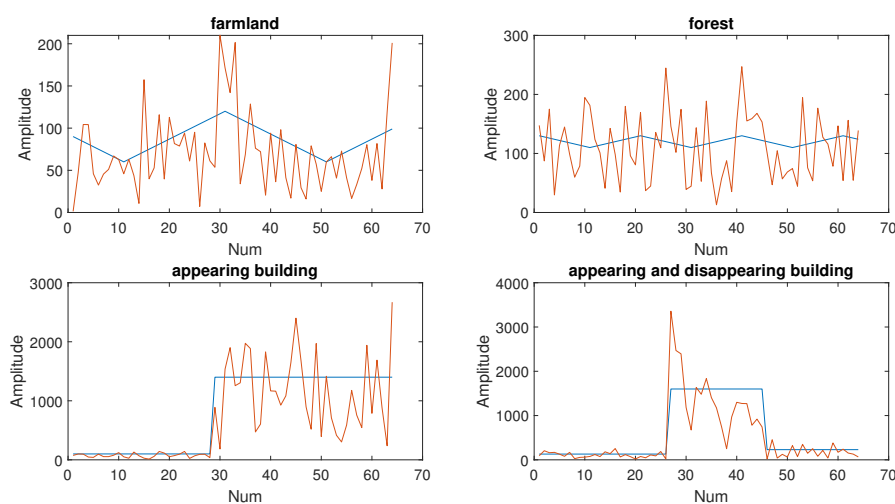
To suppress the effect of changed points, patch based weighted average is exploited. In a noniterative version, the weights are calculated using :

$$\omega(y_t, y_{t'}) = \begin{cases} 0, & d_1[y_t, y_{t'}] \geq \tau_2 \\ \exp(-d_1[y_t, y_{t'}]/h) & \tau_1 < d_1[y_t, y_{t'}] < \tau_2 \\ \omega_{max}, & d_1[y_t, y_{t'}] \leq \tau_1 \end{cases} \quad (5.19)$$

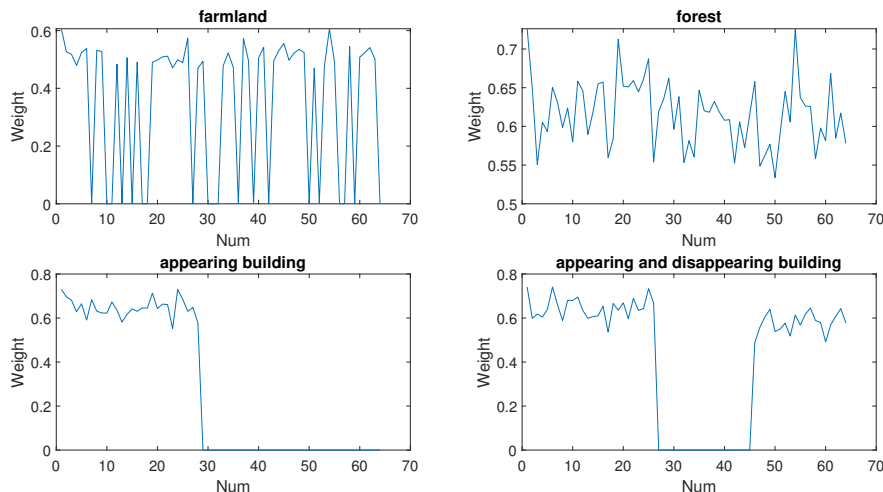
$$\omega_{max} = \arg \max_{t'} \exp(-d_1[y_t, y_{t'}]/h), \quad \tau_1 < d_1[y_t, y_{t'}] < \tau_2 \quad (5.20)$$

where  $h$  is a smoothing parameter defined as introduced in [Deledalle et al., 2009] and  $d_1$  is given by equation (5.11). The larger  $h$  will bring smoother temporal average.  $\tau_1$  and  $\tau_2$  are two thresholds used to separate different change magnitude patches.

In practise, the original images or the dissimilarities can be multilooked so as to suppress the speckle corruption. Large dissimilarities express that changes may have happened between the two patches. Some exponential kernel could be used to adjust the large distances to nearly zero weights [Kervrann and Boulanger, 2006]. Under the no change hypothesis, we propose to use Monte Carlo method to define the unchanged (noise free values are the same) and changed (changed to other objects) threshold, with probability quantiles equal to 8% and 92%, respectively.



(a) Noise free (blue) and noisy (brownish yellow) time series.



(b) Different time series weights with respect to (a).

FIGURE 5.2: Different time series and patch based weight comparison. The self-similarity value of the reference point is set equal to the maximum similarity value with others.  $h$  is set equal to 2 during the transformation.

With  $M$  temporal images, the temporal weighted average is performed as :

$$\hat{u}_t(s) = \frac{1}{\sum_{t'=1}^M \omega(y_t, y_{t'})} \sum_{t'=1}^M \omega(y_t, y_{t'}) y_{t'}(s) \quad (5.21)$$

Four kinds of object changes are taken as examples to show the dissimilarity to weight transformations (Fig.5.2). For long time series, such as more than 300 images, we suppose only using patch weighted temporal averaging to obtain the denoised values. When only a small amount of images is available, we can use spatial adaptive denoising to acquire better denoising results. SAR-BM3D is chosen as an example of the despeckling scheme. We use PATF to represent the method when applying SAR-BM3D on the output of equation (5.21).

## 5.5 Experimental results and discussion

To compare the proposed method and the influence of the nonlocal means estimation, we use different simulated data and SAR data. The effectiveness of patch based weighted temporal averaging is proved using long time series Sentinel-1 GRD images. In addition, the proposed methods will be compared with some state-of-the-art multitemporal denoising approaches (such as 2SPPB and MSAR-BM3D).

### 5.5.1 Estimation of different adaptive denoising approaches for ANLTF

40 simulated intensity images, as introduced in section 3.3.1, are used for the evaluation. The changed patch size is  $3 \times 3$ , so as to compare with large size area changes in the following section. We used the default parameters of SAR-BM3D<sup>1</sup>, PPBNakagami<sup>2</sup>, MuLoG-BM3D and Homomorphic-BM3D<sup>3</sup>.

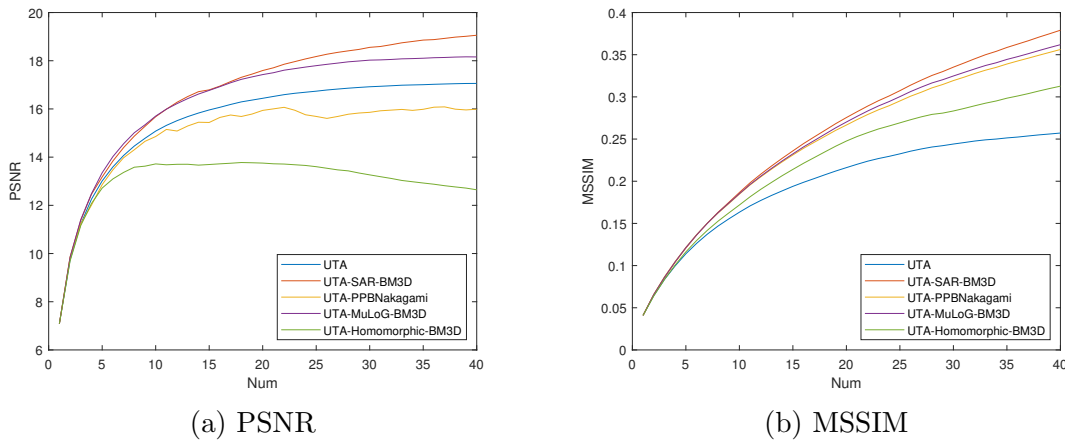


FIGURE 5.3: Different unbiased temporal average comparison using different number of simulated images. SAR-BM3D, PPBNakagami, MuLoG-BM3D, Homomorphic-BM3D are used to pursue adaptive denoising. 40 simulated images with 5 different background values and changed targets are used.

---

1. <http://www.grip.unina.it/research/80-sar-despeckling/80-sar-bm3d.html>  
2. <https://www.math.u-bordeaux.fr/~cdeledal/ppb.php>  
3. <https://www.math.u-bordeaux.fr/~cdeledal/mulog.php>

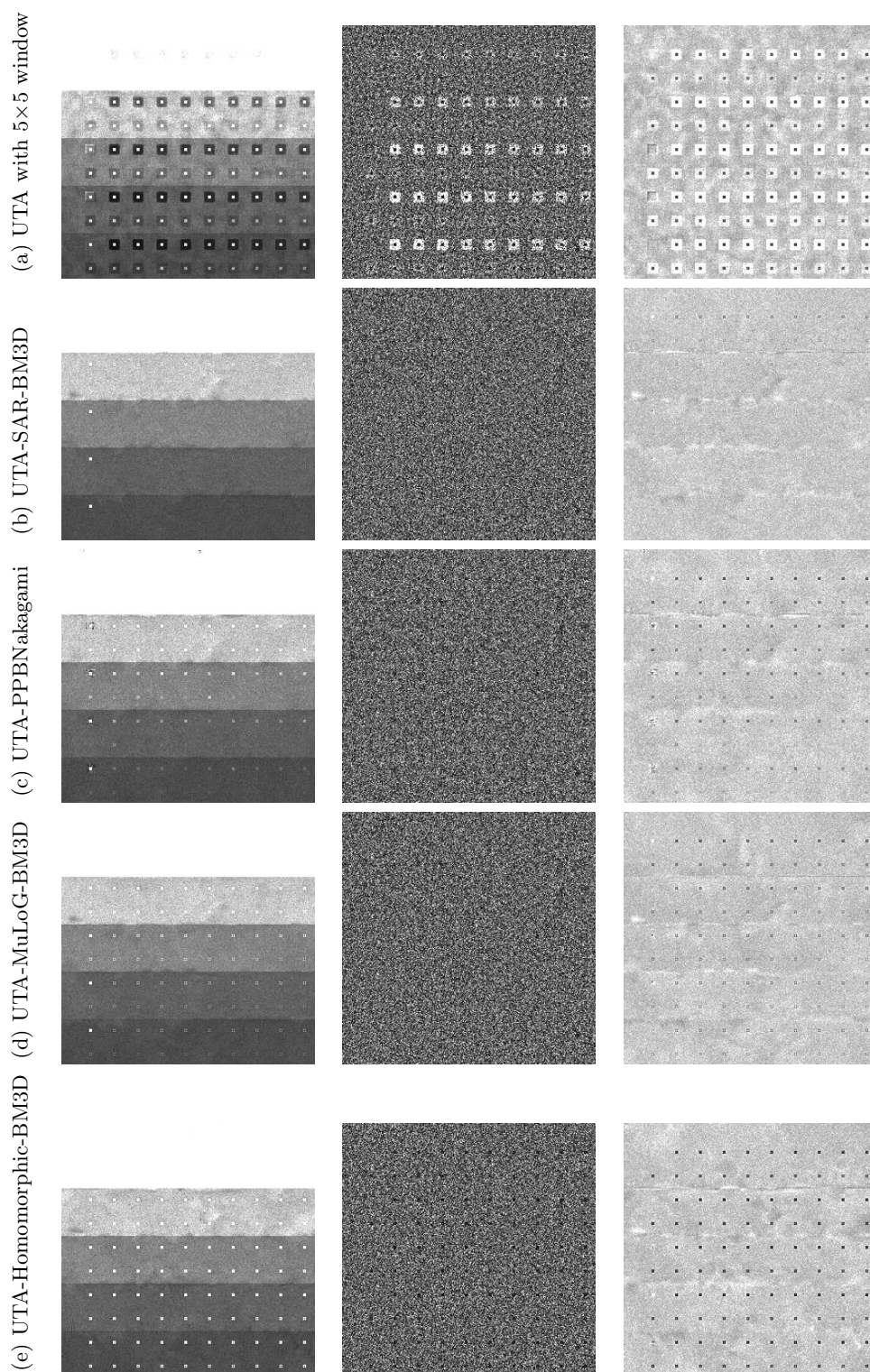


FIGURE 5.4: Denoising results (left), ratio with noisy data (middle) and ratio with noise free image (right) comparison. 40 simulated data with changes are used. The adaptive denoising methods (SAR-BM3D, PPBNakagami, MuLoG-BM3D and Homomorphic-BM3D) are used to improve UTA method.

As can be seen in figure 5.3, UTA-SAR-BM3D can provide the best results. With the increase of the used number of images, the PSNR provided by UTA-Homomorphic-BM3D even decreased. This may be caused by the changing time series and the distribution of the log-transformed data may not follow Gaussian distribution.

The results illustrated in figure 5.4 show that all ANLTF methods obtain better denoising results than the original UTA method. ANLTF methods can acquire smoother homogeneous areas. Only UTA-SAR-BM3D method is not seriously influenced by the changed points, because SAR-BM3D method can preserve the bright points when reducing SAR image speckle. UTA method is significantly affected by the changed points because of using a rectangular window to estimate the noise-free value in each image. Using adaptive denoising methods can improve UTA method, especially for edge boundaries and bright targets. Any better single image denoising method could be used for the improvement of UTA method.

To numerically evaluate these adaptive denoising methods, different numbers of simulated images are used. The speckle reduction performance is quantified by calculating the PSNR and MSSIM values of the denoising results. SAR-BM3D and MuLoG-BM3D methods provide the best results. The poor performance of homomorphic-BM3D may be caused by its poor efficiency on single-look SAR images [Chierchia et al., 2017b] and the changed points. It also proves that the log-transformed intensity SAR data is not fully following a Gaussian distribution. After log-transformation, the data stationarity will be highly improved. The bright points seem smoothed by the Gaussian denoiser, which leads to the decrease of PSNR values (Homomorphic-BM3D data).

### 5.5.2 Despeckling results comparison using simulated data

The main difference with previously introduced methods is the noise-free value estimation method. The four compared methods are shown in table 5.1. UTA [Lee et al., 1991, Quegan and Yu, 2001] method used the average value of the rectangular window. NLTF [Chierchia et al., 2017b] only averages similar points which are estimated using generalized likelihood ratio test [Deledalle et al., 2012]. ANLTF used the weighted average value of the search window. PATF used the weighted average value of the time series.

TABLE 5.1:  $\mu$  value estimation method comparison

	Methods	$\mu$ estimation method
1	UTA	$\mu_t(s) = \frac{1}{N} \sum_{i \in N_w^2} y_t(i)$
2	NLTF	$\mu_t(s) = \frac{1}{N_2 N_1^2} \sum_{n=1}^{N_2} \sum_k y_t(s+k)$
3	ANLTF	$\mu_t^{\text{NL}}(s) = \frac{1}{\sum_{i \in N_w^2} \omega(s,i)} \sum_{i \in N_w^2} \omega(s,i) y_t(i+k)$
4	PATF	$\hat{\mu}_t(s) = \frac{1}{\sum_{t'=1}^M \omega(y_t, y_{t'})} \sum_{t'=1}^M \omega(y_t, y_{t'}) y_{t'}(s)$

64 simulated time series without change and 64 simulated Sentinel-1 images with changes are used for the comparison of different multitemporal denoising methods (UTA, NLTF, ANLTF and PATF). When less time series are available, both UTA and PATF can use spatial adaptive denoising to improve the temporal denoising results.

### 5.5.2.1 Simulated data without change

To numerically compare the performances of these methods, different numbers of simulated images are used (Fig.5.5). When more than 30 images are used, PATF acquires the best PSNR and MSSIM values. It proves that PATF is very effective on denoising large unchanged time series. We propose to pursue a spatial denoising when less images are used.

UTA and NLTF used the default parameters. Comparing with ANLTF, UTA provides better PSNR with larger number of time series. The preservation of bright points causes low PSNR with NLTF. UTA, NLTF and ANLTF provide similar MSSIM values with different number of images. This may caused by the NLTF detects bright targets in advance and avoiding any denoising around them. With the increase of used images, NLTF provided PSNR even has a little decrease.

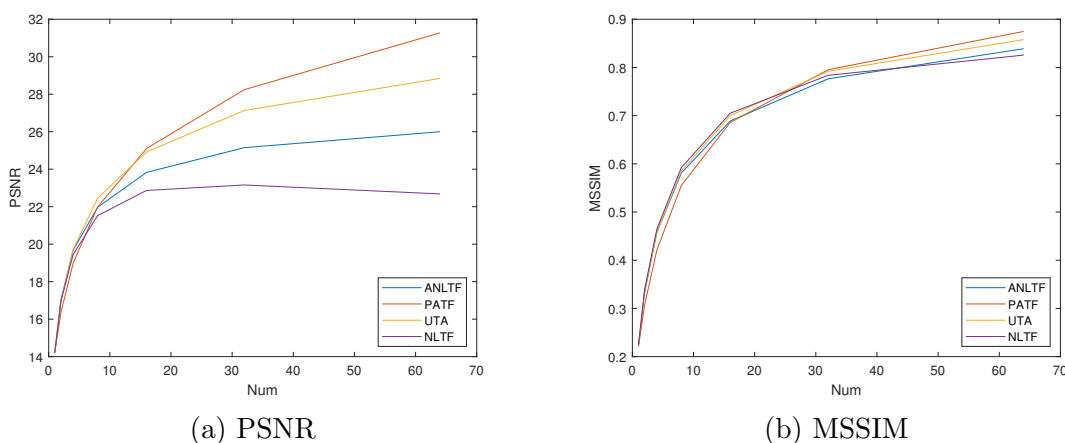


FIGURE 5.5: Different weighted temporal averages comparison with different number of simulated images. 64 simulated time series without change (Fig.3.12) are used.

### 5.5.2.2 Simulated Sentinel-1 data with changes

Unlike optical images, SAR images always contain a small number of bright points which are characterized by local structures [Oliver and Quegan, 2004b]. In order to better simulate SAR images, simulated Sentinel-1 data were created based on the arithmetic mean image (as shown in Fig.3.15(b)).

TABLE 5.2: Residual evaluation results (best value in boldface). M-index is evaluated in the automatically selected homogeneous area, while residual (Eq. (4.30)) is calculated based on the whole image. The larger PSNR and MSSIM represent better results, while smaller M-index and residual values represent better results.

Used data	Methods	UTA	NLTF	ANLTF	PATF
Denoised data and noise free image	PSNR	11.790	6.276	7.328	<b>24.389</b>
Denoised data and noise free image	MSSIM	0.908	0.769	0.854	<b>0.954</b>
Homogeneous area	M-index	3.738	<b>1.542</b>	5.673	2.738
Ratio of noisy data and denoised data	Residual	1.025	1.164	1.013	<b>0.988</b>

Using the sliding window to estimate the noise free value is very easy, but UTA will blur fine features and minor edges (Fig 5.6(a)). Comparing with the case where adaptive filtering is used, using a rectangular window results in resolution broadening. Because of high-value bright targets in the SAR image, the arbitrary spatial average also causes low-value rectangles in the ratio image. In addition, farmland areas are also not smooth enough. However, this shortcoming can be avoided by using spatial adaptive denoising (Fig.5.6(c)).

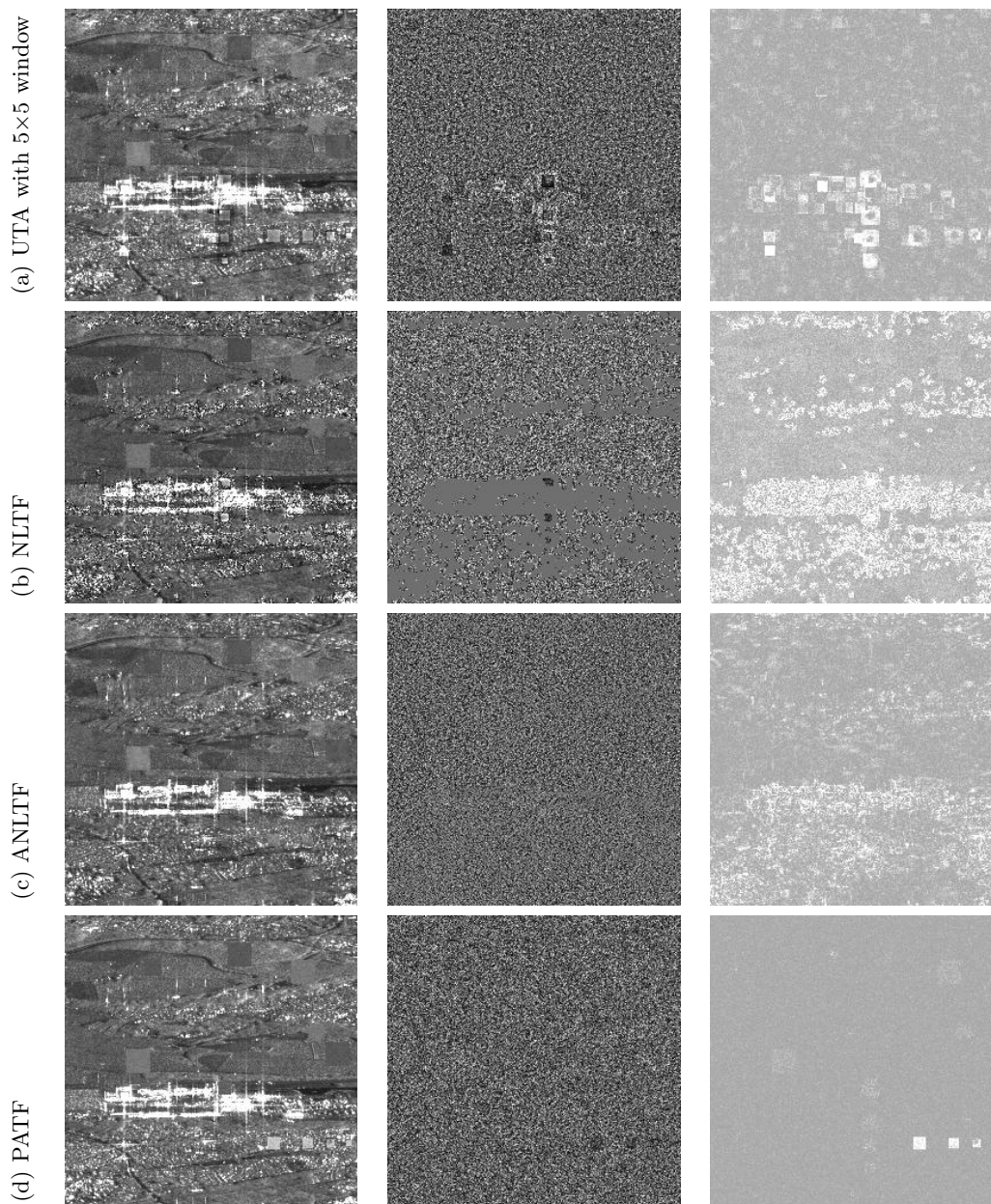


FIGURE 5.6: Denoising performances comparison based on 64 simulated Sentinel-1 images. Left : denoising results, middle : ratio with noisy data, right : ratio with noise free image. The max ratio values are used between the denoised data and the noise free image.

Visually, PATF provide better results (Fig.5.6(d)). Their denoising results have high

spatial resolution and provide good results for unchanged areas. It also provides the best PSNR and residual evaluation values, as shown in table 5.2. However, it provides biased results in some changed areas because of the used threshold (Eq.(5.21)). NLTF detects bright points in advance and prohibits any denoising around them. This step may help keeping the original backscattering values of some important objects, but it will lead to noisy building areas. This causes NLTF to provide the smallest PSNR value. Although it cannot give good results in building areas, it provides the best M-index [Gomez et al., 2017] values in homogeneous areas (Tab.5.2).

### 5.5.3 Despeckling results comparison with SAR data

#### 5.5.3.1 With long time series

To test the denoising performance of large amounts of data, we take 339 geocoded Sentinel-1 GRD images as an example. In this case, using adaptive denoising will be too time consuming. We only compare UTA, NLTF and PATF methods.

Based on the previous analysis, GLR based similarity estimation method without iteration ( $h'_{1st} = \infty$ ) is used to average the data. In this section, the threshold is calculated using simulated speckle with  $\tau = \text{quantile}(d_{1st}(s_t, s_{t'}), \alpha)$ . A similarity window of size  $7 \times 7$  is used for the single look SAR images. Spatial adaptive denoising is not used after the patch based adaptive temporal average.

The denoising results are shown in figures 5.7 and 5.8. The residual evaluation results have been classified into 4 classes with displaying value range  $[0, 4]$  and red color represents the larger values. All of them can keep the spatial resolution and suppress the speckle noise. Visually, PATF provides better denoising results than others. When taking the ratio results into account, UTA and NLTF provide bias in the bright building area. According to the ratio and residual evaluation results (red color indicates poor denoising) (Fig.5.7 (b-c) and Fig.5.8 (b-c)), UTA and NLTF provide results that have much more wrong denoising results in the changed building areas. PATF seems still contain some bias for farmland areas because of their seasonal change (low change magnitude). Empirically, the changes from vegetation to building can be well detected.

TABLE 5.3: Residual evaluation results (best value in boldface). M-index is evaluated in the automatically selected homogeneous area, while residual is calculated based on the whole image.

Figures	Methods	UTA	NLTF	PATF
Fig.5.7	M-index	18.735	<b>2.746</b>	6.340
	Residual	2.627	3.155	<b>2.553</b>
Fig.5.8	M-index	38.409	4.045	<b>2.181</b>
	Residual	<b>2.537</b>	2.970	2.723

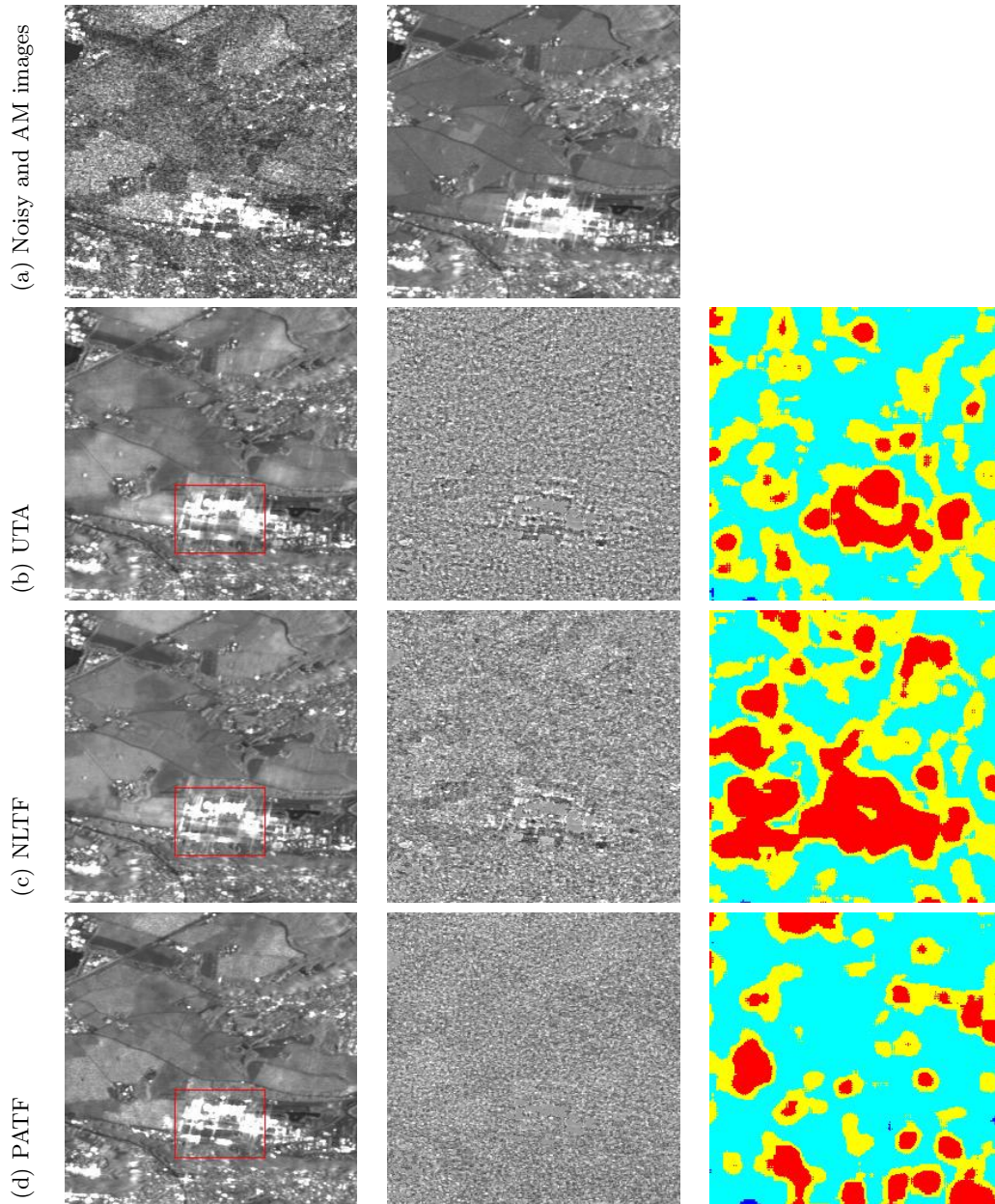


FIGURE 5.7: Different denoising results comparison based on 339 Sentinel-1 GRD images acquired over École Polytechnique area : denoising results (left), its ratio with noisy data (middle) and residual evaluation results (right). There are appearing and disappearing buildings in the red rectangle area. Google Earth Engine is used to prepare the time series data.

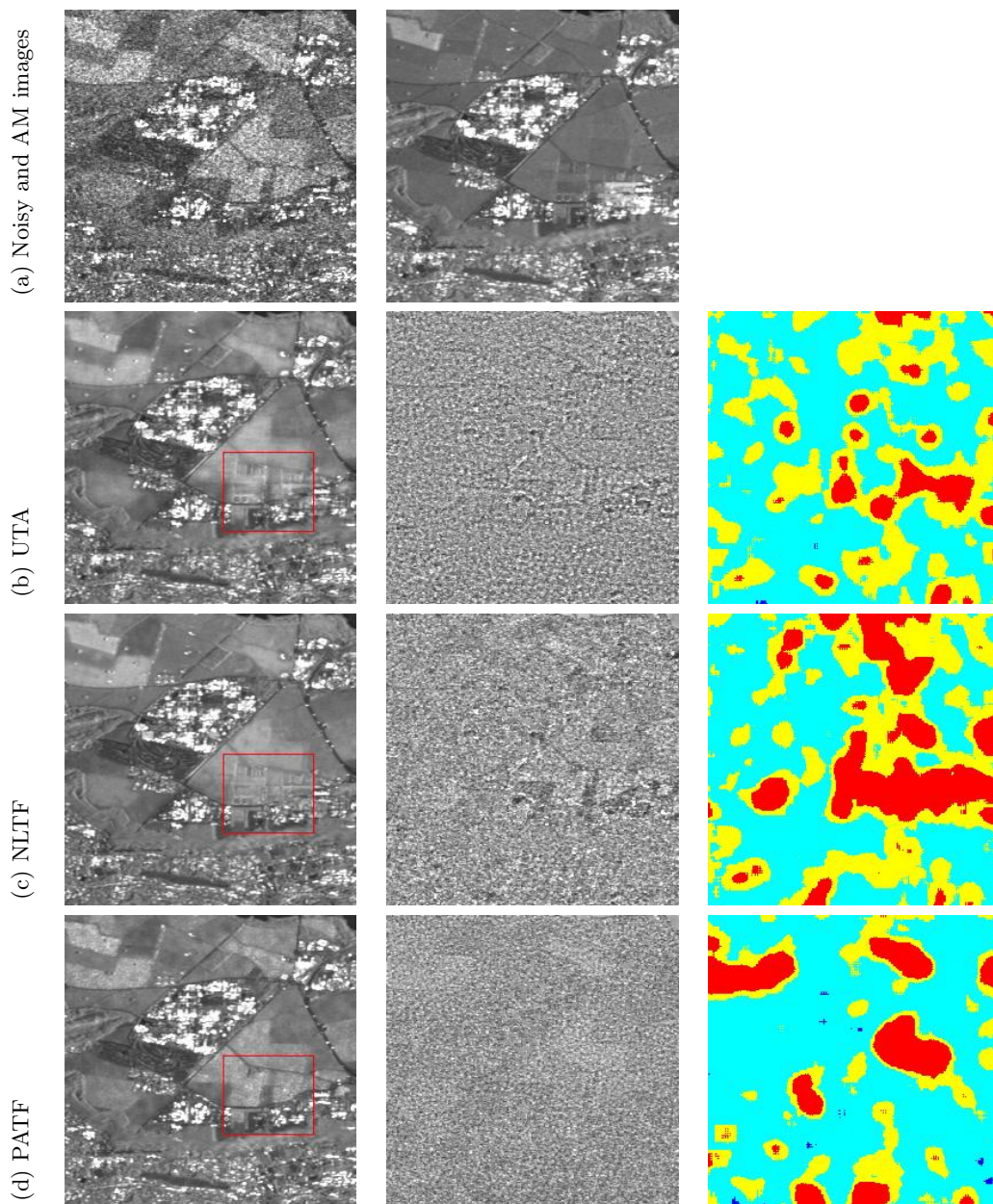


FIGURE 5.8: Different denoising results comparison based on 339 Sentinel-1 GRD images acquired over CentraleSupélec area : denoising results (left), its ratio with noisy data (middle) and residual evaluation results (right). There are appearing buildings in the red rectangle area. Google Earth Engine is used to prepare the time series data.

### 5.5.3.2 Comparison with state-of-the-art methods

Simulated SAR data has i.i.d. speckle, which is not the case of real SAR data. Therefore, we expect different results with real data. In this section, Sentinel-1 and TerraSAR-X SAR images are used for comparison. Spatial and temporal correlations exist in these images. Since there are too many temporal changes for Sentinel-1 images, a  $30 \times 30$  window is used for the ENL estimation.

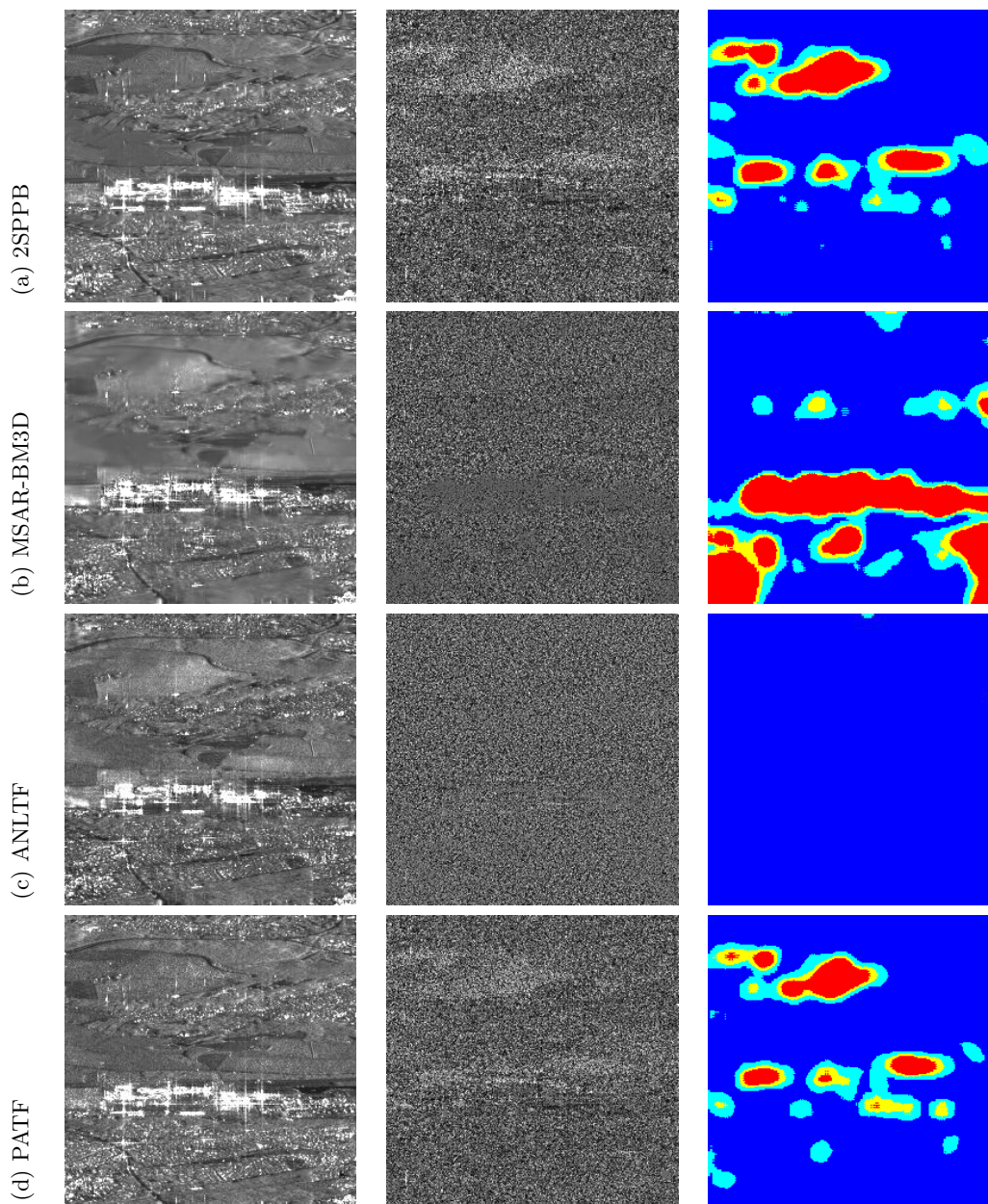


FIGURE 5.9: Different denoising results comparison based on 64 resampled (step 2) Sentinel-1 images : denoising results (left), ratio with noisy data (middle) and residual evaluation results (right). There are changed building areas in the middle of the image. The residual evaluation results have been classified into 4 classes with display value range  $[0, 4]$  and red color represents the larger values.

ANLTF always provide the best results when using Sentinel-1 images or TerraSAR-X images. Figure 5.9 shows that 2SPPB and PATF provide biased results in the farmland areas (bright areas in the ratio images of Fig.5.9(a) and (d)). This also explains their similar residual evaluation results. When testing the 64 Sentinel-1 data, using weighted average seems a little better than using binary weight in the bias area. When testing the 16 TerraSAR-X images (Fig.5.10), the biased area provided by PATF is larger than 2SPPB.

PATF can show its advantage with long time series.

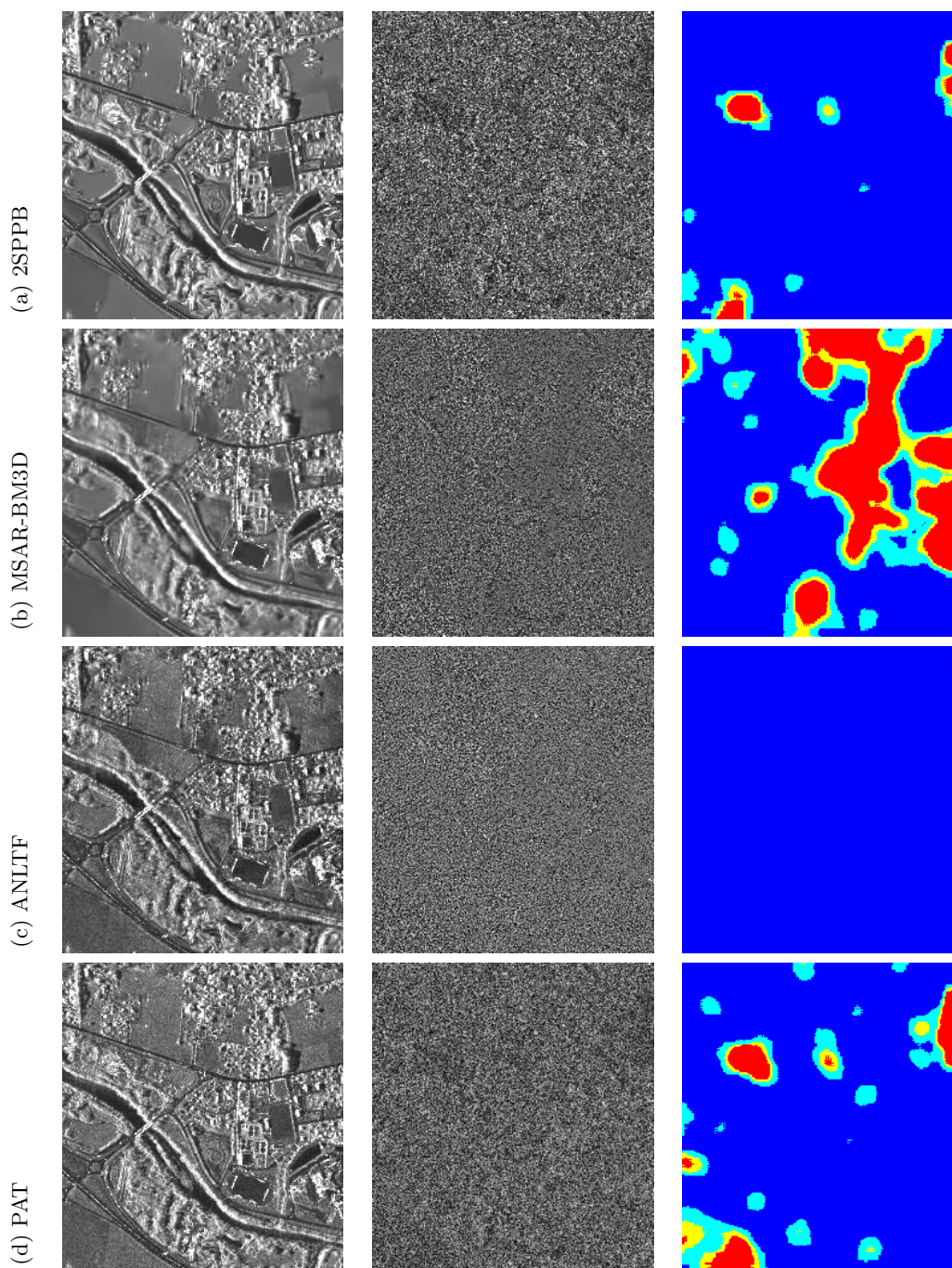


FIGURE 5.10: Different denoising results comparison based on 16 decorrelated TerraSAR-X images : denoising results (left), ratio with noisy data (middle) and residual evaluation results (right). There are changed building areas in the center of the image.

Like NLTF temporal denoising approaches, MSAR-BM3D [Chierchia et al., 2017b] processes the temporal similarity blocks. Temporal filtering is made in the transformed domain. To avoid the *rare patch effect* phenomenon, isolated bright targets are selected (Eq.5.15) and prevented from denoising. Some of the changed points and their adjacent

points could also be detected as targets, and this may cause noisy pixels and degrade the appearance of denoising results. It is also the reason why the ratio results with noisy data in these areas have low variance.

TABLE 5.4: Residual evaluation results (best value in boldface).

Figures	Methods	2SPPB	MSAR-BM3D	ANLTF	PATF
Fig.5.9	M-index	3.501	<b>1.931</b>	2.050	3.371
	Residual	1.498	2.728	<b>0.999</b>	1.403
Fig.5.10	M-index	12.928	7.839	<b>2.408</b>	2.829
	Residual	1.165	2.654	<b>1.015</b>	1.465

Comparing with 2SPPB and MSAR-BM3D methods, ANLTF always provides better results with respect to the residual evaluation results, the ratio with the noisy image. There is still obvious residue texture in the ratio results of MSAR-BM3D. When tested with Sentinel-1 SAR data, the denoising results (Fig.5.9) show that MSAR-BM3D provides the best denoising results (also provides largest M-index value) in farmland areas without introducing any clear bias.

The residual evaluation results acquired using single look intensity data seem much better than that using Sentinel-1 GRD data. Sentinel-1 GRD data is prepared using Google Earth Engine. In that platform, Sentinel-1 GRD images are preprocessed by SNAP with thermal noise suppression, radiometric calibration, and terrain correction. To save the memory space, the platform makes the choice to convert the float32 values to unsigned 2-byte uint16 integers, and retains only the values between the 1st and the 99th average percentile of the values before applying the quantization. This will lead to the modification of the original SAR signal statistics [Koeniguer et al., 2018b].

## 5.6 Conclusion

In this chapter, we proposed two schemes for introducing the temporal information into the spatially based SAR image denoising methods. Firstly, spatial adaptive denoising methods were used to improve the UTA method. Experimental results with SAR data, simulated SAR data demonstrate the effectiveness of these adaptive speckle reduction methods. UTA-SAR-BM3D provides better results, especially in the changed areas and line feature areas. ANLTF provides the best results when testing Sentinel-1 and TerraSAR-X images. Secondly, we proposed a patch based adaptive temporal filter. Different similarity methods could be used to acquire the temporal similar points. When there is no change and the number of images is large enough, arithmetic mean could provide better denoising results. However, when some changes exist, the arithmetic mean introduces artifacts in the changed areas. In this case, patch based adaptive temporal average could provide better denoising results, especially for the long time series data. Taking the real temporal SAR images into account, changes are unavoidable because of dielectric and geometrical property changes in the scattering elements. With the noncontinuous weight calculation function, PATF can not avoid the bias in the low change magnitude areas. Thus, temporal change detection despeckling methods could guarantee a good speckle reduction capability in terms of PSNR, MSSIM and perceived image quality. For the farmland areas which may still have seasonal change, patch based adaptive temporal average provided results that may still have some bias. In the next section, we will propose a different approach based on the ratio image.

## Chapter 6

# Ratio based multi-temporal SAR images denoising

In this chapter, we propose a generic multi-temporal SAR despeckling method to extend any single-image speckle reduction algorithm to multi-temporal stacks. Our method, RAtio-BAsed multi-temporal SAR despeckling (RABASAR) [Zhao et al., 2018], is based on the ratio and fully exploits a “super-image” (i.e. temporal mean) in the process. The proposed approach can be divided into three steps : 1) calculation of the “super-image” through temporal averaging ; 2) denoising the ratio images formed through dividing the noisy images by the “super-image” ; 3) computing denoised images by multiplying the denoised ratio images with the “super-image”. Thanks to the spatial stationarity improvement in the ratio images, denoising these ratio images with a speckle-reduction method is more effective than denoising the original multi-temporal stack. The data volume to be processed is also reduced compared to other methods through the use of the “super-image”. In addition, some online processing strategies are proposed. The comparison with several state-of-the-art reference methods shows numerically (peak signal-noise-ratio, structure similarity index) and visually better results both on simulated and real SAR stacks. The proposed ratio-based denoising framework successfully extends single-image SAR denoising methods to exploit the temporal information of a time series.

### 6.1 Principle of the proposed method

Temporal averaging (also called temporal multi-looking) of multi-temporal stacks of images produces images with reduced speckle where spatial resolution is preserved. Temporal averaging provides a so-called “super-image”. In this chapter, we propose to exploit this super-image to build a ratio-based denoising framework (Fig.6.1).

The proposed method mainly contains three steps.

1. In the first step, a super-image is calculated using a series of well registered and calibrated SAR images. Averaging temporal intensity samples is the simplest way to obtain an image with speckle reduction. It corresponds to the maximum likelihood estimation of the reflectivity if the variables are i.i.d. (independent and identically distributed, i.e. if temporal fluctuations are independent and only caused by fully-developed speckle). In practice, the influence of the SAR imaging system and the changes of the remote sensing areas (e.g. farmland or building areas) should be taken
-

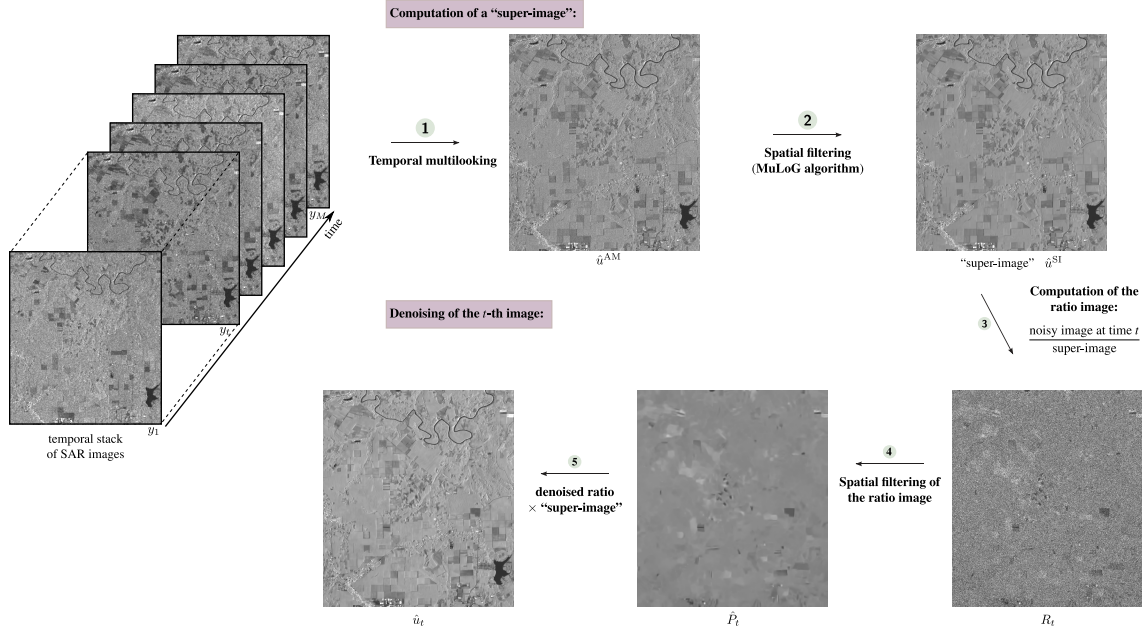


FIGURE 6.1: Multi-temporal SAR image denoising framework. Using  $y_t$  for the calculation of super-image  $\hat{u}^{SI}$  is optional [Zhao et al., 2019].

into account. Even for temporally stable areas, because of possible different temporal correlations, the noise reduction may be variable in space.

For areas with seasonal changes, a typical evolution of vegetation areas, the changed areas are rather homogeneously distributed and with low fluctuations. On the contrary, for abrupt or impulsive changes [Su et al., 2015], as often caused by human activities, the mean value may be seriously influenced by changes. Hence, it can be interesting to average unchanged or similar temporal points through binary weights, as done for instance in [Su et al., 2014, Lê et al., 2015]. Computation of the super-image, denoted as  $\hat{u}^{SI}$  in the sequel, will be presented in Section 6.2.

2. In the second step, using the obtained super-image, we calculate the ratio  $R_t$  between the image  $y_t$  at time  $t$  and the super-image :

$$R_t(s) = \frac{y_t(s)}{\hat{u}^{SI}(s)} \quad (6.1)$$

$R_t$  is named the ratio image at time  $t$ ; it contains the residual speckle noise between the two images, and the radiometric shifts when changes occur.

In stable areas, if the series is infinite, the super image is exactly the reflectivity  $u$  Gomez et al. [2017] and the ratio is formed by a collection of independent identically distributed Gamma random variables with unitary mean and the same number of looks. On the contrary, in case of a change in some area at time  $t$ , it is likely that this change will appear in the ratio image. Any speckle filtering technique can be applied to the ratio image. A good speckle reduction method is expected to preserve the possible changes at time  $t$ . This point will be discussed in Section 6.3.

3. In the third step, the filtered image is recovered by multiplying the denoised ratio image with the original super-image. Experimental results on simulated and real SAR data will be presented in section 6.5.

## 6.2 Super-image computation

With a multi-temporal stack, the super-image can be calculated through different ways. First, different Hölder means (such as arithmetic or geometric means) could be chosen; then such means may be applied either on the intensity data or on the amplitude data. We may expect from these choices to enhance different pieces of information [Quin et al., 2014]. In this chapter, registered and radiometrically corrected intensity SAR images are used. We propose to use the arithmetic mean for its good properties [Quin et al., 2014] with the option of using binary weights to discard the intensity at some dates when a change occurred.

### 6.2.1 Arithmetic mean

Given a time series of  $M$  intensity values  $[y_1(s), y_2(s), y_3(s), \dots, y_M(s)]$  indexed by time  $t$ , the arithmetic mean is calculated at location  $s$  by :

$$\hat{u}^{AM}(s) = \frac{1}{M} \sum_{t=1}^M y_t(s) \quad 1 \leq t \leq M$$

Theoretically, with *i*) no change in the time series  $[u_1(s) = u_2(s) = \dots = u_t(s) = \dots = u_M(s)]$  and *ii*)  $M$  large enough, averaging the temporal intensity data is a simple yet effective approach to reduce the speckle [Oliver and Quegan, 2004b]. The arithmetic mean  $\hat{u}^{AM}(s)$  is equal to the maximum likelihood estimation (no matter how large  $M$  is) of  $u(s)$ , and the multi-look image  $\hat{u}^{AM}$  follows a Gamma distribution  $\mathcal{G}[u, LM]$ . In practice, the resulting equivalent number of looks (ENL) may be less than the theoretical value ( $L \times M$  with i.i.d. variables) if there are temporal correlations in the time series, especially in case of images in interferometric configuration. The associated ENL is denoted by  $L^{AM}$  in the following.

When there are changes in the time series samples  $\{y_t(s)\}_{t=1}^M$ , the arithmetic mean  $\hat{u}^{AM}(s)$  has no physical meaning and therefore does not correspond to the scene reflectivity (since it varies in time). We can account for this mismatch between the temporal average and the underlying reflectivity through a correcting factor or by averaging only the unchanged temporal samples.

### 6.2.2 Binary weighted arithmetic mean

Instead of computing blindly the super-image on the time series and then relying on the ratio image to recover the reflectivity of each specific date, another option is to compute a dedicated super-image. In this case, only samples with similar and stable reflectivities are averaged. To detect these samples, a patch-based similarity estimation  $w_{t,t'}(s)$  based on the generalized likelihood ratio (GLR) test may be used.

The GLR test between two observed intensity values  $y_1$  and  $y_2$  confronts the two hypotheses : null hypothesis corresponding to a same underlying value  $u_{12}$  for  $y_1$  and  $y_2$ , and alternative hypothesis with an underlying value  $u_1$  for  $y_1$  and  $u_2$  for  $y_2$ . Taking the maximum likelihood estimate for  $u_{12}$ ,  $u_1$  and  $u_2$  and computing the ratio of the likelihood of the two hypotheses gives [Deledalle et al., 2012] :

$$\text{GLR}(y_1, y_2) = \frac{y_1 y_2}{(y_1 + y_2)^2}$$

(constant terms are omitted). Extending this comparison to all the pixels of two patches at date  $t$  and  $t'$  and taking the log gives the following formula [Deledalle et al., 2009, Su et al., 2014] :

$$w_{t,t'}(s) = \sum_k \left( \log \left( \sqrt{\frac{y_t(s+k)}{y_{t'}(s+k)}} + \sqrt{\frac{y_{t'}(s+k)}{y_t(s+k)}} \right) - \log 2 \right) \quad (6.2)$$

where  $y_t(s+k)$  is the value in the noisy patch at date  $t$ . The sum is taken over all pixel shifts  $k$  such that pixels with index  $s+k$  are located inside a patch centered on  $s$  (small square window). Based on the analysis in [Buades et al., 2005], a size of  $7 \times 7$  is chosen for the patch. Then, a binary weight  $\varphi[w_{t,t'}(s)]$ , expressing whether there are temporal changes or not, is computed as :

$$\varphi[w_{t,t'}(s)] = \begin{cases} 1, & \text{if } w_{t,t'}(s) < \tau \\ 0, & \text{otherwise} \end{cases} \quad (6.3)$$

where  $\tau$  is a threshold chosen as  $\tau = \text{quantile}(w_{t,t'}(s), \alpha)$  and is estimated with Monte Carlo simulations using Gamma distributed data and  $\alpha = 0.92$  as proposed in Su et al. [2014].

Then, the binary weighted arithmetic mean (denoted by BWAM in the sequel) is calculated through :

$$u_t^{\text{BWAM}}(s) = \frac{1}{\sum_{t'=1}^M \varphi[w_{t,t'}(s)]} \sum_{t'=1}^M \varphi[w_{t,t'}(s)] y_{t'}(s) \quad (6.4)$$

For each pixel  $s$  and each date  $t$  of the stack, the weights  $\varphi(w_{t,t'}(s))$  select the dates  $t'$  with no change compared to date  $t$ . Thus, the binary weighted mean  $u_t^{\text{BWAM}}(s)$  provides a more faithful estimation of  $y_t(s)$ . This improvement compared to the arithmetic mean is obtained at the cost of an increased complexity since the stack has to be processed for each date  $t$  (whereas the arithmetic mean can be computed once and for all).

The interest of using such a temporal mean will be evaluated in Section 6.5.

### 6.2.3 Denoising the super-image

When the number of temporal candidates used for the computation of the super-image is not large enough, the spatial information can be taken into account to improve the estimation of the speckle-free signal. The super-image may have a spatially varying ENL because of unstable areas, because of varying coherence, and because of the use of the binary weights. Let  $L$  denote the local equivalent number of looks. To robustly estimate  $L^{\text{AM}}$  in the arithmetic mean image calculated with medium or high resolution temporal SAR images, the log-cumulant method is used [Tison et al., 2004].

As introduced in section 2.3, empirical expressions for the first and second order log-cumulant estimators are (for  $N$  samples) :

$$\hat{k}_1 = \frac{1}{N} \sum_{i=1}^N [\log(\sqrt{\hat{u}_i})]$$

$$\hat{k}_2 = \frac{1}{N} \sum_{i=1}^N [\log(\sqrt{\hat{u}_i}) - \hat{k}_1]^2$$

Then, we can obtain an estimation of the ENL using the following relationship (theoretical expression) :

$$\hat{k}_2 = \frac{1}{4}\psi(1, \hat{L}^{AM})$$

where  $\psi(1, \hat{L}^{AM})$  is the first-order Polygamma function [Tison et al., 2004]. Note that the traditional estimation method (by means of the ratio  $\mathbb{E}(y_i)^2/\text{Var}(y_i)$ ), the moment estimation method or the maximum likelihood (ML) estimation method could also be used for the ENL estimation [Nicolas and Anfinson, 2002].

This ENL is locally estimated using a sliding window, and it is an important parameter in statistical modeling of multilook SAR images. A global ENL for the super-image may be deduced from the local ENL as the 0.99 quantile value (almost the max). In practice, this global value may be useful to speed up a denoising process applied on the super-image. Since SAR-BM3D can keep the fine features, the resampling trace on the SAR image may be kept and the denoised homogeneous areas are not smooth enough (as shown in Fig.6.2 (e)). In this chapter, the arithmetic mean image is filtered using MuLoG-BM3D [Deledalle et al., 2017]. Any other spatial adaptive denoising method could be used.

Therefore, 4 super-images can be computed : arithmetic mean image (AM), binary weighted arithmetic mean image (BWAM, according to Eq.(6.4)), denoised arithmetic mean image (DAM) and denoised binary weighted arithmetic mean image (DBWAM). The interest of these different temporal mean images will be evaluated in Section 6.5.

## 6.3 Ratio image denoising

Each ratio image  $R_t = y_t/\hat{u}^{SI}$  (Eq.(6.1)) should contain both the variations between the super-image  $\hat{u}^{SI}$  and  $u_t$  and the speckle of the noisy image  $y_t$ . Nonetheless, the spatial homogeneity is largely improved in the ratio image compared to the original noisy image.

### 6.3.1 Statistical analysis of the ratio

We are interested in this section in the distribution (pdf) followed by  $R_t = \frac{y_t}{\hat{u}^{AM}}$  taken in a pixel  $s$ . The distribution is derived in the case of a super-image computed by the arithmetic mean of the temporal series.

As previously said,  $y_t$  is supposed to follow a Gamma distribution  $\mathcal{G}(u_t, L)$ . For single look images,  $L$  is equal to 1.  $\hat{u}^{AM}$  is supposed to follow a Gamma distribution with an associated ENL  $L^{AM}$  :  $\mathcal{G}(u^{AM}, L^{AM})$ . The Mellin framework developed in [Nicolas and Anfinson, 2002] provides an efficient way to derive the pdf of  $R_t$ . Indeed, the pdf of the product of two random variables is the Mellin convolution of the pdf of the two random variables. We will denote by  $\hat{\times}$  the Mellin convolution, and  $\mathcal{H}(u)$  the homothetic pdf defined by  $\mathcal{H}(u)(x) = \frac{1}{u}\delta(\frac{x}{u} - 1)$ . We have the following relationship between a Gamma distributed pdf of mean 1 and a Gamma pdf of mean  $u_t$  [Nicolas and Anfinson, 2002] :

$$\mathcal{G}(u_t, L) = \mathcal{H}(u_t) \hat{\times} \mathcal{G}(1, L)$$

In the same way, we have the following relation for the pdf of  $\hat{u}^{AM}$  :

$$\mathcal{G}(u^{AM}, L^{AM}) = \mathcal{H}(u^{AM}) \hat{\times} \mathcal{G}(1, L^{AM})$$

The variable  $\frac{1}{\hat{u}^{AM}}$  follows an inverse Gamma distribution  $\mathcal{GI}$  given by :

$$\mathcal{H}\left(\frac{1}{\hat{u}^{AM}}\right) \hat{\times} \mathcal{GI}(1, L^{AM})$$

with :

$$\mathcal{GI}(\mu, M)(x) = \frac{1}{\Gamma(M)} \frac{1}{M\mu} \left( \frac{M\mu}{x} \right)^{(M+1)} e^{-\frac{M\mu}{x}}$$

Multiplying the variables  $y_t$  and  $\frac{1}{\hat{u}^{\text{AM}}}$ , we thus have the Mellin convolution of  $\mathcal{H}\left(\frac{u_t}{u^{\text{AM}}}\right)$ ,  $\mathcal{G}(1, L)$  and  $\mathcal{GI}(1, L^{\text{AM}})$  which leads to a Fisher pdf Nicolas and Anfinen [2002] :

$$\begin{aligned} \text{pdf}_{R_t}(x) &= \mathcal{H}\left(\frac{u_t}{u^{\text{AM}}}\right) \hat{\times} \mathcal{G}(1, L) \hat{\times} \mathcal{GI}(1, L^{\text{AM}})(x) & (6.5) \\ &= \mathcal{H}\left(\frac{u_t}{u^{\text{AM}}}\right) \hat{\times} \mathcal{F}(1, L, L^{\text{AM}})(x) \\ &= \mathcal{F}\left(\frac{u_t}{u^{\text{AM}}}, L, L^{\text{AM}}\right)(x) \\ &= \frac{L}{L^{\text{AM}}} \frac{u^{\text{AM}}}{u_t} \frac{\Gamma(L + L^{\text{AM}})}{\Gamma(L)\Gamma(L^{\text{AM}})} \frac{\left(\frac{Lu^{\text{AM}}}{L^{\text{AM}}u_t}x\right)^{L-1}}{\left(1 + \frac{Lu^{\text{AM}}}{L^{\text{AM}}u_t}x\right)^{(L+L^{\text{AM}})}} \end{aligned}$$

Thus the ratio image follows a Fisher distribution depending on the following variables for each pixel :  $u_t$  the reflectivity for the pixel at date  $t$ ,  $u^{\text{AM}}$  the reflectivity of the arithmetic mean of the temporal series,  $L$  the number of looks of the original image, and  $L^{\text{AM}}$  the equivalent number of looks of the super-image<sup>1</sup>. This pdf should be taken into account in the denoising of the ratio image. It can be approximated by a Gamma distribution when  $L^{\text{AM}}$  is big enough.

### 6.3.2 MuLoG adaptation

At this point, any denoising method can be used to denoise the ratio image  $R_t$ . In this chapter, MuLoG [Deledalle et al., 2017] has been chosen. Unlike homomorphic approaches, and inspired by [Bioucas-Dias and Figueiredo, 2010], MuLoG relies on the Fisher-Tippett distribution to approximate the reflectivities of the log-transformed data. To lighten the notation,  $R$  is the ratio image of a date  $t$ ,  $r = \log R$  and  $P$  is the true ratio with  $\rho = \log P$ .

Its estimation is based on a MAP optimization approach as :

$$\rho \in \arg \min_{\rho \in \mathbb{R}^n} (-\log p_r(r|\rho) + \mathcal{R}(\rho)) \quad (6.6)$$

with

$$-\log p_r(r|\rho) = L \sum_{h=1}^N \rho_h + e^{r_h - \rho_h} + C \quad (6.7)$$

and  $\mathcal{R}(\rho) = -\log p_\rho(\rho)$  is a prior term enforcing some regularity on the solution,  $N$  is the number of pixels and  $C$  is the constant term. Then, the denoised data is reconstructed by  $\hat{P} = \exp(\rho)$ . In this paper, we consider MuLoG+BM3D that uses BM3D [Dabov et al., 2007] as an implicit regularization term  $\mathcal{R}(\rho)$ .

An example is shown in figure 6.2. A typical filtering result on a ratio image is presented on figure 6.2(d) along with the original image, super-image and the ratio image.

After obtaining the estimated noise free value  $\hat{P}_t$  of the ratio, we obtain the denoised image  $\hat{P}_t$  through :

$$\hat{u}_t = \hat{u}^{\text{SI}} \hat{P}_t \quad (6.8)$$

---

1. In general, this equivalent number of looks could vary in this image and depends on the pixel  $s$ . For the sake of simplicity, it will be taken constant for the whole image in the following

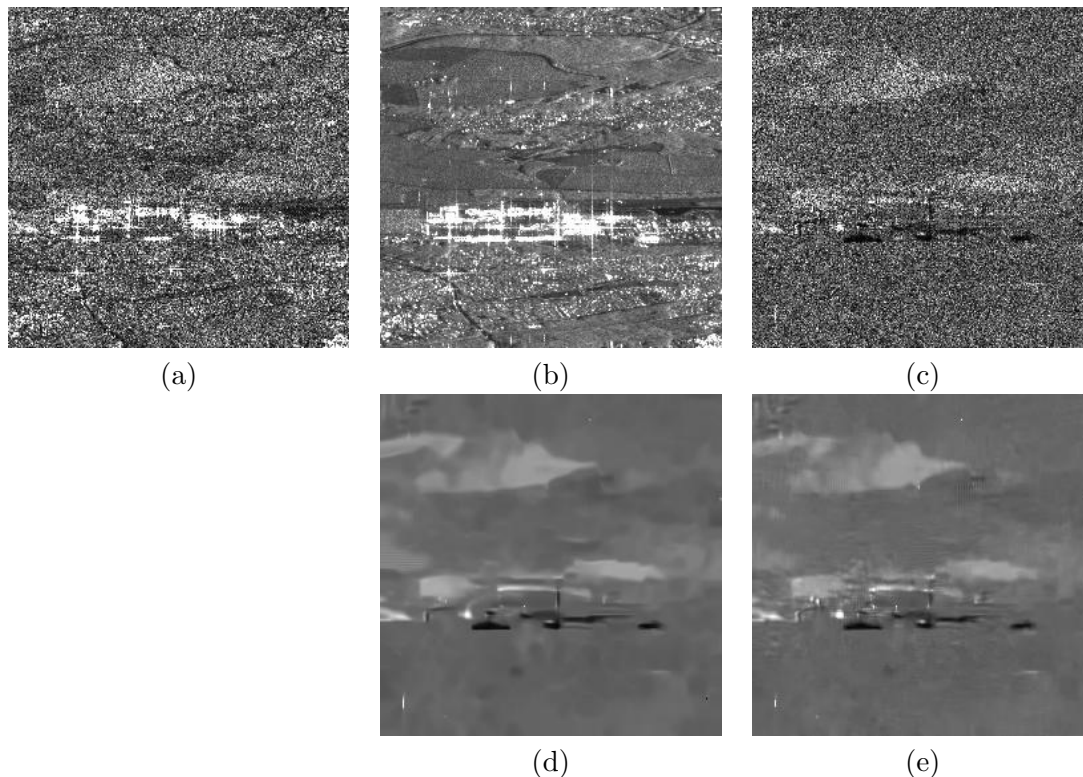


FIGURE 6.2: (a) Sentinel-1 noisy image, (b) Arithmetic mean image, (c) Ratio image, (d) MuLoG-BM3D denoising result on ratio image, (e) SAR-BM3D denoising results on ratio image. Appearing (dark areas in (d)) and disappearing buildings (clear areas) are located in the middle of the image.

## 6.4 Online processing of long SAR time series

With the rapid growth of SAR temporal series, new challenges for temporal SAR data processing arise to deliver useful information to the end-user. Other challenges appear for fast exploiting and efficiently storing the huge amount of collected data.

The proposed approach can be expressed in an online form, which requires minimal computation for the information updating when adding a new image. With a new incoming image, the denoising procedure applied to this image depends on the available super-image. In this section, fast denoising and super-image updating strategies working on the flow of incoming image are studied. Besides, a reset process, computing a new super-image from time to time (fixed temporal frequency, sliding temporal window) or driven by detected changes, could be applied.

- *Exploiting the whole stack*

We discuss first the case when the whole stack of multi-temporal images is available (i.e., off-line processing). To form the super-image, the arithmetic mean is well adapted to vegetated areas and regions without changes. The binary weighted arithmetic mean is better suited to handle changes such as in urban areas. Given the large speed gain of the (unweighted) arithmetic mean, we suggest that is a relevant choice. Differences in results when using different super-images and related parameters selection will be presented in

**Algorithm** Multi-temporal speckle reduction (RABASAR)

---

**Input :**  $M$  co-registered SAR images  $\{y_1, y_2, \dots, y_M\}$   
**Output :**  $M$  images with reduced speckle  $\{\hat{u}_1, \hat{u}_2, \dots, \hat{u}_M\}$

- 1: *Step 1 : computation of the super-image*
- 2: **for** each pixel  $s$  **do**
- 3:   *(optional : compute binary weights in the time serie)*
- 4:    $w_{t,t'}(s) \leftarrow \text{estimate\_weights}(y_t(s), y_{t'}(s))$
- 5:    $\hat{u}(s) \leftarrow \frac{1}{\sum_{t,t'} w_{t,t'}(s)} \sum_{t'=1}^M w_{t,t'}(s) y_t(s)$
- 6: **end for**
- 7: *Step 2 (optional) : denoise the super-image*
- 8: **if** denoise super-image **then**
- 9:    $\hat{L} \leftarrow \text{estimate\_looks}(\hat{u})$
- 10:    $\hat{u} \leftarrow \text{MuLoG\_BM3D}(\hat{u}, L = \hat{L})$
- 11: **end if**
- 12: **for**  $t$  from 1 to  $M$  **do**
- 13:   *Step 3-4 : denoising of the ratio image*
- 14:    $\hat{P}_t \leftarrow \text{MuLoG\_BM3D}(y_t/\hat{u}, L = 1)$
- 15:   *Step 5 : computation of the restored image*
- 16:    $\hat{u}_t \leftarrow \hat{u} \cdot \hat{P}_t$
- 17: **end for**
- 18: **return**  $\{\hat{u}_1, \hat{u}_2, \dots, \hat{u}_M\}$

---

section 6.5.

- *Updating strategy*

In the most recent satellite programs, the revisit time has been significantly reduced. Therefore, a new image is likely to be mostly similar to the previously acquired ones. Let us use Sentinel-1 A/B images as example. Their revisit time is 6 days with repeat cycle at the Equator, and the actual revisit time, with ascending or descending tracks and overlap, is around 2 days near Paris [Torres et al., 2012]. When the number of images in the temporal series is large enough, we can choose to denoise the new coming image based on the previously acquired super-images. Then, we may adopt a refreshing strategy to update the super-image from time to time (for instance every 50 images). This is well adapted for large image denoising, like Sentinel-1 Interferometric image in the Wide Swath mode (250 km swath and  $5 \times 20$  m spatial resolution) or with TerraSAR-X in the StripMap mode ( $30 \times 50$  km<sup>2</sup> and up to 3 m resolution).

#### 6.4.1 Strategy to update the arithmetic mean

In the previous analysis, the filtering of the arithmetic mean image was presented as an optional stage and the new image could either be involved in the computation of the arithmetic mean image or not. This difference in strategy appears less and less noticeable when increasing the number of images involved in the computation of the super-image. This point is illustrated on figure 6.3, using series of simulated SAR images<sup>2</sup> without any change and computing the PSNR and MSSIM differences in estimating the reflectivity from the noisy series. When increasing the number of images involved in the computation

---

2. The way to simulate SAR images is presented on Section 3.3.1.

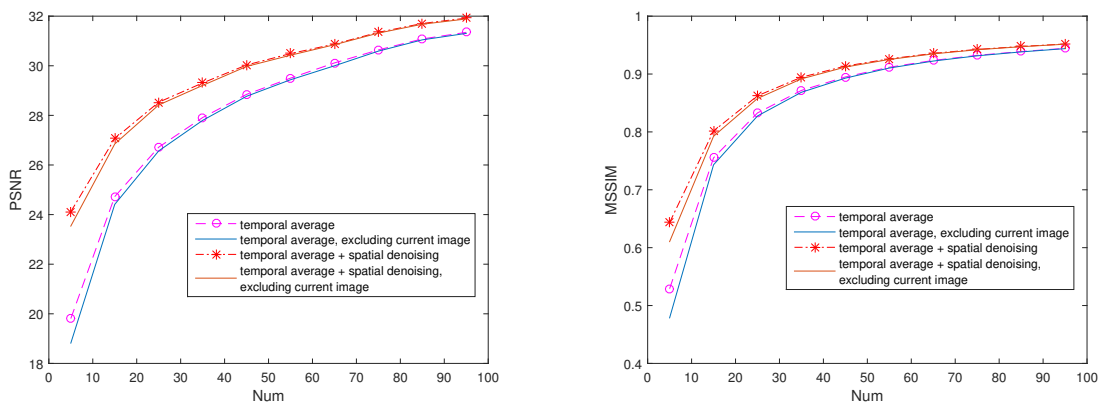


FIGURE 6.3: Impact of the method to compute the super-image in the speckle reduction performance. RABASAR performances, with the new image joining the calculation of temporal average or excluded, are compared based on providing PSNR and MSSIM values. The ENL is set equal to the number of used temporal simulated images.

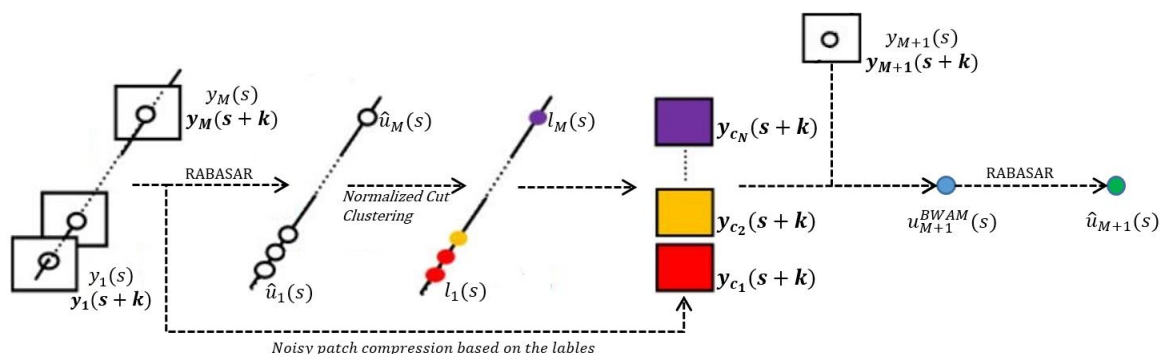


FIGURE 6.4: Binary weighted arithmetic mean preparation procedure for the new coming image. The bold font  $\mathbf{y}$  represents the patch centered around  $s$  with  $s + k \in W_s$ .

of the super-image, the difference in the reflectivity errors obtained either by involving the actual image or not, measured as PSNR or as MSSIM are less and less important.

With few images in the series, a light benefit exists in the estimation when using the actual image in the computation of super-images (Fig.6.3). However this benefit disappears with about 20 images in the series.

As a conclusion, with large image stacks, we suggest not to involve the arriving image to up-date the super-image.

#### 6.4.2 Using binary weighted arithmetic mean

Compared with the arithmetic mean image computation, BWAM image computation is much more heavy, especially when the time series is large. To accelerate this computation, we propose a preparation stage (Fig.6.4) which builds up a library of meaningful patches, collected before hand. The comparison of the new image will be made only with the patches of the library and not with all the possible patches of the series.

In the off-line preparation stage we make use of the SAR time series  $\{y_1(s), y_2(s), \dots$

$\cdot, y_M(s)\}$ , limited to time  $M$ , in order to process an incoming image at time  $M + 1$ . With this series, the associated denoised values  $\{\hat{u}_1(s), \hat{u}_2(s), \dots, \hat{u}_M(s)\}$  are computed by applying RABASAR.

Then, the temporal samples  $\hat{u}_k(s)$  can be classified in  $N$  classes using the method of [Su et al., 2015] and each pixel is indexed by the class  $l_k(s)$  it belongs to. This provides  $M$  images of labels :  $\{l_1(s), l_2(s), \dots, l_M(s)\}$  corresponding to labels at each position  $s$  with  $N$  clusters [Su et al., 2015]. For each cluster, only the temporal average values of the patches which are centered around  $s$  are kept, so as to compress the patches. The compressed patches  $\{\mathbf{y}_{c_1}(s+k), \mathbf{y}_{c_2}(s+k), \dots, \mathbf{y}_{c_N}(s+k)\}$  are calculated through :

$$\mathbf{y}_{c_n}(s+k) = \frac{1}{\sum_{t=1}^M w(t)} \sum_{t=1}^M w(t) \mathbf{y}_t(s+k) \quad (6.9)$$

where  $k$  is used to scan the patches centered around  $s$  with clustering label  $l_t(s)$ ,  $n$  is the index of clusters with  $1 \leq n \leq N$ ,  $w(t)$  is the binary weight with  $w(t) = 1$  when  $l_t = n$ .

When there is a new image, let us take the point  $s$  surrounded by patch  $\mathbf{y}_{M+1}(s+k)$  for example. Firstly, the patch is separately compared with  $\{\mathbf{y}_{c_1}(s+k), \mathbf{y}_{c_2}(s+k), \dots, \mathbf{y}_{c_N}(s+k)\}$  using the similarity criterion (Eq.(6.10)) proposed in [Su et al., 2014], with  $L$  represents the ENL of the new image and  $L_{c_n}$  denotes the ENL of the patch  $\mathbf{y}_{c_n}(s+k)$  used for comparison.

$$S_G(s) = \sum_k \left( (L + L_{c_n}) \log \left( \frac{L \mathbf{y}_{M+1}(s+k) + L_{c_n} \mathbf{y}_{c_n}(s+k)}{L + L_{c_n}} \right) - L \log(\mathbf{y}_{M+1}(s+k)) - L_{c_n} \log(\mathbf{y}_{c_n}(s+k)) \right) \quad (6.10)$$

For each position  $s$  in the new image, the similar patches are selected by use of a predefined threshold. Based on the acquired BWAM, we can acquire the denoised image using RABASAR method. Then, we directly update the averaged patches based on the similarity test (Eq.(6.10)) and a maximum likelihood estimation. This method reduces both the computation time and the storage requirement.

In the experimental implementation, a Normalized Cut method [Shi and Malik, 2000, Su et al., 2015] was used to cluster the denoised values.  $M$  was chosen equal to 127 and the threshold is obtained based on Monte Carlo simulations (simulations of pure speckle noise). The experimental implementation and related parameters setting are illustrated in section 6.5.3.

## 6.5 Experimental results

To evaluate the performances of the proposed method, different experiments have been conducted on simulated and real SAR images (Chapter 3). The influence of different super-images on the RABASAR denoising results are commented (section 6.5.1). Then, the ratio-based multi-temporal denoising methods are compared with some methods selected from the literature : UTA [Lee et al., 1991, Quegan et al., 2000a], NLTF [Chierchia et al., 2017b], 2SPPB [Su et al., 2014] and MSAR-BM3D [Chierchia et al., 2017b] (section 6.5.2).

TABLE 6.1: Parameter setting with different super-images ( $L$  is the ENL of the noisy image)

Super-image	Denoising step (MuLoG-BM3D)	ENL estimation	Similarity window [Buades et al., 2005]
AM	Step 4	$L$	
DAM	Step 2, 4	log-cumulant	
BWAM	Step 3-4	$L$	$7 \times 7$
DBWAM	Step 2-4	log-cumulant	$7 \times 7$

### 6.5.1 Which super-image gives the best denoising ?

As proposed earlier (see section 6.2.3), different super-images (AM, BWAM and their spatially denoised versions) may be computed with the same multi-temporal stack. This section presents quantitative (Fig.6.5-6.8) and qualitative (Fig.6.9-6.10) results of the denoising stage, obtained by using different super-images with different stack lengths. The parameters used with each super-image are shown in table 6.1. The ENL of the super-image is estimated using the log-cumulant method with a window size  $30 \times 30$ , and the maximum estimated ENL is used. The ENL of the ratio image is supposed to be the same as the one of the noisy image ( $L$ ).

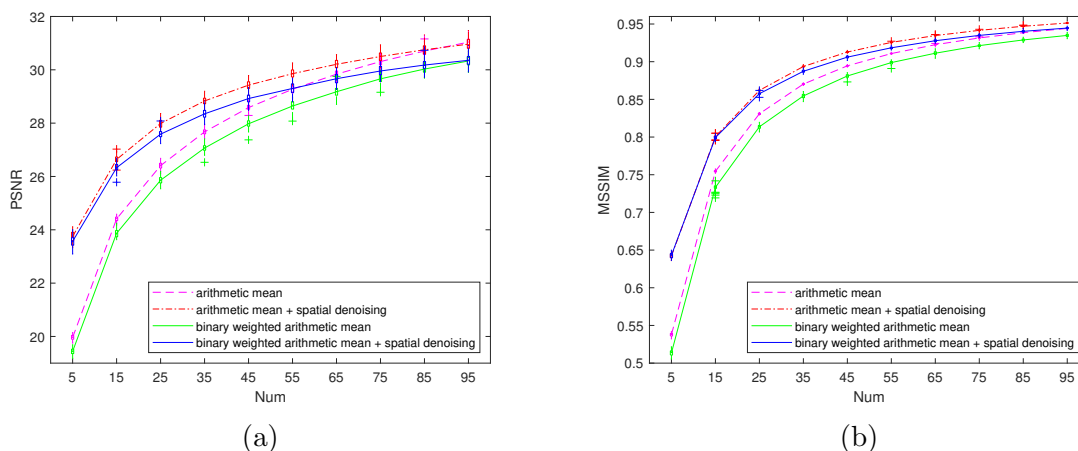


FIGURE 6.5: RABASAR performances with different super-images measure with PSNR (a) and MSSIM (b) as a function of the number of temporal images. The unchanged time series (Fig.3.15(a)) are used. The denoising performances are evaluated on the first image in the time series. The line represent the mean value of 50 times test. On each index box, the bottom and top edges of the box indicate the 25th and 75th percentiles, respectively. The outliers are plotted individually using the ‘+’ symbol.

#### 6.5.1.1 Using simulated radar images

Simulated images allow to evaluate numerically the performances obtained with four different super-images by measuring PSNR and MSSIM values (50 experiments are done to compute the average value). The number of images in the time series varies from 5 to 95.

For temporal images without changes (Fig.6.5(a-b)), using denoised super-images provides better PSNR and MSSIM values when using a small number of images, but this

benefit disappears with long stacks of images (more than 60). When using denoised super-images, the obtained PSNR and MSSIM values are seriously influenced by the used ENL. Smaller ENL estimation window size is recommended when fewer temporal images are available. Because of the i.i.d. time series variables, we set the ENL equal to the number of used simulated temporal images. We recommend using a spatially adaptive ENL for the denoising of BWAM, because different numbers of temporal samples may be used for its computation.

For changed areas, we compare the denoising results for the different temporal profiles (Fig.6.6). To evaluate the denoising performances when using different super-images, the mean value of 50 denoising results are computed. We also present the mean and standard deviation of RABASAR-AM and RABASAR-BWAM obtained results in figure 6.7 and figure 6.8, respectively.

For the farmland and forest areas, RABASAR provides good denoising results with the four kinds of super-images. For the appearing building case, a bias is introduced when using the temporal arithmetic mean (without binary weights). Such a behavior is caused by the low contrast in the ratio image, and the patch based non-local searching strategy of the denoiser smooths these areas. For the appearing and disappearing building area, the contrast is high enough between the structure and the super-image value, and is thus preserved in the denoising of the ratio image.

In conclusion, using the binary weighted arithmetic mean limits the bias, at the cost of a residual noise, specially when few temporally similar samples are found.

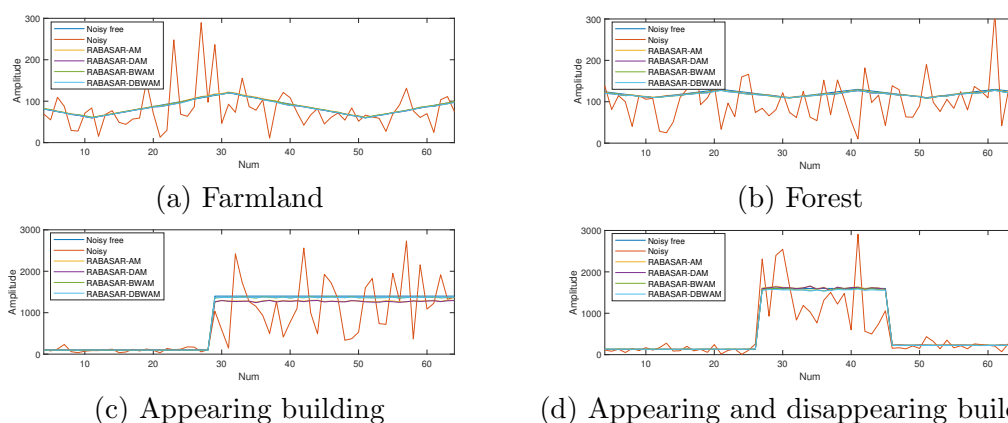


FIGURE 6.6: RABASAR denoising performance comparison with different super-images in the changed area. Only the middle points in the biggest changed rectangles are used. 100 simulated temporal images are used for the calculation of super-images. RABASAR provided time series results are the mean values of 50 tests. These four kinds of temporal changes correspond to the four different object changes in Fig.3.15 (b).

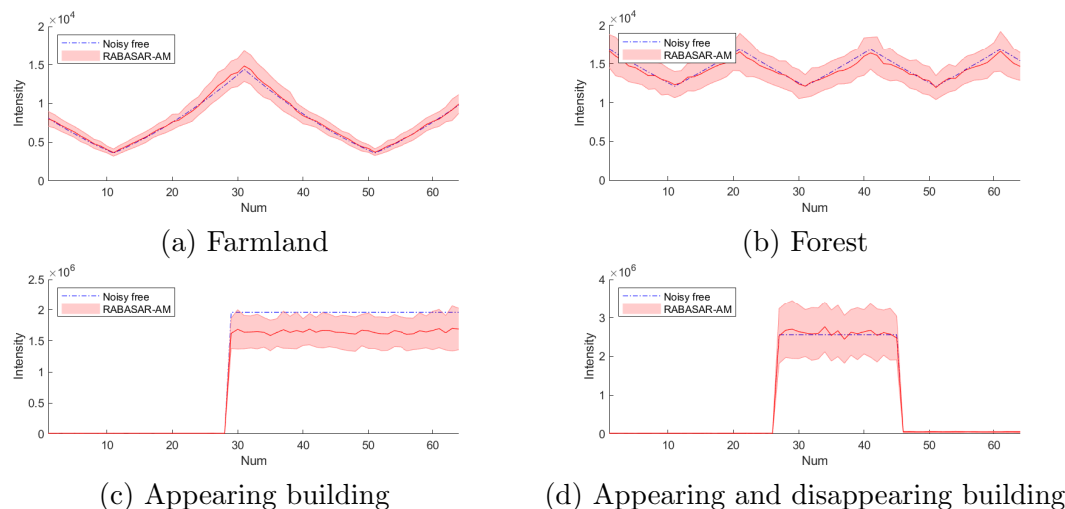


FIGURE 6.7: RABASAR-AM denoising performance on four different time series. The mean (red line) and standard deviation of 50 times experimental results are used for the comparison.

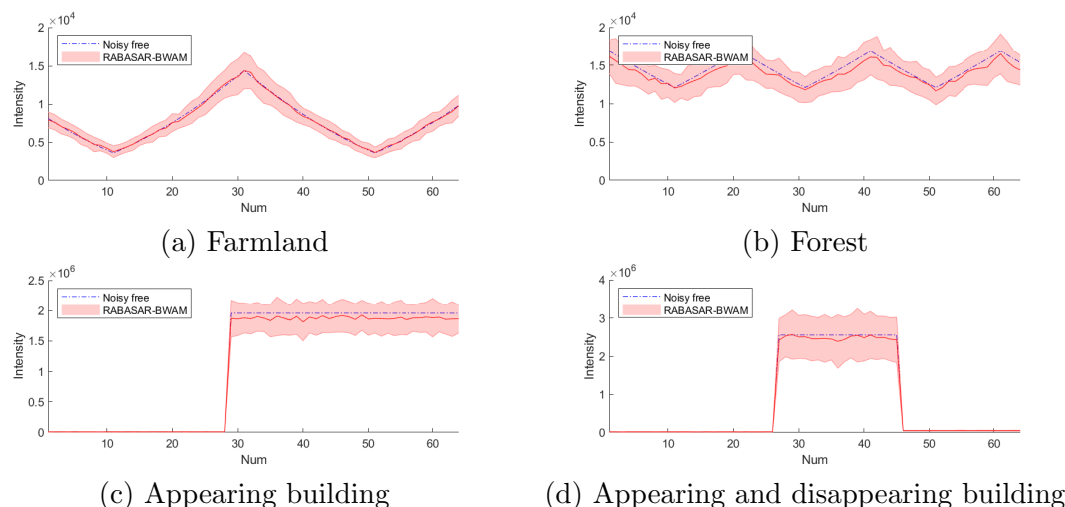


FIGURE 6.8: RABASAR-BWAM denoising performance on four different time series. The mean (red line) and standard deviation of 50 times experimental results are used for the comparison. Threshold is set equal to 0.92 during the BWAM calculation.

### 6.5.1.2 Using Sentinel-1 images

The temporal series of 69 Sentinel-1 images on the Saclay area is used to test the method on real SAR images. Figure 6.9 can be used to visually assess the noise reduction efficiency of using different “super-images”. RABASAR provides good denoising results with the four different super-images. The use of an additional spatial filtering step to form the super-image seems beneficial in terms of restoration quality : the obtained images are smoother.

For results which used AM and DAM, small areas with low values were sometimes smoothed leading to the apparition of new points in the denoised results (Fig.6.9(a-b) red

rectangular). This phenomenon is obvious for impulsive and abrupt changes in building areas. Using BWAM and DBWAM reduces this problem (Fig.6.9(c-d)). In some changing parts of the image, using BWAM, however, leads to poor filtering results because of using only few similar points to compute the super-image.

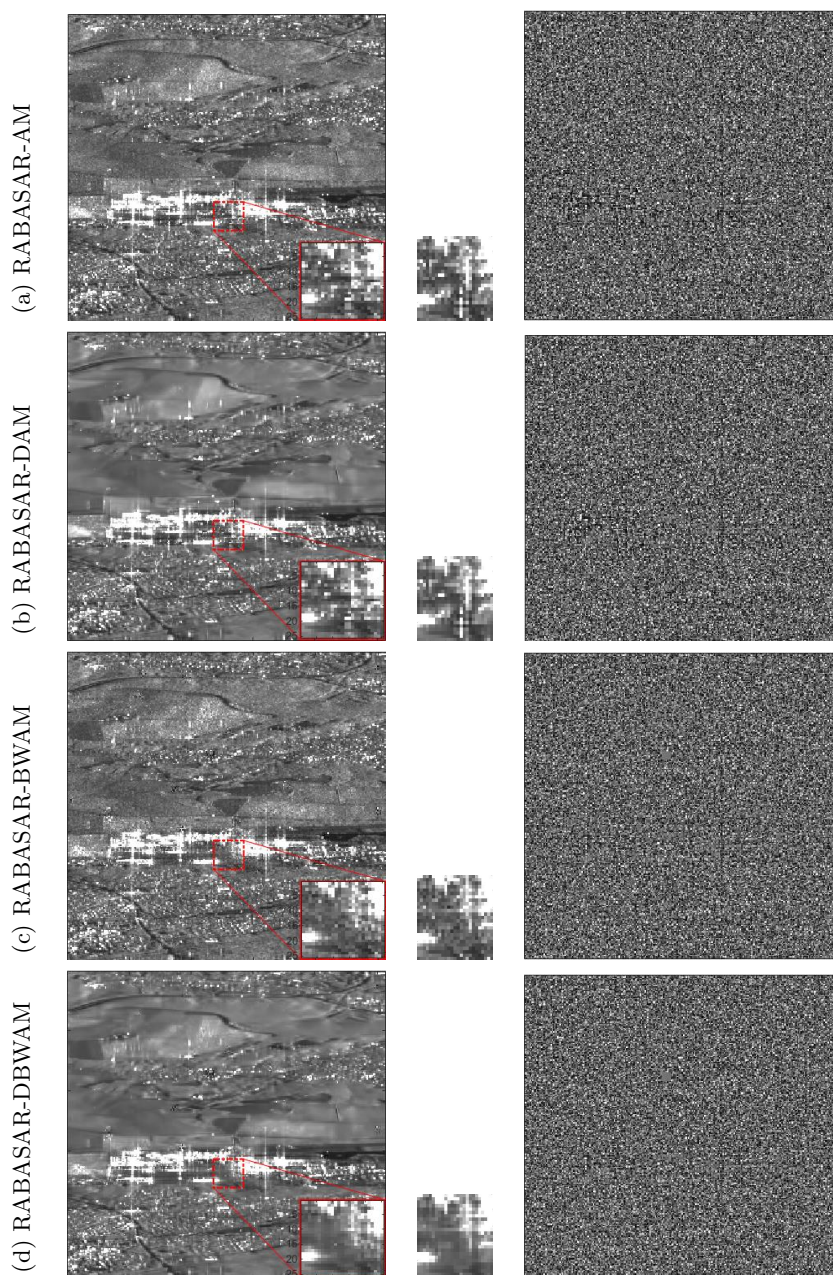


FIGURE 6.9: RABASAR denoising results comparison. Denoised Sentinel-1 images over the Saclay area (left), used super-images for the enlarged areas (middle), ratio-images (right) with the noisy data. 69 resampled Sentinel-1 images are used.

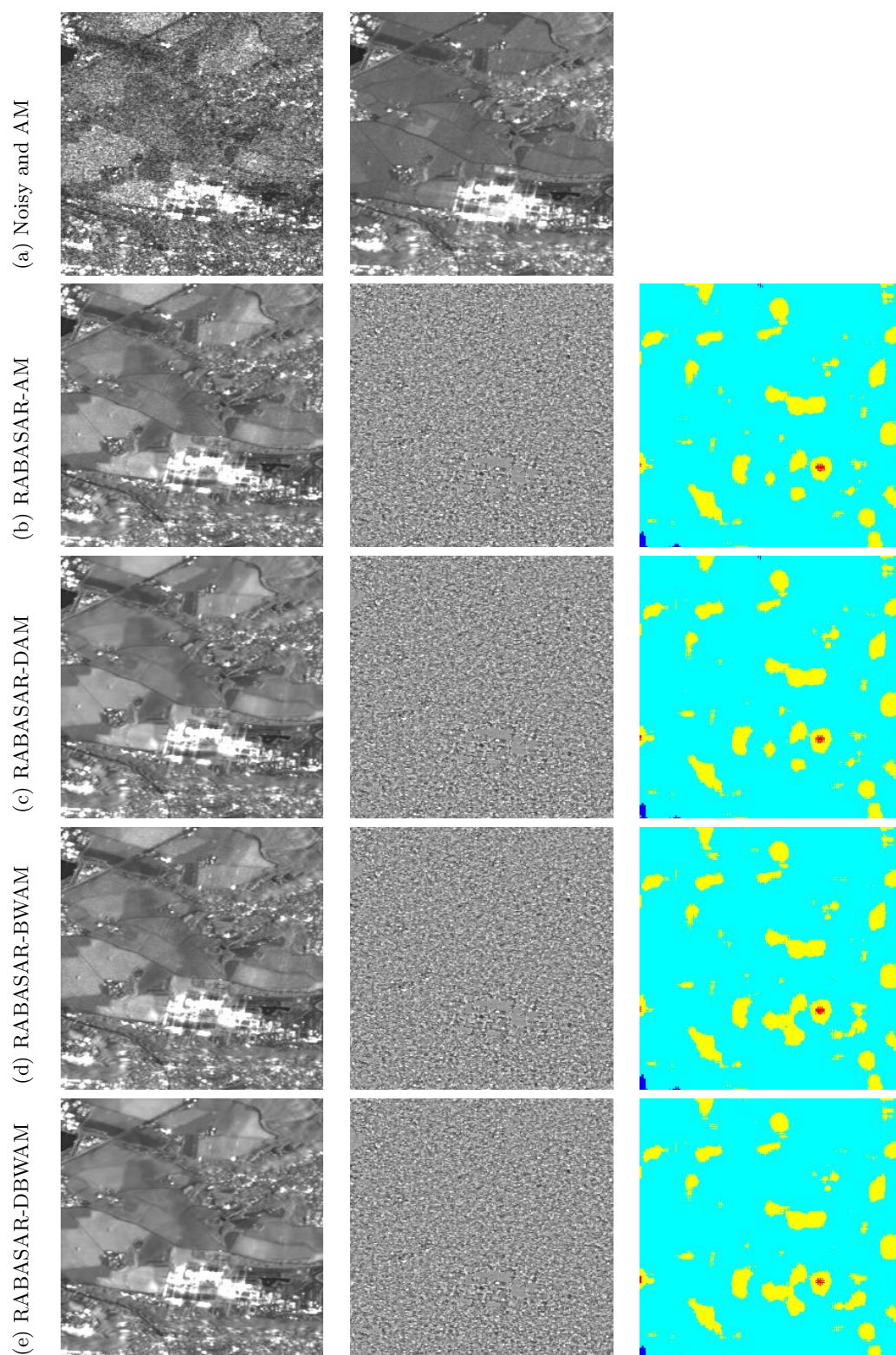


FIGURE 6.10: RABASAR denoising results with different super-images. (a) noisy and arithmetic mean image, (b-e) denoised results (left), ratio with noisy data (middle) and residual evaluation results with displaying value range  $[0, 4]$  (right). 339 Sentinel-1 GRD images are used.

When processing long time series Sentinel-1 GRD images, RABASAR-DAM can acquire the best M-index and residual values (Tab.6.2). The denoising results are shown in figure 6.10. Comparing with the results acquired in the former chapter (Fig.5.7), RABASAR-DAM can acquire better denoising results with respect to the residual evaluation value. RABASAR-DAM provides smaller M-index values than NLTF in the homogeneous areas, but NLTF cannot provide as good results as RABASAR-DAM in building areas. RABASAR-DAM provides better M-index values and residual values than PATF.

TABLE 6.2: Residual evaluation of RABASAR denoising results with different super-images (best value in boldface). M-index is evaluated in the automatically selected homogeneous area, while residual is calculated based on the whole image.

Figures	Methods	AM	DAM	BWAM	DBWAM
Fig.6.10	M-index	11.287	<b>6.105</b>	17.164	13.617
	Residual	2.173	<b>2.169</b>	2.182	2.176

### 6.5.1.3 Computation time

The computation time of the algorithm depends on the adopted RABASAR version (type of super-images, binary weighted or not, ENL estimation method and choice of the spatial denoising).

When running the experiments on a time serie of 69 SAR images of size  $512 \times 768$  (Saclay) in the MATLAB environment on a computer (4 cores, Intel(R) Core(TM) i7-7600U CPU @ 2.80GHz), the elapsed time of RABASAR-DBWAM is given in table 6.3.

TABLE 6.3: Computation time of the different steps for a time series of 69 images with size  $512 \times 768$ .

Weight computation (step 1) eq. 6.2	0.74 sec (1%)
ENL estimation (step 2)	0.12 sec (0.2%)
MuLog-BM3D (step 3 and 4)	$2 \times 34.4$ sec (49%)
Total time	70 sec.

As can be seen, the main part of RABASAR computing time is due to the denoising step. If both the super-image and the ratio image are denoised, the time is multiplied by 2. Using convolution kernels, the similarity and weight computation represents only 1% of the total time. Nevertheless, when using binary weighted arithmetic mean, the super-image has to be computed again for each image to process, whereas the super image computation is done only once for AM or DAM versions of RABASAR.

### 6.5.2 Denoising performances of RABASAR compared to existing methods

The proposed method is compared with state-of-the-art multi-temporal denoising methods, both with simulated and real SAR images. Numerical and visual results are provided when comparing RABASAR with the chosen methods : UTA [Quegan et al., 2000a], NLTF [Chierchia et al., 2017b], 2SPPB [Su et al., 2014] and MSAR-BM3D [Chierchia et al., 2017b].

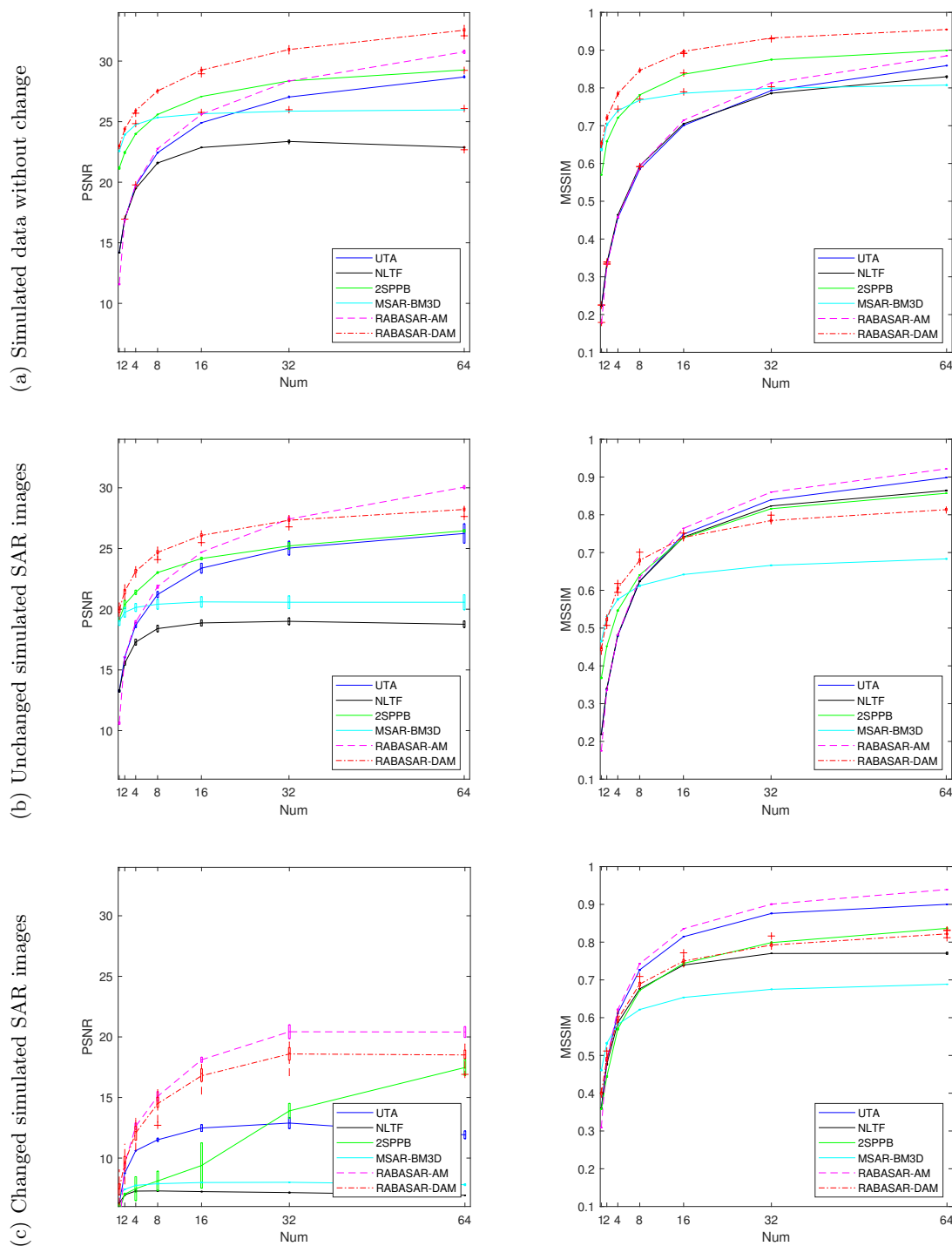


FIGURE 6.11: Comparison of different temporal denoising methods : UTA, NLTF, 2SPPB, MSAR-BM3D, RABASAR-AM and RABASAR-DAM. PSNR (left) and MSSIM (right) as a function of the number of images. Each case was test for 50 times, with the same noise free value multiplied by different Gamma distribution noise. The line features shows the mean value. The bottom and top edges of the box indicate the 25th and 75th percentiles, respectively.

### 6.5.2.1 Quantitative comparison

As in the previous sections, to quantitatively compare the filtering performance of these methods, averaged PSNR and MSSIM are computed. Only RABASAR-AM and RABASAR-DAM performances are presented in the curves of figure 6.11. Since MSAR-BM3D released code requires a number of time series equal to a power of 2, we only tested such cases, to keep the original performances of this method.

To make a fair comparison with other methods, three kinds of temporal data are tested (Fig.6.11). In the case where no change or bright echo exist in the simulated image, we see, from figure 6.11, that RABASAR generally provides better PSNR than other filtering methods. This may be explained because, under these hypotheses, the ratio image is very homogeneous.

With fewer images in the stack, MSAR-BM3D and 2SPPB also provide competitive PSNR and MSSIM. However, with the increase of the number of images, MSAR-BM3D curve does not rise as fast as 2SPPB. When using less than 4 simulated images, MSAR-BM3D provides the best MSSIM values.

With an increasing number of images without change, UTA PSNR and MSSIM values keep increasing. Due to the use of a sliding window to estimate the reflectivity, UTA does not give good results when few images are used. Since there are large building areas in the time series, it suffers from blurred boundaries. Table 6.4 presents some results about PSNR and MSSIM results.

TABLE 6.4: Numerical results provided by different methods with 32 images in the series. Evaluation is made by PSNR and MSSIM. For PSNR and MSSIM, larger values express better denoising results.

Sentinel-1	Evaluation methods	UTA	NLTF	2SPPB	MSAR -BM3D	RABASAR			
						-AM	-DAM	-BWAM	-DBWAM
without changes	PSNR	25.65	19.00	25.17	21.03	27.56	<b>29.10</b>	26.64	28.40
	MSSIM	0.84	0.82	0.81	0.67	0.86	<b>0.89</b>	0.84	0.88
with changes	PSNR	13.01	6.88	13.11	7.12	19.34	<b>20.10</b>	19.00	19.50
	MSSIM	0.88	0.77	0.80	0.68	0.90	<b>0.91</b>	0.88	0.90

### 6.5.2.2 Simulated SAR data with different ENL

To evaluate the effects of the ENL on the denoising performances, different denoising methods are applied on the simulated images which are selected over various landscapes. Results are presented in table 6.5. In the case of long time series (here 64 temporal images are used), the various RABASAR methods always provide better results than other methods. When there are changes in the time series, using BWAM may be better than using AM. Since the simulated time series are affected by i.i.d. speckle, their temporal average are nearly equal to the noise free value with infinite samples. This is the reason why RABASAR can provide much larger PSNR and MSSIM.

### 6.5.2.3 Sentinel-1 and TerraSAR-X image denoising

This section presents and discusses the results obtained when denoising Sentinel-1 and TerraSAR-X images. Since the noise free images are not available, the denoised results and the residual noise (ratio of the original image by the denoised image) are visually evaluated. The residual noise should correspond to pure gamma-distributed noise samples

TABLE 6.5: PSNR-MSSIM values provided by different denoising methods using different data issued from the simulated SAR images (see section 3.3.2). The number of images in the series is 64. Sentinel-1 images are expressed by S-, TerraSAR-X images are denoted with T-. Each case was test for 50 times, with the same noise free value multiplied by different Gamma distribution noise. The PSNR-MSSIM values are the average values acquired through 50 tests.

Data	ENL	UTA	2SPPB	NLTF	MSAR-BM3D	RABASAR-AM	RABASAR-BWAM
S-Farmland	1	28.177 - 0.876	27.422 - 0.831	20.590 - 0.862	22.581 - 0.617	<b>30.863 - 0.902</b>	29.710 - 0.877
S-Farmland	4	34.381 - 0.965	30.154 - 0.882	30.586 - 0.972	27.005 - 0.777	<b>36.677 - 0.973</b>	35.662 - 0.965
S-Farmland	8	36.636 - 0.982	31.834 - 0.894	34.583 - 0.986	28.948 - 0.846	<b>39.569 - 0.986</b>	38.324 - 0.982
S-Building	1	20.000 - 0.941	18.635 - 0.887	10.731 - 0.763	13.405 - 0.774	<b>26.540 - 0.962</b>	25.407 - 0.952
S-Building	4	26.771 - 0.984	26.984 - 0.937	19.827 - 0.979	19.413 - 0.893	<b>32.331 - 0.990</b>	31.293 - 0.987
S-Building	8	28.585 - 0.992	31.532 - 0.960	23.577 - 0.992	21.658 - 0.931	<b>35.472 - 0.995</b>	34.245 - 0.993
S-Change	1	11.803 - 0.899	15.449 - 0.832	6.688 - 0.770	7.246 - 0.690	18.662 - <b>0.939</b>	<b>19.764 - 0.925</b>
S-Change	4	15.460 - 0.957	23.170 - 0.892	12.562 - 0.963	13.532 - 0.843	24.343 - <b>0.981</b>	<b>25.369 - 0.975</b>
S-Change	8	16.572 - 0.969	27.220 - 0.931	14.758 - 0.978	16.349 - 0.898	27.161 - <b>0.989</b>	<b>28.098 - 0.986</b>
T-Farmland	1	27.958 - 0.893	26.880 - 0.851	20.299 - 0.866	22.818 - 0.686	<b>30.442 - 0.917</b>	29.164 - 0.897
T-Farmland	4	34.126 - 0.970	29.319 - 0.893	30.267 - 0.976	27.135 - 0.818	<b>36.249 - 0.977</b>	35.180 - 0.970
T-Farmland	8	36.747 - 0.985	30.933 - 0.907	35.022 - 0.988	28.592 - 0.875	<b>39.201 - 0.988</b>	37.934 - 0.984
T-Building	1	19.873 - 0.943	19.153 - 0.901	10.619 - 0.803	12.588 - 0.811	<b>26.223 - 0.965</b>	25.053 - 0.956
T-Building	4	26.644 - 0.985	25.679 - 0.941	21.584 - 0.985	19.215 - 0.907	<b>31.863 - 0.990</b>	30.765 - 0.988
T-Building	8	28.975 - 0.992	30.607 - 0.963	26.244 - 0.994	21.475 - 0.938	<b>35.175 - 0.995</b>	33.926 - 0.993
T-Change	1	19.114 - 0.934	18.927 - 0.848	11.949 - 0.740	14.222 - 0.759	<b>26.649 - 0.955</b>	25.688 - 0.948
T-Change	4	25.971 - 0.978	26.158 - 0.928	20.342 - 0.971	19.512 - 0.884	<b>32.672 - 0.985</b>	31.673 - 0.983
T-Change	8	29.197 - 0.986	31.351 - 0.961	24.355 - 0.984	22.212 - 0.926	<b>35.803 - 0.991</b>	34.747 - 0.990

of mean 1. Residual structures, homogeneous areas, and radiometric variations correspond to the following perturbations : the destruction of structures, the absence of filtering, and bias introduction.

First, compared to MuLoG-BM3D applied on a single image, RABASAR-DAM provides a much better result, preserving fine structures and isolated objects (Fig.6.12). This experiment shows that the exploitation of the super-image and the ratio image, which is much more stationary than the original noisy image, helps preserving the original resolution.

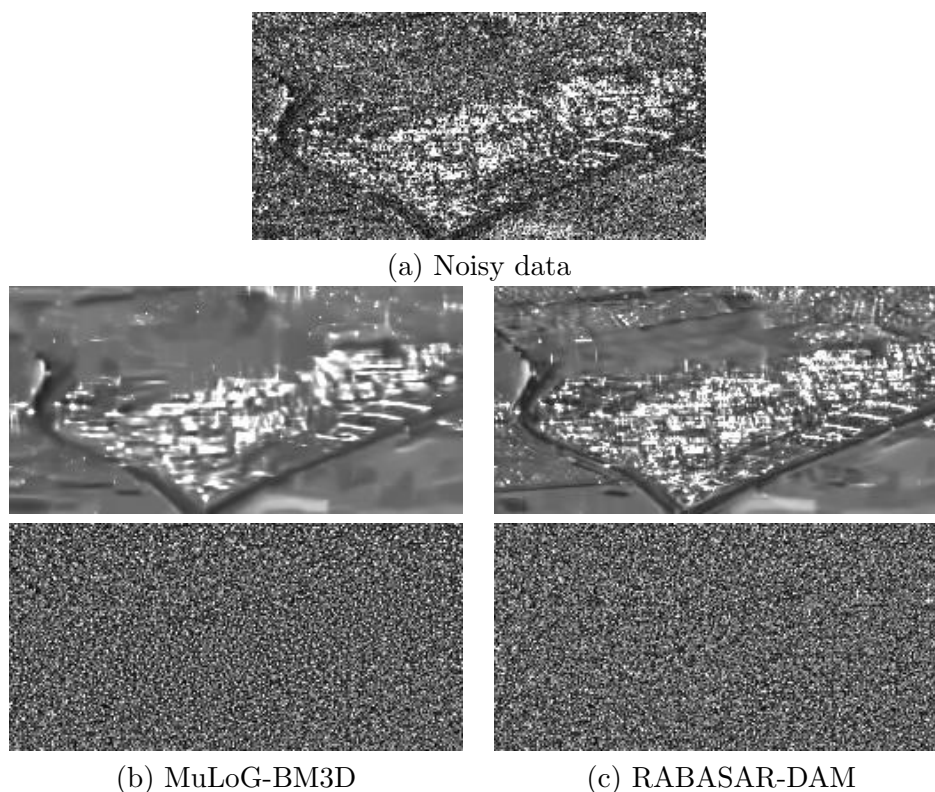


FIGURE 6.12: Denoising results and ratio with noisy data of MuLoG-BM3D and RABASAR-DAM. 64 resampled Sentinel-1 images are used to calculate the arithmetic mean image.

TABLE 6.6: Residual evaluation results (best value in boldface).

Figures	Methods	2SPPB	MSAR-BM3D	RABASAR-DAM	RABASAR-DBWAM
Fig.6.13	M-index	6.786	<b>6.298</b>	13.435	11.526
	Residual	1.479	2.728	<b>0.969</b>	0.971
Fig.6.14	M-index	24.130	14.964	6.383	<b>5.311</b>
	Residual	1.334	4.184	<b>0.974</b>	0.976

Figure 6.13 presents different filtering results on a Sentinel-1 time serie of Saclay. Compared to 2SPPB and MSAR-BM3D methods, RABASAR-DAM and RABASAR-DBWAM provide better denoising results since they take both the ratio results and the texture characteristics into account. Some noisy areas can be observed in the RABASAR-DBWAM results due to the temporal samples selection (for some pixles, only few similar temporal

samples can be found to compute the binary weighted arithmetic mean). 2SPPB method does not give good results for seasonal changing farmland areas, and shows an obvious bias in the residual noise (see for instance the blue rectangle area in Fig.6.13(e)).

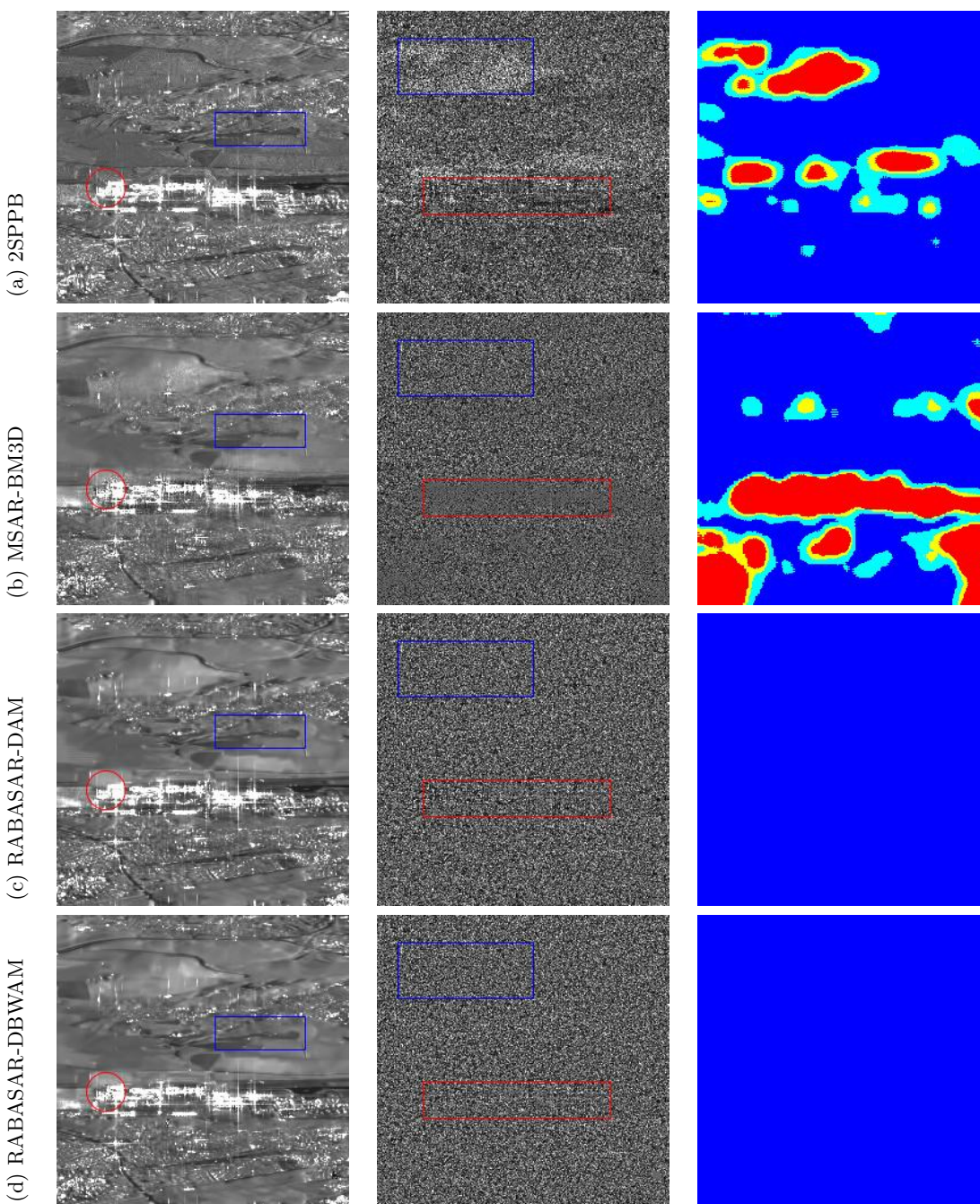


FIGURE 6.13: Denoising real Sentinel-1 images over the region of Saclay (the original noisy image is available in figure 6.2(a)). Left column : denoised results ; middle column : residual ratio images ; right column : residuals evaluation results with displaying value range  $[0, 4]$ . 64 Sentinel-1 images are used.

Since MSAR-BM3D method detects the bright points in advance and prohibits any

denoising around these points [Chierchia et al., 2017b], building areas in the residual noise are homogeneous (Fig.6.13(f) red rectangle area) showing that no filtering has been applied in these areas (Fig.6.13(b) red circle area).

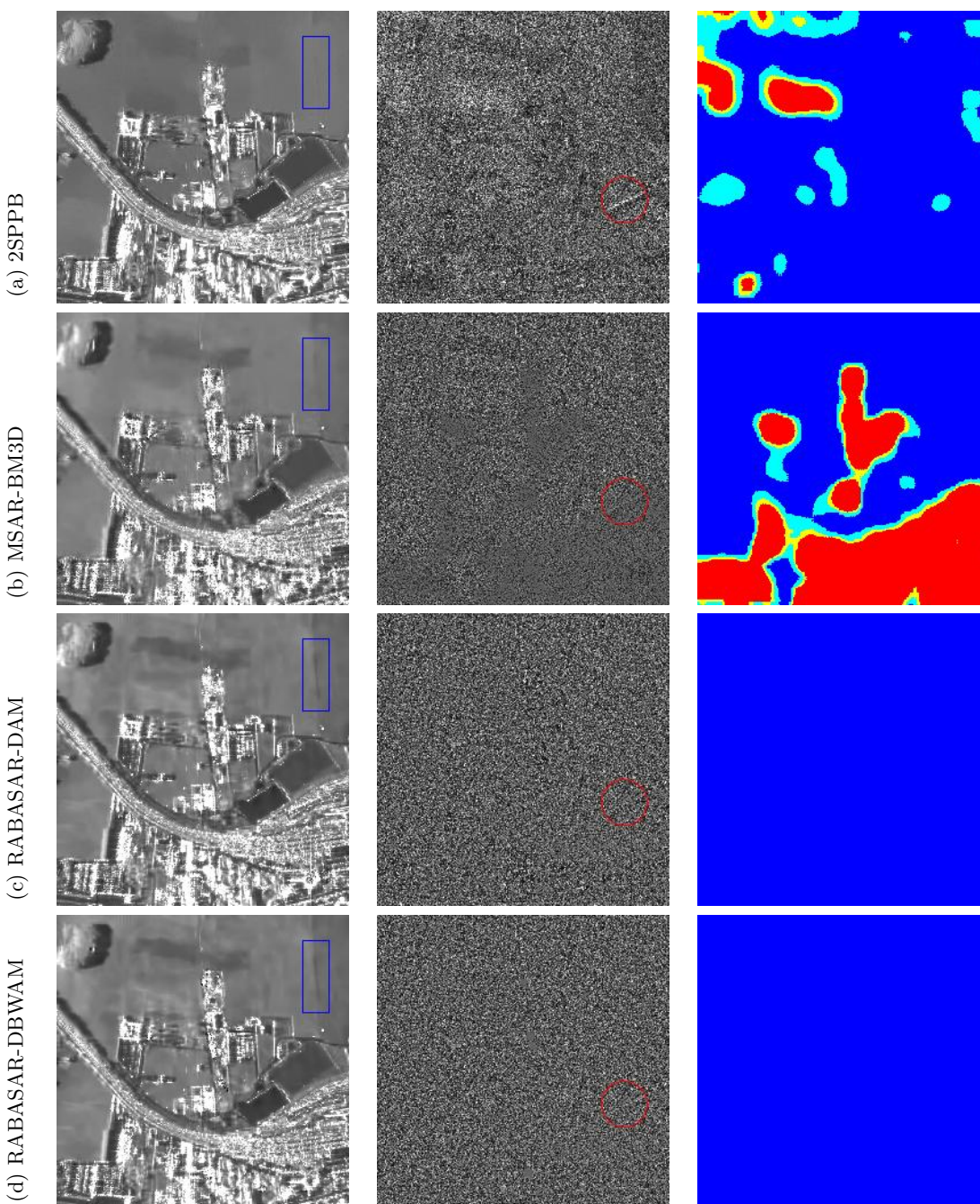


FIGURE 6.14: Different denoising results with TerraSAR-X images over Saint-Gervais. The original noisy image is available in figure 3.3. Left column : denoised results ; middle column : residual ratio images ; right column : residuals evaluation results with displaying value range  $[0, 4]$ . 16 TerraSAR-X images are used.

This also explains why MSAR-BM3D has lower PSNR values. In addition, some of the

textures in MSAR-BM3D results are over smoothed, such as the blue rectangle area in figure 6.13(b). MSAR-BM3D can acquire good Sentinel-1 denoising results in the homogeneous areas. It provides the best M-index values (Tab.6.6). M-estimator [Gomez et al., 2017] can automatically select the homogeneous areas. However, in different time, it may select different homogeneous areas which lead to different M-index calculation results.

Comparing the Sentinel-1 images denoising results with that in figure 5.9, RABASAR-DAM and RABASAR-DBWAM provide much better results than PATF-BSAR-BM3D. ANLTF can keep the fine features of the denoised image. However, it is a little bit time consuming due to the requirement of denoising all the temporal images separately before pursue temporal denoising.

Similar phenomena can be observed on the TerraSAR-X images presented figure 6.14. Whereas figure 6.14(c) and (d) visually provide satisfying results and homogeneous residual noise images, both 2SPPB and MSAR-BM3D smoothed out some textures (Fig.6.14 blue rectangle areas), or keep unchanged some noisy areas. RABASAR can provide large M-index values in the automatically selected homogeneous areas.

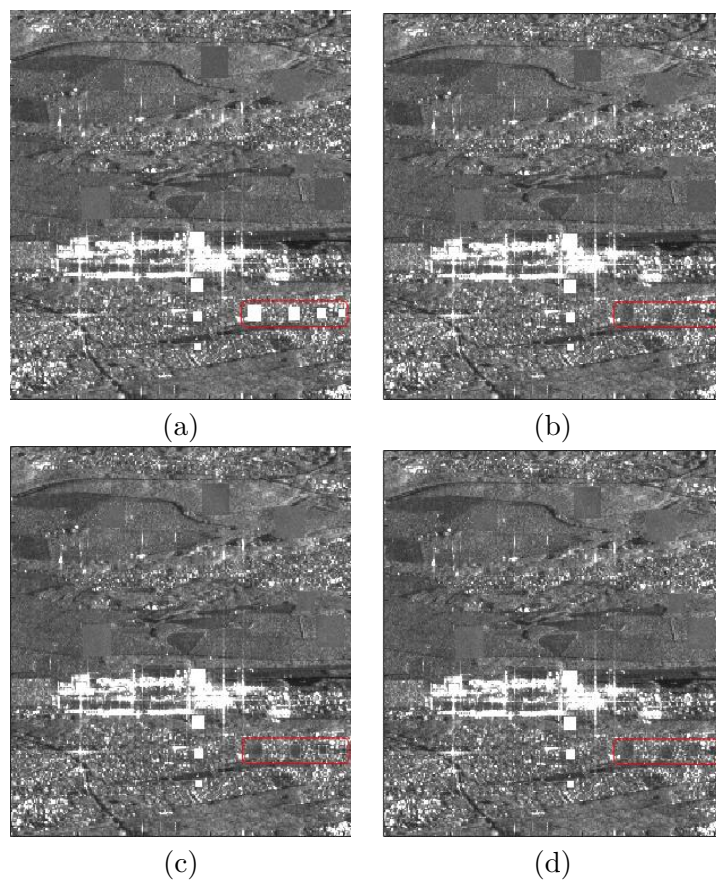


FIGURE 6.15: (a) Arithmetic mean image computed up to the previous image, (b) results of BWAM, (c) RABASAR-AM denoising results without join the AM, (d) RABASAR-BWAM denoising results. 128 simulated Sentinel-1 images are used, and there are different changed areas in the time series.

### 6.5.3 Updating strategy with a new image

This updating strategy is illustrated on multi-temporal simulated Sentinel-1 data, which is demonstrated in figure.3.15(b). Using RABASAR-AM approach, the arithmetic mean,  $u^{AM}$ , (Fig.6.15(a)) is calculated using the previous temporal images  $\{y_1, y_2, \dots, y_M\}$ . When a new image  $y_{M+1}$  arrives, the ratio of this image with  $R_{M+1} = y_{M+1}/u^{AM}$  may be directly calculated, and the estimated result after ratio image denoising can be computed  $\hat{u}_{M+1} = \hat{R}_{M+1}u^{AM}$ .

With RABASAR-BWAM method, taking the disappearing building (in the red rectangular area of Fig.6.15) as example, we could get two different kinds of BWAM for this building area based on Normalized Cut method [Shi and Malik, 2000, Su et al., 2015] and equation (6.9). For the surrounding stable areas, only one arithmetic mean is computed. When there is a new incoming image, we could use patch similarity test (Eq.(6.10)) to acquire the best BWAM (Fig.6.15(b)). Then, the RABASAR denoised results (Fig.6.15(d)) could be obtained.

When the new image is very large, using this approach could save plenty of time.

## 6.6 Conclusion

This chapter has proposed a ratio-based multi-temporal denoising framework. During the restoration of each SAR image, it exploits the temporal information through a super-image. The use of few kinds of super-images has been analyzed. RABASAR can provide better PSNR and MSSIM values when using a spatially denoised super-image. With the increase of the number of images in the time series, the differences of using different super-images decrease. When there are changes in the time series, using a binary weighted arithmetic mean can provide better results in the building areas. Based on the processing of simulated time-series, actual Sentinel-1 stacks and TerraSAR-X stacks, the qualitative and quantitative comparison with UTA, NLTF, MSAR-BM3D and 2SPPB methods showed the potential of RABASAR to better preserve structures in multi-temporal SAR images while efficiently removing speckle. Besides, the super-image can be easily updated when a new data becomes available so as to process new images on-line.

The proposed method can use other super-images such as geometric mean, quadratic mean, etc., without modifying the calculation procedure. The ratio image denoising method can be replaced by any other single-image speckle reduction method.

## Part III

# Multi-temporal images change detection

---



## Chapter 7

# Introduction to SAR and optical images change detection

Timely, accurately and continuously monitoring land cover and land use changes is important for land resource management. According to [Khorram, 1999], land cover changes can be classified into several categories :

- Changed from one land cover class to another
- Change of shape : expand, shrink or transform
- Change of position
- Fragment or merge adjacent regions

Based on the change reason or change type, changes can be classified into :

- Short term change (synoptic weather events)
- Cyclic change (seasonal phenology)
- Directional change (urban development)
- Multidirectional change (deforestation & regeneration)
- Event change (catastrophic fires)

We will pay more attention on building and farmland area changes, which are shown in figure 7.1-7.2.

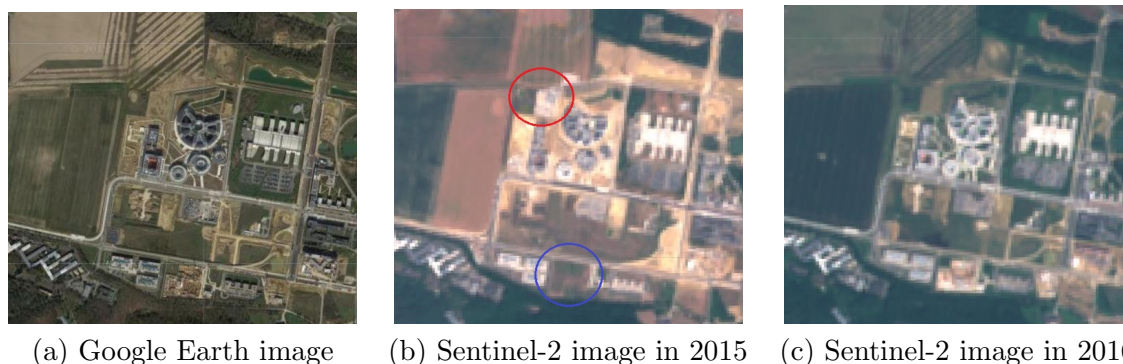


FIGURE 7.1: Farmland and building area changes over Saclay area, South of Paris. Red circle area : disappearing building, blue circle area : appearing building.

Changes happen spatially and temporally. More and more available multispectral, multitemporal, multisensor satellite data enhance the capability of detecting, identifying, mapping and monitoring these changes [Coppin et al., 2004, Habib et al., 2007].

Optical remote sensing images with high spatial and spectral resolutions can be easily acquired and have been widely used for land cover monitoring [Bruzzone and Bovolo, 2013]. The passive acquisition model of optical sensors and the use of near visible light wavelengths, sun illumination (or thermal radiation) and cloud free weather requirements heavily limit its wide application.

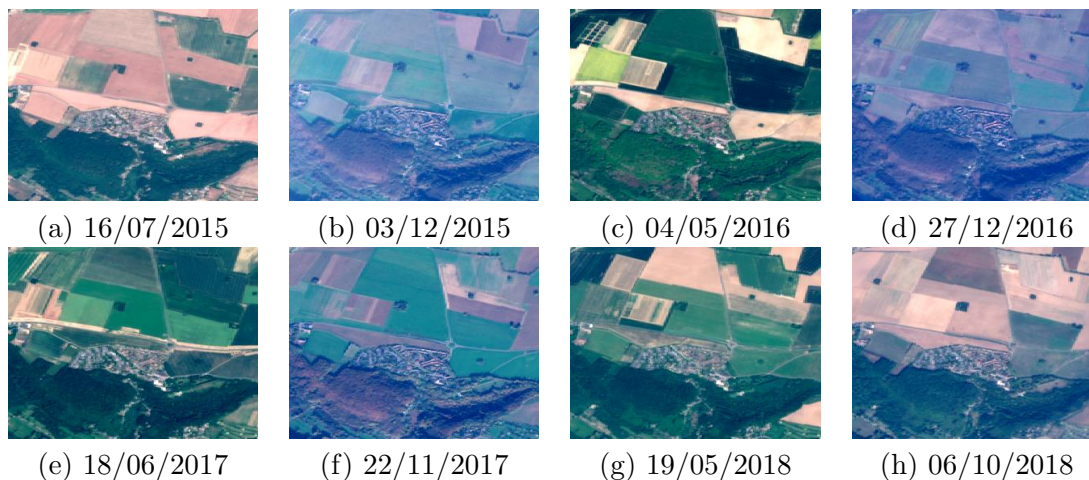


FIGURE 7.2: Farmland area and forest area changes. Sentinel-2 images are acquired over Saclay area, South of Paris. The acquisition time of Sentinel-2 images are shown below them.

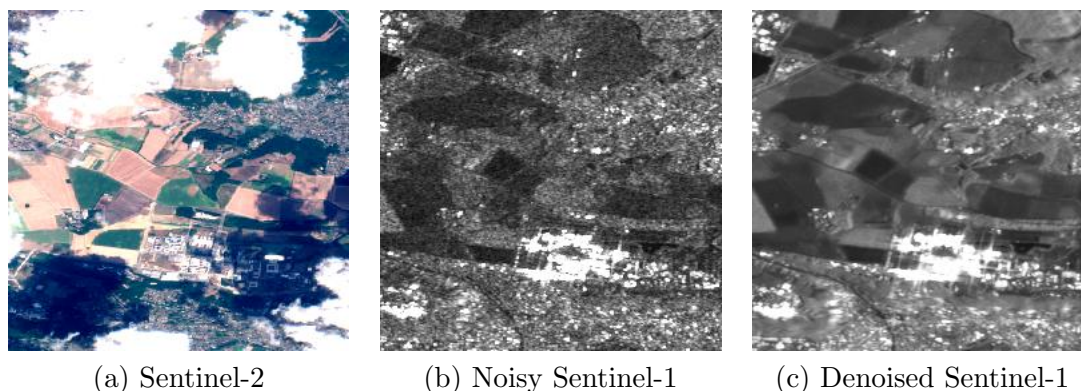


FIGURE 7.3: SAR and optical images comparison over cloudy weather. The images are acquired on 17/08/2018 over Saclay area, South of Paris. RABASAR-AM is utilized to provide the denoised Sentinel-1 GRD image.

SAR sensors are ideal to fulfill this task, because of their all-time and all-weather capabilities, with a very good accuracy of the acquisition geometry and without effects of atmospheric constituents for amplitude data (Fig.7.3). They have been widely used for environmental change detection, urban area change detection and disaster monitoring. The past few years have seen the launch of numerous synthetic aperture radar (SAR) sensors and new sensors will also be launched soon, such as TSX-NG, Cosmo-SkyMed second generation, Radarsat constellation and NISAR. The increasing availability of SAR data allows the high accuracy of change detection, such as abrupt (step) changes, seasonal

changes and longer-term developments. Some optical and SAR images acquired in cloudy weather are shown in figure 7.3.

In this chapter, we organize the change detection review into three categories according to the analyzed images : Optical, SAR and mutisensor images.

## 7.1 Optical remote sensing images change detection

Optical images play a major role in land resource and environment monitoring. Some of the operational optical Satellites are shown in figure 7.4. They have been widely used in land-cover change detection [Abuelgasim et al., 1999], forest change analysis [Huang et al., 2008], topographic map revision [Metternicht, 1999], environmental change detection [Eklund et al., 2000], urban disaster analysis [Tomowski et al., 2011] and urban land cover change analysis [Quarmby and Cushnie, 1989].

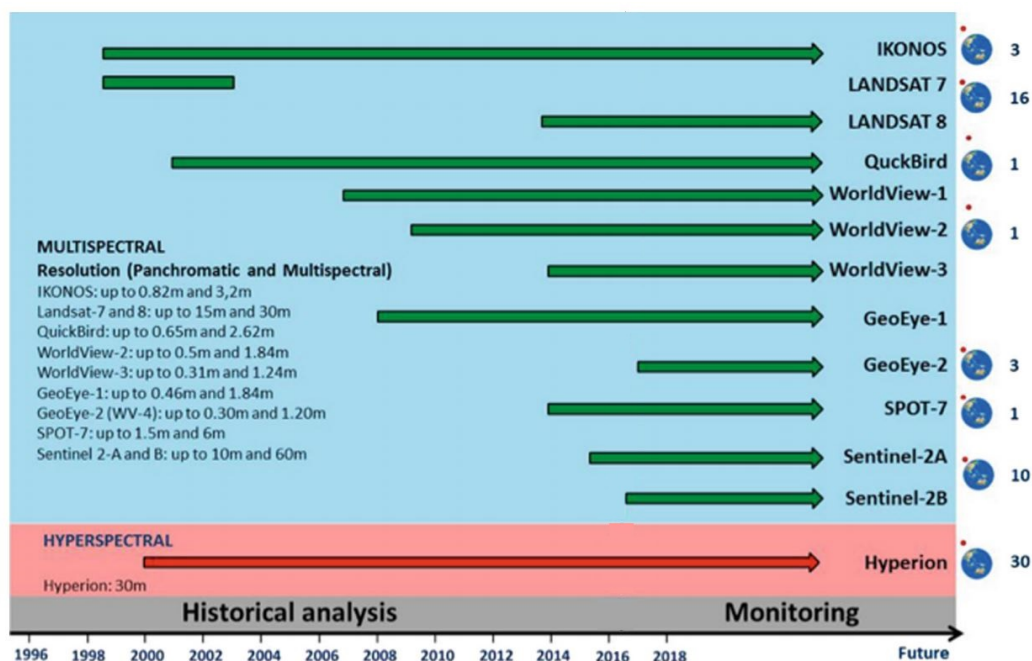


FIGURE 7.4: Some of the important operating optical Satellites [Casagli et al., 2017]

Optical images change detection can be classified in different ways, such as pixel based and object based methods, supervised and unsupervised techniques, image pair based and time series based approaches, etc. In detail, the change detection can be obtained through direct comparison, image transformation, classification, machine learning, GIS based comparison, spectral mixture analysis, direct object comparison, multitemporal object change analysis and data mining techniques [Hussain et al., 2013]. Normally, the choice of the change detection method does not just depend on the detection precision, it also relies on the used data and the application.

Here, we mainly pay attention to image pair change detection and time series change analysis. Most of these methods work at pixel level. The goal of change detection is to detect the important changes and omit unimportant changes. To precisely analyze object changes, the time series usually have to be well coregistered and radiometrically corrected.

Here after, we will list some popularly used optical image comparison operators. Some of the recently proposed deep learning change detection methods will be discussed later.

### 7.1.1 Comparison operators

The simplest way to obtain image changes is by computing pixel-wise differences. Based on the difference map, different post analyzing techniques can be applied.

There are many change detection algorithms [Hussain et al., 2013], such as post-classification change detection and object based change detection. Most of them are designed based on some of these basic comparison operators [Bruzzone, 2015], such as univariate image differencing, vegetation index differencing, change vector analysis, regression, principal component analysis, etc.

Usually, change detection algorithms always need a threshold to define the changed and unchanged areas. The detected changes are seriously affected by the choice of this threshold.

### 7.1.2 Deep learning based optical images change detection

Among the traditional optical image change detection methods, image transformation can provide more satisfying detection results because it linearly transforms multispectral images into higher feature space. However, both linear and nonlinear transformation features can be obtained using deep learning method. Deep learning methods can provide better change detection performance. Some of the related studies are shown in table.7.1.

In [Zhang et al., 2016a], the authors jointly used stacked restricted Boltzmann machine (RBM) and cosine angle distance to detect feature level changes. Changes are easier to be detected in the feature space. During the post-processing, they propose to use unsupervised fuzzy local information c-means to detect different change types. To acquire both binary and multiclass changes, [Lyu et al., 2016] proposed to learn a transferable change rule from a recurrent neural network for change detection. It provides the change information of multitemporal multispectral images using an improved Long Short-Term Memory (LSTM) model. To detect optical aerial image changes, [Zhan et al., 2017] designed a supervised deep Siamese Convolutional Neural Network (CNN). It used SZTAKI AirChange Benchmark Set<sup>1</sup> as training samples. Unlike the training in [Liu et al., 2016a], they take both changed and unchanged pixels into account with a weighted contrastive loss. With long time series remote sensing Satellite images, the object-based forest change detection task in [Khan et al., 2017a] is transferred into region classification problem. With pre-trained CNN architecture, it can predict onset and offset timings of the change regions. When processing long time series, this method may require an extreme computational load.

---

1. [http://web.eee.sztaki.hu/remotesensing/airchange\\_benchmark.html](http://web.eee.sztaki.hu/remotesensing/airchange_benchmark.html)

---

TABLE 7.1: Optical image change detection methods based on deep learning

	Training set	Used networks	Pro and con	Reference
1	Patch by patch	Stacked RBM	Unsupervised, postprocessing with cosine angle distance and unsupervised fuzzy local information c-means	[Zhang et al., 2016a]
2	Labeled binary ground truth and multiclass ground truth	Recurrent neural network (improved LSTM model)	Supervised, detect multiclass changes, some unchanged samples may be detected as changed samples.	[Lyu et al., 2016]
3	SZTAKI Air-Change Benchmark Set	Siamese CNN	Supervised, postprocessing with threshold segmentation and k-nearest neighbor approach	[Zhan et al., 2017]
4	Training the first 14 layers with ImageNet data set, thresholding difference image based on yearly multiresolution profile	CNN architecture (VGG-16 network)	Object level, need reconstructing the missing data and the residual cloudy regions (image inpainting with sparse encoding).	[Khan et al., 2017a]
5	Predetection results (change vector analysis, PCA and IR-MAD), joint classifier based on fuzzy c-means [Gong et al., 2016b]	GANs	Postprocessing with fuzzy local information c-means to generate difference image, no need to reconstruct the training data.	[Gong et al., 2017a]
6	ImageNet	Two stream CNN, conditional random field and part of VGG network	Provide change detection and localization, requires a very large labeled training set.	[Khan et al., 2017b]
7	Manually annotated samples	CNN, recurrent neural network and fully connected network	Binary and multiclass detection results, k-means algorithm is used to automatically select threshold.	[Mou et al., 2018]
8	Superpixel segmentation and classification	Stacked RBM and denoising autoencoders	Semisupervised classifier	[Gong et al., 2017c]

Unlike the aforementioned discriminative algorithms which classify input data, [Gong et al., 2017a] choose to combine CNN and generative adversarial networks (GANs) to detect bi-temporal multispectral image changes. The final change map is generated using unsupervised fuzzy local information c-means method. This new method is more effective and robust than those based on deep neural network, variational autoencoder, and even deep convolutional GAN. Because of the unstable training dynamics, GANs are more difficult to optimize.

In addition, [Khan et al., 2017b] designed a deep neural network based on directed acyclic graph topology. To strengthen the pixel labeling smoothness, it used a densely connected conditional random field. This method can predict image pair changes and their locations, even for unregistered image pairs. [Gong et al., 2017c] proposed to select the samples based on a superpixel segmentation and classification results. Based on deep belief networks (stacked RBM) and sparse denoising autoencoders, [Gong et al., 2017c] obtained hierarchical differences in the feature space. The training samples are selected

using Otsu thresholding algorithm [Otsu, 1979] based on a superpixel segmentation results. [Mou et al., 2018] proposed to use a recurrent convolutional neural network architecture to predict change types. It uses CNN to generate spectral-spatial features and uses recurrent neural network to analyze the temporal dependencies of features.

## 7.2 SAR images change detection

Unlike optical images, SAR images are seriously affected by speckle noise, which makes the SAR image change detection much harder. SAR images change detection can be applied on image pairs or multitemporal series. Different SAR image characteristics are used for change detection. In this chapter, we mainly consider SAR images acquired through the same orbit with similar incidence angles. The current change detection methods are mainly based on likelihood ratio [Lombardo and Pellizzeri, 2002, Su et al., 2015, Conradsen et al., 2003, 2016], coherence [Pulvirenti et al., 2016], image texture and structure analysis [Pham et al., 2016].

### 7.2.1 Ratio and log-ratio based change detection

Because of the multiplicative nature of speckle noise, a number of studies have applied to SAR data change detection methods based on mean-ratio [Touzi et al., 1988], image ratio [Oliver and Quegan, 2004a, Akbari et al., 2016], log-ratio operator [Bazi et al., 2005a, Bovolo and Bruzzone, 2005]. The true distribution of these ratio images depends on the relative change of the SAR reflectivities [Bovolo and Bruzzone, 2015]. These methods are easily applied and the associated threshold can be calculated automatically. Hereafter, we will introduce some hypothesis based change detection.

Due to the multiplicative noise influence of coherent SAR images, hypothesis test (such as likelihood ratio test) are often used [Kay, 1998, Radke et al., 2005]. In statistics, change detection can be considered as the comparison of two hypotheses  $H_0$  and  $H_1$ , which corresponds to the null and alternative hypothesis, respectively.

$$H_0 : u_1 = u_2 = u_{12} \text{ (no change)}$$

$$H_1 : u_1 \neq u_2 \text{ (change)}$$

The likelihood ratio test (LRT) is based on the likelihood ratio of observations  $y_1, y_2$ , which is defined as :

$$LRT(y_1, y_2) = \frac{P(y_1, y_2 | u_{12}, H_0)}{P(y_1 | u_1, H_1)P(y_2 | u_2, H_1)} \quad (7.1)$$

where  $u_1$  and  $u_2$  are the noise free intensity values corresponding to  $y_1$  and  $y_2$  with associated ENL  $L_1$  and  $L_2$ ,  $u_{12}$  is the noise free value when there is no change between the intensity values. Considering that  $L$  look intensity data follows a gamma distribution, we have :

$$P(y_1, y_2 | u_1, u_2, H_1) = \frac{1}{\Gamma(L_1)} \frac{1}{\Gamma(L_2)} \left(\frac{L_1}{u_1}\right)^{L_1} \left(\frac{L_2}{u_2}\right)^{L_2} y_1^{L_1-1} y_2^{L_2-1} \exp\left(-\frac{y_1 L_1}{u_1} - \frac{y_2 L_2}{u_2}\right) \quad (7.2)$$

and under the hypothesis  $H_0$ , with  $u_1 = u_2 = u_{12}$  we get :

$$P(y_1, y_2 | u_{12}, H_0) = \frac{1}{\Gamma(L_1)} \frac{1}{\Gamma(L_2)} \frac{L_1^{L_1} L_2^{L_2}}{u_{12}^{L_1+L_2}} y_1^{L_1-1} y_2^{L_2-1} \exp\left(-\frac{y_1 L_1 + y_2 L_2}{u_{12}}\right) \quad (7.3)$$

These joint probability density functions allow us to use the hypothesis testing framework describing their similarities.

### 7.2.1.1 Generalized likelihood ratio test (GLRT)

Since  $u_1$ ,  $u_2$  and  $u_{12}$  are not available, they can be replaced by their maximum likelihood estimations under  $H_0$  :

$$\hat{u}_1^{ML} = y_1 \quad (7.4)$$

$$\hat{u}_2^{ML} = y_2 \quad (7.5)$$

$$\hat{u}_{12}^{ML} = \frac{L_1 y_1 + L_2 y_2}{L_1 + L_2} \quad (7.6)$$

Then, the generalized likelihood ratio test (GLRT) is given by :

$$GLRT(y_1, y_2) = (L_1 + L_2)^{L_1 + L_2} \frac{y_1^{L_1} y_2^{L_2}}{(L_1 y_1 + L_2 y_2)^{L_1 + L_2}} \quad (7.7)$$

In addition,  $u_1$  and  $u_2$  can also be estimated using  $N_1$  and  $N_2$  i.i.d. gamma distribution random samples :

$$\hat{u}_1^{ML} = \frac{1}{N_1} \sum_{k_1} y_1(s + k_1) \quad (7.8)$$

$$\hat{u}_2^{ML} = \frac{1}{N_2} \sum_{k_2} y_2(s + k_2) \quad (7.9)$$

where  $y_1$  and  $y_2$  are different images,  $s$  is the coordinate in the image,  $k_1$  and  $k_2$  are the pixels location shifts around  $s$ . We can get the similarity comparison of two improved SAR intensity values, as proposed in [Lombardo and Oliver, 2001, Conradsen et al., 2003].

Based on the maximum likelihood estimation results (Eq.(7.4-7.6)), the logarithmic version of  $GLRT$  is given by [Su et al., 2014] :

$$S_{GLR}(y_1, y_2) = \log \left[ \frac{y_1}{\hat{u}_{12}^{ML}} \left( \frac{\hat{u}_1^{ML}}{\hat{u}_{12}^{ML}} \right)^{L_1 - 1} \exp \left( L_1 - \frac{L_1 y_1}{\hat{u}_{12}^{ML}} \right) \right]^{-1} + \log \left[ \frac{y_2}{\hat{u}_{12}^{ML}} \left( \frac{\hat{u}_2^{ML}}{\hat{u}_{12}^{ML}} \right)^{L_2 - 1} \exp \left( L_2 - \frac{L_2 y_2}{\hat{u}_{12}^{ML}} \right) \right]^{-1} = L_1 \log \frac{L_1 y_1 + L_2 y_2}{y_1 (L_1 + L_2)} + L_2 \log \frac{L_1 y_1 + L_2 y_2}{y_2 (L_1 + L_2)} \quad (7.10)$$

Suppose the corresponding pixels have the same ENL  $L_1 = L_2 = L$ , the simplified logarithmic version of  $GLRT$  method [Deledalle et al., 2009, Su et al., 2014] turns out to be :

$$S_{GLR}(y_1, y_2) = 2L \log \left( \sqrt{\frac{y_1}{y_2}} + \sqrt{\frac{y_2}{y_1}} \right) - 2L \log 2 \quad (7.11)$$

GLRT change criterion can be used in different ways [Lombardo and Pellizzeri, 2002, Su et al., 2015, Conradsen et al., 2003] which are discussed in the following sections.

### 7.2.1.2 Multitemporal GLRT

For multitemporal SAR images change detection, Lombardo and Pellizzeri [2002] proposed to use the ratio between the geometric and arithmetic means within the same segmentation area ( $L_1 = L_2 = L$ ). Based on the change and no change hypothesis of the time series, the multitemporal GLRT (MGLRT) is expressed as :

$$MGLRT = \frac{\sqrt[M]{\prod_{t=1}^M y_t L}}{\frac{1}{M} \sum_{t=1}^M (y_t L)} \quad (7.12)$$

The logarithmic version of  $MGLRT$  is given by :

$$LMGLRT = \frac{1}{M} \sum_{t=1}^M \ln(y_t L) - \ln\left(\frac{1}{M} \sum_{t=1}^M (y_t L)\right) \quad (7.13)$$

Except using SAR intensity values, Conradsen et al. [2003] also used hypothesis test to detect PolSAR data changes. When only taking single band SAR data into account, the equality GLRT (EGLRT) test boils down to :

$$EGLRT = \left\{ M^M \frac{\prod_{t=1}^M (y_t L)}{(\sum_{t=1}^M y_t L)^M} \right\}^L \quad (7.14)$$

The logarithmic version of  $EGLRT$  for temporal single polarization SAR test is given by :

$$LEGLRT = L \left\{ M \ln M + \sum_{t=1}^M \ln(y_t L) - M \ln\left(\sum_{t=1}^M y_t L\right) \right\} \quad (7.15)$$

where  $LEGLRT$  is  $LM$  times of  $LMGLRT$ .

In addition, MIMOSA [Quin et al., 2014] used the ratio of geometric and quadratic means of SAR amplitude data to detect the image pair and multitemporal SAR image changes. Instead of using multilooked values to calculate the change criterion, MIMOSA directly used the noisy pixels :

$$MIMOSA = \frac{\sqrt[M]{\prod_{t=1}^M A_t}}{\frac{1}{M} \sum_{t=1}^M A_t} \quad (7.16)$$

with  $M = 2$  being the image pair change detection case. The joint probability density function is calculated using Meijer function.

For these temporal generalized likelihood ratio test, the distribution of SAR images is taken into account and theoretical thresholds can be computed corresponding to specific false alarm rates. During the multitemporal SAR images change detection test, all the pixels are supposed to have the same ENL.

### 7.2.1.3 GLRT combining noisy and denoised values

Instead of only using the original SAR image information, Su et al. [2015] proposed AGLRT (approximation of GLRT) and CGLRT (combined GLRT) methods using the original SAR data, the denoised data and their corresponding ENL.

(1) AGLRT (approximate GLRT)

A joint way following [Su et al., 2015] is to simply replace the unknown  $u_1$ ,  $u_2$  and  $u_{12}$  by the multitemporal denoised values  $\hat{u}_1$ ,  $\hat{u}_2$  and  $\frac{\hat{u}_1 + \hat{u}_2}{2}$ . It does not take into account the ENL of the denoised data.

$$AGLRT(y_1, y_2) = \frac{P(y_1, y_2 | u_{12}, H_0)}{P(y_1, y_2 | \hat{u}_1, \hat{u}_2, H_1)} \quad (7.17)$$

$$AGLRT(y_1, y_2) = \left[ \frac{1}{4} \left( \frac{\hat{u}_2}{\hat{u}_1} + \frac{\hat{u}_1}{\hat{u}_2} + 2 \right) \right]^{-L} \exp \left[ L \left( \frac{y_1}{\hat{u}_1} + \frac{y_2}{\hat{u}_2} - \frac{2(y_1 + y_2)}{\hat{u}_1 + \hat{u}_2} \right) \right] \quad (7.18)$$

(2) CGLRT (combined GLRT)

In this approach, both the original and denoised data are taken into account in the likelihood probability of  $H_0$  and  $H_1$  as  $P(y_1, y_2, \hat{u}_1, \hat{u}_2 | H_0)$  and  $P(y_1, y_2, \hat{u}_1, \hat{u}_2 | H_1)$ .

The likelihood ratio test is given by :

$$CGLRT(y_1, y_2) = \frac{P(y_1, \hat{u}_1 | u_{12}, H_0) P(y_2, \hat{u}_2 | u_{12}, H_0)}{P(y_1, \hat{u}_1 | u_1, H_1) P(y_2, \hat{u}_2 | u_2, H_1)} \quad (7.19)$$

The maximum likelihood estimation of  $u_1$ ,  $u_2$ ,  $u_{12}$  are given as follows :

$$\hat{u}_1^{ML} = \frac{Ly_1 + \hat{L}_1 \hat{u}_1}{L + \hat{L}_1} \quad (7.20)$$

$$\hat{u}_2^{ML} = \frac{Ly_2 + \hat{L}_2 \hat{u}_2}{L + \hat{L}_2} \quad (7.21)$$

$$\hat{u}_{12}^{ML} = \frac{Ly_1 + Ly_2 + \hat{L}_1 \hat{u}_1 + \hat{L}_2 \hat{u}_2}{2L + \hat{L}_1 + \hat{L}_2} \quad (7.22)$$

where  $L$  is the ENL of noisy data,  $\hat{L}_1$  and  $\hat{L}_2$  are the ENL of the denoised value  $\hat{u}_1$  and  $\hat{u}_2$ , respectively.

In the case of gamma distribution with different number of looks, each probability term in  $CGLRT(y_1, y_2)$  equation can be approximated under conditional independence assumption.

Then, the change criterion boils down to :

$$CGLRT(y_1, y_2) = \left( \frac{Ly_1 + \hat{L}_1 \hat{u}_1}{L + \hat{L}_1} \right)^{L + \hat{L}_1} \left( \frac{Ly_2 + \hat{L}_2 \hat{u}_2}{L + \hat{L}_2} \right)^{L + \hat{L}_2} \left( \frac{2L + \hat{L}_1 + \hat{L}_2}{Ly_1 + Ly_2 + \hat{L}_1 \hat{u}_1 + \hat{L}_2 \hat{u}_2} \right)^{2L + \hat{L}_1 + \hat{L}_2} \quad (7.23)$$

CGLRT [Su et al., 2015] (GLRT extended to noisy and denoised data) takes into account the different ENL for each pixel, but the change detection threshold is difficult to compute. Moreover, Krylov et al. [2012] proposed to use Wilcoxon statistic in the likelihood ratio test for SAR image change detection.

All these hypothesis test methods take the noisy data into account. However, pixel based image ratio change detection techniques are affected by a large amount of false alarms and sensitive to image registration noise. Thanks to the convolutional neural networks [Chierchia et al., 2017a, Wang et al., 2017a] or state-of-the-art multitemporal denoising methods, we can acquire high signal-to-noise ratio (SNR) despeckled SAR images now. In addition, most of the change detection methods only provide a binary change mask. Current multitemporal change detection mainly deals with the temporal points where changes occur [Lobry et al., 2016b], and they pay less attention on the change type and change magnitude detection.

### 7.2.2 Coherent change detection

In the case of interferometric images, coherent change detection are popularly used. Instead of only using the mean backscattering power of a scene, coherent change detection takes both the amplitude and phase into account. Thus, it has the potential to detect subtle scene changes to the sub-resolution cell scattering structure that may be undetectable using incoherent change detection techniques [Preiss and Stacy, 2006].

The coherence is a measure of the degree of similarity in the interferometric image pair. With short interval acquired images, Corr and Rodrigues [1998] proposed to use the coherent information to detect large vehicle movements. Because of the sensitivity of phase to terrain displacement, Zebker [2000] used it to detect subsidence and deformations of Earth surface. To suppress the low coherence estimation effect, Cha et al. [2015] jointly use intensity and coherence information to pursue change detection. Pulvirenti et al. [2016] and Jung et al. [2016] used the cross-correlation of an interferometric SAR image pair to quantify changes within the SAR image pair.

However, the coherence between separate images is easily affected by some decorrelation sources, such as thermal noise, motion errors, processing errors, etc.[Bickel, 2014]. These corruption factors seriously limit the application of coherence based change detection methods.

### 7.2.3 Image texture and structure based change operator

Change detection can also be performed through analyzing image texture and structure. Dellinger et al. [2014] proposed to detect SAR image changes through detecting and matching building structures with SAR-SIFT method. Based on texture analysis, Pham et al. [2016] proposed a graph based change detection. In addition, information similarity measure of SAR images mainly process at feature level [Bovolo and Bruzzone, 2015]. Widely used statistical similarity measures are Kullback-Leibler distance [Inglada and Mercier, 2007], mutual information [Aiazzi et al., 2013], variational information, etc.

However, texture and structure based methods often fail to detect isolated changed buildings with low resolution single polarization SAR images. Most of these change detection methods mainly pay attention to a single kind of change type or changed object.

### 7.2.4 Deep learning based SAR images change detection

Over the past several years, deep learning techniques have been applied to SAR image processing. But they have mainly been used in some specific SAR image applications. We only review the studies in change detection area.

---

After obtaining the log-ratio of multitemporal images, [Liu et al., 2016b] proposed to use stacked RBM to classify the pixels in the ratio image into unchanged and changed types. To reduce the amount of parameters, the network only connects to a patch instead of the whole image. Without generating the difference image, [Zhao et al., 2014, Gong et al., 2016b] used pre-trained RBM to transfer the change detection to classification process. They computed training data with a fuzzy *c*-means algorithm. In addition, this method can process the image pairs which have different ENL. [Liao et al., 2017] used a similar method to pursue SAR images change detection. However, the training images are converted to integers which ruined the original statistic distributions of SAR images. With the change magnitude map prepared by Gabor wavelets and fuzzy *c*-means method, [Gao et al., 2016] used PCANet to classify the extracted features into changed and unchanged classes.

TABLE 7.2: SAR image change detection methods based on deep learning

	Training set	Used networks	Pro and con	Reference
1	Samples obtained by a level set method, generalized Kittler and Illingworth thresholding algorithm, fuzzy <i>c</i> -means, etc.	Stacked RBM	Unchanged and changed types, change detection based on log-ratio image	[Liu et al., 2016b]
2	Fuzzy <i>c</i> -means	Stacked RBM	Supervised, results suffer from the accumulation of classification errors	[Zhao et al., 2014, Gong et al., 2016b]
3	Gabor wavelets and fuzzy <i>c</i> -means based on log-ratio image	PCANet	Unsupervised	[Gao et al., 2016]
4	Log-ratio image classified by sparse autoencoder and fuzzy <i>c</i> -means	Sparse autoencoder, CNN	Acquiring unchanged, positive and negative changed labels	[Gong et al., 2017b]

Unlike the previous methods which detect the changed and unchanged pixels, [Gong et al., 2017b] proposed using ternary change detection method to detect the unchanged, positive and negative changed labels. The method combined sparse autoencoder, CNN and unsupervised clustering method.

Although deep learning method is very powerful to detect the changes, the detection performance highly relies on the training set precision.

### 7.2.5 Decision threshold

Most of the previous change detection methods only provide the similarity or dissimilarity of the temporal points. Based on the similarity or dissimilarity maps, we can visually determine which area has changed. To numerically distinguish the changed areas from the unchanged regions, a threshold has to be chosen. Usually, the chosen threshold depends on the specific applications. There are lots of threshold definition approaches to segment the similarity map into binary image [Sahoo et al., 1988, Sezgin and Sankur, 2004]. Hereafter, we list some popularly used SAR images change detection threshold definition methods (Tab.7.3). We mainly use the approximate cumulative distribution function of change criterion to obtain the threshold in the next two chapters.

TABLE 7.3: Threshold definition methods

	Methods	Reference
1	Empirical strategies	[Tung and LeDrew, 1988]
2	Quantile method	[Kervrann and Boulanger, 2006]
3	Bayesian selective thresholding method	[Bruzzone and Prieto, 2000]
4	Cumulative distribution function of change criterion	[Quin et al., 2014]
5	Approximate cumulative distribution function of change criterion	[Conradsen et al., 2003]
6	Fuzzy clustering method	[Gong et al., 2012]
7	Kittler-Illingworth (KI) threshold selection criterion	[Bazi et al., 2005b]

### 7.2.6 Change detection performance evaluation

Usually, we can evaluate the detection results visually and quantitatively. Visually evaluating the change detection results is always the first and simplest way to evaluate the change detection results. It can directly provide the distribution and the shapes of changed areas and it allows us to link the results with the performance of used algorithms. As introduced in [Berger et al., 2000, Radke et al., 2005], we can check the results through displaying the registered images in a video with seconds interval.

If a ground truth map is available, the true positive (TP), false positive (FP), true negative (TN) and false negative (FN) can be used to quantitatively evaluate the change detection performance (Tab.7.4). Receiver operating characteristic (ROC) is often used to display the detection performance with different false positive rate and true positive rate. Since it can not illustrate which area or which kind of changes is well detected, visual evaluation is still needed [Radke et al., 2005].

TABLE 7.4: Quantitative change detection evaluation methods

	Methods	Reference
1	Percentage of correct classification, Jaccard coefficient and Yule coefficient	[Rosin and Ioannidis, 2003]
2	Receiver operating characteristic (ROC) curve of true positive rate and false positive rate	[Quin et al., 2014]
3	Test simulated SAR data with accurate ground truth map	[Cui, 2014]

## 7.3 Multisensor images change detection

Compared to homogeneous images change detection, heterogeneous images change detection is much more challenging. Different sensors provide different descriptions on the same ground truth, while the same sensor even reflects different information of the same object with different acquisition geometry and time. However, this different information can reflect different physical properties of same ground objects, which makes the image fusion an important research topic. Some of the differences between optical and SAR images are shown in table 7.5. Some images are illustrated in figure 7.5.

TABLE 7.5: Some important differences of SAR and optical remote sensing images

	Wavelengths	Band	Sensing time	Looking angle
Optical image	Near visible light	Multiband	Day time	Nadir
SAR image	1 cm to 1 m	Polarimetry, phase and amplitude	All day and night	Side-looking

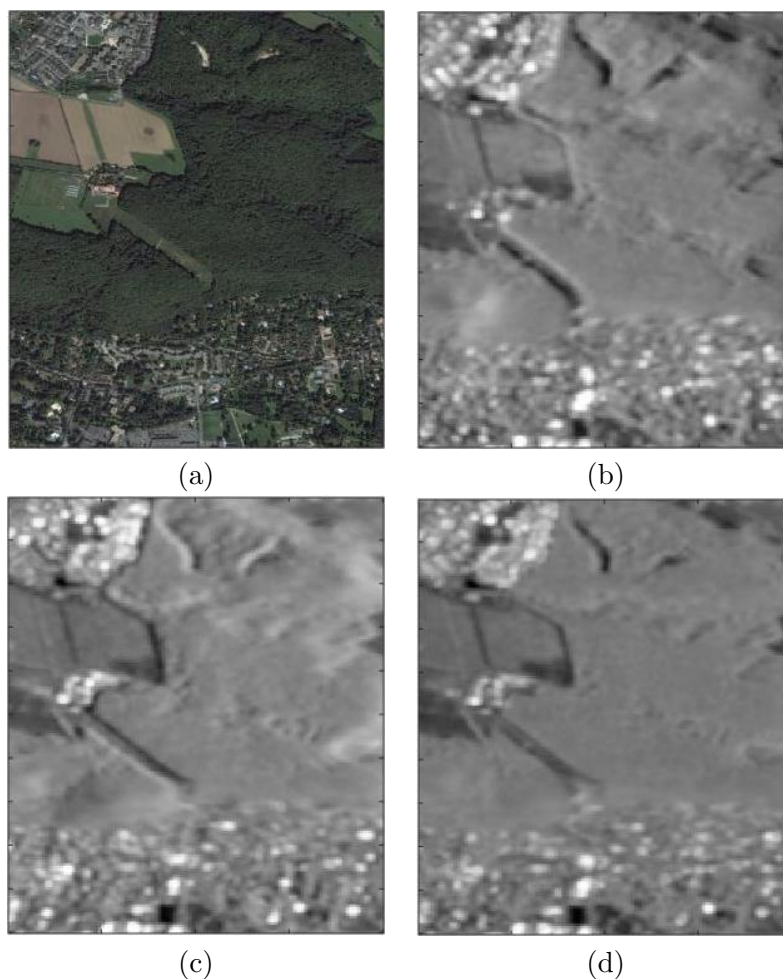


FIGURE 7.5: Images of different sensor and different acquisitions over Sacaly area, South of Paris. Only the geocoded IW VV polarization Sentinel-1 GRD SAR images (25/12/2014-01/04/2018) are used for the arithmetic mean image computation. (a) Google Earth image, (b, c, d) SAR time series arithmetic mean images calculated using : ascending data, descending data, ascending and descending data.

With complementary properties of optical and SAR images, jointly using them to monitor land and environment changes is significant, especially when one of them is not available in the time series analysis [Hussain et al., 2013] or in emergency situations [Touati and Mignotte, 2018]. Due to the different image attributes, only few works deal with mul-

tisensor images change detection [Brunner et al., 2010, Longbotham et al., 2012, Prendes et al., 2015, Volpi et al., 2015].

Different fusion technologies have to be applied during the joint use of multisensor data, such as resampling to the same spatial or spectral resolution. Classification-based change detection methods [Liu et al., 2014] can be utilized to transfer the different information attributes to the same domain. Copula theory [Mercier et al., 2008], mixture distributions similarity test [Prendes et al., 2015], Bayesian nonparametric model coupled with a Markov random field [Prendes et al., 2016] and automated kernel canonical correlation analysis [Volpi et al., 2015] are also used to detect changes of multisensor images.

With deep learning methods, the statistical differences between SAR and optical images can be learned automatically. Some of the state-of-the-art deep learning based multisensor change detection methods are listed in table 7.6.

TABLE 7.6: Heterogeneous images change detection methods based on deep learning

	Training set	Used networks	Pro and con	Reference
1	Selected manually or by available algorithms (object-based change detection method)	Stacked denoising autoencoders with mapping-based feature change analysis	Semi-supervised	[Zhang et al., 2016b]
2	Select unchanged pixels with a symmetric convolutional coupling network and user defined weighting parameter $\lambda$	Symmetric convolutional coupling network (CNN+stacked denoising autoencoders)	User-defined weighting parameter $\lambda$ affects the unchanged samples, needs predenoising step	[Liu et al., 2016a]
3	Select unchanged samples using iterative coupled dictionary learning framework	Iterative coupled dictionary learning model (CNN)	Fuzzy local information c-means is used to generate binary change maps	[Gong et al., 2016a]
4	Fuzzy c-means algorithm	Stacked denoising autoencoders, stacked mapping network	Sample selection is not accurate, postclassification with fuzzy c-means algorithm	[Su et al., 2017]
5	Approximately symmetric deep RBM	Approximately symmetrical deep neural network	Unsupervised, postprocessing with fuzzy c-means algorithm to get binary change maps	[Zhao et al., 2017]

To monitor the changes between multi-resolution and multisensor (SAR/optical) image pairs, [Zhang et al., 2016b] combined stacked denoising autoencoders and mapping-based feature change analysis method. However, that method is not completely unsupervised because the training samples are selected manually or by available algorithms from the coarse difference image. [Liu et al., 2016a] also applied stacked denoising autoencoders to reconstruct the feature maps in the visible layers which are corrupted by gamma and Gaussian distribution noise. They used a new objective function to constrain the updating of the network parameters. Based on a symmetric convolutional coupling network, it provides good change detection results with heterogeneous or homogeneous images. The training samples are selected with a user defined weighting parameter in the network. However, this method only considers the unchanged pixels and it ignores the influence of changed areas which leads to poor detection of some changed positions. [Gong et al., 2016a] proposed using an iterative coupled dictionary learning model to detect multisource image changes. Their differences are calculated in a high-dimension common feature space. Only the un-

---

changed samples which are selected using iterative coupled dictionary learning are used for the network training. Unlike traditional methods which pay more attention to image pair similarity properties, [Su et al., 2017] used three kinds of inner features differences. After acquiring the features using stacked denoising autoencoders, feature differences are used as the initial training samples. Then, the stacked mapping network is used to establish the relationship between the features of each class. The final ternary map is acquired by clustering the differences between the original features and the mapping features.

Instead of reconstructing the image features similarly to [Liu et al., 2016a], [Zhao et al., 2017] proposed using an approximately symmetric deep RBM to transfer the heterogeneous images into the same feature space and obtain two kinds of labels. To reduce the training samples and ensure the accuracy of the results, it used a user defined coefficient parameter.

## 7.4 Conclusion

We briefly presented some state-of-the-art change detection methods. The methods are categorized according to the processing data types, such as optical, SAR and heterogeneous images.

For SAR images change detection, some popularly used threshold definition methods and change evaluation methods are also summarized. Due to the multiplicative noise in coherent SAR images, likelihood ratio test is popularly used for change detection. To avoid the negative influence of noisy data, we will present an improved GLRT method using only denoised data in the next chapters. Moreover, the change magnitude and time series change classes will be studied.

Most of the deep learning based change detection methods have transferred the change detection to a classification task, which separates changed and unchanged results. However, classification based methods always suffer from the accumulation of classification errors. In addition, during the sample selection, the change magnitude will be omitted. Although well studied, the change criterion based methods always require significant preprocessing and have difficulties with applications that require high accuracy and flexibility [Liao et al., 2017]. With deep neural networks, the differences are mainly calculated in the feature space. With fully connected layers, deep belief networks and multilayer perceptron will be limited by a large amount of learnable parameters. The network may be hard to optimize with limited training samples [Mou et al., 2018]. For some of the methods, the network needs to be retrained for each image pair.

The aforementioned change detection methods mainly process remote sensing images. There are many other kinds of image change detection methods, such as medical image segmentation [Wang et al., 2017b] or classification methods, video change detection, etc.

---



---

## Chapter 8

# Multitemporal SAR data change analysis based on simplified GLR

Taking into account the aforementioned issues, this section proposes a simplified generalized likelihood ratio ( $S_{GLR}$ ) method assuming that corresponding temporal pixels have the same ENL. Thanks to the denoised data provided by RABASAR [Zhao et al., 2018], we successfully applied this similarity test approach to compute the change areas, with change magnitude and change type detection. A new change magnitude index method and an improved spectral clustering based change classification method are developed. The effectiveness of the proposed methods is demonstrated through the processing of simulated and SAR images, and the comparison with classical methods. In particular, numerical experiments proved that the developed method has good performances in detecting farmland and building area changes, container changes and cargo ship appearance.

### 8.1 Simplified GLR based change detection

In this section, we derive a generalized log-likelihood ratio criterion based on gamma distribution using denoised data. Based on the obtained similarity functions, strategies to apply this similarity criterion to image pair change detection, cumulative change detection and change classification are introduced.

#### 8.1.1 Similarity test with simplified GLR

Under Goodman's hypothesis [Goodman, 1976], the intensity distribution under a fully developed speckle follows a gamma distribution. To compare the similarity of two gamma distributed variables  $(y_t, y_{t'})$ , a log-likelihood ratio test can be used (Eq.(7.10)). Speckle is an inherent problem for SAR image interpretation which brings much drawbacks for traditional SAR image change detection methods. We propose to exploit the denoising framework proposed in chapter 6. When dealing with denoised images  $\hat{u}_t$  and  $\hat{u}_{t'}$ , with associated ENL  $L_t$  and  $L_{t'}$ , we have :

$$S_{GLR}(\hat{u}_t, \hat{u}_{t'}) = L_t \log \frac{L_t \hat{u}_t + L_{t'} \hat{u}_{t'}}{\hat{u}_t (L_t + L_{t'})} + L_{t'} \log \frac{L_t \hat{u}_t + L_{t'} \hat{u}_{t'}}{\hat{u}_{t'} (L_t + L_{t'})} \quad (8.1)$$

Unlike *CGLRT* and *AGLRT* methods [Su et al., 2015], we fully trust the denoising results and do not take the noisy data into account any more. In practise, we directly calculate the similarity of the multilooked SAR data with the use of their corresponding ENL.

---

Suppose the corresponding pixels in despeckling images have the same ENL  $L_t = L_{t'} = \hat{L}$ , the simplified GLR method [Deledalle et al., 2009, Su et al., 2014] turns out to be :

$$S_{GLR}(\hat{u}_t, \hat{u}_{t'}) = 2\hat{L} \log \left( \sqrt{\frac{\hat{u}_t}{\hat{u}_{t'}}} + \sqrt{\frac{\hat{u}_{t'}}{\hat{u}_t}} \right) - 2\hat{L} \log 2 \quad (8.2)$$

where  $\hat{u}$  is the estimated reflectivity,  $t$  represents the time index in the time series.

ENL is an important parameter in statistical modeling of multilooked SAR images. Different ENL could reflect the temporal changes of the scene, it may represent different estimated reflectivities. Due to the homogeneous distribution, the ENL in farmland areas are always larger than in building areas. When setting the pixels in the whole image have the same ENL, using larger  $\hat{L}(s)$  will cause the increase of  $S_{GLR}(\hat{u}_t(s), \hat{u}_{t'}(s))$ . Thus, using larger ENL, which is similar to the ENL of farmland area and larger than that in building area, will suppress the changes in farmland areas. This similarity method will be used to detect changes between different images.

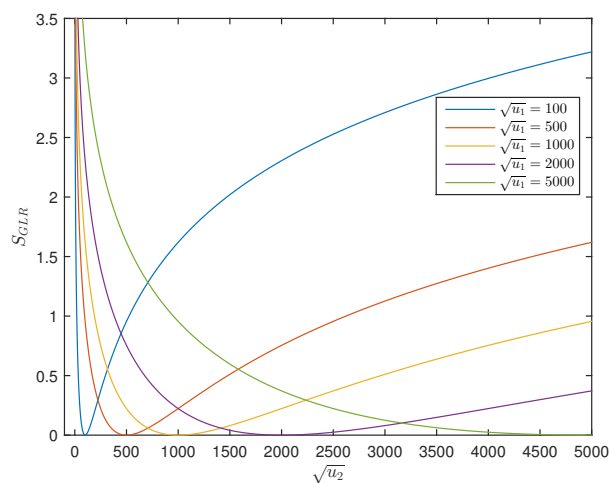


FIGURE 8.1:  $S_{GLR}$  value changes with different  $u_1$  and  $u_2$  values.

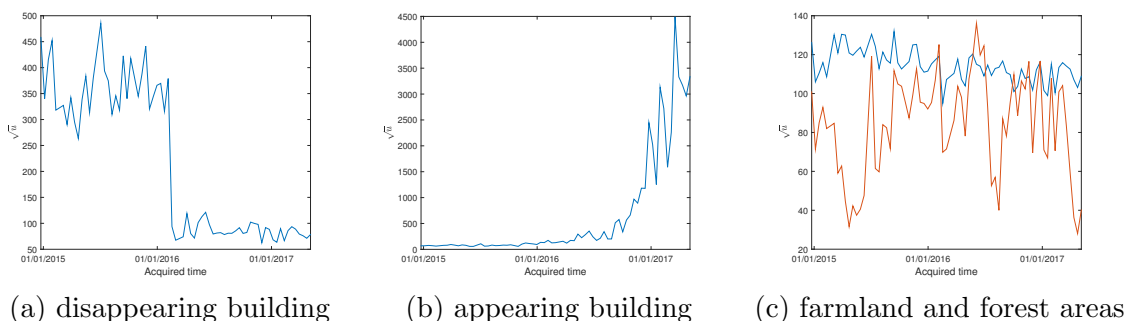


FIGURE 8.2: Amplitude backscattering value changes of different areas. 69 well registered Sentinel-1 images are used. Sentinel-1 images are acquired over Saclay area, South of Paris. The acquisition times of these images are from 24/12/2014 to 18/01/2017.

To analyze the relationship between  $S_{GLR}$  and the change of corresponding estimated

reflectivities, we choose several typical values of  $u_t$  and  $u_{t'}$  (Fig.8.1) according to four kinds of changes in Sentinel-1 time series (Fig.8.2). As we can see from figure 8.1,  $S_{GLR}$  mainly relies on the ratio of compared points and it can suppress the large values. Thus, the proposed  $S_{GLR}$  algorithm can enlarge the changes between different land covers and suppress the float of high backscattering values in building areas. Specifically, the changes between vegetation and building areas or the farmland area seasonal changes are enlarged. In addition, small changes of the Satellite acquisition geometry may lead to large change of the building area backscattering values, which are suppressed by the similarity algorithm.

In practise, other similarity criteria, like popular kernel methods [Ben Salah et al., 2011], can be used as well.

### 8.1.2 Changed area detection

During the acquisition of temporal SAR images, changes could not be avoided. Due to the spatial varying ENL (the width of pdf), the similarities calculated using both vegetation area values and building area values have a large value range. This large similarity value range will lead to large overlapping areas. Using Monte Carlo method to acquire the threshold, it is very hard to reject the null hypothesis for specific objects. Vegetation area and changed building area have obviously different backscattering values, a weighted similarity is recommended when the user is only interested in building changes.

Defining a global threshold is a simple and widely used approach to distinguish changed from unchanged points. To detect the changed areas, we used a thresholding function :

$$\varphi[S_{GLR}(\hat{u}_t, \hat{u}_{t'})] = \begin{cases} 1, & \text{if } S_{GLR}(\hat{u}_t, \hat{u}_{t'}) \geq \tau \\ 0, & \text{otherwise} \end{cases} \quad (8.3)$$

Here are three threshold definition methods which are under the same no change hypothesis framework that can be used for this method :

- The threshold can be defined according to the desired false positive under the no change hypothesis [Lombardo and Oliver, 2001]. This method uses the asymptotic way to acquire the false alarm probability.
- As introduced in section 8.1.1, the temporal values are supposed to have the same ENL. Theoretically, we can simulate pure speckle values to calculate the threshold and use spatial adaptive threshold to define the changes. In practise, we could use a quantile method [Kervrann and Boulanger, 2006, Su et al., 2015] to define the threshold based on the denoising of simulated SAR images without change. And a look-up table for the thresholds could be prepared in advance, so as to speed up the process.
- In addition, as introduced by Wilks [1938], when the sample size approaches infinity, the log-likelihood statistic model asymptotically converges towards chi-squared distributed probability under the null hypothesis. Thus, we can use chi-square cumulative function to estimate the change probability of  $S_{GLR}(\hat{u}_t, \hat{u}_{t'})$  with :

$$\rho = 1 - \frac{1}{4\hat{L}} \quad (8.4)$$

$$\omega_2 = -\frac{1}{4}\left(1 - \frac{1}{\rho}\right)^2 \quad (8.5)$$

$$P\{2\rho S_{GLR}(\hat{u}_t, \hat{u}_{t'}) \leq \delta\} \simeq P\{\chi^2(1) \leq \delta\} + \omega_2[P\{\chi^2(5) \leq \delta\} - P\{\chi^2(1) \leq \delta\}] \quad (8.6)$$

where  $\delta$  is the statistical significance. For the detailed derivation of this probability calculation method, we recommend to refer to [Anderson and Mathématicien, 1958, Conradsen

et al., 2003]. Unlike Conradsen's PolSAR change detection analysis, we mainly pay attention to spatially adaptive denoised single channel SAR images with the same estimated ENL. In the following sections, we mainly use this way to define the threshold.

### 8.1.3 Change magnitude index for visualization

To distinguish appearing from disappearing changes, we used a signum function  $\text{sign}(x)$  to convert  $S_{GLR}(\hat{u}_t, \hat{u}_{t'})$  to positive and negative values. In this case, if we set the image acquired at time  $t$  as the reference image, the positive and negative values correspond to the increase and decrease of the object backscattering values.

$$\text{sign}(x) \begin{cases} -1 & \text{if } x < 0 \\ 0 & \text{if } x = 0 \\ 1 & \text{if } x > 0 \end{cases} \quad (8.7)$$

$$x = \log \left( \sqrt{\frac{\hat{u}_{t'}}{\hat{u}_t}} \right) \quad (8.8)$$

To clearly illustrate the temporal changes, the similarity ratio are normalized and transformed to values within range  $[0, 255]$ .

$$S_{GLR}^{conv}(\hat{u}_t, \hat{u}_{t'}) = \begin{cases} 255, & \text{if } \frac{2(S_{GLR}(\hat{u}_t, \hat{u}_{t'}) - \alpha_1)}{\alpha_2 - \alpha_1} \geq 2 \\ 127 \frac{2(S_{GLR}(\hat{u}_t, \hat{u}_{t'}) - \alpha_1)}{\alpha_2 - \alpha_1} + 1, & \text{otherwise} \end{cases} \quad (8.9)$$

where  $\alpha_1$  and  $\alpha_2$  represent the minimum and maximum in the temporal dissimilarities  $S_{GLR}(\hat{u}_t, \hat{u}_{t'})$ . To suppress the outliers, we empirically set  $\alpha_1 = -2$  and  $\alpha_2 = 2$ . The value range will be converted to  $[-255, 255]$  by multiplying  $S_{GLR}^{conv}(\hat{u}_t, \hat{u}_{t'})$  with  $\text{sign}(x)$ . The rainbow index color is used to represent different change magnitudes (appearing, disappearing and slow changes).

In practise, we can arbitrarily combine the reference and slave image through RGB composition (R : slave image, G : reference image, B : slave image). Although different colors could indicate the increase and decrease of backscattering values, the illustration performance is not as good as aforementioned strategy.

### 8.1.4 Multitemporal SAR images change classification

During the time series acquisition, changes may occur at multiple times and with different magnitudes. To detect the change types, we propose an improved change classification method inspired by NORCAMA method [Su et al., 2015] and spectral clustering method [Shi and Malik, 2000, Ng et al., 2002]. In practise, the change types are transferred into a partitioning problem and detected using spectral clustering.

#### 8.1.4.1 Change Criterion Matrix (CCM)

Through making use of the eigenvalues of the similarity matrix of the data, spectral clustering techniques perform dimensionality reduction before clustering in fewer dimensions. It has been successfully used to cluster the temporal pixels based on their similarity symmetric matrix [Ng et al., 2002]. Given a time series  $\{\hat{u}_1, \hat{u}_2 \cdots \hat{u}_M\}$ , the affinity matrix

is defined as a symmetric matrix  $A(s)$ , with elements  $S(\hat{u}_t, \hat{u}_{t'})$  representing the change criterion between different data points.

$$A(s) = \begin{bmatrix} S(\hat{u}_1, \hat{u}_1) & S(\hat{u}_1, \hat{u}_2) & S(\hat{u}_1, \hat{u}_3) & \dots & S(\hat{u}_1, \hat{u}_{t'}) \\ S(\hat{u}_2, \hat{u}_1) & S(\hat{u}_2, \hat{u}_2) & S(\hat{u}_2, \hat{u}_3) & \dots & S(\hat{u}_2, \hat{u}_{t'}) \\ \vdots & \vdots & \vdots & \ddots & \vdots \\ S(\hat{u}_t, \hat{u}_1) & S(\hat{u}_t, \hat{u}_2) & S(\hat{u}_t, \hat{u}_3) & \dots & S(\hat{u}_t, \hat{u}_M) \end{bmatrix} \quad (8.10)$$

where  $A(s)$  is a symmetric change criterion matrix with size  $M \times M$ ,  $s$  is the location in one image,  $t$  and  $t'$  are time index with  $1 \leq t \leq M$  and  $1 \leq t' \leq M$ .

To avoid the overlapping of different clusters, Xin *et al.* [Su et al., 2015] proposed to binarize the change criterion matrix  $A(s)$ . The binary process can tight the clusters, but it will force the clustering results seriously depending on the used thresholds. In practise, we use binarized change criterion matrix. In addition,  $k$ -nearest neighbors algorithm could be used to classify this change criterion matrix as well. To suppress the temporal variance caused by the residual speckle, we can apply the exponentially weighted moving average [Schubert et al., 2014] to the time series.

#### 8.1.4.2 Clustering by spectral clustering method

Based on the acquired change criterion matrix, the Laplacian matrix  $A^L(s)$  is computed by :

$$A^L(s) = D(s) - A(s) \quad (8.11)$$

$$D(s) = \begin{bmatrix} \sum S(\hat{u}_1, \hat{u}_{t'}) & 0 & \dots & 0 \\ 0 & \sum S(\hat{u}_2, \hat{u}_{t'}) & \dots & 0 \\ \vdots & \vdots & \ddots & \vdots \\ 0 & 0 & \dots & \sum S(\hat{u}_t, \hat{u}_{t'}) \end{bmatrix} \quad (8.12)$$

$$\sum S(\hat{u}_t, \hat{u}_t) = \sum_{t'=1}^M S(\hat{u}_t, \hat{u}_{t'}) \quad (8.13)$$

The former steps (Eq.(8.10)~(8.13)) are the same as NORCAMA [Su et al., 2015] except the similarity calculation. Then, the Laplacian matrix  $A^L(s)$  is normalized using :

$$A_{norm}^L = D^{-1/2} A^L D^{-1/2} \quad (8.14)$$

The eigenvalues  $\lambda$  are computed through :

$$A_{norm}^L V = \lambda V \quad (8.15)$$

where  $V$  is the eigenvector. After sorting the acquired eigenvalues  $\{\lambda_1, \lambda_2, \dots, \lambda_M\}$  in ascending order, the clustering number  $k$  is calculated using the eigengap heuristic method [Von Luxburg, 2007] :

$$k = \arg \max_{1 \leq t < M} (\lambda_{t+1} - \lambda_t) \quad (8.16)$$

To reduce the data dimension, only the eigenvectors  $\vec{v}_i$  ( $M \times 1$  column vector) which correspond to the  $k$  largest eigenvalues of  $L^{norm}$  are used with  $U = [\vec{v}_1, \vec{v}_2 \dots \vec{v}_k]$ . To obtain the unit norm, we re-normalize the matrix rows. Finally, the  $k$ -means method is used to

cluster each row  $u_t$  in  $U$  and the cluster labels  $\{l_1, l_2, \dots, l_M\}$  are assigned to each cluster element with  $1 \leq l_t \leq k$ .

The aforementioned method is similar to the normalized cut method [Shi and Malik, 2000, Su et al., 2015]. However, they normalize the rows of  $A(s)$  to sum to 1 and use its eigenvectors instead of the normalized Laplacian matrix  $A^L(s)$  calculated using equation (8.14). In addition, they do not re-normalize the rows of  $U$  to unit length [Ng et al., 2002].

### 8.1.4.3 Change type recognition

Based on the number of clusters  $k$  and cluster labels  $\{l_1, l_2, \dots, l_M\}$  acquired by the  $k$ -means algorithm, the change type of the time series points can be recognized [Su et al., 2015] according to table 8.1.

TABLE 8.1: Label of different change types

Classes	Types	$k$	Label series $\{l_1, l_2, \dots, l_M\}$
1	Unchanged	1	1, 1, ...1
2	Step	2	1, 1, ...1, 2, 2, ...2
3	Impulse	2	1, 1, ...1, 2, 2, ...2, 1, 1, ...1
4	Cycle	2	1, ...1, 2, ...2, 1, ...1, 2, ...2, ...
5	Complex	$\geq 3$	1, 1, ..., 2, 2..., 3, 3...4, 4...

---

#### Algorithm 2 Algorithm for change classification

---

**Input :** Well registered multitemporal denoised SAR images

**Output :** Change classification map

- 1: **for** time series  $\{\hat{u}_1, \hat{u}_2 \dots \hat{u}_M\}$  in each location  $s$  **do**
  - 2: Form the change criterion matrix  $A \in R^{M \times M}$  with Eq.(8.10)
  - 3: Compute the normalized Laplacian matrix with :
 
$$D_{tt'} = \sum_{t'=1}^M S(\hat{u}_t, \hat{u}_{t'})$$

$$A^L = D - A$$

$$A_{norm}^L = D^{-1/2} A^L D^{-1/2}$$
  - 4: Calculate the eigenvalues  $\lambda$  and eigenvectors  $V$  of  $A_{norm}^L$ .
  - 5: Find the number of clusters using eigengap heuristic method.
  - 6: Reduce the data dimensions through only using the first  $k$  eigenvectors  $U = [\vec{v}_1, \vec{v}_2 \dots \vec{v}_k]$ , then normalize each row of  $U$ .
  - 7: Treat each row of  $U^{norm}$  as a point, cluster them into  $k$  clusters with  $k$ -means method.
  - 8: Recognize the change types based on the assigned labels.
  - 9: **end for**
  - 10: **return** Change classification map
- 

## 8.2 Experimental results and discussion

To illustrate and compare the proposed methods with state-of-the-art change detection methods, simulated SAR images and SAR images are tested in this section. All the data are

---

despeckled by RABASAR before change analysis : image pair change detection in section 8.2.1, continuous change monitoring in section 8.2.2 and change classification experiments in section 8.2.3. Numerical comparison and evaluation mainly pay attention to the false positive and true positive values, while visual comparison pay more attention to different changed objects detection, change type detection, changed area shape preservation and wrongly detected points distribution.

### 8.2.1 Image pair change detection

To evaluate the change detection performances and validate the effectiveness of  $S_{GLR}$  method, the image pair change detection results are compared with Conradsen's method [Conradsen et al., 2003, 2016] and  $CGLRT$  method [Su et al., 2015].

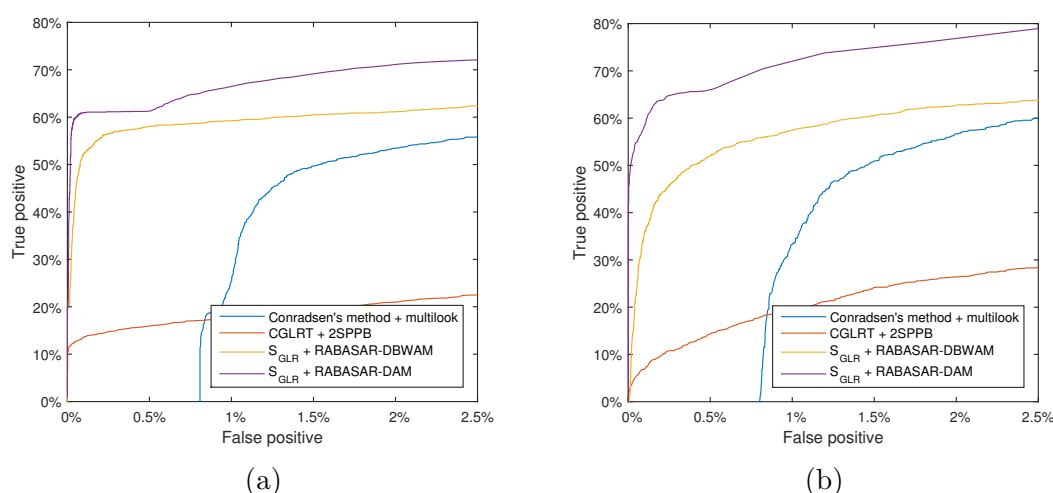


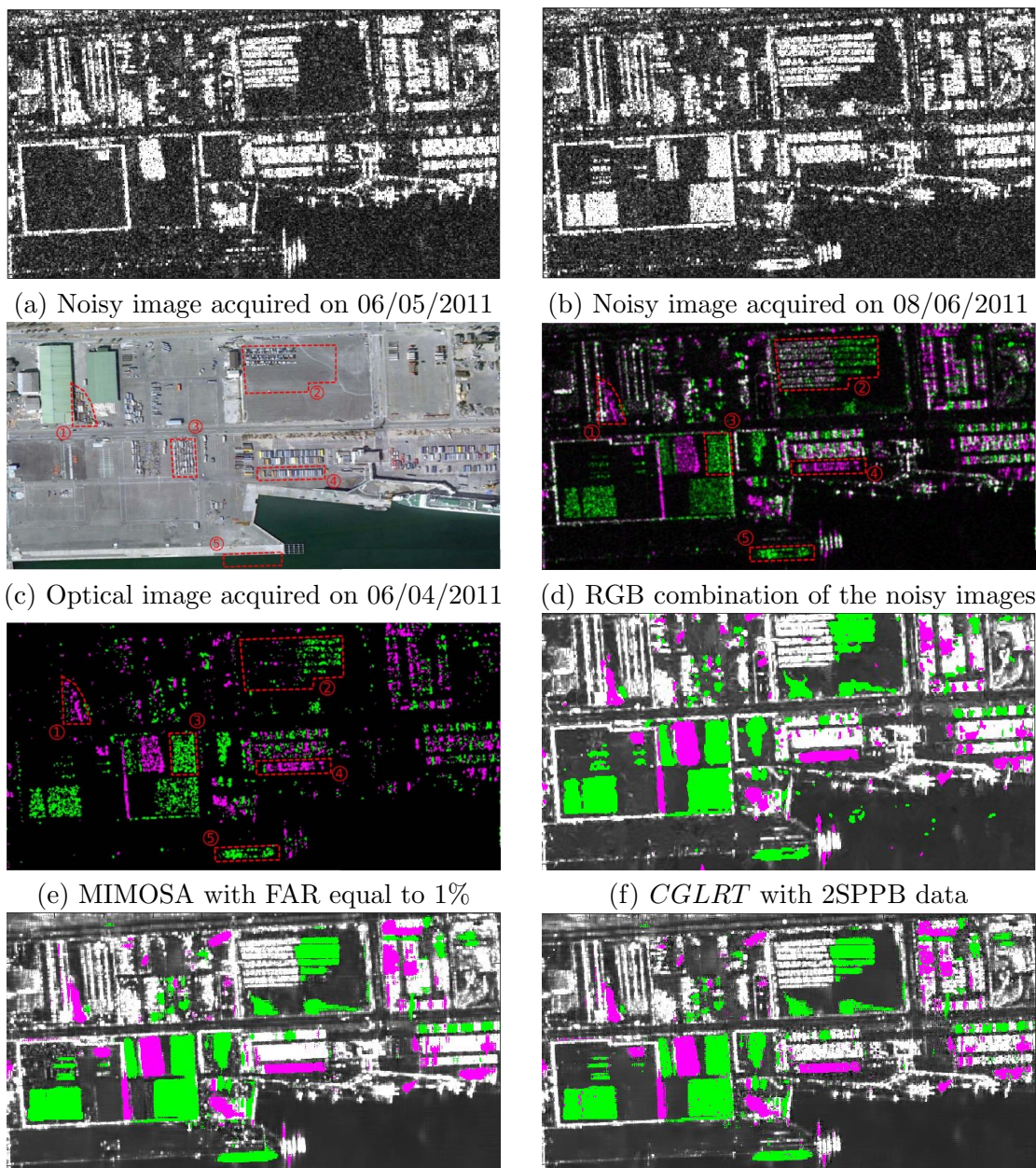
FIGURE 8.3: False positive vs true positive curves comparison based on simulated SAR images. (a) ROC curve results using simulated Sentinel-1 data (Fig.3.15(b)), (b) ROC curve results using simulated TerraSAR-X data (Fig.3.16(a)). Multilooked data with  $3 \times 3$  window size, 2SPPB and RABASAR provided data are used for the comparison of Conradsen's method,  $CGLRT$  method and  $S_{GLR}$  method, respectively.

During the acquisition of SAR time series, changes may happen for different kinds of objects, such as buildings, farmland and forest, etc. Generally, different kinds of objects have different change magnitudes. To comprehensively and quantitatively evaluate the performances of different methods, we processed the simulated SAR images which have different kinds of object changes (section 3.3).

Because of the small change magnitude in SAR intensity images, identifying forest area changes is much harder than farmland and building changes. It is obvious that  $S_{GLR}$  method can obtain the best detection results. In addition,  $S_{GLR}$  method can obtain better results with RABASAR-DAM provided data. Comparing with other methods,  $CGLRT$  method is good at detecting building area changes which have large change magnitude. This characteristic causes  $CGLRT$  method to provide worse results when the false positive are larger than 1%. According to the results shown in figure 8.3, Conradsen's method always have more false positive because of using multilooked data.

To fairly compare with the state-of-the-art change detection methods, we processed popularly used TerraSAR-X images acquired over *Sendai*. 9 temporal well registered SAR

images are used for the preparation of denoised data, both for 2SPPB and for RABASAR. Only the two images which were acquired on 06/05/2011 and 08/06/2011 are used for the change detection.



(a) Noisy image acquired on 06/05/2011 (b) Noisy image acquired on 08/06/2011  
(c) Optical image acquired on 06/04/2011 (d) RGB combination of the noisy images  
(e) MIMOSA with FAR equal to 1% (f) *CGLRT* with 2SPPB data  
(g) *SGLR* with RABASAR-DAM data (h) *SGLR* with RABASAR-DBWAM data

FIGURE 8.4: Sendai SAR image pair change detection comparison. Pink represents disappearing areas, while green represents appearing areas. The comparison areas are indexed using red circles with associated numbers.

Although MIMOSA [Quin et al., 2014] detects all the changes directly using the noisy data, there are too much wrong detections in the unchanged areas. The detections are seriously influenced by the noise. *CGLRT* can provide good results, but the changed area boundaries are blurred compared with *SGLR*. In addition, *CGLRT* provides some wrong

results in water area.

$S_{GLR}$  method obtains the best results both with RABASAR-DAM and RABASAR-DBWAM. They all precisely detect the 5 typical changed areas (Fig.8.4 (c)). However, there are some noise inside the changed areas when using RABASAR-DBWAM.  $S_{GLR}$  method obtained better results for the objective change detection with RABASAR-DAM.

### 8.2.2 Continuous change monitoring

Continuous change monitoring is a good way to track the development of object changes. In this section, 5 Sentinel-1 images are processed using this method, which provided satisfying multitemporal change detection results. Yellow lines are used to highlight the farmland area boundaries, as shown in the first column of figure 8.5. Comparing with the farmland backscattering values in the reference image, the others seem to have smaller values. Thus, we create the background image by dividing the reference image with other images, so as to highlight the changed farmland areas.

There are valleys in this area, even the farmland areas are not flat. The threshold is defined empirically, according to the detecting change types or changed areas. For example, big threshold values lead to the detection of high change magnitude areas. With the false alarm rate equal to 0.54% (computed using the denoised simulated SAR images without change), we can detect the farmland area changes (Fig.8.5).

The positive values (red) indicate the increase of backscattering values according to the reference data, and the negative values (blue) represent the decrease of the backscattering values. The appearing or disappearing buildings always have a large change magnitude. Seasonal changed areas (like farmland areas, some kinds of forest areas) have dynamic changes during the time line. With the false alarm rate equal to 0.54% (Fig.8.5), the proposed method detects 83.23% of the appearing and disappearing buildings.

Since farmland areas and building areas have different mean intensity values, we could suppress the detection of farmland area changes by adding this information as a weight, with  $\exp(\sqrt{\hat{u}_t} + \sqrt{\hat{u}_{t'}}/2)S_{GLR}(\hat{u}_t, \hat{u}_{t'})$ . The exponential function is used to enlarge the backscattering value differences between different objects.

In addition, these two areas usually have different change magnitudes. For example, with weights calculated using the log version distance of the corresponding amplitude values :

$$S_{GLR}^D(\hat{u}_t, \hat{u}_{t'}) = \log(|\sqrt{\hat{u}_t} - \sqrt{\hat{u}_{t'}}|)S_{GLR}(\hat{u}_t, \hat{u}_{t'}) \quad (8.17)$$

we could acquire new change detection results (third column of Fig.8.5). However, after multiplying the weights, the threshold has to be defined empirically.

### 8.2.3 Change classification

In this section, the proposed change classification method is compared with NOR-CAMA [Su et al., 2015] and Conradsen's method [Conradsen et al., 2016] with the use of simulated and real multitemporal SAR images. The used data and ENL of these change classification methods are demonstrated in table 8.3. This process can distinguish farmland area changes from building area changes, which have seasonal and non-seasonal changes, respectively.

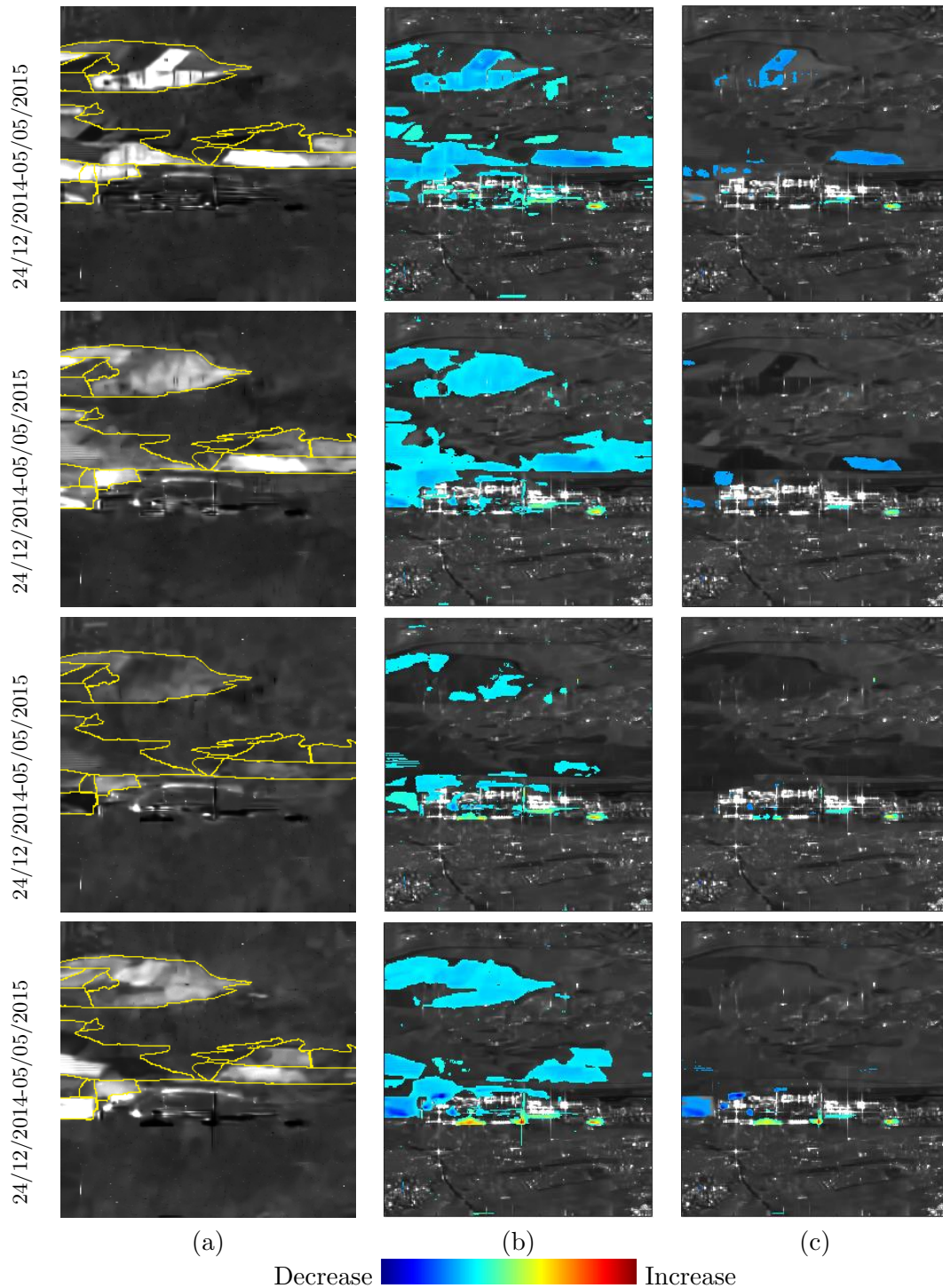


FIGURE 8.5: Continuous change monitoring results. (a) the reference image divided by the other images, (b) changes detection results, (c) changes with change magnitude weights. The thresholds chosen for column (b) with  $P_{fa}=0.54\%$  and  $P_{fa}=1\%$  for column (c). The time intervals of the changes are shown on the left. Different colors represent the decrease and increase of the backscattering values. The temporal images are denoised using RABASAR-DAM.

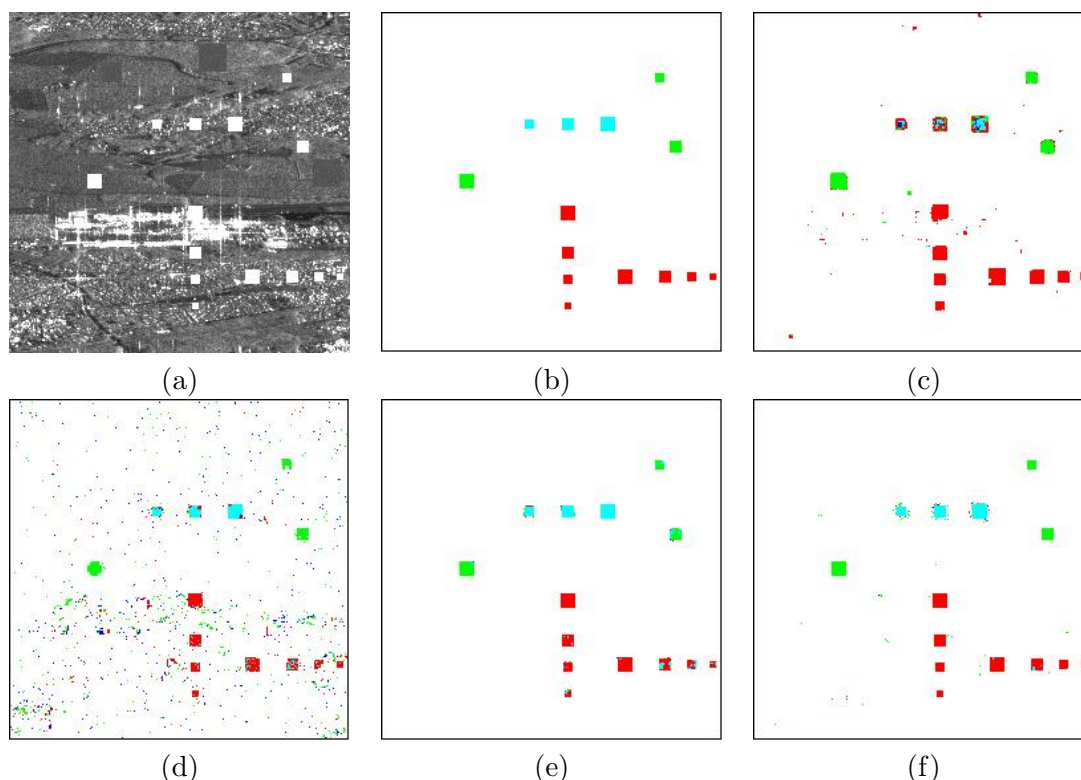


FIGURE 8.6: Change classification comparison with simulated data. (a) noise free image. (b) changing class reference map, (c) Conradsen's method with  $\alpha = 0.01$ , (d) NORCAMA with  $\alpha = 0.02$ , (e)  $S_{GLR}$  using RABASAR-DAM with  $\alpha = 0.04$ , (f)  $S_{GLR}$  using RABASAR-DBWAM with  $\alpha = 0.04$ . Different colors represent different change types : white : no change, red : step change, green : impulse change, blue : cycle change and cyan : complex change. The changed values are extracted from changed building areas, with large change magnitude.

### 8.2.3.1 Test on simulated temporal images

6 simulated Sentinel-1 SAR data, which are corrupted by single look gamma distribution noise and have different change types, are used for the comparison. Their detection results are shown in figure 8.6. The threshold is chosen according to the detection of the amount of changed points. Quantitative evaluation results of the change classification performances are shown in table 8.3.

For NORCAMA method, the wrong detection results are randomly distributed in the whole image. Because of using 2SPPB provided adaptive ENL and denoised data, NORCAMA method is very sensitive to the wrongly denoised points. In practise, NORCAMA could acquire better change type detection results when using RABASAR-DBWAM data.

TABLE 8.2: Difference of used data and ENL for the change classification methods

Method	Used data	ENL
Conradsen's method	multilooked data	same ENL
NORCAMA	2SPPB provided and noisy data	temporally & spatially vary ENL
NORCAMA	RABASAR-DAM/DBWAM	temporally & spatially vary ENL
$S_{GLR}$	RABASAR-DAM/DBWAM	spatially vary ENL

We applied Conradsen’s time series change detection method to the change type detection process. The increase or decrease of the adjacent changed values are associated with the time of changes. This simple index is used for the change type detection. Conradsen’s change type detection method provides good results (Tab.8.3). It has high processing efficiency. However, the detected changed areas are larger than the real changed areas because of using sliding rectangle window (size of  $3\times 3$ ) to filter the noisy image.

Compared to NORCAMA and Conradsen’s method,  $S_{GLR}$  based method acquires better detection results using RABASAR-DBWAM provided data, with higher true positive rate and lower false positive rate. In this case,  $S_{GLR}$  change classification method provides better detection results for the changed areas (Fig.8.6(f)). But some unchanged points near the changed areas are wrongly detected as changed points. With RABASAR-DAM provided data,  $S_{GLR}$  obtains the best change area detection results. However, some of the change types are wrongly detected, such as some step changes are detected as complex changes.

TABLE 8.3: True positive rate (TPR) and false positive rate (FPR) of different methods

	Conradsen’s method	NORCAMA	RABASAR-DAM	RABASAR-DBWAM
TPR	0.752	0.641	0.667	0.759
FPR	0.013	0.024	0.006	0.005

### 8.2.3.2 Change classification with Sentinel-1 data

Since change type detection results are seriously affected by the used data, we also compare  $S_{GLR}$  based change classification method with NORCAMA method that uses RABASAR provided data.

With high frequency acquisition data, the whole duration of the changed buildings will be monitored. During the construction of the building, its backscattering values may keep changing which leads to complex change monitoring results. To suppress the complex or high frequency changes of construction areas and keep the cycle changes of farmland areas, we under sampled the frequency of the time series. The acquisition time of the Sentinel-1 time series are 24/12/2014, 05/05/2015, 25/11/2015, 05/04/2016, 02/10/2016 and 18/01/2017.

However, all the SAR images are used during the speckle reduction process, so as to acquire better denoising results. RABASAR-DAM denoised images and all change classification results are illustrated in figure 8.7. Since the actual backscattering values of the farmland areas are controlled by the surface roughness and soil moisture, we could observe the weak backscatter fields in SAR images acquired in spring. This phenomenon also reflects the seasonal changes in the time series.

Compared to NORCAMA provided results,  $S_{GLR}$  based change classification method provides much better results. All the detected changed areas are well corresponding to the previous cumulative change detection results demonstrated in figure 8.5. Visually,  $S_{GLR}$  gives better detection results (Fig.8.7(k)) when using RABASAR-DAM provided data. There are less isolated points in the detection results and the changed farmland areas are very smooth. The changed types are similar to that using RABASAR-DBWAM provided data.

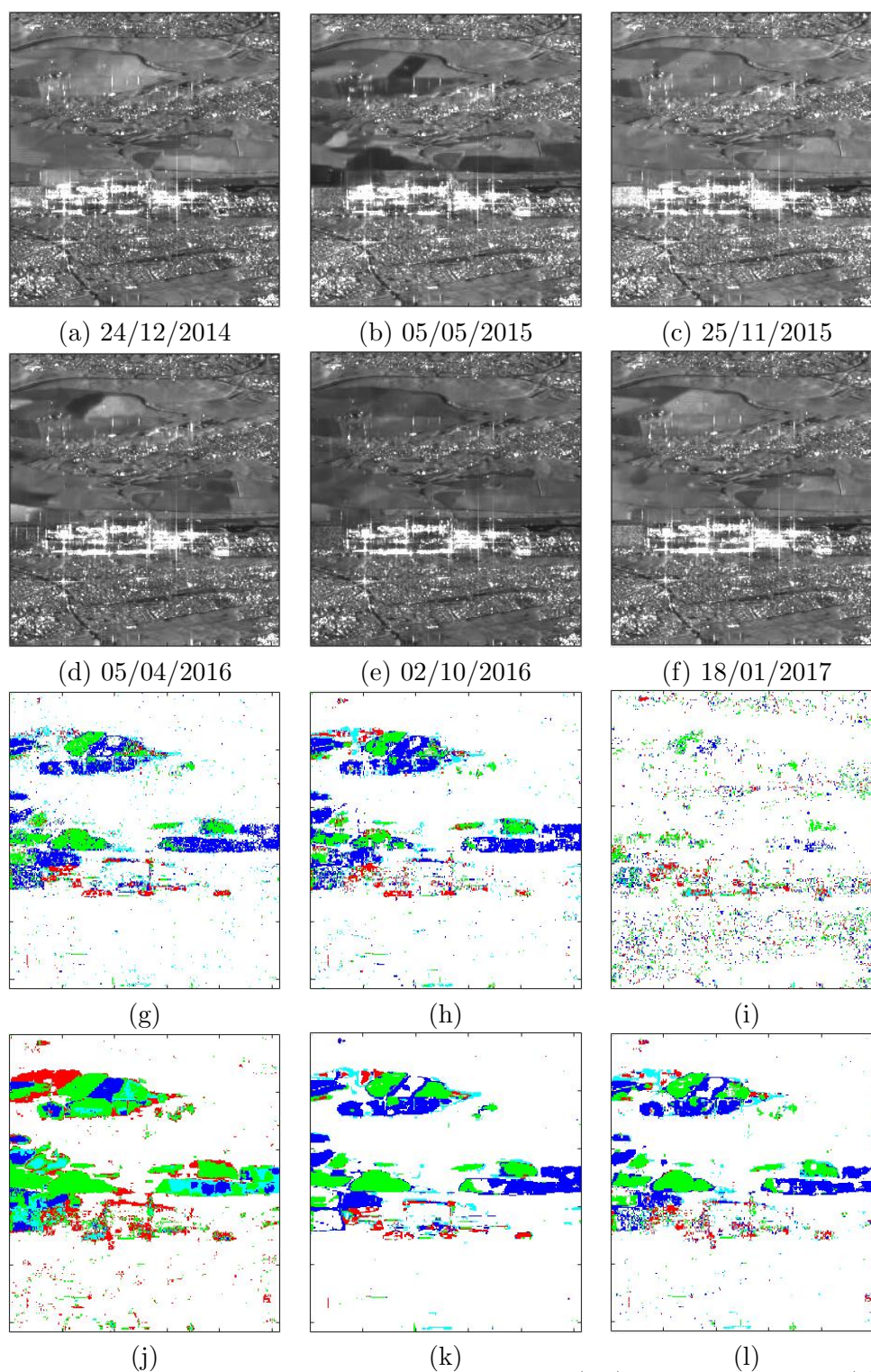


FIGURE 8.7: Sentinel-1 time series change classification. (a-f) Sentinel-1 images, (g) NORCAMA with RABASAR-DAM provided data, (h) NORCAMA with provided RABASAR-DBWAM data, (i) NORCAMA with 2SPPB provided data, (j) Conradsen's method with RABASAR-DBWAM provided data, (k)  $S_{GLR}$  with RABASAR-DAM provided data, (l)  $S_{GLR}$  with RABASAR-DBWAM provided data. 6 images are used for the change type detection. The change type results are : white : no change, red : step change, green : impulse change, blue : cycle change and cyan : complex change.

Global threshold is used for  $S_{GLR}$  based change type detection method, so as to speed up the processing. The denoising results of RABASAR seem good when using binary weighted arithmetic mean image, but the change type detection results are not better than that using arithmetic mean image. When using RABASAR provided data, NORCAMA method can obtain much better results than using 2SPPB provided data. Conradsen's method detects similar areas as  $S_{GLR}$  method. However, the detected areas are much larger than other methods and some of the cycle changed farmland areas are detected as impulse changed type.

For the same crop with similar growth period monitored in different years with the same SAR sensor, they have similar backscattering values. It seems that using less images is not enough to detect all kinds of vegetation interannual variations. It is recommended to use  $S_{GLR}$  change type detection method with RABASAR-DAM provided data.

### 8.3 Conclusion

In this chapter, we proposed a simple  $S_{GLR}$  based similarity test which could be applied and benefit to any denoised SAR images. The simple  $S_{GLR}$  similarity is based on gamma distribution and used for the calculation of the criteria map. Based on the prefiltered data, this method has been used for image pair change detection, continuous change monitoring and change classification. In particular, we mainly used RABASAR provided data in this chapter.

The processing results of simulated and real SAR images show that  $S_{GLR}$  based change detection method provided good results both in the processing of image pairs and temporal images.  $S_{GLR}$  method gives better change classification results compared to NORCAMA method. Using RABASAR-DAM provided data,  $S_{GLR}$  acquired much better change classification results, with smooth changed areas and less noisy points. In addition, using RABASAR provided data can improve the change detection performance of  $CGLRT$ . Through combining use the change time and change magnitude information, we applied Conradsen's time series change detection method to change type detection.

Future work will take into account the object attributes of the changed areas, so as to acquire better analysis results. To precisely identify the seasonal change of vegetation areas, we will pay attention to the multitemporal coherence maps.

---

## Chapter 9

# Detection of change times of interest in multitemporal SAR data and visualization with extended REACTIV

Detecting the exact time when changes occur is important for land surface monitoring. Changes usually represent transitions that occur between states [Aminikhanghahi and Cook, 2017]. In this work, we only consider abrupt changes (above some threshold), excluding slowly varying changes. Using a colorful image can ease results interpretation highlighting changed areas. In change detection field, a number of studies have used different colors to show different changes. Su et al. [2015] associate different colors to highlight different change types of time series, Mou et al. [2018] propose using different colors to represent different change phenomenons, and Domínguez et al. [2018] use different fusion strategies to illustrate the real changes and false alarms. With short time series, Nielsen et al. [2016] propose to use RGB colors to represent different change times and use black color to represent the unchanged areas. In addition, Amitrano et al. [2016] proposed using new bi-temporal and multitemporal RGB combination frameworks to illustrate temporal SAR images. The effectiveness of these two RGB visualization approaches have been verified by change detection and classification, respectively. However, none of them associate the colors with different long time series change times.

Recently, Rapid and EAsy Change detection in radar TIme-series by Variation coefficient (REACTIV) method has been proposed by Koeniguer et al. [2018a]. It is a simple and highly efficient time series change detection and visualization algorithm. It is based on HSV space and exploits only time domain estimates without any spatial estimation. The color saturation is coded by the temporal coefficient of variation. However, the detection results are corrupted by speckle noise. Even using some state-of-the-art denoising methods, the bias estimation in vegetation area still prohibits REACTIV to provide accurate performance. In addition, the color in REACTIV results only represents the appearing date of maximum values.

In this chapter, our objective is to adapt REACTIV method to integrate our proposed denoising results. In addition, we apply a generalized likelihood ratio test in this framework to detect the change time of interest, such as change starting and ending times under

---

predefined threshold, the maximum change magnitude appearing time.

## 9.1 REACTIV visualization method

The principle of REACTIV is to exploit the HSV color space and a temporal stack of SAR images. The hue channel H represents the maximum value appearing time, the saturation channel S corresponds to the temporal coefficient of variation, and the value V corresponds to maximum radar intensity of the temporal series in each pixel [Koeniguer et al., 2018b].

### 9.1.1 Hue (H)

This color component represents a specific time. For the time series acquired from time  $t_1$  to time  $t_2$ , the hue color index for each image (acquired at time  $t$ ) can be calculated through :

$$f_t = \frac{t - t_1}{t_2 - t_1} \quad (9.1)$$

In REACTIV, time is chosen as the date of maximum amplitude value.

### 9.1.2 Saturation (S)

This color component defines whether there are changes or not in the time series. Unlike popularly used change detection methods which mainly pay attention to the intensity value changes, REACTIV method uses the dynamics of the coefficient of variation. Based on Rayleigh Nakagami's distribution [Goodman, 1976], it is possible to derive the empirical moments expression of pure speckle with [Nicolas, 2006] :

$$m_1 = u_A \frac{\Gamma(L + \frac{1}{2})}{\sqrt{L}\Gamma(L)} \quad (9.2)$$

$$m_2 = u_A^2 \quad (9.3)$$

Based on the ratio of standard deviation and the amplitude average, the coefficient of variation can be calculated through :

$$\gamma = \frac{\sigma}{u_A} = \frac{\sqrt{m_2 - m_1^2}}{m_1} = \sqrt{\frac{\Gamma(L)\Gamma(L+1)}{\Gamma(L+1/2)^2} - 1} \quad (9.4)$$

To know the behavior of this parameter, the variance of this estimator can be calculated according to [Kendall and Stuart, 1977, Nicolas, 2006] :

$$\text{Var}(\gamma) = \frac{1}{4M} \frac{4m_2^3 - m_2^2 m_1^2 + m_1^2 m_4 - 4m_1 m_2 m_3}{m_1^4 (m_2 - m_1^2)} \quad (9.5)$$

where  $M$  is the number of samples to compute the estimation which corresponding here to the temporal images considered. In addition, based on the order 1 to 4 moments of the Nakagami distribution and  $L$ , the variance of this estimator can be written :

$$\text{Var}(\gamma) = \frac{1}{4M} \frac{L\Gamma(L)^4(4L^2\Gamma(L)^2 - 4L\Gamma(L + \frac{1}{2})^2 - \Gamma(L + \frac{1}{2})^2)}{\Gamma(L + \frac{1}{2})^4(L\Gamma(L)^2 - \Gamma(L + \frac{1}{2})^2)} \quad (9.6)$$

Usually, the number of available images on the same area varies. In order to overcome the dependency of the coefficient of variation on the number of images, it is possible to

---

normalize the distribution with the theoretical mean and standard deviation. Koeniguer et al. [2018b] propose to use the following empirical normalization :

$$\gamma \leftarrow \frac{\gamma - \mathbb{E}[\gamma]}{10\sigma(\gamma)} + 0.25 \quad (9.7)$$

with the theoretical mean and standard deviation values for a “stable” speckle and  $L = 4.9$  for Sentinel-1 GRD data. This empirical normalization aims to reduce the saturation values of the stable zones around a low saturation to 0.25, and to spread the changes on higher saturation.

### 9.1.3 Value (V)

The REACTIV visualization method uses the maximum amplitude value of each time series as the value channel.

The hue color component is computed using equation (9.1) with time  $t$  corresponding to the maximum amplitude value appearing time. This choice is particularly suitable for an abrupt event (such as the presence of a boat).

## 9.2 Change time visualization method

To take advantage of REACTIV visualization method, we introduce some improvements according to our change time detection purpose.

### 9.2.1 Times of interest (Hue)

As introduced in [Koeniguer et al., 2018b], one can associate a color with a particular time according to the change. During the procedure, different change types can be considered, such as abrupt change, seasonal change, deforestation & regeneration, etc. REACTIV visualization method chooses to highlight the appearing time of the maximum value. Although REACTIV visualization method can well associate the maximum value appearing time with the color, the first and last dates have very similar colors because the HSV color palette is continuous and loop on itself. Thus, we propose to highlight the interested time using the normalized time in the interval :

$$f_t = \frac{5}{6} \times \frac{t - t_1}{t_2 - t_1} \quad (9.8)$$

where  $t_1$  and  $t_2$  are the first and last images acquisition time in the time series,  $t$  is the time of interest.  $5/6$  is used to suppress the time interval, so as to avoid using the starting color category (loop) again.

Given a time series intensity SAR data  $\{y_1, y_2, \dots, y_M\}$ , we can compute the  $GLRT(y_t, y_{t'})$  through equation (7.7). The threshold calculation method introduced in section 8.1.2 can be used for the two images change detection [Conradsen et al., 2003] :

$$\rho = 1 - \frac{1}{6} \left( \frac{1}{L_t} + \frac{1}{L_{t'}} - \frac{1}{L_t + L_{t'}} \right)$$

$$\omega_2 = -\frac{1}{4} \left( 1 - \frac{1}{\rho} \right)^2$$

where  $L_t, L_{t'}$  are the equivalent number of looks. According to the general asymptotic expansion theory [Wilks, 1938],

$$P\{-2\rho\ln(GLRT(y_t, y_{t'})) \leq \delta\} \simeq P\{\chi^2(1) \leq \delta\} + \omega_2[P\{\chi^2(5) \leq \delta\} - P\{\chi^2(1) \leq \delta\}] \quad (9.9)$$

The value of  $\delta$  can be computed using  $-2\rho \ln Q = \delta$ . The probability of finding a smaller value of  $-2\rho \ln Q$  can be obtained by using chi-square cumulative distribution function. According to the significance level, we can detect which area has changed or not.

With the time series  $\{y_1(s), y_2(s), \dots, y_M(s)\}$ , we can use GLRT to detect times of interest :

(1) Start changing time

When detecting the start changing time in the time series, points similarities  $GLRT(y_1(s), y_t(s))$  are calculated with the reference to the value of the first date  $y_1(s)$ . After transforming the similarity to change probability  $P\{-2\rho\ln(GLRT(y_1(s), y_t(s)))\}$ , we can decide whether there is a change or not based on a predefined change probability  $\tau$  (such as 99%).

$$T_{start} = \begin{cases} t & \text{if } P\{-2\rho\ln(GLRT(y_1(s), y_t(s)))\} > \tau \\ 0 & \text{else} \end{cases} \quad (9.10)$$

where  $t$  is the start changing time with  $1 < t \leq M$ . It corresponds to the first time that the change probability is larger than the threshold  $\tau$ .

(2) Maximum change time

Generally, the abrupt changes are associated with large change magnitude [Basseville et al., 1993]. The maximum logarithm of GLRT  $S_{GLR}(y_t(s), y_{t'}(s))$  is supposed to be the maximum change. In this case,  $t$  and  $t'$  are set as the adjacent times.  $t'$  is the maximum change time.

$$T_{max} = \begin{cases} t' & \text{if } S_{GLR}(y_t(s), y_{t'}(s)) = \tau_{max} \\ 0 & \text{else} \end{cases} \quad (9.11)$$

where  $\tau_{max}$  equals to the maximum dissimilarity  $\tau_{max} = \arg \max_{t'} S_{GLR}(y_t(s), y_{t'}(s))$ .

(3) Stop changing time

For the detection of stop changing time, the last changed point in the time series is used as the reference point. In practice, the calculation is carried out in reverse order.

$$T_{stop} = \begin{cases} t & \text{if } P\{-2\rho\ln(GLRT(y_t(s), y_M(s)))\} > \tau \\ 0 & \text{else} \end{cases} \quad (9.12)$$

where  $t$  corresponds to the dates going from  $M, M - 1, \dots$  to 1.

Apart from this pairwise test, the time series change time detection method introduced in [Conradsen et al., 2016] can also be utilized. However, that method may be limited by its heavy time consumption because all the changed points are detected, especially when processing large amounts of data.

### 9.2.2 Changed area detection (Saturation)

To suppress the noise effect, we propose to calculate the coefficient of variation with the denoised time series. The application of a despeckling method on a SAR image has the effect of modifying the parameter  $L$ . In this case, we estimate the ENL using moment method as introduced in Section 2.3. The empirical normalization proposed by REACTIV is based on original ENL ( $L = 4.9$ ) of Sentinel-1 GRD data [Koeniguer et al., 2018b].

Instead of using the coefficient of variation to obtain the saturation, we can classify the change significant results (acquired using Eq.(9.9)) into changed and unchanged areas with a threshold. In addition, the multitemporal GLRT methods introduced in section 7.2.1.2 can be used with the hypothesis that the time series points have the same ENL ( $\hat{L}$ ). In this case, the threshold of equality GLRT (EGLRT) test can be calculated through [Conradsen et al., 2016] :

$$f = M - 1 \quad (9.13)$$

$$\rho = 1 - \frac{1}{6(M-1)} \left( \frac{M}{\hat{L}} - \frac{1}{\hat{L}M} \right) \quad (9.14)$$

$$\omega_2 = -\frac{(M-1)}{4} \left( 1 - \frac{1}{\rho} \right)^2 \quad (9.15)$$

where  $M$  represents the number of images. With image pairs  $M = 2$ , the equations boil down to GLRT test with two images which have the same ENL ( $L_t = L_{t'} = \hat{L}$ ). According to the general asymptotic expansion theory,

$$P\{-2\rho \ln(\text{EGLRT}) \leq \delta\} \simeq P\{\chi^2(f) \leq \delta\} + \omega_2 [P\{\chi^2(f+4) \leq \delta\} - P\{\chi^2(f) \leq \delta\}] \quad (9.16)$$

### 9.2.3 Background value (Value)

Although using maximum values can highlight abrupt appearing objects, the acquired results seems too noisy. Apart from this choice, we can use the denoising results or the temporal average image to have a clear vision of the ground. To avoid the different acquisition angle effects, we only use the SAR images acquired through similar incidence angles. We only use the maximum time series values in the following experiments.

### 9.2.4 Other visualization strategy

Apart from the visualization approach proposed in REACTIV method, we can apply the change magnitude visualization method to index time series change times. After detecting specific change times, the detection results can be normalized using equation (9.1). Then, we can transform it to a  $N$  jet color space through  $(N-1)f_t + 1$ .  $N$  is the number of parts for red, green, and blue intensities, which can be defined by user. With the detected changed areas by EGLRT, we can replace unchanged areas using their corresponding SAR amplitude values.

## 9.3 Experimental results and discussion

In this section, simulated SAR images and Sentinel-1 images are used to illustrate the capability of the proposed method. To illustrate the effectiveness of the denoising

process, different kinds of data are used. Four kinds of changes (such as farmland, forest, appearing building and disappearing building changes) are used to demonstrate the change area and change time detection potential of the method. Finally, the improved method will be applied to flooding area monitoring and urban area development monitoring. In the following sections, the time series saturation are mainly acquired using REACTIV original method. In practice, with a proper threshold, using EGLRT method can obtain similar changed areas as achieved by REACTIV method.

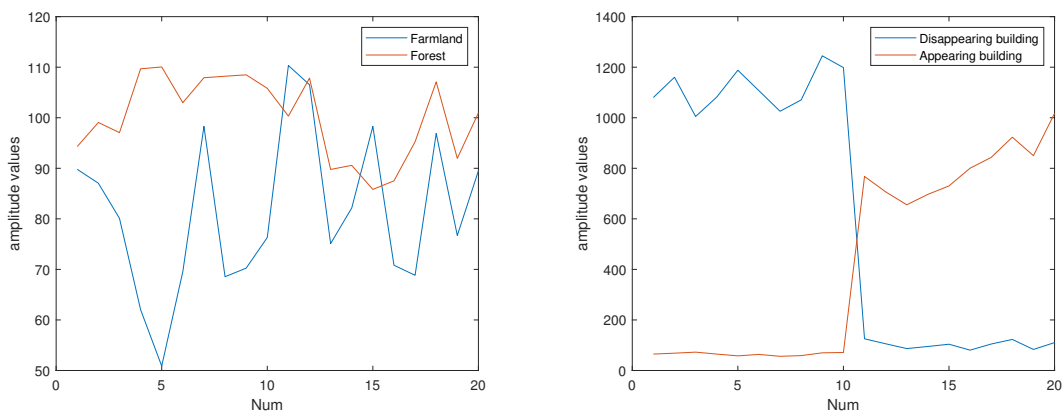


FIGURE 9.1: Different object changes in the simulated Sentinel-1 images.

### 9.3.1 Change detection performance with different kinds of data

#### (1) Simulated Sentinel-1 data

In the detection results, the changed areas are labelled using different colors as shown in the color bar, while the unchanged points are illustrated using maximum denoised SAR amplitude values of each time series. In order to provide explanations for the detected changed areas, the noise free value changes of different objects are illustrated in figure 9.1.

Using the denoised data, REACTIV can provide much better detection results (Tab.9.1). With short acquisition time interval for Sentinel-1 data, normally, there are much more available images than we need in the test site. To keep the good performance of the denoising method, more images are used for the denoising than the change detection. With the despeckled data, the contents in the test areas can be clearly seen (Fig.9.2). When using RABASAR-DAM, the detected changed areas are a little bit larger than the real changed areas. While using the RABASAR-DBWAM, the wrongly detected points are randomly distributed in the building areas. In addition, even using the denoised data, all the pixel colors in each rectangular are not the same. It seems that the noise is not totally removed.

Due to the volume backscattering mechanism of forest, their amplitude values do not have large changes during the whole year. Even using the denoised data, only part of the forest area changes can be detected.

When taking the color index into account, we can find that building area colors are corresponding to the maximum values. However, the abrupt changes in these areas are happening between the 10th and 11th images. To acquire and display more useful information in the results, we will take the change time into account in the next section.

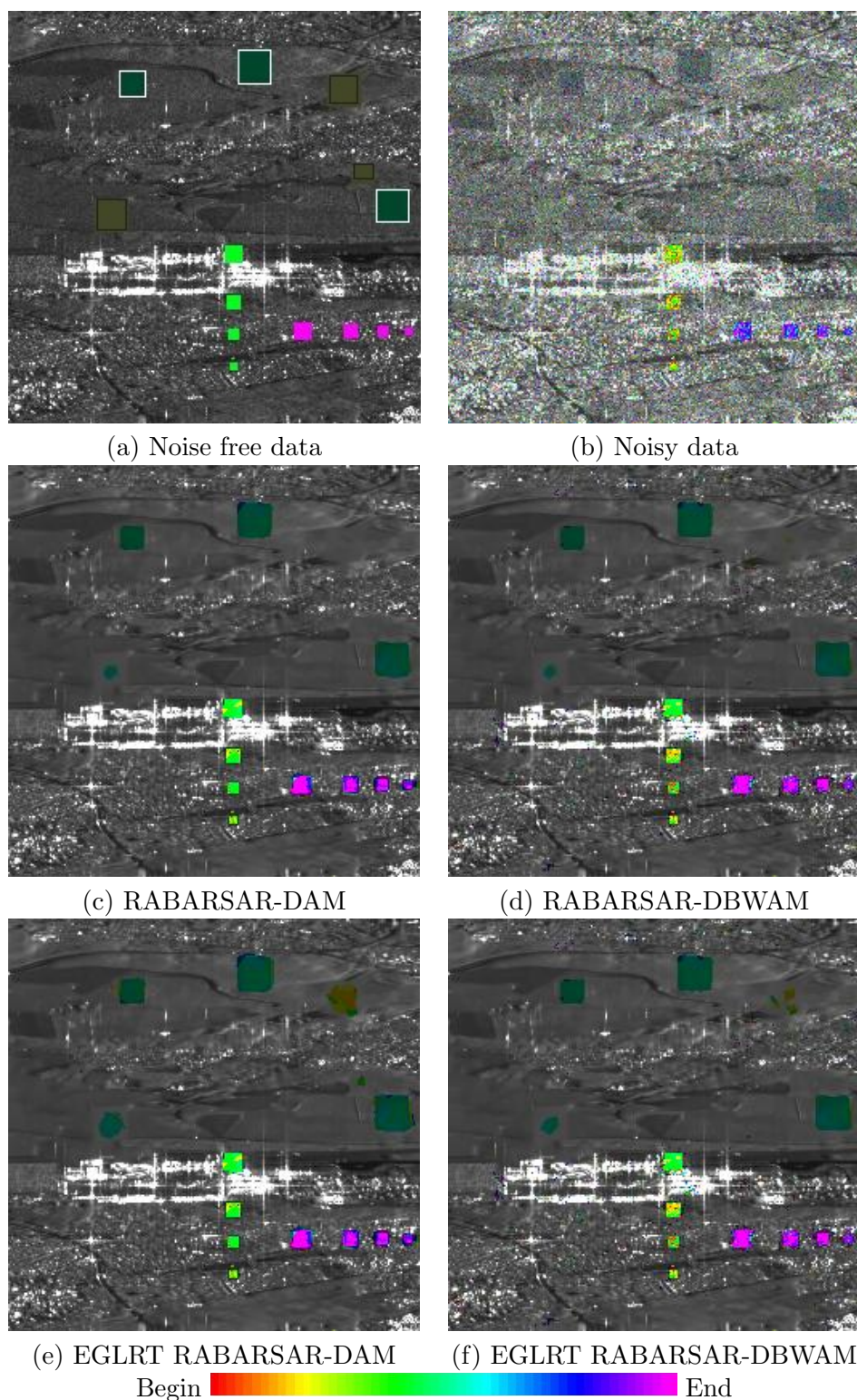


FIGURE 9.2: Maximum value appearing time detection comparison with simulated data. Change areas are detected using (a-d) : variation coefficient, (e-f) : equality GLRT (EGLRT) with change probability significance level equals 99.99%. 20 simulated Sentinel-1 images (Fig.3.15) are used for the comparison. 58 simulated time series images are used during the RABASAR denoising. White rectangle area in (a) : farmland, black rectangle area : forest.

TABLE 9.1: REACTIV detection results comparison with different data. 20 simulated Sentinel-1 images are used.

Detection probability	Noisy data	RABASAR-DAM	RABASAR-DBWAM
True positive rate (TPR)	0.884	0.650	0.660
False positive rate (FPR)	0.796	0.006	0.015

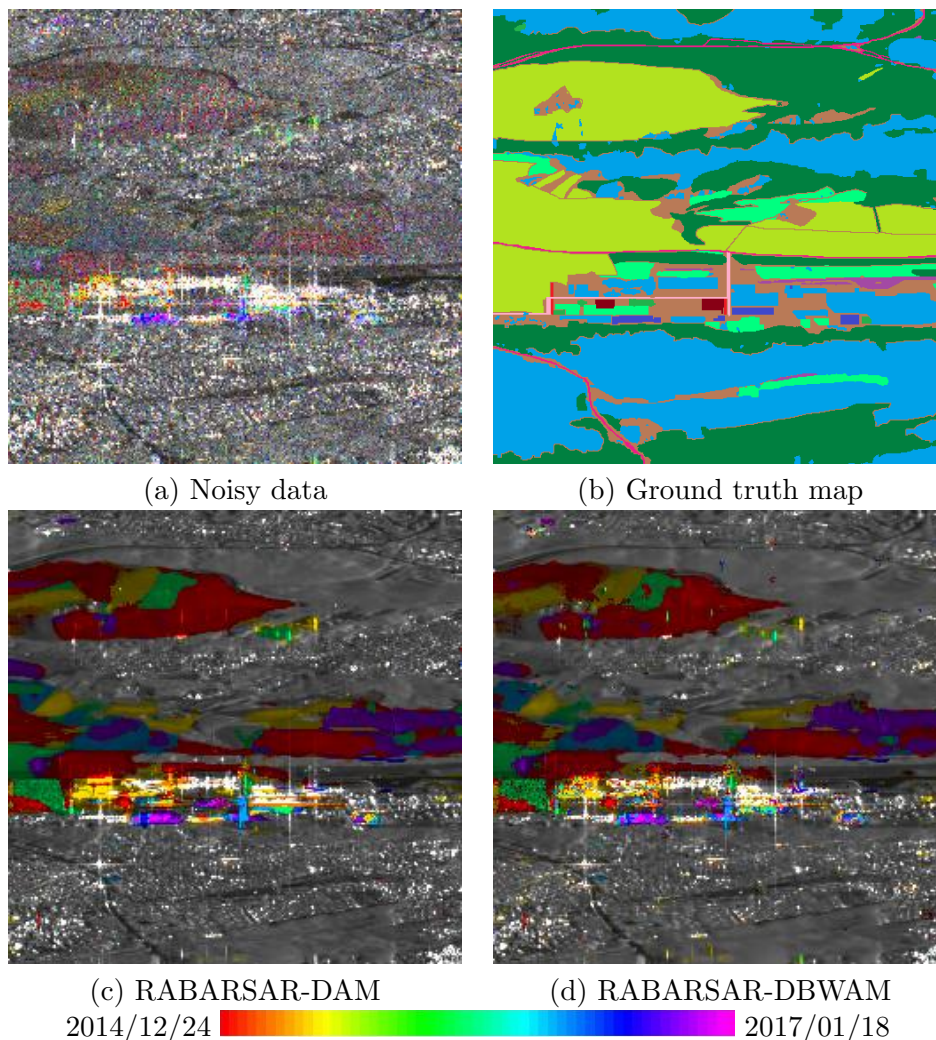


FIGURE 9.3: Maximum amplitude value time comparison with different data. The red color indexed 10 Sentinel-1 images in table 3.4 are used for the comparison. 69 time series images are used during the RABASAR denoising. Ground truth map is prepared according to the arithmetic mean image, with different colors represent different objects.

(2) Sentinel-1 time series

To make a comprehensive evaluation for the method, we processed the temporal Sentinel-1 SAR images. The detection results are shown in figure 9.3. Although the changing area can be roughly detected by the test statistics with original SAR data, the results are seriously affected by the noise. With the RABASAR provided data, REACTIV method can obtain much better change detection results. The previously

prepared ground truth map is shown in figure 9.3(b) to help the interpretation and evaluation of change detection results.

According to the ground truth, REACTIV can detect the changed building areas and farmland areas. With the default parameter, it can not detect the changes of forest area which have low change magnitude in the temporal amplitude SAR images. Based on the detection results, we can even distinguish different kinds of farmlands. Since most farmland areas are not totally flat, this may cause different parts of the same farmland reach their maximum value at different time. Therefore, the detection results in these areas are not smooth enough. Generally, construction area are larger than the under-construction building, and this area may keep changing before the building is completed. All these phenomena lead to the complex change shapes in the detection results.

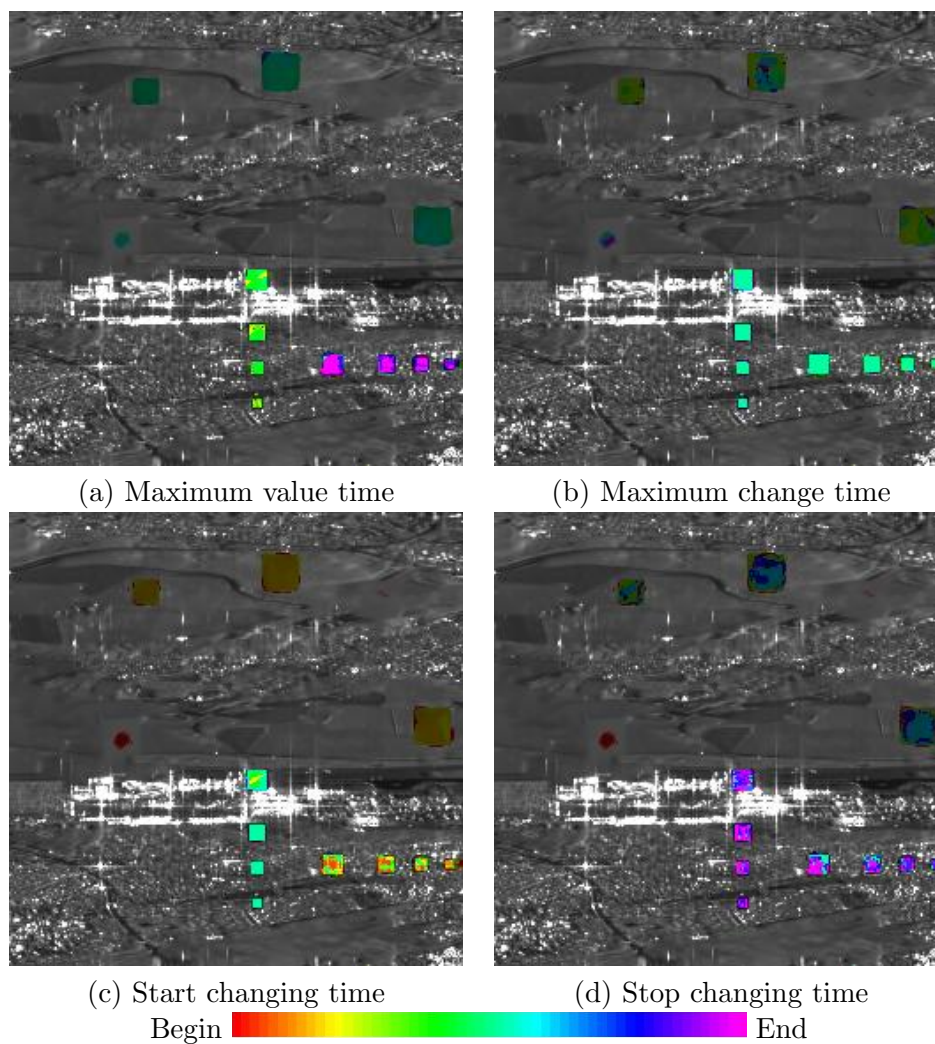


FIGURE 9.4: Comparison of different times of interest with simulated Sentinel-1 data. The data are provided by RABASAR-DAM. A threshold is set at 99% on the change probability.

### 9.3.2 Change time detection

In this section, different change time detection strategies described in Section 9.2.1 are utilized to process the simulated SAR images and Sentinel-1 time series. The spatial adaptive denoising leads to spatially variable ENL. During the change time detection test, we suppose they have the same ENL so as to speed up the process. In addition, the red color in the end of color bar is removed so as to avoid the mix of red colors. All the time are compressed to the set of color index bar.

With the reference of different object changes (Fig.9.1), the maximum change magnitude time and start changing time are the same for disappearing building areas (Fig.9.4). The detection results in the appearing building areas are much more complex.

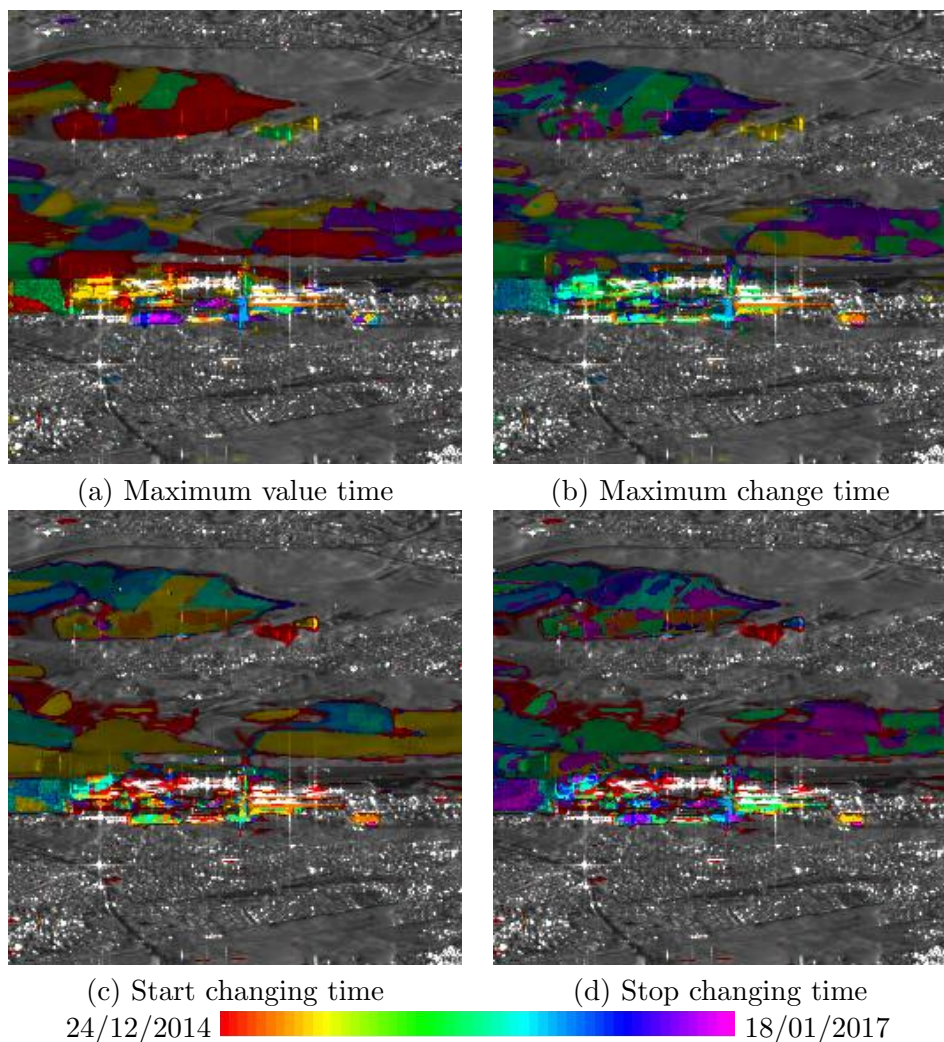


FIGURE 9.5: Different change time detection comparison with 10 Sentinel-1 data. The time series data are denoised by RABASAR-DAM. A threshold is set at 99% on the change probability.

Then, a small stack of Sentinel-1 images are processed. As shown in figure 9.5, the detected changed areas are the same as introduced in figure 9.3(c). Different seasonal changes of different crops can even be distinguished based on the change time detection

results. With different change indexes, we can study the seasonal changes of different farmland areas. In addition, we can obtain the construction duration of different buildings and analyze their effects on the surroundings.

Normally, some of the changes will last for a long time, such as appearing buildings. When the change happens between the first two or the last two images, the index color appears to be the same in the start changing and stop changing results because of the hue channel attribute. Using part of the hue color channel can successfully avoid this problem.

### 9.3.3 Applications with Sentinel-1 GRD data

Change detection is a significant application for remote sensing technology. In this section, we try to apply the improved method to some public issues, such as flooding area monitoring and urbanization development monitoring.

#### (1) Monitoring abrupt floods in Southern Laos<sup>1</sup>

There exist a large number of Sentinel-1 GRD data over the test site, all the images which have similar acquisition geometry are used to prepare the super-image. The geometrical coregistration is vital in change detection applications, so as to keep all the time series corresponding to the same object. All the images are coregistered using geometric based registration method<sup>2</sup>.

Sentinel-1 GRD images have the ability of monitoring large area changes. We only test the improved method over the water storage area. The amount of flooding water can be estimated according to the changes of the water area and local digital elevation model. As shown in figure 9.6, most of the areas are changed between the image pairs which were acquired in 17/07/2018 and 29/07/2018. The black areas surrounded by blue areas are the final water area during the image acquisition period. The detection results have high similarity with the results provided by ESA<sup>3</sup>.

#### (2) Tracking urbanization development in Southern TianJin city

With fast development of urbanization in China, remote sensing is an efficient tool for land and resource monitoring. Although optical images are popular to fulfill this task, there are some changes that optical images can not detect. For example, when the farmlands have been destroyed for the preparation of the construction and covered by green gauze, their changes may not be detected by optical images. In addition, optical images are always influenced by the clouds. However, SAR images have the advantage of overcoming this limitation.

During the past four years, there are a large number of new buildings near the south railway station of TianJin city. Some of the buildings are still under construction. To track the changes of this area, 16 Sentinel-1 GRD images with acquisition time interval around 3 months are used. Since 183 Sentinel-1 GRD images (all with IW mode, VV polarization, relative orbit number 47 and descending path) are used to prepare the arithmetic mean, we used RABASAR-AM method to denoise the 16 images.

As shown in figure 9.7, there are lots of farmland areas that have been transferred to building areas in this period. The building area changes can be predicted based on their stop changing time.

---

1. Flooding from Dam Break : <http://www.mrcmekong.org/news-and-events/news/extent-of-flooding-and-water-level-rise-from-dam-break-in-southern-laos/>

2. SNAP : <http://step.esa.int/main/toolboxes/snap/>

3. [https://www.esa.int/Our\\_Activities/Observing\\_the\\_Earth/Copernicus/Sentinel-1/Sentinel-1\\_maps\\_flash\\_floods\\_in\\_Laos](https://www.esa.int/Our_Activities/Observing_the_Earth/Copernicus/Sentinel-1/Sentinel-1_maps_flash_floods_in_Laos)

---

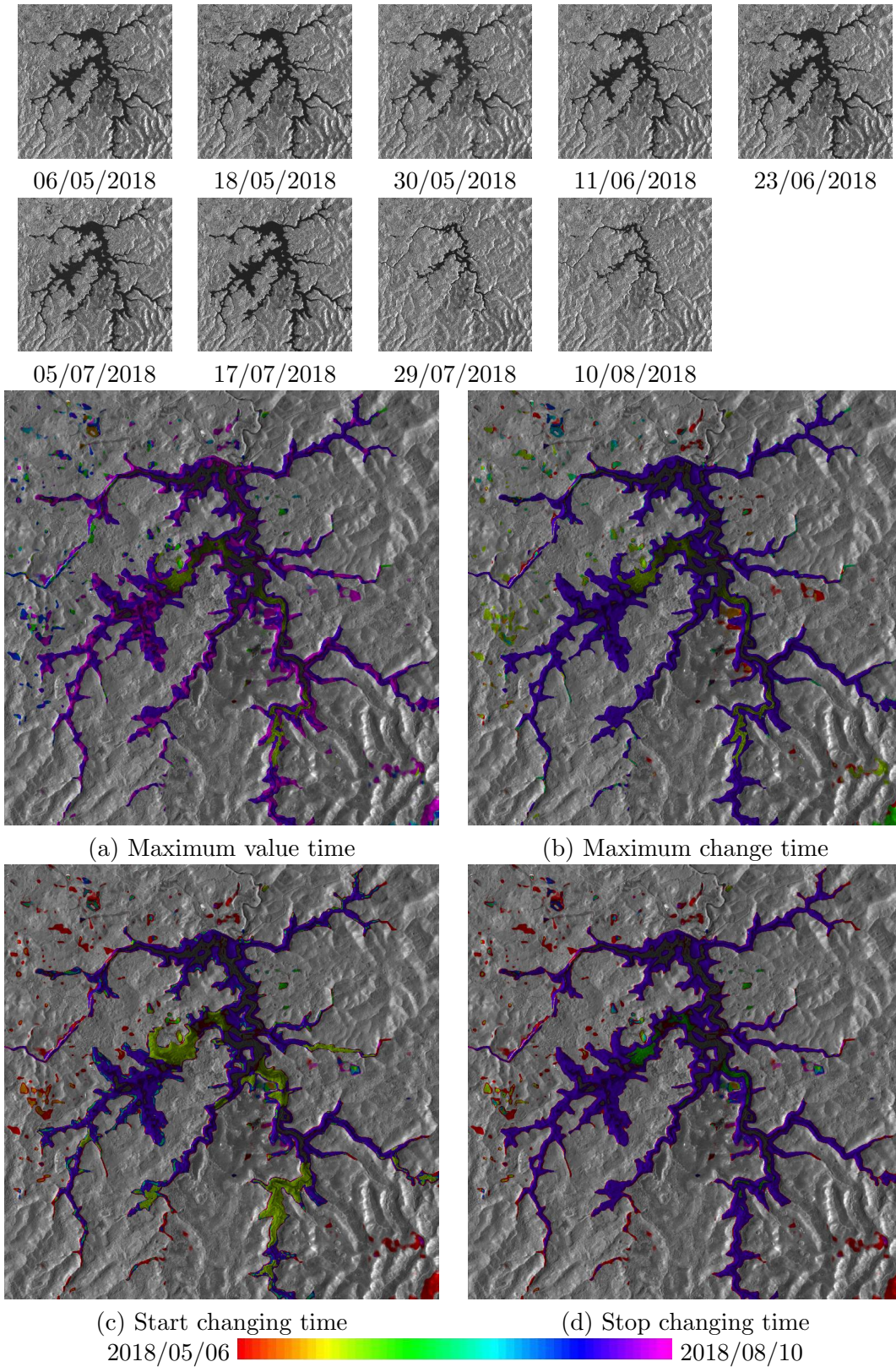


FIGURE 9.6: Flooding area change time detection comparison with 9 Sentinel-1 GRD data. 9 noisy images are shown above. The images are acquired over Xe-Pian Xe-Namnoy dam in the southeastern province of Attapeu in Laos. 87 temporal Sentinel-1 GRD images are used for the preparation of the arithmetic mean image. All the test images are provided by RABASAR-AM.

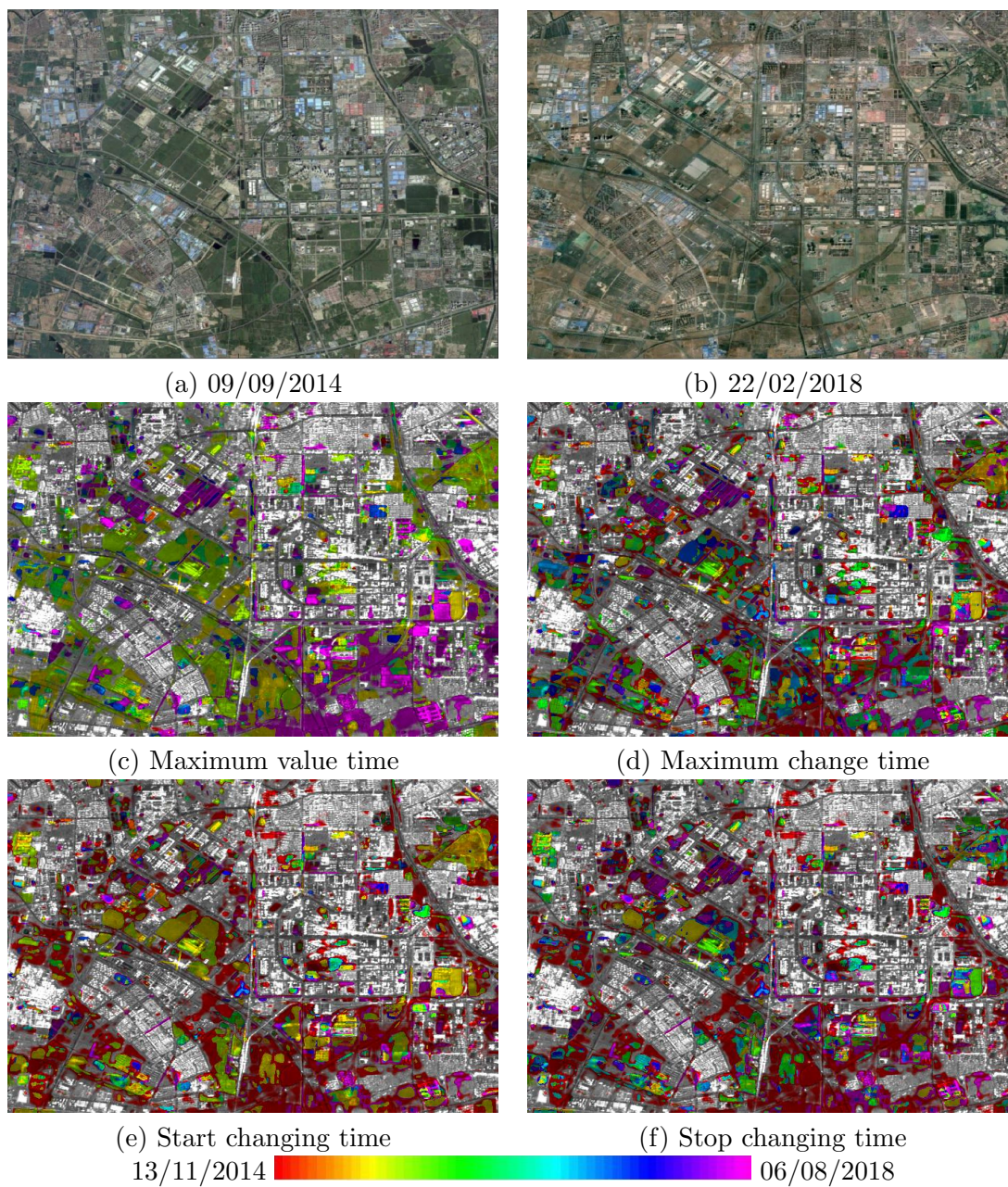


FIGURE 9.7: Change time detection comparison with 16 Sentinel-1 GRD images. The images are acquired over the south railway station of TianJin city, north of China.

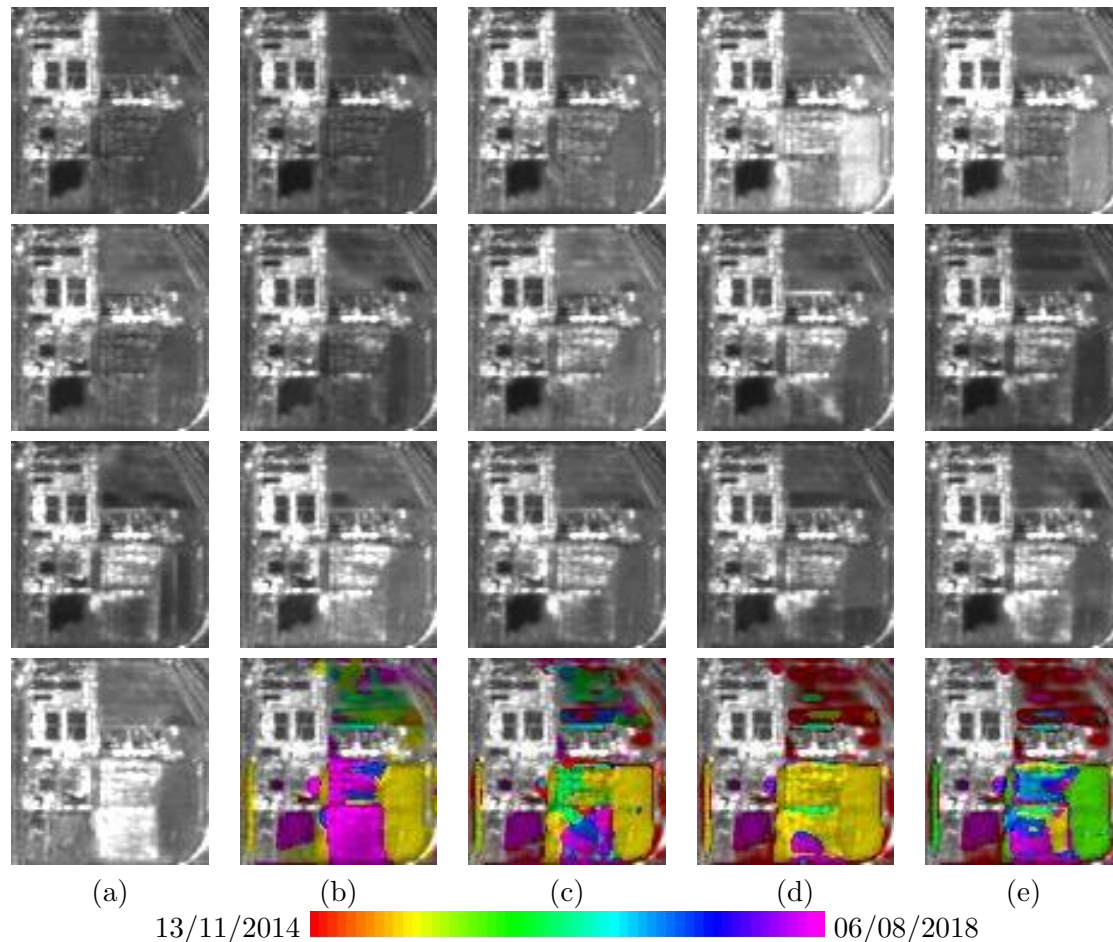


FIGURE 9.8: Enlarged area of figure 9.7. RABASAR-AM provided data are used to demonstrate the time series changes. The time series order is : from left to right and from up to bottom. (a)The last denoised image, (b) Maximum value time, (c) Maximum change time, (d) Start changing time, (e) Stop changing time.

## 9.4 Conclusion

Based on the detection areas acquired by REACTIV method (dynamics of time series coefficient of variation), we associated the colors with different kinds of change times and changed the background with denoised image or arithmetic mean image. Through only using part of the hue color channel, we successfully avoid the mixture of red color index. The results obtained by the improved method provided useful information and allow extended interpretation.

The change time detection is much effective for the homogeneous area changes and for the abrupt changes, which is suitable for monitoring farmland area, earthquake area, flooding area and some human activities (harbor activities, urbanization and airport dynamics). However, the method has less capability to detect the seasonal changes in forest area. The phase information will be used to monitor vegetation area changes in future work.

## Chapter 10

# Conclusion and perspective

With the availability of higher resolution, higher acquisition frequency, multi-acquisition model SAR images, SAR image exploration has attracted more people's interest. SAR despeckling is a vital step to remove the obstacle of its higher level application such as change detection, segmentation or classification. This thesis mainly deals with multitemporal SAR images denoising and change analysis. In this section, we will briefly review the whole thesis and illustrate some future works.

### 10.1 Conclusion

#### Database creation

Different multitemporal Sentinel-1 SLC/GRD, TerraSAR-X images were registered separately with a geometric registration method. A multitemporal ground truth map over Saclay area has been prepared, it can be used to assess the multitemporal SAR images denoising, change detection, classification and segmentation results. In addition, different kinds of simulated SAR data have been prepared, so as to control the changes in the time series. Furthermore, we also prepared well-registered Sentinel-1 and Sentinel-2 images, along with maps of overground changes. It can be used to detect homogeneous or heterogeneous image changes or to train deep learning networks.

#### Denoising results evaluation

When a reference image is available, we proposed to use its ratio with denoised data to illustrate the biased areas. The unrealistic behaviors and biased regions can be selected according to the image pair dissimilarity map and visualized with the jet colormap.

Without reference image, we proposed to use a patch-based auto-covariance residual evaluation method to examine the residual image and look for possible remaining structural contents. It can process automatically and does not rely on a supervised selection of homogeneous regions. It also provides a global score for the whole image.

#### Multitemporal denoising frameworks

On this topic, our study was directed in three directions :

- (1) **Adaptive nonlocal temporal filter** : State-of-the-art spatial adaptive denoising methods are used to improve the unbiased temporal average. The improved method can provide better results, especially in changed building areas and boundary areas.
-

- (2) **Patch based adaptive temporal filter** : This method offers a scheme for introducing the temporal information into the spatial adaptive SAR image denoising approaches. Different similarity calculation methods could be used to acquire temporally similar points. With long time series data, this method can effectively give good denoising results, with or without spatial denoising. The simple scheme allows its successful application on Google Earth Engine platform. With a proper threshold and dissimilarity to weight transformation function, it can provide good denoising results in changed building areas.
- (3) **RABASAR** : During the restoration of each SAR image, it exploits the temporal information through a super-image. When using more temporal images, the differences of using different super-images decrease. When changes exist in the time series, using a binary weighted arithmetic mean can provide better results in building areas. Besides, the super-image can be easily updated when new data become available so as to process new images on-line. Because of high stability in the ratio image, RABASAR can avoid introducing bias in farmland areas.

These frameworks can help researchers extend spatial denoising to temporal domain. Well denoised data can reduce the heavy load of interpreting SAR images.

### Multitemporal SAR data change analysis based on simplified GLR

In order to take advantage of multitemporal denoised data, we proposed a simplified generalized likelihood ratio ( $S_{GLR}$ ) test based on the hypothesis that the time series variables have the same ENL. This similarity test is applied to detect :

- (1) **Changed area** : Changed areas are detected based on their change probability under the no change hypothesis. Quantile method and Chi-squared distributed probability function are successfully used to detect the changed areas.
- (2) **Change magnitude** : According to the increase or decrease of the time series, the similarities in changed areas are transferred to positive and negative values. With the application of jet color map and mosaic with denoised image or temporal average image, the change magnitude can be easily visualized.
- (3) **Change type** : To detect the change types, we proposed an improved change classification method based on RABASAR, the simplified GLR and the improvement of spectral clustering method. Different change types can be represented by different colors and displayed with the SAR image as background.

### Multitemporal SAR data change time detection

With this method, we can detect the maximum value appearing time, the start and stop changing times, the maximum change magnitude appearing time and the maximum change significance appearing time. Through using different visualization method, the time series change times are vividly shown in two-dimensional space. We mainly use two ways to fulfill this task :

- (1) **Improve REACTIV method** : The REACTIV visualization method has been improved by using multitemporal denoised data, using only 5/6 hue color channels, detecting different change times and using denoised background values. Through only using part of the hue color channel, we successfully avoid the mixture of red color index. The change time detection is much effective for the homogeneous area changes and

for the abrupt changes, a suitable point for monitoring farmland, earthquake, flooding and some human activities (harbor activities, urbanization and airport dynamics).

- (2) **Application of EGLRT method** : After detecting the changed areas of multitemporal SAR images with EGLRT, we used the jet color map to index the different change times.

The effectiveness of these detection methods has been proved through the processing of various Sentinel-1 images. We successfully applied the methods to monitoring flooding areas and the development of cities.

## 10.2 Limitations and perspectives

The proposed multitemporal denoising and change detection algorithms only considered the data acquired through the same polarization and similar incidence angle.

### Deep learning based change detection

Current deep learning methods mainly process visual data. Only a few published papers are using deep learning to detect SAR image changes. The noise effect (gamma or Gaussian distribution noise) could be reduced through transforming the input image into feature space, such as using CNN and stacked denoising autoencoders. Since optical and SAR images have precise geolocation, they can be well registered. CNN takes into account 2-D data and automatically learn new kernels to represent the matrix in high-dimensional space. With large time series data which share the same ground truth with different representations, we can apply deep learning method to mining the user interested information.

Semantic segmentation is nowadays a popular application of deep convolution neural networks. It associates each image pixel with a class label. We can use semantic segmentation network to classify the multi-temporal multisensor images into different change types and unchanged areas. The proposed change detection method can be used to assist the preparation of the ground truth data. In the future step, we can consider detecting different kinds of changes, such as appearing and disappearing changes, farmland area changes.

### Object based heterogeneous images change detection

The proposed change detection is conducted at pixel level. However, users may be more interested in object changes. Based on the geometric registration algorithm, we can extract accurate object boundaries using Sentinel-2 data, and make use of the SAR time series change analysis inside each object. To obtain better multitemporal change analysis results, we can take into account object attributes in the changed areas.

### Coherent change detection

Since the backscattering values in forest areas are similar during different seasons, the proposed change detection method cannot detect forest area changes. To precisely identify the vegetation area seasonal changes, we may pay attention to the coherence maps of temporal SAR images. For the forest area coherent change detection, we can apply it to monitor firing areas.

In addition, with large amount of data, we can use sequence analyzing methods to exploit the long time series.

---

# Publication list

## Papers in refereed journals

[1] W. Zhao, L. Denis, C.A. Deledalle, H. Maître, J-M. Nicolas and F. Tupin. Ratio-based multi-temporal SAR images denoising. *IEEE Transactions on Geoscience and Remote Sensing*. 2019.

[2] H. Fan, W. Gu, W. Zhao, L. Lu. Long time series mining subsidence monitoring in a wide area with an accumulative DInSAR method : A case study in Fengfeng coalfield in China. *Computer Modeling in Engineering & Sciences* (under revision). 2018.

## International conference papers

[3] W. Zhao, C.A. Deledalle, L. Denis, H. Maître, J-M. Nicolas and F. Tupin. RA-BASAR : A FAST RATIO BASED MULTI-TEMPORAL SAR DESPECKLING. *IEEE International Geoscience and Remote Sensing Symposium (IGARSS)*. Valencia, Spain. July 2018.

[4] S. Lobry, L. Denis, F. Tupin. W. Zhao. Décomposition de séries temporelles dimages SAR pour la détection de changement. *Traitement du Signal (GRETSI, Lavoisier)*. 2017.

[5] W. Zhao, S. Lobry, H. Maître, J-M. Nicolas and F. Tupin. Urban area change detection based on generalized likelihood ratio test. *9th International Workshop on the Analysis of Multitemporal Remote Sensing Images (MultiTemp)*. Bruges, Belgium. June 2017.

---



---

## List of Abbreviations

2SPPB	Two-Step Probabilistic Patch Based denoising
3D	Three Dimensional
AGLRT	Approximate GLRT
AM	Arithmetic Mean image
ANLTF	Adaptive Nonlocal Temporal Filter
AWGN	Additive White Gaussian Noise
BM3D	Block-Matching and 3D filtering
BWAM	Binary Weighted Arithmetic Mean image
CCM	Change Criterion Matrix
CGLRT	Combined GLRT
CNN	Convolutional Neural Network
DAM	Denoised Arithmetic Mean image
DBWAM	Denoised Binary Weighted Arithmetic Mean image
DEM	Digital Elevation Model
EGLRT	Equality GLRT
ENL	Equivalent Number of Looks
FPR	False Positive Rate
GANs	Generative Adversarial Networks
GLRT	Generalised Likelihood Ratio Test
GRD	Ground Range Detected
IW	Interferometric Wide
LEGLRT	Logarithmic version of EGLRT
LMGLRT	Logarithmic version of MGLRT
LRT	Likelihood Ratio Test
LSTM	Long Short-Term Memory
MGLRT	Multitemporal GLRT
MIMOSA	Method for generalIzed Means Ordered Series Analy- sis
ML	Maximum Likelihood estimation
MSAR-BM3D	Multitemporal SAR-BM3D
MSSIM	Mean Structure Similarity Index
MuLoG	MULTi-channel LOGarithm with Gaussian denoising
NL-SAR	A Unified Nonlocal Framework for Resolution- Preserving (Pol)(In)SAR Denoising
NLTF	Nonlocal Temporal Filter
NORCAMA	NORMALized Cut on chANGE criterion MATrix
PATF	Patch based Adaptive Temporal Filter
PCA	Principal component analysis

---

PPB	Probabilistic Patch-Based filter
PSNR	Peak Signal-noise-ratio
RABASAR	RAtio-BAsed multi-temporal SAR images denoising
RBM	Restricted Boltzmann Machine
RCS	Radar Cross Section
REACTIV	Rapid and EAsy Change detection in radar TIme-series by Variation coefficient
ROC	Receiver Operating Characteristic
SAR	Synthetic Aperture Radar
SAR-BM3D	A novel despeckling algorithm for SAR images based on the concepts of nonlocal filtering and wavelet-domain shrinkage
SAR-SIFT	A SIFT-Like Algorithm for SAR Images
$S_{GLR}$	Simplified Generalized Likelihood Ratio
SLC	Single Look Complex
SNR	Signal-to-noise ratio
TPR	True Positive Rate
UTA	Unbiased Temporal Average

---

# Bibliography

- R. Abergel, L. Denis, S. Ladjal, and F. Tupin. Subpixellic methods for sidelobes suppression and strong targets extraction in single look complex SAR images. *IEEE Journal of Selected Topics in Applied Earth Observations and Remote Sensing*, 11(3):759–776, 2018.
- A. Abuelgasim, W. Ross, S. Gopal, and C. Woodcock. Change detection using adaptive fuzzy neural networks: environmental damage assessment after the Gulf War. *Remote Sensing of Environment*, 70(2):208–223, 1999.
- B. Aiazzi, L. Alparone, and S. Baronti. Multiresolution local-statistics speckle filtering based on a ratio Laplacian pyramid. *IEEE Transactions on Geoscience and Remote Sensing*, 36(5):1466–1476, 1998.
- B. Aiazzi, L. Alparone, S. Baronti, A. Garzelli, and C. Zoppetti. Nonparametric change detection in multitemporal SAR images based on mean-shift clustering. *IEEE Transactions on Geoscience and Remote Sensing*, 51(4):2022–2031, 2013.
- V. Akbari, S. Anfinsen, A. Doulgeris, T. Eltoft, G. Moser, and S. Serpico. Polarimetric SAR Change Detection With the Complex Hotelling-Lawley Trace Statistic. *IEEE Transactions on Geoscience and Remote Sensing*, 54(7):3953–3966, 2016.
- L. Alparone, S. Baronti, R. Carl, and C. Puglisi. An adaptive order-statistics filter for SAR images. *International journal of remote sensing*, 17(7):1357–1365, 1996.
- S. Aminikhanghahi and D. Cook. A survey of methods for time series change point detection. *Knowledge and information systems*, 51(2):339–367, 2017.
- D. Amitrano, F. Cecinati, G. Di Martino, A. Iodice, P. Mathieu, D. Riccio, and G. Ruello. An end-user-oriented framework for rgb representation of multitemporal sar images and visual data mining. In *Image and Signal Processing for Remote Sensing XXII*, volume 10004, page 100040Y. International Society for Optics and Photonics, 2016.
- T. Anderson and E. Mathématique. *An introduction to multivariate statistical analysis*, volume 2. Wiley New York, 1958.
- S. Anfinsen, A. Doulgeris, and T. Eltoft. Estimation of the equivalent number of looks in polarimetric Synthetic Aperture Radar imagery. *IEEE Transactions on Geoscience and Remote Sensing*, 47(11):3795–3809, 2009.
- F. Argenti and L. Alparone. Speckle removal from SAR images in the undecimated wavelet domain. *IEEE Transactions on Geoscience and Remote Sensing*, 40(11):2363–2374, 2002.
-

- F. Argenti, A. Lapini, T. Bianchi, and L. Alparone. A tutorial on speckle reduction in Synthetic Aperture Radar images. *IEEE Geoscience and remote sensing magazine*, 1(3):6–35, 2013.
- V. Arsigny, P. Fillard, X. Pennec, and N. Ayache. Log-Euclidean metrics for fast and simple calculus on diffusion tensors. *Magnetic resonance in medicine*, 56(2):411–421, 2006.
- M. Aulard-Macler. Sentinel-1 Product Definition, MDA Technical Note Ref. Technical report, S1-RS-MDA-52-7440, MacDonald, Dettwiler and Associates (MDA): Richmond, BC, Canada, 2012.
- N. Baghdadi and M. Zribi. *Land Surface Remote Sensing in Agriculture and Forest*. Elsevier, 15 Sept. 2016.
- M. Basseville, I. V. Nikiforov, et al. *Detection of abrupt changes: theory and application*, volume 104. Prentice Hall Englewood Cliffs, 1993.
- Y. Bazi, L. Bruzzone, and F. Melgani. An unsupervised approach based on the generalized Gaussian model to automatic change detection in multitemporal SAR images. *IEEE Transactions on Geoscience and Remote Sensing*, 43(4):2972–2982, 2005a.
- Y. Bazi, L. Bruzzone, and F. Melgani. An unsupervised approach based on the generalized Gaussian model to automatic change detection in multitemporal SAR images. *IEEE Transactions on Geoscience and Remote Sensing*, 43(4):874–887, 2005b.
- M. Ben Salah, A. Mitiche, and I. B. Ayed. Multiregion image segmentation by parametric kernel graph cuts. *IEEE Transactions on Image Processing*, 20(2):545–557, 2011.
- J. Berger, T. Patel, D. Shin, J. Piltz, and R. Stone. Computerized stereochronoscopy and alternation flicker to detect optic nerve head contour change. *Ophthalmology*, 107(7):1316–1320, 2000.
- D. Bickel. SAR image effects on coherence and coherence estimation. *Sandia National Laboratories Report, SAND2014-0369*, 2014.
- J. M. Bioucas-Dias and M. A. Figueiredo. Multiplicative noise removal using variable splitting and constrained optimization. *IEEE Transactions on Image Processing*, 19(7):1720–1730, 2010.
- F. Bovolo and L. Bruzzone. A detail-preserving scale-driven approach to change detection in multitemporal SAR images. *IEEE Transactions on Geoscience and Remote Sensing*, 43(12):2963–2972, 2005.
- F. Bovolo and L. Bruzzone. The time variable in data fusion: A change detection perspective. *IEEE Geoscience and Remote Sensing Magazine*, 3(3):8–26, 2015.
- G. Brigot, E. Colin-Koeniguer, A. Plyer, and F. Janez. Adaptation and evaluation of an optical flow method applied to coregistration of forest remote sensing images. *IEEE Journal of Selected Topics in Applied Earth Observations and Remote Sensing*, 9(7):2923–2939, 2016.
-

- 
- D. Brunner, G. Lemoine, and L. Bruzzone. Earthquake damage assessment of buildings using VHR optical and SAR imagery. *IEEE Transactions on Geoscience and Remote Sensing*, 48(5):2403–2420, 2010.
- L. Bruzzone. Multitemporal analysis. 6th ESA advanced training course on land remote sensing, 2015. URL [http://seom.esa.int/landtraining2015/files/Day\\_5/D5T2\\_LTC2015\\_Bruzzone.pdf](http://seom.esa.int/landtraining2015/files/Day_5/D5T2_LTC2015_Bruzzone.pdf).
- L. Bruzzone and F. Bovolo. A novel framework for the design of change-detection systems for very-high-resolution remote sensing images. *Proceedings of the IEEE*, 101(3):609–630, 2013.
- L. Bruzzone and D. F. Prieto. Automatic analysis of the difference image for unsupervised change detection. *IEEE Transactions on Geoscience and Remote Sensing*, 38(3):1171–1182, 2000.
- A. Buades, B. Coll, and J.-M. Morel. A non-local algorithm for image denoising. In *Computer Vision and Pattern Recognition, 2005. CVPR 2005. IEEE Computer Society Conference on*, volume 2, pages 60–65. IEEE, 2005.
- G. Camps-Valls, L. Gómez-Chova, J. Muñoz Marí, J. Rojo-Álvarez, and M. Martínez-Ramón. Kernel-based framework for multitemporal and multisource remote sensing data classification and change detection. *IEEE Transactions on Geoscience and Remote Sensing*, 46(6):1822–1835, 2008.
- N. Casagli, V. Tofani, S. Morelli, W. Frodella, A. Ciampalini, F. Raspini, and E. Intrieri. Remote sensing techniques in landslide mapping and monitoring, keynote lecture. In *Workshop on World Landslide Forum*, pages 1–19. Springer, 2017.
- M. Cha, R. Phillips, P. Wolfe, and C. Richmond. Two-stage change detection for synthetic aperture radar. *IEEE Transactions on Geoscience and Remote Sensing*, 53(12):6547–6560, 2015.
- H. Chen, M. Arora, and P. Varshney. Mutual information-based image registration for remote sensing data. *International Journal of Remote Sensing*, 24(18):3701–3706, 2003.
- G. Chierchia, D. Cozzolino, G. Poggi, and L. Verdoliva. SAR image despeckling through convolutional neural networks. *arXiv preprint arXiv:1704.00275*, 2017a.
- G. Chierchia, M. El Gheche, G. Scarpa, and L. Verdoliva. Multitemporal SAR image despeckling based on block-matching and collaborative filtering. *IEEE Transactions on Geoscience and Remote Sensing*, 55(10):5467–5480, 2017b.
- M. Ciuc, P. Bolon, E. Trouvé, V. Buzuloiu, and J. Rudant. Adaptive-neighborhood speckle removal in multitemporal Synthetic Aperture Radar images. *Applied Optics*, 40(32):5954–5966, 2001.
- D. Coltuc, E. Trouvé, F. Bujor, N. Classeau, and J. Rudant. Time-space filtering of multitemporal SAR images. In *Geoscience and Remote Sensing Symposium, Proceedings. IGARSS 2000.*, 7:2909–2911, 2000.
-

- D. Coltuc, J. Becker, and R. Radescu. A mean based algorithm for the multi-temporal SAR image filtering. In *Geoscience and Remote Sensing Symposium, 2002. IGARSS'02. 2002 IEEE International*, volume 3, pages 1798–1800. IEEE, 2002.
- K. Conradsen, A. Nielsen, J. Schou, and H. Skriver. A test statistic in the complex Wishart distribution and its application to change detection in polarimetric SAR data. *IEEE Transactions on Geoscience and Remote Sensing*, 41(1):4–19, 2003.
- K. Conradsen, A. Nielsen, and H. Skriver. Determining the points of change in time series of polarimetric SAR data. *IEEE Transactions on Geoscience and Remote Sensing*, 54(5):3007–3024, 2016.
- P. Coppin, I. Jonckheere, K. Nackaerts, B. Muys, and E. Lambin. Review article digital change detection methods in ecosystem monitoring: a review. *International journal of remote sensing*, 25(9):1565–1596, 2004.
- D. Corr and A. Rodrigues. Coherent change detection of vehicle movements. 5:2451–2453, 1998.
- S. Cui. *Spatial and temporal SAR image information mining*. PhD thesis, University of Siegen, September 2014. URL <http://dokumentix.ub.uni-siegen.de/opus/volltexte/2014/823/>.
- S. Cui, G. Schwarz, and M. Datcu. A benchmark evaluation of similarity measures for multitemporal SAR image change detection. *IEEE Journal of Selected Topics in Applied Earth Observations and Remote Sensing*, 9(3):1101–1118, 2016.
- K. Dabov, A. Foi, V. Katkovnik, and K. Egiazarian. Image denoising by sparse 3-D transform-domain collaborative filtering. *IEEE Transactions on image processing*, 16(8):2080–2095, 2007.
- R. Dautt, B. Le Saux, A. Boulch, and Y. Gousseau. Urban change detection for multispectral earth observation using convolutional neural networks. In *International Geoscience and Remote Sensing Symposium (IGARSS)*, 2018.
- C. Deledalle, L. Denis, and F. Tupin. Iterative weighted maximum likelihood denoising with probabilistic patch-based weights. *IEEE Transactions on Image Processing*, 18(12):2661–2672, 2009.
- C. Deledalle, L. Denis, and F. Tupin. How to compare noisy patches? Patch similarity beyond Gaussian noise. *International journal of computer vision*, 99(1):86–102, 2012.
- C. Deledalle, L. Denis, G. Poggi, F. Tupin, and L. Verdoliva. Exploiting patch similarity for SAR image processing: the nonlocal paradigm. *IEEE Signal Processing Magazine*, 31(4):69–78, 2014.
- C. Deledalle, L. Denis, F. Tupin, Reigber, and M. A. and Jäger. NL-SAR: A unified non-local framework for resolution-preserving (Pol)(In) SAR denoising. *IEEE Transactions on Geoscience and Remote Sensing*, 53(4):2021–2038, 2015.
- C. Deledalle, L. Denis, S. Tabti, and F. Tupin. MuLoG, or how to apply Gaussian denoisers to multi-channel SAR speckle reduction? *IEEE Transactions on Image Processing*, 26(9):4389–4403, 2017.
-

- 
- F. Dellinger, J. Delon, Y. Gousseau, J. Michel, and F. Tupin. Change detection for high resolution satellite images, based on SIFT descriptors and an a contrario approach. In *Geoscience and Remote Sensing Symposium (IGARSS), 2014 IEEE International*, pages 1281–1284. IEEE, 2014.
- F. Dellinger, J. Delon, Y. Gousseau, J. Michel, and F. Tupin. SAR-SIFT: a SIFT-like algorithm for SAR images. *IEEE Transactions on Geoscience and Remote Sensing*, 53(1):453–466, 2015.
- O. D’Hondt, S. Guillaso, and O. Hellwich. Iterative bilateral filtering of polarimetric SAR data. *IEEE Journal of Selected Topics in Applied Earth Observations and Remote Sensing*, 6(3):1628–1639, 2013.
- E. Domínguez, E. Meier, D. Small, M. Schaepman, L. Bruzzone, and D. Henke. A multisquint framework for change detection in high-resolution multitemporal SAR images. *IEEE Transactions on Geoscience and Remote Sensing*, 56(6):3611–3623, 2018.
- P. Eklund, J. You, and P. Deer. Mining remote sensing image data: an integration of fuzzy set theory and image understanding techniques for environmental change detection. In *Data Mining and Knowledge Discovery: Theory, Tools, and Technology II*, volume 4057, pages 265–273. International Society for Optics and Photonics, 2000.
- S. Foucher. SAR image filtering via learned dictionaries and sparse representations. In *IGARSS (1)*, pages 229–232, 2008.
- S. Foucher, G. Bénéié, and J.-M. Boucher. Multiscale MAP filtering of SAR images. *IEEE Transactions on image processing*, 10(1):49–60, 2001.
- V. Frost, J. Stiles, K. Shanmugan, and J. Holtzman. A model for radar images and its application to adaptive digital filtering of multiplicative noise. *IEEE Transactions on Pattern Analysis and Machine Intelligence*, (2):157–166, 1982.
- L. Gagnon and A. Jouan. Speckle filtering of SAR images: a comparative study between complex-wavelet-based and standard filters. In *Wavelet Applications in Signal and Image Processing V*, volume 3169, pages 80–92. International Society for Optics and Photonics, 1997.
- F. Gao, J. Dong, B. Li, and Q. Xu. Automatic change detection in synthetic aperture radar images based on PCANet. *IEEE Geoscience and Remote Sensing Letters*, 13(12):1792–1796, 2016.
- L. Gomez, M. Buemi, J. Jacobo-Berlles, and M. Mejail. A new image quality index for objectively evaluating despeckling filtering in SAR images. *IEEE Journal of Selected Topics in Applied Earth Observations and Remote Sensing*, 9(3):1297–1307, 2016.
- L. Gomez, R. Ospina, and A. Frery. Unassisted quantitative evaluation of despeckling filters. *Remote Sensing*, 9(4):389, 2017.
- M. Gong, Z. Zhou, and J. Ma. Change detection in synthetic aperture radar images based on image fusion and fuzzy clustering. *IEEE Transactions on Image Processing*, 21(4):2141–2151, 2012.
-

- 
- M. Gong, P. Zhang, L. Su, and J. Liu. Coupled dictionary learning for change detection from multisource data. *IEEE Transactions on Geoscience and Remote Sensing*, 54(12):7077–7091, 2016a.
- M. Gong, J. Zhao, J. Liu, Q. Miao, and L. Jiao. Change detection in synthetic aperture radar images based on deep neural networks. *IEEE transactions on neural networks and learning systems*, 27(1):125–138, 2016b.
- M. Gong, X. Niu, P. Zhang, and Z. Li. Generative adversarial networks for change detection in multispectral imagery. *IEEE Geoscience and Remote Sensing Letters*, 14(12):2310–2314, 2017a.
- M. Gong, H. Yang, and P. Zhang. Feature learning and change feature classification based on deep learning for ternary change detection in SAR images. *ISPRS Journal of Photogrammetry and Remote Sensing*, 129:212–225, 2017b.
- M. Gong, T. Zhan, P. Zhang, and Q. Miao. Superpixel-based difference representation learning for change detection in multispectral remote sensing images. *IEEE Transactions on Geoscience and Remote Sensing*, 55(5):2658–2673, 2017c.
- J. Goodman. Some fundamental properties of speckle. *Journal of the Optical Society of America*, 66(11):1145–1150, 1976.
- J. Goodman. *Speckle phenomena in optics: theory and applications*. Roberts and Company Publishers, 2007.
- H. Griffiths, C. Baker, and D. Adamy. *Stimson’s introduction to airborne radar*. Scitech Pub Incorporated, 2014.
- H. Guo, J. Odegard, M. Lang, R. Gopinath, I. Selesnick, and C. Burrus. Wavelet based speckle reduction with applications to SAR based ATD/R. In *IEEE International Conference on Image Processing*, 1994.
- T. Habib, J. Chanussot, J. Inglada, and G. Mercier. Abrupt change detection on multitemporal remote sensing images: a statistical overview of methodologies applied on real cases. In *Geoscience and Remote Sensing Symposium, 2007. IGARSS 2007. IEEE International*, pages 2593–2596. IEEE, 2007.
- C. Huang, K. Song, S. Kim, J. Townshend, P. Davis, J. Masek, and S. Goward. Use of a dark object concept and support vector machines to automate forest cover change analysis. *Remote Sensing of Environment*, 112(3):970–985, 2008.
- M. Hussain, D. Chen, A. Cheng, H. Wei, and D. Stanley. Change detection from remotely sensed images: From pixel-based to object-based approaches. *ISPRS Journal of Photogrammetry and Remote Sensing*, 80:91–106, 2013.
- J. Inglada and A. Giros. On the possibility of automatic multisensor image registration. *IEEE Transactions on Geoscience and Remote Sensing*, 42(10):2104–2120, 2004.
- J. Inglada and G. Mercier. A new statistical similarity measure for change detection in multitemporal SAR images and its extension to multiscale change analysis. *IEEE transactions on geoscience and remote sensing*, 45(5):1432–1445, 2007.
-

- 
- J. Jung, D. Kim, M. Lavalley, and S. Yun. Coherent Change Detection Using InSAR Temporal Decorrelation Model: A Case Study for Volcanic Ash Detection. *IEEE Transactions on Geoscience and Remote Sensing*, 54(10):5765–5775, 2016.
- S. M. Kay. Fundamentals of statistical signal processing. detection theory, Volume ii. 1998.
- M. Kendall and A. Stuart. The advanced theory of statistics. Vol. 1: Distribution theory. London: Griffin, 1977, 4th ed., 1977.
- C. Kervrann and J. Boulanger. Optimal spatial adaptation for patch-based image denoising. *IEEE Transactions on Image Processing*, 15(10):2866–2878, 2006.
- S. Khan, X. He, F. Porikli, and M. Bennamoun. Forest change detection in incomplete satellite images with deep neural networks. *IEEE Transactions on Geoscience and Remote Sensing*, 55(9):5407–5423, 2017a.
- S. Khan, X. He, F. Porikli, M. Bennamoun, F. Sohel, and R. Togneri. Learning deep structured network for weakly supervised change detection. In *Proc. Int. Joint Conf. Artif. Intell. (IJCAI)*, pages 1–7, 2017b.
- S. Khorram. *Accuracy assessment of remote sensing-derived change detection*. Asprs Publications, 1999.
- E. Koeniguer, A. Boulch, P. Trouvé, and F. Janez. Colored visualization of multitemporal SAR data for change detection : issues and methods. In *Synthetic Aperture Radar (EUSAR), 20018 12th European Conference on. VDE*, 2018a.
- E. Koeniguer, J.-M. Nicolas, B. Pinel-Puysegur, J.-M. Lagrange, and F. Janez. Visualisation des changements sur séries temporelles radar: méthode REACTIV évaluée à l'échelle mondiale sous Google Earth Engine. *Conférence Française de Photogrammétrie et de Télédétection (CFPT)*, 2018b.
- V. Krylov, G. Moser, A. Voisin, S. Serpico, and J. Zerubia. Change detection with synthetic aperture radar images by Wilcoxon statistic likelihood ratio test. In *Image Processing (ICIP), 2012 19th IEEE International Conference on*, pages 2093–2096. IEEE, 2012.
- D. Kuan, A. Sawchuk, T. Strand, and P. Chavel. Adaptive noise smoothing filter for images with signal-dependent noise. *IEEE transactions on pattern analysis and machine intelligence*, (2):165–177, 1985.
- T. Lê, A. Atto, E. Trouvé, and J.-M. Nicolas. Adaptive multitemporal SAR image filtering based on the change detection matrix. *IEEE Geoscience and Remote Sensing Letters*, 11(10):1826–1830, 2014.
- T. Lê, A. Atto, E. Trouvé, A. Solikhin, and V. Pinel. Change detection matrix for multi-temporal filtering and change analysis of SAR and PolSAR image time series. *ISPRS Journal of Photogrammetry and Remote Sensing*, 107:64–76, 2015.
- J. Lee. Digital image enhancement and noise filtering by use of local statistics. *IEEE Transactions on Pattern Analysis and Machine Intelligence*, (2):165–168, 1980.
-

- 
- J. Lee. Refined filtering of image noise using local statistics. *Computer graphics and image processing*, 15(4):380–389, 1981a.
- J. Lee. Speckle analysis and smoothing of Synthetic Aperture Radar images. *Computer graphics and image processing*, 17(1):24–32, 1981b.
- J. Lee. A simple speckle smoothing algorithm for synthetic aperture radar images. *IEEE Transactions on Systems, Man, and Cybernetics*, (1):85–89, 1983.
- J. Lee. Speckle suppression and analysis for Synthetic Aperture Radar images. *Optical engineering*, 25(5):636–643, 1986.
- J. Lee, M. Grunes, and S. Mango. Speckle reduction in multipolarization, multifrequency SAR imagery. *IEEE Transactions on Geoscience and Remote Sensing*, 29(4):535–544, 1991.
- F. Liao, E. Koshelev, M. Milton, Y. Jin, and E. Lu. Change detection by deep neural networks for synthetic aperture radar images. In *Computing, Networking and Communications (ICNC), 2017 International Conference on*, pages 947–951. IEEE, 2017.
- J. Liu, M. Gong, K. Qin, and P. Zhang. A deep convolutional coupling network for change detection based on heterogeneous optical and radar images. *IEEE transactions on neural networks and learning systems*, 2016a.
- J. Liu, M. Gong, J. Zhao, H. Li, and L. Jiao. Difference representation learning using stacked restricted Boltzmann machines for change detection in SAR images. *Soft Computing*, 20(12):4645–4657, 2016b.
- Z. Liu, G. Mercier, J. Dezert, and Q. Pan. Change detection in heterogeneous remote sensing images based on multidimensional evidential reasoning. *IEEE Geoscience and Remote Sensing Letters*, 11(1):168–172, 2014.
- S. Lobry, L. Denis, and F. Tupin. Multi-temporal SAR image decomposition into strong scatterers, background, and speckle. *IEEE Journal of Selected Topics in Applied Earth Observations and Remote Sensing*, 9(8):3419–3429, 2016a.
- S. Lobry, L. Denis, and F. Tupin. Multitemporal SAR image decomposition into strong scatterers, background, and speckle. *IEEE Journal of Selected Topics in Applied Earth Observations and Remote Sensing*, 9(8):3419–3429, 2016b.
- P. Lombardo and C. Oliver. Maximum likelihood approach to the detection of changes between multitemporal SAR images. *IEE Proceedings-Radar, Sonar and Navigation*, 148(4):200–210, 2001.
- P. Lombardo and T. Pellizzeri. Maximum likelihood signal processing techniques to detect a step pattern of change in multitemporal SAR images. *IEEE Transactions on Geoscience and Remote Sensing*, 40(4):853–870, 2002.
- N. Longbotham, F. Pacifici, T. Glenn, A. Zare, M. Volpi, D. Tuia, E. Christophe, J. Michel, J. Inglada, J. Chanussot, and Q. Du. Multi-modal change detection, application to the detection of flooded areas: Outcome of the 2009-2010 data fusion contest. *IEEE Journal of selected topics in applied earth observations and remote sensing*, 5(1):331, 2012.
-

- 
- A. Lopes, E. Nezry, R. Touzi, and H. Laur. Structure detection and statistical adaptive speckle filtering in SAR images. *International Journal of Remote Sensing*, 14(9):1735–1758, 1993.
- H. Lyu, H. Lu, and L. Mou. Learning a transferable change rule from a recurrent neural network for land cover change detection. *Remote Sensing*, 8(6):506, 2016.
- P. Meer, R. Park, and K. Cho. Multiresolution adaptive image smoothing. *CVGIP: Graphical Model and Image Processing*, 56(2):140–148, 1994.
- J. Mercer. Functions of positive and negative type, and their connection with the theory of integral equations. *Philosophical transactions of the royal society of London. Series A, containing papers of a mathematical or physical character*, 209:415–446, 1909.
- G. Mercier, G. Moser, and S. Serpico. Conditional copulas for change detection in heterogeneous remote sensing images. *IEEE Transactions on Geoscience and Remote Sensing*, 46(5):1428–1441, 2008.
- G. Metternicht. Change detection assessment using fuzzy sets and remotely sensed data: an application of topographic map revision. *ISPRS Journal of Photogrammetry and Remote Sensing*, 54(4):221–233, 1999.
- L. Mou, L. Bruzzone, and X. Zhu. Learning spectral-spatial-temporal features via a recurrent convolutional neural network for change detection in multispectral imagery. *arXiv preprint arXiv:1803.02642*, 2018.
- A. Ng, M. Jordan, and Y. Weiss. On spectral clustering: Analysis and an algorithm. In *Advances in neural information processing systems*, pages 849–856, 2002.
- J.-M. Nicolas. Application de la transformée de Mellin: étude des lois statistiques de l'imagerie cohérente. *Rapport de recherche, 2006D010*, 2006.
- J.-M. Nicolas. Application de la transformée de Mellin: étude des lois statistiques de l'imagerie cohérente version corrigée. 2017.
- J.-M. Nicolas and S. Anfinson. Introduction to second kind statistics: Application of log-moments and log-cumulants to the analysis of radar image distributions. *Trait. Signal*, 19(3):139–167, 2002.
- J.-M. Nicolas, E. Trouve, R. Fallourd, F. Vernier, F. Tupin, O. Harant, M. Gay, and L. Moreau. A first comparison of Cosmo-Skymed and TerraSAR-X data over Chamonix Mont-Blanc test-site. In *Geoscience and Remote Sensing Symposium (IGARSS)*, pages 5586–5589, July 2012.
- A. Nielsen, K. Conradsen, and H. Skriver. Change detection in a short time sequence of polarimetric C-band SAR data. In *ESA Living Planet Symposium 2016*. European Space Agency, ESA, 2016.
- C. Oliver and S. Quegan. *Understanding synthetic aperture radar images*. SciTech Publishing, 2004a.
- C. Oliver and S. Quegan. *Understanding Synthetic Aperture Radar images*. SciTech Publishing, 2004b.
-

- N. Otsu. A threshold selection method from gray-level histograms. *IEEE transactions on systems, man, and cybernetics*, 9(1):62–66, 1979.
- J. Park, W. Song, and W. Pearlman. Speckle filtering of SAR images based on adaptive windowing. *IEE Proceedings-Vision, Image and Signal Processing*, 146(4):191–197, 1999.
- S. Parrilli, M. Poderico, C. Angelino, and L. Verdoliva. A nonlocal SAR image denoising algorithm based on LLMMSE wavelet shrinkage. *IEEE Transactions on Geoscience and Remote Sensing*, 50(2):606–616, 2012.
- M. Pham, G. Mercier, and J. Michel. Change detection between SAR images using a pointwise approach and graph theory. *IEEE Transactions on Geoscience and Remote Sensing*, 54(4):2020–2032, 2016.
- A. Plyer, E. Colin-Koeniguer, and F. Weissgerber. A new coregistration algorithm for recent applications on urban SAR images. *IEEE Geoscience and Remote Sensing Letters*, 12(11):2198–2202, 2015.
- M. Preiss and N. Stacy. Coherent change detection: Theoretical description and experimental results. Technical report, DEFENCE SCIENCE AND TECHNOLOGY ORGANISATION EDINBURGH (AUSTRALIA), 2006.
- J. Prendes, M. Chabert, F. Pascal, A. Giros, and J. Tourneret. A new multivariate statistical model for change detection in images acquired by homogeneous and heterogeneous sensors. *IEEE Transactions on Image Processing*, 24(3):799–812, 2015.
- J. Prendes, M. Chabert, F. Pascal, A. Giros, and J. Tourneret. A Bayesian nonparametric model coupled with a Markov random field for change detection in heterogeneous remote sensing images. *SIAM Journal on Imaging Sciences*, 9(4):1889–1921, 2016.
- L. Pulvirenti, M. Chini, N. Pierdicca, and G. Boni. Use of SAR data for detecting flood-water in urban and agricultural areas: The role of the interferometric coherence. *IEEE Transactions on Geoscience and Remote Sensing*, 54(3):1532–1544, 2016.
- N. Quarmby and J. Cushnie. Monitoring urban land cover changes at the urban fringe from SPOT HRV imagery in south-east England. *International Journal of Remote Sensing*, 10(6):953–963, 1989.
- S. Quegan and J. Yu. Filtering of multichannel SAR images. *IEEE Transactions on Geoscience and Remote Sensing*, 39(11):2373–2379, 2001.
- S. Quegan, T. Le Toan, J. Yu, F. Ribbes, and N. Floury. Multitemporal ERS SAR analysis applied to forest mapping. *IEEE Transactions on Geoscience and Remote Sensing*, 38(2):741–753, 2000a.
- S. Quegan, J. Yu, and T. LeToan. Iterated multi-channel filtering of SAR images. In *Geoscience and Remote Sensing Symposium, 2000. Proceedings. IGARSS 2000. IEEE 2000 International*, volume 2, pages 657–659. IEEE, 2000b.
- G. Quin. *Dtection de Changement en Imagerie Radar*. PhD thesis, Tlcom ParisTech, France, May 2011. URL <https://tel.archives-ouvertes.fr/pastel-00597421/>.
-

- 
- G. Quin, B. Pinel-Puysegur, J.-M. Nicolas, and P. Loreaux. MIMOSA: An automatic change detection method for SAR time series. *IEEE Transactions on Geoscience and Remote Sensing*, 52(9):5349–5363, 2014.
- R. Radke, S. Andra, O. Al-Kofahi, and B. Roysam. Image change detection algorithms: a systematic survey. *IEEE transactions on image processing*, 14(3):294–307, 2005.
- P. Riot, A. Almansa, Y. Gousseau, and F. Tupin. A correlation-based dissimilarity measure for noisy patches. In *International Conference on Scale Space and Variational Methods in Computer Vision*, pages 184–195. Springer, 2017.
- P. Rosin and E. Ioannidis. Evaluation of global image thresholding for change detection. *Pattern recognition letters*, 24(14):2345–2356, 2003.
- L. Rudin, P. Lions, and S. Osher. Multiplicative denoising and deblurring: theory and algorithms. In *Geometric Level Set Methods in Imaging, Vision, and Graphics*, pages 103–119. Springer, 2003.
- P. Sahoo, S. Soltani, and A. Wong. A survey of thresholding techniques. *Computer vision, graphics, and image processing*, 41(2):233–260, 1988.
- A. Schubert, D. Small, M. Jehle, and E. Meier. COSMO-SkyMed, TerraSAR-X, and RADARSAT-2 geolocation accuracy after compensation for earth-system effects. In *Geoscience and Remote Sensing Symposium (IGARSS), 2012 IEEE International*, pages 3301–3304. IEEE, 2012.
- A. Schubert, D. Small, N. Miranda, D. Geudtner, and E. Meier. Sentinel-1A product geolocation accuracy: commissioning phase results. *Remote Sensing*, 7(7):9431–9449, 2015.
- E. Schubert, M. Weiler, and H. Kriegel. Signitrend: scalable detection of emerging topics in textual streams by hashed significance thresholds. In *Proceedings of the 20th ACM SIGKDD international conference on Knowledge discovery and data mining*, pages 871–880. ACM, 2014.
- M. Sezgin and B. Sankur. Survey over image thresholding techniques and quantitative performance evaluation. *Journal of Electronic imaging*, 13(1):146–166, 2004.
- J. Shi and J. Malik. Normalized cuts and image segmentation. *IEEE Transactions on pattern analysis and machine intelligence*, 22(8):888–905, 2000.
- D. Small and A. Schubert. Guide to ASAR geocoding. *University of Zurich*, (1), 2008.
- L. Su, M. Gong, P. Zhang, M. Zhang, J. Liu, and H. Yang. Deep learning and mapping based ternary change detection for information unbalanced images. *Pattern Recognition*, 66:213–228, 2017.
- X. Su, C. Deledalle, F. Tupin, and H. Sun. Two-step multitemporal nonlocal means for synthetic aperture radar images. *IEEE Transactions on Geoscience and Remote Sensing*, 52(10):6181–6196, 2014.
- X. Su, C. Deledalle, F. Tupin, and H. Sun. NORCAMA: Change analysis in SAR time series by likelihood ratio change matrix clustering. *ISPRS Journal of Photogrammetry and Remote Sensing*, 101:247–261, 2015.
-

- C. Tison, J.-M. Nicolas, F. Tupin, and H. Maître. A new statistical model for Markovian classification of urban areas in high-resolution SAR images. *IEEE transactions on geoscience and remote sensing*, 42(10):2046–2057, 2004.
- D. Tomowski, M. Ehlers, and S. Klonus. Colour and texture based change detection for urban disaster analysis. In *Urban Remote Sensing Event (JURSE), 2011 Joint*, pages 329–332. IEEE, 2011.
- R. Torres, P. Snoeij, D. Geudtner, D. Bibby, M. Davidson, E. Attema, P. Potin, B. Rommen, N. Floury, M. Brown, and I. Traver. GMES sentinel-1 mission. *Remote Sensing of Environment*, 120:9–24, 2012.
- R. Touati and M. Mignotte. An energy-based model encoding nonlocal pairwise pixel interactions for multisensor change detection. *IEEE Transactions on Geoscience and Remote Sensing*, 56(2):1046–1058, 2018.
- R. Touzi, A. Lopes, and P. Bousquet. A statistical and geometrical edge detector for SAR images. *IEEE Transactions on geoscience and remote sensing*, 26(6):764–773, 1988.
- F. Tung and E. LeDrew. The determination of optimal threshold levels for change detection using various accuracy indexes. *Photogrammetric Engineering and Remote Sensing*, 54(10):1449–1454, 1988.
- F. Tupin. How advanced image processing helps for SAR image restoration and analysis. *IEEE Geoscience and Remote Sensing Newsletter, Cumulative*, (158):10–17, 2011.
- F. Tupin, J. Inglada, and J.-M. Nicolas. *Remote Sensing Imagery*. John Wiley & Sons, 2014.
- G. Vasile, E. Trouvé, J. Lee, and V. Buzuloiu. Intensity-driven adaptive-neighborhood technique for polarimetric and interferometric SAR parameters estimation. *IEEE Transactions on Geoscience and Remote Sensing*, 44(6):1609–1621, 2006.
- J. Vert, K. Tsuda, and B. Schölkopf. A primer on kernel methods. *Kernel Methods in Computational Biology*, pages 35–70, 2004.
- M. Volpi, G. Camps-Valls, and D. Tuia. Spectral alignment of multi-temporal cross-sensor images with automated kernel canonical correlation analysis. *ISPRS Journal of Photogrammetry and Remote Sensing*, 107:50–63, 2015.
- U. Von Luxburg. A tutorial on spectral clustering. *Statistics and computing*, 17(4):395–416, 2007.
- P. Wang, H. Zhang, and V. Patel. SAR image despeckling using a convolutional neural network. *IEEE Signal Processing Letters*, 24(12):1763–1767, 2017a.
- S. Wang, M. Zhou, Z. Liu, Z. Liu, D. Gu, Y. Zang, D. Dong, O. Gevaert, and J. Tian. Central focused convolutional neural networks: Developing a data-driven model for lung nodule segmentation. *Medical image analysis*, 40:172–183, 2017b.
- Z. Wang, A. Bovik, H. Sheikh, and E. Simoncelli. Image quality assessment: from error visibility to structural similarity. *IEEE Transactions on Image Processing*, 13(4):600–612, 2004.
-

- 
- S. Wilks. The large-sample distribution of the likelihood ratio for testing composite hypotheses. *The Annals of Mathematical Statistics*, 9(1):60–62, 1938.
- H. Xie, L. Pierce, and F. Ulaby. Despeckling SAR images using a low-complexity wavelet denoising process. In *Geoscience and Remote Sensing Symposium, 2002. IGARSS'02. 2002 IEEE International*, volume 1, pages 321–324. IEEE, 2002a.
- H. Xie, L. Pierce, and F. Ulaby. Statistical properties of logarithmically transformed speckle. *IEEE Transactions on Geoscience and Remote Sensing*, 40(3):721–727, 2002b.
- J. Yu and S. Quegan. Multi-channel filtering of SAR images. In *Proceedings of the International Geoscience and Remote Sensing Symposium (IGARSS)*, 2000.
- Y. Yu and S. Acton. Speckle reducing anisotropic diffusion. *IEEE Transactions on image processing*, 11(11):1260–1270, 2002.
- H. Zebker. Studying the Earth with interferometric radar. *Computing in Science & Engineering*, 2(3):52–60, 2000.
- Y. Zhan, K. Fu, M. Yan, X. Sun, H. Wang, and X. Qiu. Change detection based on deep siamese convolutional network for optical aerial images. *IEEE Geoscience and Remote Sensing Letters*, 14(10):1845–1849, 2017.
- H. Zhang, M. Gong, P. Zhang, L. Su, and J. Shi. Feature-level change detection using deep representation and feature change analysis for multispectral imagery. *IEEE Geoscience and Remote Sensing Letters*, 13(11):1666–1670, 2016a.
- K. Zhang, W. Zuo, Y. Chen, D. Meng, and L. Zhang. Beyond a Gaussian denoiser: Residual learning of deep CNN for image denoising. *IEEE Transactions on Image Processing*, 26(7):3142–3155, 2017.
- P. Zhang, M. Gong, L. Su, J. Liu, and Z. Li. Change detection based on deep feature representation and mapping transformation for multi-spatial-resolution remote sensing images. *ISPRS Journal of Photogrammetry and Remote Sensing*, 116:24–41, 2016b.
- W. Zhang, Q. Zhang, and C. Yang. Improved bilateral filtering for SAR image despeckling. *Electronics letters*, 47(4):286–288, 2011.
- J. Zhao, M. Gong, J. Liu, and L. Jiao. Deep learning to classify difference image for image change detection. In *Neural Networks (IJCNN), 2014 International Joint Conference on*, pages 411–417. IEEE, 2014.
- W. Zhao, Z. Wang, M. Gong, and J. Liu. Discriminative feature learning for unsupervised change detection in heterogeneous images based on a coupled neural network. *IEEE Transactions on Geoscience and Remote Sensing*, 55(12):7066–7080, 2017.
- W. Zhao, C. Deledalle, L. Denis, H. Maitre, J.-M. Nicolas, and F. Tupin. RABASAR: A fast ratio based multi-temporal SAR despeckling. In *IEEE International Geoscience and Remote Sensing Symposium, IGARSS 2018*, 2018.
- W. Zhao, C. Deledalle, L. Denis, H. Maitre, J.-M. Nicolas, and F. Tupin. Ratio-based multitemporal SAR images denoising: RABASAR. *IEEE Transactions on Geoscience and Remote Sensing*, 2019.
-

B. Zitova and J. Flusser. Image registration methods: a survey. *Image and vision computing*, 21(11):977–1000, 2003.

---